Diagnostics of comprehensive simulations of the chromosphere

Dissertation
zur Erlangung des mathematisch-naturwissenschaftlichen Doktorgrades

“Doctor rerum naturalium”

der Georg-August-Universität Göttingen

im Promotionsstudiengang Physik
der Georg-August University School of Science (GAUSS)

vorgelegt von

Patrick Alexander Ondratschek

aus Ulm, Germany

Göttingen, 2025

Betreuungsausschuss

Prof. Dr. Laurent Gizon
Max-Planck-Institut für Sonnensystemforschung, Göttingen, Germany

Prof. Dr. Sami K. Solanki
Max-Planck-Institut für Sonnensystemforschung, Göttingen, Germany

Dr. Damien Przybylski
Max-Planck-Institut für Sonnensystemforschung, Göttingen, Germany

Mitglieder der Prüfungskommision

Referent: Prof. Dr. Laurent Gizon
Max-Planck-Institut für Sonnensystemforschung, Göttingen, Germany

Korreferent: Prof. Dr. Sami K. Solanki
Max-Planck-Institut für Sonnensystemforschung, Göttingen, Germany

Weitere Mitglieder der Prüfungskommission:

Prof. Dr. Stefan Dreizler
Georg-August-Universität Göttingen Institut für Astrophysik,
Göttingen, Germany

Prof. Dr. Arnulf Quadt
Georg-August-Universität Göttingen, II. Physikalisches Institut,
Göttingen, Germany

Prof. Dr. Fabian Heidrich-Meisner
Georg-August-Universität Göttingen, Institut für Theoretische Physik,
Göttingen, Germany

Prof. Dr. Andreas Dillmann
Deutsches Zentrum für Luft- und Raumfahrt (DLR) Institut für Aerodynamik
und Strömungstechnik, Göttingen, Germany

Tag der mündlichen Prüfung: 13.03.2025

Printed in Germany

Cover figure:
3D rendering of a snapshot from the MURaM-ChE enhanced network simulation. Shown is the temperature with increased contrast in the chromosphere. The figure was created with the vapor visualization software (Li et al. 2019, Sgpearse et al. 2023).

Contents

Acronyms

ALI approximate Lambda iteration 50

ALMA Atacama Large Millimeter/submillimeter Array 30

AR active regions 25

bb bound-bound 32

bf bound-free 32

CHROMIS CHROMospheric Imaging Spectrometer 21

CLV center-to-limb variation 20

CM composite model 102

CRD complete frequency redistribution 42

DFAs profiles averaged over columns showing downflows 108

DOT Dutch open telescope 25

EN enhanced network 11

EoS equation of state 101

EUV extreme ultra violet 101

fb free-bound 32

Summary

The solar chromosphere is a highly dynamic and complex region of the solar atmosphere. It plays an important role in the formation of many of the observed solar features, such as, prominences, spicules, and flares. In addition, the chromosphere provides the mass for the solar wind. The chromosphere can be seen in many aspects as a region of transitions. The plasma, which is mostly neutral in the photosphere, becomes partly ionized in the chromosphere. The temperature starts to increase to values that are higher than in the photosphere. The gas density decreases approximately exponentially. Filling almost the entire space in the chromosphere, the magnetic field becomes dynamically important. Many approximations that are valid in the photosphere such as local thermodynamic equilibrium break down in the chromosphere. The change in physical conditions within a relatively small height difference (typically 1–3 Mm) leads to a highly corrugated region. Interpreting observations of the chromosphere is thus challenging. Therefore, the chromosphere is probably the least understood part of the solar atmosphere.

Nowadays the chromosphere can be observed at high spatial and spectral resolution either from the ground with for example the Swedish-Solar-Telescope, from space for example with the Interface-Region-Imaging-Spectrograph, or from stratospheric balloons with for example the SUNRISE observatory. Interpreting the observations is difficult due to the complex nonequilibrium (NE) and nonlocal formation of chromospheric spectral lines. Numerical simulations of the solar atmosphere can be a valuable tool to tackle this difficulty. Within the last two decades, it became possible to include a comprehensive set of physics in such models to treat the chromosphere with an unprecedented degree of realism. Until recently, Bifrost was the only simulation code that was capable of simulating the chromosphere. While present models of the chromosphere can produce features that are very similar in structure and appearance to those seen in observations, there are still discrepancies. For example, the line widths of simulated chromospheric spectral lines are typically too narrow and their intensities are too faint compared with observations.

In this work, a simulation of the chromosphere is used that was computed with the "Max Planck Institute for Solar System Research/University of Chicago Radiation Magneto-hydrodynamics (MURaM)" code. MURaM is an radiaton-MHD (rMHD) code and was recently upgraded to treat the physics of the chromosphere under non-LTE (NLTE) and NE conditions. The new version is named chromospheric extension of MURaM (MURaM-ChE). An important step in validating a numerical model of the solar chromosphere is the forward modeling of spectral lines. To this end, important chromospheric spectral lines from the simulation have been synthesized and were compared with observations.

In the first project, a simulation of an enhanced network (EN) region was used. Under the approximation of 1.5D radiative transfer (RT), the Mg II h&k lines from this simulation have been synthesized. It was found that the line width is significantly increased compared to previous models. This is attributed to the magnitude of velocity variations along the

line-of-sight (LOS), which is larger in the MURaM-ChE simulation compared to a similar simulation computed with the previously used Bifrost code. The spatially averaged spectra from the MURaM-ChE simulation compare well in terms of line width to the observations, but the peak intensities of the Mg II h&k lines appear a bit too strong. The higher peak intensity in the simulation is partly due to a higher magnetic flux density in the simulation than in the observation but also due to the 1.5D RT approximation, which is known to overestimate the peak intensities.

In the second project, the effects of full 3D RT on the Mg II h&k spectra have been studied as well as correlations between spectral line properties and the underlying atmosphere in the same simulation as in the first project. 3D RT is computationally more expensive than 1.5D RT. The synthesis of a spectral line in a single snapshot from the simulation can be as expensive as the rMHD simulation itself. The computations presented in this project confirmed, however, that 3D RT effects play an important role in the synthesis of the Mg II h&k lines and must be taken into account. In particular, the differences between 3D and 1.5D RT are larger in MURaM-ChE than in the Bifrost model. Additionally, it was found that correlations between spectral line properties and the underlying atmosphere are valid, which were found by similar studies with the Bifrost model. The scatter in these correlations is, however, larger in the more dynamic MURaM-ChE simulation. A general finding of the studies on the Mg II h&k lines is that in the MURaM-ChE model, a reasonably good match of the line profiles with the observations can be achieved at a relatively moderate spatial resolution of the simulation of 23.46 km (horizontal) and 20 km (vertical).

In the third project, the Ca II λ854.2 nm spectral line has been synthesized. This line forms in the lower to middle chromosphere and is widely used for magnetic field measurements in the chromosphere. The line itself has an asymmetric shape whose origin is under debate in the literature. On the one hand, the dynamic motions of the chromosphere might lead to the asymmetry, on the other hand, it could be due to isotopic splitting as there are six stable isotopes of calcium in the solar atmosphere. The width of this line could not be reproduced in previous models, which typically resulted in too-narrow line profiles. It was found that both the velocities and the isotopic splitting contribute significantly to the observed asymmetric line shape. The spatially averaged line profile of Ca II λ854.2 nm computed from the MURaM-ChE simulation shows a relatively close match with an observed line profile both in line width and asymmetry when the effect of isotopic splitting is taken into account. The close match of the line width is, similar to the findings for the Mg II h&k lines, a result of the dynamic motions in the MURaM-ChE simulation.

This work contributes to the scientific literature in that it presents the first forward-modeled spectra of the new chromospheric extension of MURaM. The improved match with observations helps to interpret complex chromospheric spectral lines. Additionally, the here presented findings demonstrate the need to properly model the large velocities in the solar chromosphere, to account for horizontal RT effects in strong lines with considerable scattering, as well as to take the isotopic splitting into account for elements for which multiple isotopes are present in the solar atmosphere.

Keywords: Solar atmosphere: (QB528), Solar chromosphere: (QB528), Radiative transfer (175.25.R3), Simulation methods (541.15.S5), MURaM-ChE code

Zusammenfassung

Die Chromosphäre ist ein hochdynamischer und komplexer Bestandteil der Sonnenatmosphäre. Sie spielt eine wichtige Rolle bei der Bildung vieler beobachteter Sonnenphänomene, wie z.B. Protuberanzen, Spiculen und Flares. Darüber hinaus liefert die Chromosphäre die Masse für den Sonnenwind. Die Chromosphäre kann in vieler Hinsicht als eine Region von Übergängen betrachtet werden. Das Plasma, das in der Photosphäre größtenteils neutral ist, wird in der Chromosphäre teilweise ionisiert. Die Temperatur beginnt, Werte zu erreichen, die höher sind als in der Photosphäre. Die Gasdichte nimmt etwa exponentiell ab. Das Magnetfeld füllt beinahe den gesamten Raum in der Chromosphäre und nimmt Einfluss auf die Dynamik des chromosphärischen Gases. Viele Annahmen, die in der Photosphäre gültig sind, wie z.B. das lokale thermodynamische Gleichgewicht, sind in der Chromosphäre nicht länger gültig. Der Wechsel in den physikalischen Bedingungen innerhalb einer relativ kleinen Atmosphärenschicht (typischerweise 1–3 Mm) führt zu höchst inhomogenen Strukturen. Die Interpretation von Beobachtungen der Chromosphäre ist daher schwierig, weshalb die Chromosphäre das wahrscheinlich am wenigsten verstandene Gebiet der Sonnenatmosphäre ist.

Heutzutage kann die Chromosphäre mit hoher räumlicher und spektraler Auflösung beobachtet werden, entweder von der Erde aus mit z.B. dem Swedish 1 m Solar Telescope (SST), von Weltraumobservatorien wie z.B. dem Interface-Region-Imaging-Spectrograph (IRIS) oder von stratosphärischen Ballonen mit z.B. dem SUNRISE-Observatorium. Die Interpretation der Beobachtungen ist jedoch aufgrund der komplexen Formierung chromosphärischer Spektrallinien schwierig. Numerische Simulationen der Sonnenatmosphäre können ein wertvolles Werkzeug sein, um diese Schwierigkeit zu überwinden. Im Laufe der letzten zwei Jahrzehnte wurde es möglich, eine umfassende physikalische Beschreibung in solchen Modellen zu berücksichtigen, um die Chromosphäre mit einem hohen Grad an Realismus zu simulieren. Bis vor Kurzem war Bifrost der einzige Simulationscode, der in der Lage war, die Chromosphäre in dieser Art zu simulieren. Während die gegenwärtigen Modelle der Chromosphäre in der Lage sind, Merkmale zu produzieren, die sehr ähnlich in Struktur und Erscheinung zu denen in den Beobachtungen sind, gibt es immer noch Unterschiede. Zum Beispiel sind die Linienbreiten der simulierten chromosphärischen Spektrallinien im Vergleich zu den Beobachtungen typischerweise zu schmal und ihre Intensitäten sind zu schwach.

In dieser Arbeit wurde eine Simulation der Chromosphäre verwendet, die mit dem "MURaM"-Code berechnet wurde. Muram ist ein radiativer magnetohydrodynamischer (rMHD) Code und wurde kürzlich erweitert, um die Physik der Chromosphäre unter NLTE- und NE-Bedingungen zu simulieren. Die neue Version heißt MURaM-ChE. Ein wichtiger Schritt bei der Validierung eines numerischen Modells der Sonnen-Chromosphäre ist die Berechnung von synthetischen Spektrallinien und deren Vergleich mit Beobachtungen. Zu diesem Zweck wurden in dieser Arbeit wichtige chromosphärische Spektrallinien aus der Simulation berechnet und mit Beobachtungen verglichen.

In dem ersten Projekt wurden, unter der Annahme von 1,5D Strahlungstransport, die Mg II h&k Linien von der Simulation berechnet. Es wurder herausgefunden, dass die Linienbreite signifikant erhöht ist im Vergleich zu vorherigen Modellen. Dies wird auf die in der Simulation vorhanden Geschwindigkeitsvariationen entlang der Sichtlinie zurückgeführt, die in der MURaM-ChE Simulation größer sind als in einer ähnlichen Simulation, die mit dem zuvor erwähnten Bifrost-Code berechnet wurden. Die räumlich gemittelten Spektren aus der MURaM-ChE Simulation vergleichen sich gut in Bezug auf Linienbreite mit den Beobachtungen, aber die Intensitäten in den Peaks der Mg II h&k Linien erscheinen etwas zu hoch. Die höhere Peakintensität in der Simulation ist teilweise auf eine höhere magnetische Flussdichte in der Simulation im Vergleich zu der verwendeten Beobachtung zurückzuführen. Aber auch der 1,5D Strahlungstransport Ansatz ist dafür bekannt, die Peakintensititäten zu überschätzen.

In dem zweiten Projekt wurden die Auswirkungen von 3D Strahlungstransport auf die Mg II h&k Spektren sowie Korrelationen zwischen Spektrallinien-Eigenschaften und der zugrunde liegenden Atmosphäre in derselben Simulation wie im ersten Projekt untersucht. 3D Strahlungstransport ist kostenintensiver als 1,5D Strahlungstransport. Die Berechnung einer Spektrallinie in einem einzelnen Snapshot aus der Simulation kann so teuer sein wie die rMHD-Simulation selbst. Die durchgeführten Berechnungen bestätigten jedoch, dass 3D Effekte des Strahlungstransports eine wichtige Rolle bei der Formierung der Mg II h&k Linien spielen und berücksichtigt werden müssen. Insbesondere sind die Unterschiede zwischen 3D- und 1,5D Strahlungstransport in MURaM-ChE größer als in dem Bifrost-Modell. Darüber hinaus wurde herausgefunden, dass viele Korrelationen zwischen Spektrallinien-Eigenschaften und der zugrunde liegenden Atmosphäre, die in ähnlichen Studien mit dem Bifrost-Modell gefunden wurden, auch in der dynamischeren MURaM-ChE Simulation gültig sind. Der Streuung in diesen Korrelationen ist jedoch größer in der MURaM-ChE Simulation. Eine allgemeine Erkenntnis dieser Untersuchungen über die Mg II h&k Linien ist, dass in dem MURaM-ChEModell eine gute Übereinstimmung der Linienprofile mit den Beobachtungen bei einer relativ moderaten räumlichen Auflösung der Simulation von 23,46 km (horizontal) und 20 km (vertikal) erreicht werden kann.

In dem dritten Projekt wurde die Ca II λ854.2 nm Linie modelliert. Diese Linie formiert sich in der unteren bis mittleren Chromosphäre und wird für Magnetfeldmessungen in der Chromosphäre verwendet. Die Linie selbst hat eine asymmetrische Form, deren Ursprung in der wissenschaftlichen Literatur umstritten ist. Einerseits könnten die dynamischen Bewegungen der Chromosphäre zu der Asymmetrie führen, andererseits könnte sie durch die Zusammenwirkung mehrerer Isotope verursacht werden, da es in der Sonnenatmosphäre sechs stabile Kalziumisotope gibt. Die Breite dieser Linie konnte in vorherigen Modellen nicht reproduziert werden, was typischerweise in zu schmalen Linienprofilen resultierte. Es wurde herausgefunden, dass sowohl die dynamischen Bewegungen des Gases als auch die Zusammenwirkung der mehreren Isotope signifikant zum beobachteten asymmetrischen Linienprofil beitragen. Das räumlich gemittelte Linienprofil der Ca II λ854.2 nm Linie, das aus der MURaM-ChE Simulation berechnet wurde, zeigt eine relativ gute Übereinstimmung mit einem beobachteten Linienprofil, sowohl in Bezug auf die Linienbreite als auch auf die Asymmetrie, wenn mehrere Isotope berücksichtigt werden. Die gute Übereinstimmung der Linienbreite ist ähnlich wie bei den Untersuchungen zu den Mg II h&k Linien, ein Ergebnis der dynamischen Bewegungen in der MURaM-ChE Simulation.

Diese Arbeit trägt zur wissenschaftlichen Literatur bei, indem sie die ersten berechneten Spektren der neuen chromosphärischen Erweiterung von MURaM präsentiert. Die verbesserte Übereinstimmung mit den Beobachtungen hilft bei der Interpretation kom-

plexer chromosphärischer Spektrallinien. Darüber hinaus zeigen diese Ergebnisse die Notwendigkeit, die dynamischen Bewegungen in der Chromosphäre richtig zu modellieren und die horizontalen Strahlungstransport Effekte in starken Linien mit beträchtlicher Streuung zu berücksichtigen. Zudem sollten alle wichtigen Isotope eines Elements, die in der Sonnenatmosphäre vorkommen, bei der Modellierung der Spektrallinien berücksichtigt werden.

1. Introduction

The Sun has fascinated mankind since antiquity, likely even earlier. The curiosity involved in studying the bright shining star in the sky has led to significant contributions to knowledge ranging from understanding basic physical principles to our world picture of the universe. In a way, the Sun can be seen as a common star. It was formed in a collapsing molecular cloud, and approximately 4.6 billion years ago, the Sun began to fuse Hydrogen. This evolutionary stage is called the main sequence based on the classification of stellar luminosities. The fate of every star is mostly set by its initial mass. As long as hydrogen is fused stably, the star does not change significantly in terms of its radius or luminosity. However, not everything remains unchanged. The rotation of the star, together with other motions in the convection zone, drives a dynamo that leads to the star being magnetized. The magnetic field, in turn, leads the atmosphere of stars with outer convection zones, stars like the Sun, to be dynamic. It is the interaction of the Sun's dynamic atmosphere with the solar system that underlines the importance of studying the Sun still today.

Sunspots, dark patches on the solar surface, are direct manifestations of the existence and time evolution of the magnetic field in the Sun's interior and atmosphere. The number of Sunspots on the solar surface follows a roughly 11-year cycle (Schwabe 1844, Wolf 1852). The associated time variation in the Sun's magnetic field follows a roughly 22-year cycle in which the polarity of the magnetic field flips, that is, the north and south poles are exchanged. Most Sunspots have lifetimes from hours to days (Solanki 2003), indicating that near the surface and in the heliosphere the magnetic field is highly time variable. Imprints of the magnetic field on the solar atmosphere can be seen during a solar eclipse. While the moon obscures most of the solar disk, a large-scale structure becomes visible surrounding the Sun, the solar corona. In its simplest form it can look like iron files aligned by a dipole magnet, but it can be much more complex. From the corona on, the solar magnetic field permeates the whole solar system, it interacts with the Earth's magnetic field and shields us from the interstellar medium at the very outskirts of the solar system, the heliopause.

A more detailed view during an eclipse reveals yet another part of the solar atmosphere. A thin red ring, caused by Hα emission, sometimes accompanied by irregular loop-like structures, called prominences, that extend further out. Named after its colorful appearance, the chromosphere can be seen as the interface between the lower solar atmosphere and the corona. Early observations during solar eclipses indicated dynamic processes on time scales of a few minutes (see e.g., Roberts 1945).

Being between the photosphere and the corona, the chromosphere is a place between multiple extremes. In the lower solar atmosphere, the dynamics are mostly dominated by the forces in the plasma through oscillations and turbulent convection, except in regions of very strong magnetic fields, such as Sunspots. Above the photosphere, the plasma density decreases approximately exponentially. In the chromosphere, the magnetic field begins to prevail over the dynamics. Consequently, the chromosphere is rather corrugated and

displays considerable fine structure. The source of the chromospheric fine structure is not the only thing about the chromosphere that is not well understood. For example, the Hα emission at the solar limb requires temperatures higher than predicted by radiative equilibrium estimations. This increase of temperature in the chromosphere, without a detailed understanding of the heating mechanisms, is referred to as the chromospheric heating problem (see e.g., Carlsson et al. 2019).

Studying the chromosphere is based on observations of strong spectral lines that form in this relatively thin part of the solar atmosphere. There are, however, only comparatively few spectral lines that are strong enough to sense the properties of the plasma in the bulk of the chromosphere. Some of these lines are in the optical part of the spectrum and are thus accessible from ground-based telescopes. Prominent examples are hydrogen Hα, helium 10830 Å, Ca II H & K, and the Ca II infrared triplet lines some of which can be observed for example with the CRisp Imaging SpectroPolarimeter (Scharmer et al. 2008). Although ground-based telescopes have numerous advantages, they are, in addition to the restricted atmospheric window, limited by seeing conditions. An alternative are sounding-rocket experiments or balloon-borne observatories such as the SUNRISE mission (Solanki et al. 2010, 2012, Barthol et al. 2011, Solanki et al. 2017), which combine the advantages of ground and space-based observatories, including also spectral lines in the ultraviolet (UV) such as Mg II h&k. The Interface Region Imaging Spectrometer (IRIS) satellite (De Pontieu et al. 2014), launched in 2013, is currently the main source of Mg II h&k observations and of other lines in the UV.

Sophisticated models of the solar atmosphere are needed to interpret observations of ever-increasing spatial and temporal resolution. The ultimate goal of these models is the prediction of features comparable with observations in their spatial appearance but also in their observed spectrum. The semi-empirical models of Vernazza et al. (1981, VAL models) or Fontenla et al. (1993, FAL models) use a one-dimensional geometry and are aimed to reproduce temporally and spatially averaged conditions on the Sun. Pioneered by Nordlund (1982) there exist nowadays simulations that aim to model the solar atmosphere in three-dimensional geometry, including a convection zone. Comprehensive simulations must include the interaction of radiation with matter. The equations describing the interaction between light and matter were developed earlier (see e.g., Mihalas 1978) but to reproduce the complexity observed in the solar atmosphere requires a numerical solution of these equations. This is computationally expensive in accordance with the nonlocal and nonlinear nature of RT. The simulations of Carlsson & Stein (2002) are well-known examples that include the radiation-matter interaction rather completely but are restricted to one-dimensional geometry. Bifrost (Gudiksen et al. 2011) is a three-dimensional rMHD code capable of modeling the solar atmosphere, including a convection zone, and contains prescriptions for a NE treatment of RT in the chromosphere. To compare spectra resulting from the model with observations, the computed spectra have to undergo a postprocessing step from the simulation output. Bifrost models were used in literature to study line formation in the solar chromosphere for a range of chromospheric spectral lines (see e.g., the series formation of IRIS diagnostics). While the Bifrost simulations reproduce the overall shape of observed features, there are discrepancies in the details of the computed spectra. For example, the predicted spectral lines are too narrow and too faint when compared with observations (Carlsson et al. 2016).

In this work, I use a model of the solar atmosphere simulated with the recently developed MURaM-ChE code to forward model chromospheric spectral lines. This is a crucial step in validating the model. The previous coronal extension of MURaM (Rempel 2017) has been used to study the chromosphere and corona under the assumption of local thermodynamic equilibrium (LTE). This includes the modeling of flares (Cheung et al.

2019), solar campfires (Chen et al. 2021), line Doppler shifts (Chen et al. 2022), and coronal loop turbulence (Breu et al. 2022).

The chromospheric extension includes a NE treatment for hydrogen ionization and NLTE modeling of radiative line losses.

This thesis is structured as follows. In the rest of Chapt. 1 I will provide the necessary background to this work. Followed by this, I present in Chapt. 2 forward modeled spectra of the Mg II h&k lines in the 1.5D RT approach. Chapt. 3 deals with 3D RT effects in the forward modeled Mg II h&k spectra and correlations between spectral features and atmospheric properties. In Chapt. 4, results of the Ca II λ854.2 nm line are presented. After this, a summary, conclusions, and an outlook are presented in Chapt. 5.

1.1. The Sun

In this section, I will briefly describe the interior (Sect. 1.1.1) and atmosphere (Sect. 1.1.2) of the Sun to provide the necessary context for this thesis. After this, I will provide some background on chromospheric diagnostics that are relevant to this work. For the general structure of the Sun and its atmosphere I refer to Priest (2014). A schematic overview of the Sun's structure is presented in Figure 1.1.

1.1.1 Solar interior

The Sun is an almost perfect sphere consisting mostly of hydrogen and helium. Consisting of plasma, there is no well-defined solar surface as on a rocky planet like the Earth. The solar radius of $R_\odot \approx 6.957 \times 10^5$ km (Seriu & Wu 2008) can be measured for example from the intensity profile at the limb of the Sun. With a mass of $M_\odot \approx 1.98 \times 10^{30}$ kg the Sun's average density is only $\rho_{\odot,\mathrm{mean}} \approx 1400\,\mathrm{kg\,m^{-3}}$, that is only slightly higher than water. The density profile and the structure inside the Sun is, however, not homogeneous but depth dependent. In the innermost core ($r \leq 0.2\,R_\odot$) the density, pressure, and temperature are high enough to fuse hydrogen atoms to helium. The energy is released in the form of electron neutrinos and gamma rays. Because the neutrinos hardly interact with the solar interior they can escape unhindered into space. This means any solar neutrinos that we can detect on Earth were produced approximately eight minutes before in the deep interior of the Sun. Photons interact with the surrounding matter and it can take several 10^5 years until they reach the surface. Within $r \leq 0.7\,R_\odot$ the energy is mainly transported through radiation towards the outer layers of the Sun. Above this radiation zone, there is a transition between solid body rotation in the inner part of the Sun and the layer above. This layer is called tachocline and is just below the convection zone which rotates differentially. The shear between the two layers is an important candidate for the driving of the dynamo that generates the Sun's magnetic field. In the convection zone, the plasma rises in large cells. At the top of the convection zone, the plasma cools via radiation and sinks again.

1.1.2 Solar atmosphere

The solar atmosphere can be schematically subdivided into the photosphere, chromosphere, transition region, and corona. The different parts should not be understood as clearly separated layers that only change as a function of radius. Instead, they show detailed fine structure as a result of convection, magnetism, and propagating wavefronts. In the following, I describe these atmospheric components in the order they occur from the bottom of the atmosphere upwards.

Photosphere From the top of the convection zone, the photosphere extends to roughly 400 km in altitude. Within this height range the atmosphere cools from $\approx$ 6000 K to 4000 K. This part of the atmosphere is of special importance as most of the radiation is escaping from there with a spectral power maximum at a wavelength of 500 nm. From the light emitted in the photosphere the effective temperature T_eff, Gravity, radius, rotation, and chemical composition of the Sun can be obtained. The inference of the chemical abundance of the Sun (see e.g., Asplund et al. 2009) and other stars is of high importance for studying the chemical evolution of the Universe in a cosmological context. Observations of the photosphere show a center-to-limb variation (CLV) where the solar disk appears brighter in the center of the disk than at the limb. This is because light rays pointing toward the solar limb travel a larger distance through the atmosphere. Therefore, only the higher cooler layers of the photosphere are visible, resulting in a decrease in intensity. The CLV

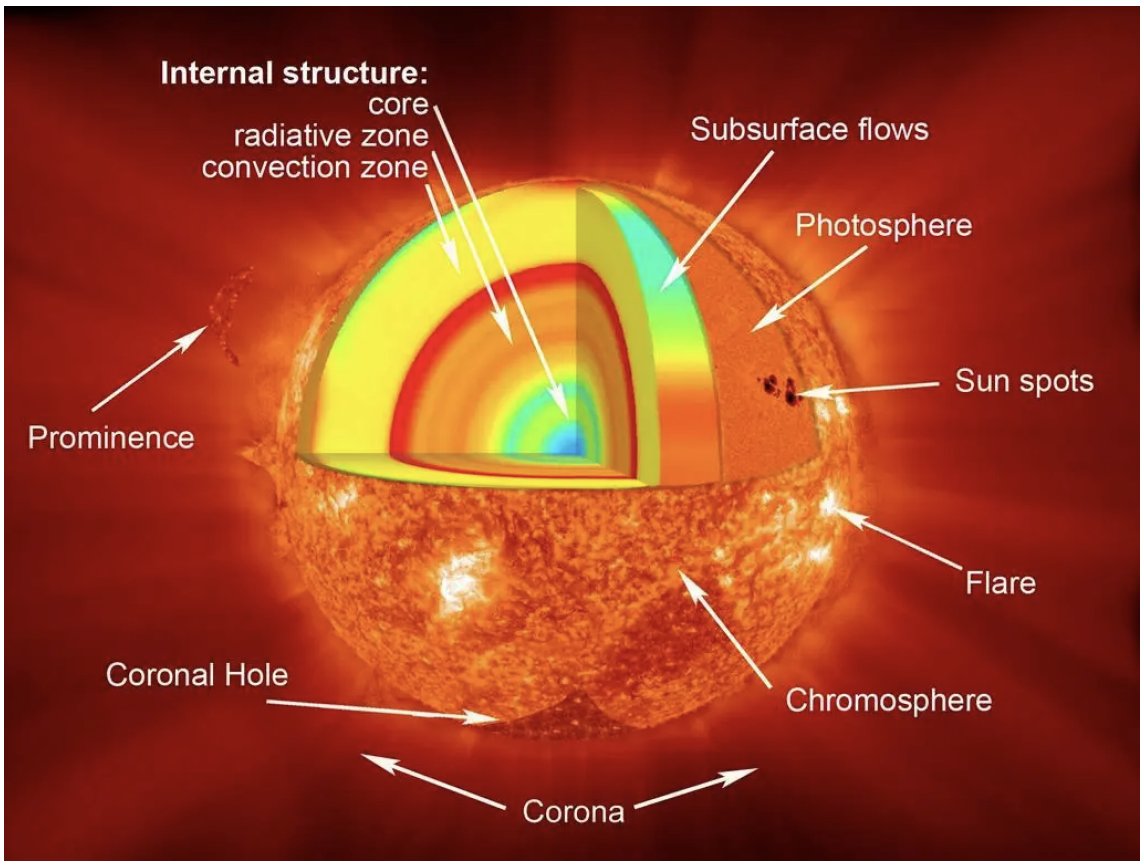

Figure 1.1: Schematic overview of the Sun. The image shows a composite image of different layers of the Sun. The interior consists of the core, the radiation zone, and the convection zone. The photosphere begins where the solar plasma becomes almost fully transparent, and the energy can escape in the form of radiation. The chromosphere begins above a temperature minimum in the photosphere. After a gradual temperature increase in the chromosphere, the temperature rises to millions of kelvin in the corona. In this outermost layer of the solar atmosphere hot loop-like structures are visible which can be birthplaces of the solar wind and coronal mass ejections. Image credit: NASA/Goddard.

effect is more pronounced in the blue than in the red part of the spectrum due mainly to the temperature dependence of the Planck function. The photosphere itself is not homogeneous but shows small granular structures resulting from the convection cells. The left panel of Fig. 1.2 shows an example of the granulation pattern observed in the wing of the Ca II K line with the CHROMospheric Imaging Spectrometer (CHROMIS) instrument at the SST (Scharmer et al. 2003). The darker web-like structure is called intergranular lanes. There are small bright features inside the intergranular lanes, which are called bright points. Here the magnetic field can reach values of up to 1-2 kG. The convective motions result in asymmetric line profiles which can be used as an indicator for convection in other stars.

During high-activity phases of the solar cycle, the convective patterns are accompanied by dark patches, called Sunspots. These features are direct indicators of the solar magnetic field interacting with the solar atmosphere. In Sunspots, the magnetic field is strong enough to suppress the convective motions. The lack of effective heat transport inside a Sunspot leads, therefore, to lower radiative intensities. An example of a Sunspot observed in the Fe I 6302Å spectral line with the Solar Optical Universal Polimeter (SOUP) instrument at the SST is shown in the right panel of Fig. 1.2. In the center of a Sunspot, called the umbra, the magnetic field is almost vertical. The umbra is surrounded by a filamentary

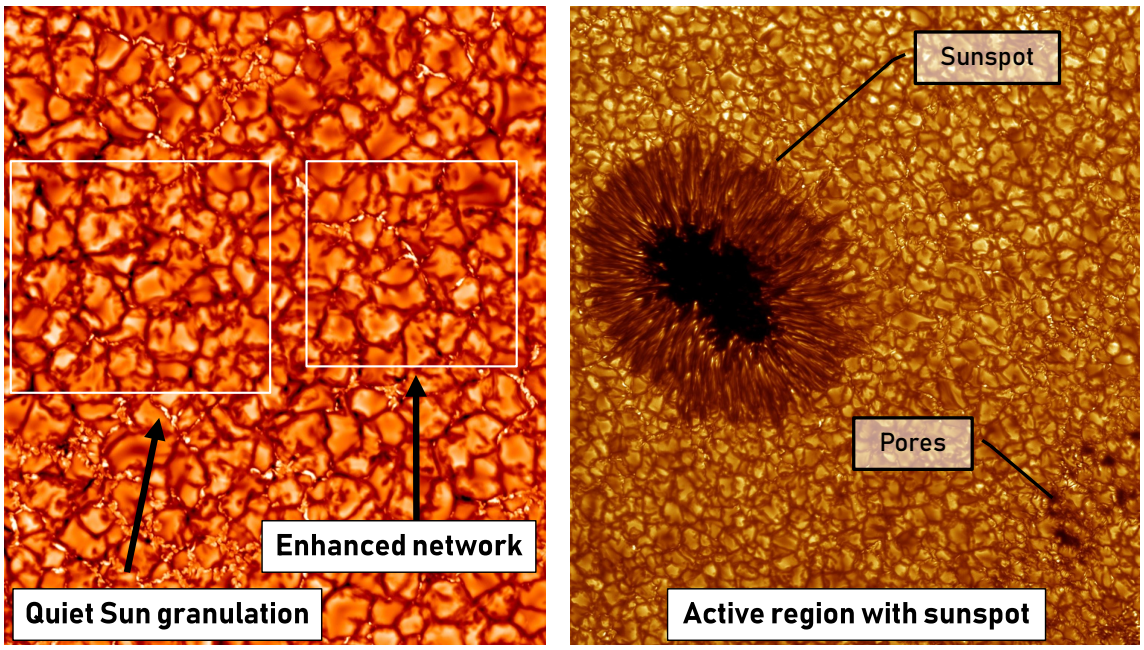

Figure 1.2: Left: Granulation pattern in the QS and the enhanced magnetic network. The image was observed in the wing of the Ca II K line with the CHROMIS instrument at the SST. Image credit: Vasco Henriques and Ainar Drews (ITA, University of Oslo). Right: Sunspot in an active region. The observation was taken with the SOUP instrument at the SST. Image credit: Göran Scharmer, Kai Langhans, Mats Löfdahl (ISP/Stockholm).

structure called the penumbra, which is less dark and harbors a more horizontal magnetic field. There exist also other features, which appear darker than the surroundings, called pores. These features have no penumbra. Sunspots and pores are embedded in regions that show mean magnetic fields of $\approx 100\,\mathrm{G}$, which are formed in intense flux tubes. These regions are called plage and appear bright in Hα observations higher up in the atmosphere. An example can be seen in a full disk observation taken by Global Oscillation Network Group (GONG) instruments in Fig. 1.4.

The quiet Sun (QS) is the area on the solar surface outside of plages, pores, and Sunspots. There are however strong magnetic fields harbored in the QS. The magnetic network exists at the boundaries of supergranular cells, which reach diameters of up to 30 Mm. In the network, the magnetic field is organized in flux tubes with field strengths of the order of kG. Inside the supergranular cells, the magnetic field is organized in the internetwork. For a recent review of QS magnetic fields see Bellot Rubio & Orozco Suárez (2019).

Chromosphere The chromosphere is, in many respects, a complicated and unresolved part of the solar atmosphere. It remains the missing puzzle piece to resolve open questions in solar physics, such as the mass and energy transport through the atmosphere as well as the heating of the same. After decreasing to a minimum value of $T_{\mathrm{min}} \approx 4,000\,\mathrm{K}$ in the photosphere, the temperature increases again with height. This is in contrast to the radiative equilibrium assumption, where the temperature is expected to decrease with distance. The name chromosphere was given because of its red color produced by Hα light, which is visible during a solar eclipse around the disk (Lockyer 1868). While the emission of the Hα light requires a certain temperature, observations of the CO bands suggest that at chromospheric heights, extremely cool gas coexists (Solanki et al. 1994). The chromosphere extends approximately up to $\approx 3\,\mathrm{Mm}$ above the photosphere, although

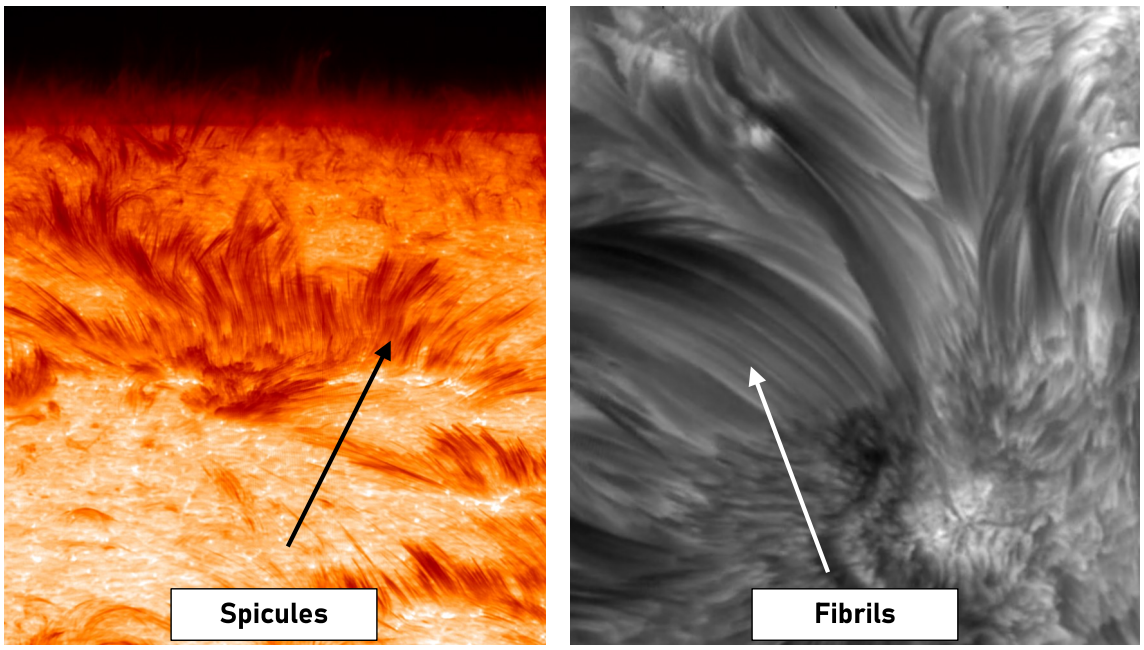

Figure 1.3: Left: Observation of spicules near the limb of the Sun. The image was observed with the SOUP instrument at the SST in red wing of the Hα line. Image credit: Luc Rouppe van der Voort (ITA, University of Oslo). Observation: Oystein Langangen (ITA, University of Oslo). The picture has been adapted. Right: Observation of fibrils in the Hα spectral line observed at the SST. Image credit: Michiel van Noort and Luc Rouppe van der Voort (ITA, University of Oslo), adapted. The picture is a still from a movie and has been adapted. Both images were taken from `https://est-east.eu/solar-gallery` with permission.

this upper boundary is extremely variable, ranging from a thousand km to up to 10 Mm above the solar surface. Observations of the fine structure during an eclipse indicate the irregular shape of the chromosphere, which changes over a time scale of minutes (Roberts 1945). From the photosphere upwards, the plasma density decreases approximately exponentially with a scale height of $\approx 100\,\mathrm{km}$. At chromospheric heights, the magnetic pressure decreases less rapidly with height than the plasma pressure (Solanki & Steiner 1990), and therefore, the magnetic field becomes dynamically important. In astrophysics, the ratio of gas to magnetic pressure is expressed by

$$\text{plasma}\,\beta = \frac{\text{gas pressure}}{\text{magnetic pressure}}. \tag{1.1}$$

In the chromosphere the plasma β coefficient changes from $\beta > 1$ to $\beta < 1$. In addition, in the chromosphere, the plasma becomes partly ionized, in contrast to the photosphere, where the plasma is mostly neutral. The change of the above-mentioned quantities within the chromosphere makes it a highly complex environment that is challenging to interpret. For example, the exact mechanisms that heat the chromosphere are only poorly understood. Withbroe & Noyes (1977) estimated that some $4,000\,\mathrm{W\,m^{-2}}$ are needed to heat the quiet chromosphere.

Possible explanations are that the chromosphere is heated through the dissipation of acoustic and MHD waves and small-scale jets, called spicules. These features can be observed in the wing of the Hα line and are best visible towards the limb. An example observation taken with the SOUP instrument at SST is shown in Fig. 1.3a. They can reach heights of up to 6 Mm and can have speeds of up to $100\,\mathrm{km\,s^{-1}}$. They are considered to play an important role in the mass and energy balance of the upper solar atmosphere.

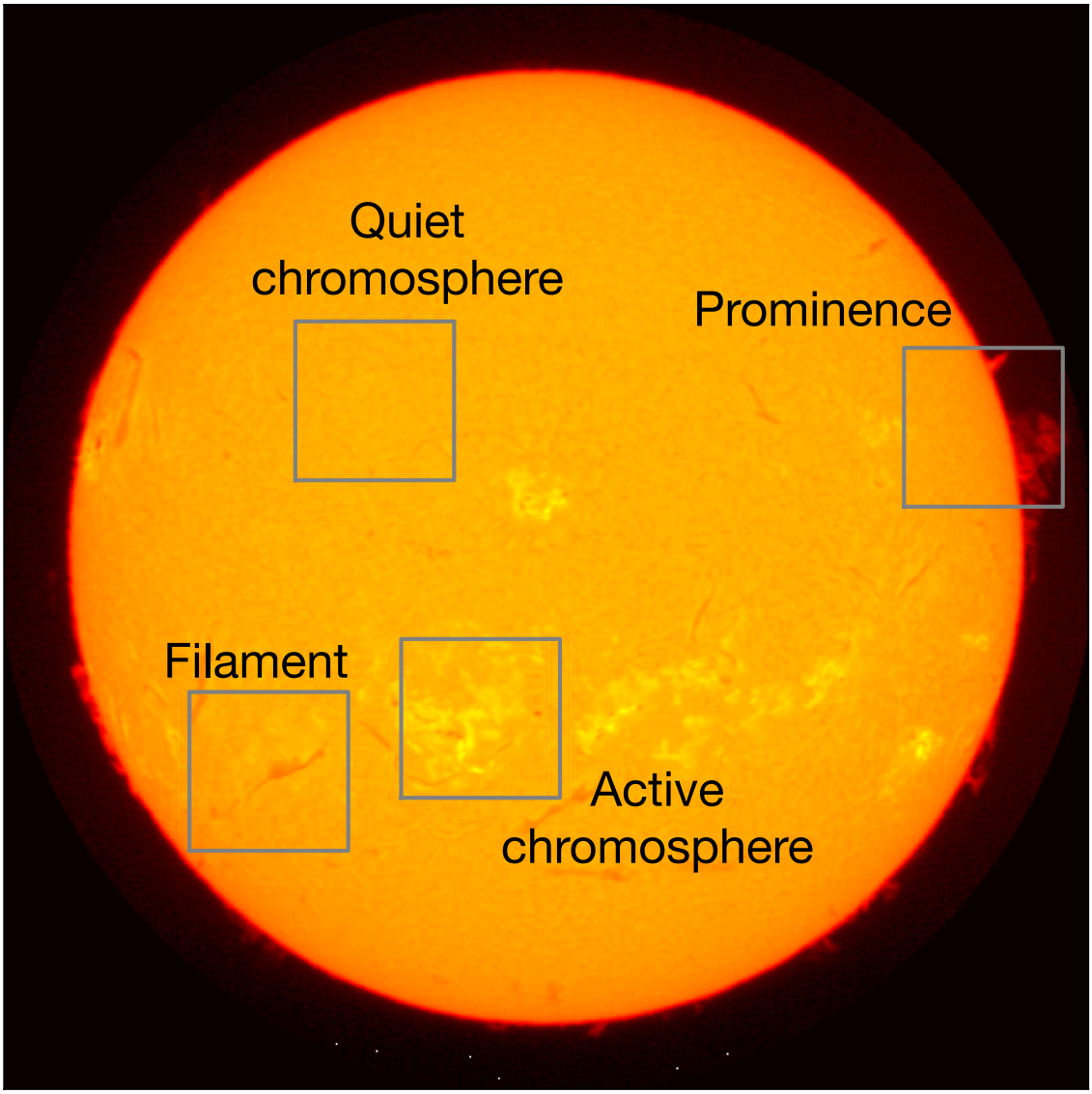

Figure 1.4: Full disk observation of the chromospheric Hα line at 6563 Å. The observation shows different features of the chromosphere. The quiet chromosphere is absent of any stronger magnetic field concentrations and makes up roughly 90% of the chromosphere. In contrast, the active chromosphere shows brighter structures. There are also larger scale darker structures visible on the disk. They are called filaments and consist of cool chromospheric gas which is supported by the magnetic field against gravity in the low corona. Off the limb more irregular structures are visible. They are the counterparts of filaments on the disk but seen from the side and are called prominences. Data were acquired by GONG instruments operated by NISP/NSO/AURA/NSF with contributions from NOAA.

However, their exact formation mechanism is still under debate. For a recent review on spicules, see for example Carlsson et al. (2019).

In the core of the Hα line, the chromosphere shows long thin structures called fibrils. They are believed to trace the chromospheric magnetic field which connects opposite polarities. They can have widths of 0.7 Mm to $\approx$ 2 Mm and an average length of 11 Mm with lifetimes of 10–20 min. In the QS, they seem to arch over supergranular cells. An example of fibrils is shown in Fig. 1.3b. Smaller dynamic fibrils appear in the QS and are called dark mottles. They are believed to be the on-disc counterpart of spicules.

There exist also large-scale structures of chromospheric plasma that reach coronal

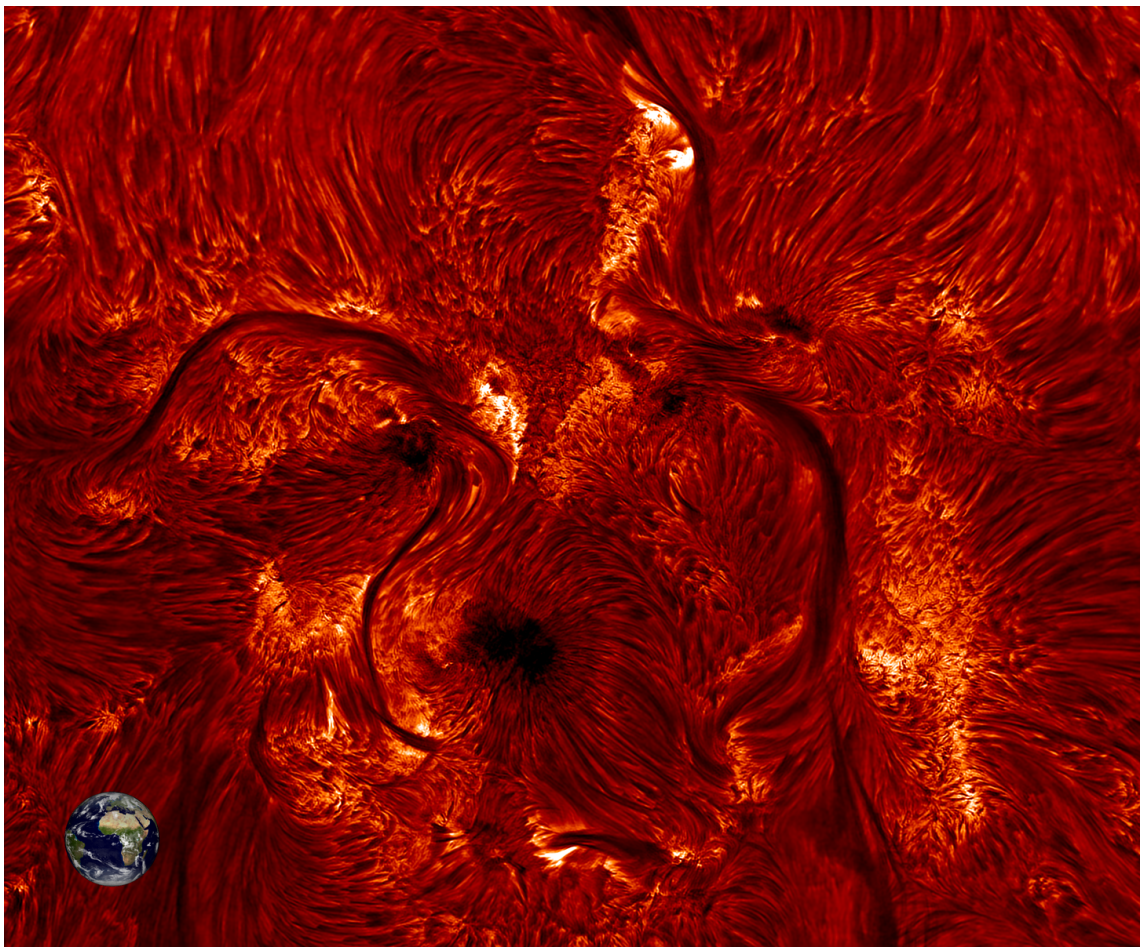

Figure 1.5: Hα observation of an AR by the Dutch open telescope (DOT). Visible are plage regions as bright patches, filaments as dark structures, and fibrils as elongated structures. The dark circular structures lie above Sunspot umbrae. Image credit: Rob Rutten. Observation taken by the Dutch Open Telescope, operated at the Spanish Observatorio del Roque de los Muchachos of the Instituto de Astrofísica de Canarias.

heights. They can be observed for example in Hα above the solar limb and are called prominences. Examples can be seen in the full disk image of a GONG Hα observation in Fig. 1.4. When they are observed on the solar disk, they appear as dark filaments. Figure 1.5 shows an active region with dark filaments observed with the Dutch open telescope (DOT) which are surrounded by fibrils and plage. Prominences and filaments can appear both in the QS and in active regionss (ARs). In the QS, they are larger and longer lived, whereas in the AR they are shorter and more dynamic. It is believed that the plasma in filaments and prominences is supported by the magnetic field against gravity. For a review of prominences see, for example, Parenti (2014).

Transition region The transition region is an interface between chromospheric temperatures and the millions of kelvin hot corona. In 1D models of the solar atmosphere, it extends less than 100 km. In reality, it is not a plane but rather a thin envelope around all chromospheric features such as spicules, fibrils, or prominences where the plasma is heated to coronal temperatures.

Corona The corona can be separated into dark coronal holes, brighter coronal loops, and small intense features called bright points. In the lower corona, the magnetic field

is aligned in close loops. In coronal holes the magnetic field lines are open and the plasma is colder and less dense. Coronal holes play an important role in driving the fast solar wind (for a review of coronal holes see Cranmer 2009). The corona is also a place of highly energetic events called flares (see e.g., Benz 2017) where the magnetic field is spontaneously restructured and large amounts of energy are released. The high temperature of the corona is inferred from spectral lines of highly ionized elements. Similar to the chromosphere the detailed processes that heat the corona are poorly understood but there is strong evidence that heating processes are associated with the magnetic field (e.g. Klimchuk 2006, Reale 2010).

1.2. Diagnostics of the solar chromosphere

The solar spectrum contains a continuum and spectral lines. The continuum intensity results from interactions that continuously emit and absorb radiation. On top of the continuum radiation, there are emission or absorption features visible as spectral lines. An overview of these features can be seen in Fig. 1.6, where the wavelength window around the calcium infrared (IR) triplet lines is shown together with the continuum. The shown data is taken from the Hamburg Fourier-transform-spectrograph atlas (Hamburg FTS atlas) (Neckel & Labs 1984).

The solar chromosphere is optically thin in the near-ultraviolet (NUV), visible, and near-infrared (NIR) continua. There are, however, a few strong spectral lines in which the chromosphere is optically thick. Spectral line features such as intensity, line shape, and position in the spectrum carry information about the thermodynamics of the atmosphere, the magnetic field, or elemental abundances. In the following, I will review the most common chromospheric diagnostics with a focus on the spectral lines dealt with in this thesis.

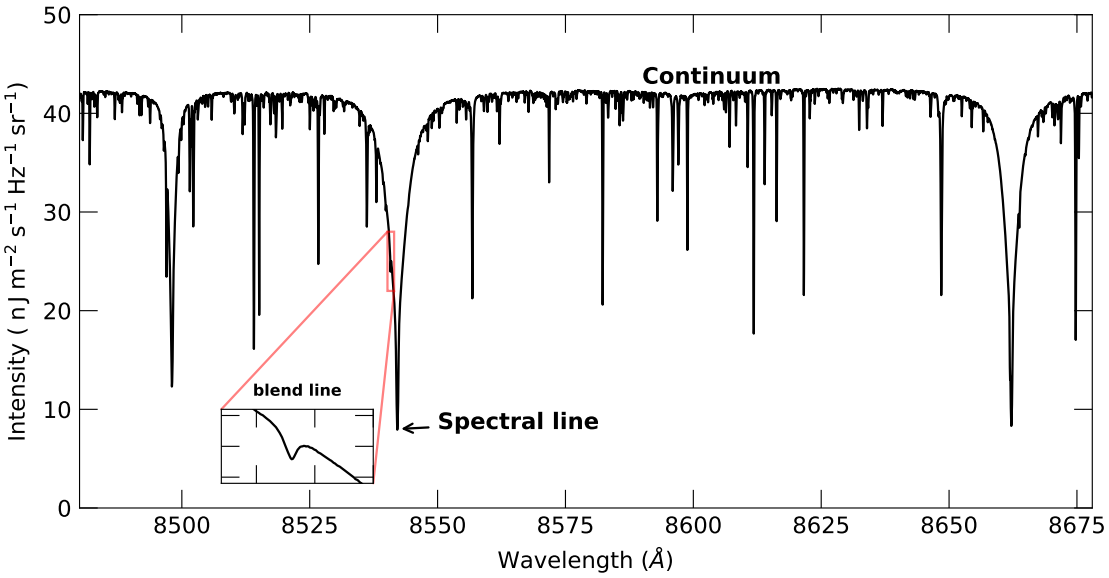

Figure 1.6: Spectral lines and continuum. The figure shows a cut of the solar spectrum in the optical wavelength range. Indicated is the continuum and spectral lines that appear as absorption lines. The inset panel shows a zoom to the Ca II λ854.2 nm spectral line and indicates a "blend" line, that is a weaker spectral line that overlaps with a stronger spectral line. The data is taken from the Hamburg FTS atlas, see also Chapt. 4.

1.2.1 Diagnostics in the optical part of the spectrum

Chromospheric spectral lines in the optical part of the electromagnetic spectrum come with many advantages. As they can be observed from ground-based telescopes, the costs for instruments are significantly lower. In addition, there is room for experimental instruments which can easily be installed and removed from the telescope. The disadvantages are reduced observation times, atmospheric distortions, and the limited wavelength range. Below a few of the most commonly used chromospheric spectral lines observable from the ground are listed:

Hα The Hα line at 6563 Å line is likely the most popular spectral line in the chromosphere due to its appearance during solar eclipses and accessibility from ground-based telescopes. Because of the low atomic weight of hydrogen, the Hα line is broad as a result of thermal motions. This makes the line a good temperature diagnostic (Cauzzi et al. 2009) but less suitable for inferring non-thermal motions. The line core of Hα is optically thick in the chromosphere and thus a good indicator of the morphology and structure of the chromosphere. Forming in the low plasma β regime (see Eq. 1.1), Hα is a preferred line to study the magnetic structures and energetic events in the upper chromosphere. For example Leenaarts et al. (2012a) showed that the intensity in the line core resembles the structure of the magnetic field. Forward modeling of the Hα line demonstrates the crux of chromospheric radiation. The radiation field is nonlocal and scattering processes are important. These effects must be taken into account to reproduce observed line profiles.

Ca II H&K The H & K lines (named following Fraunhofer 1817) of singly ionized calcium at 3968 Å and 3933 Å have been observed for a long time. Their cores form in the middle to upper chromosphere and can be used to infer the temperature stratification. Besides Hα, these were the first lines that revealed the complex structure of the chromosphere. The line profiles are characterized by deep absorption wings with a double reversed core. Modeling the double reversed core demonstrated the need for an NLTE treatment of chromospheric spectral lines (Jefferies & Thomas 1959, 1960). Bjørgen et al. (2018) studied the diagnostic potential of Ca II H&K using a comprehensive model of the solar chromosphere in combination with 3D RT and compared it with observations. The authors found the Ca II H&K lines provide a good temperature diagnostic for the temperature minimum in the atmosphere and at the formation heights of the peaks. In addition, the Doppler shift of the central depression can be used to probe the LOS velocity in the upper chromosphere. The Ca II H&K lines are also of high importance for the study of other cool stars. They are good indicators of magnetic activity, and their width can be used to infer stellar luminosity (Wilson-Bappu effect, Wilson & Vainu Bappu 1957) A review of studying stellar chromospheres with Ca II H&K is presented in Hall (2008).

Ca II λ854.2 nm The Ca II λ854.2 nm line is part of a triplet system in the infrared part of the spectrum at 8498 Å, 8542 Å, and 8662 Å (see Fig. 1.6). In recent years, the Ca II λ854.2 nm became a preferred diagnostic for inferring the chromosphere's magnetic field (de la Cruz Rodríguez et al. 2012, de la Cruz Rodríguez & van Noort 2017). The other two triplet lines share similar properties but are blended by other spectral lines. The line core of Ca II λ854.2 nm shows an asymmetry towards the red. Uitenbroek (2006) suggested the asymmetry might result from an imbalance of up and downflows in the chromosphere. Leenaarts et al. (2014) showed that the asymmetry can be reproduced in model computations when multiple isotopes of calcium are taken into account, which have slightly different rest wavelengths. So far, no numerical models could reproduce the observed asymmetry and line width, see for example Leenaarts et al. (2009) and Hansteen et al. (2023, Fig. 1). In Chapt. 4 we present results of the Ca II λ854.2 nm line modeled with the MURaM-ChE code.

He I 10830 Å The He I 10830 Å line forms in the infrared and can be observed from ground-based telescopes. This spectral line is optically thin in the chromosphere. In AR, its magnetic sensitivity through the Zeeman and Hanle effect may be used to infer the chromospheric magnetic field. In addition, it can be used to reveal the chromospheric morphology above ARs.

1.2.2 Diagnostics in the ultraviolet part of the spectrum

Spectral lines forming in the UV part of the spectrum are not accessible from ground-based telescopes as the UV radiation is blocked by the Earth's atmosphere. Sounding-rockets (e.g., Morrill & Korendyke 2008) are a reasonable alternative as they are cheaper than space-based observatories. However, the observation time is limited and the instruments might not be reusable after a flight. Baloon-borne observatories such as RASOLBA (Staath & Lemaire 1995) and SUNRISE (Solanki et al. 2010, 2012, Barthol et al. 2011) combine advantages of ground-based and space-based observatories with high-resolution long-term observations at relatively low cost. However, in the UV there might still be residual absorption from the Earth's atmosphere. Since its launch in 2013, the IRIS satellite mission (De Pontieu et al. 2014) became the main source of high-resolution observations in the NUV.

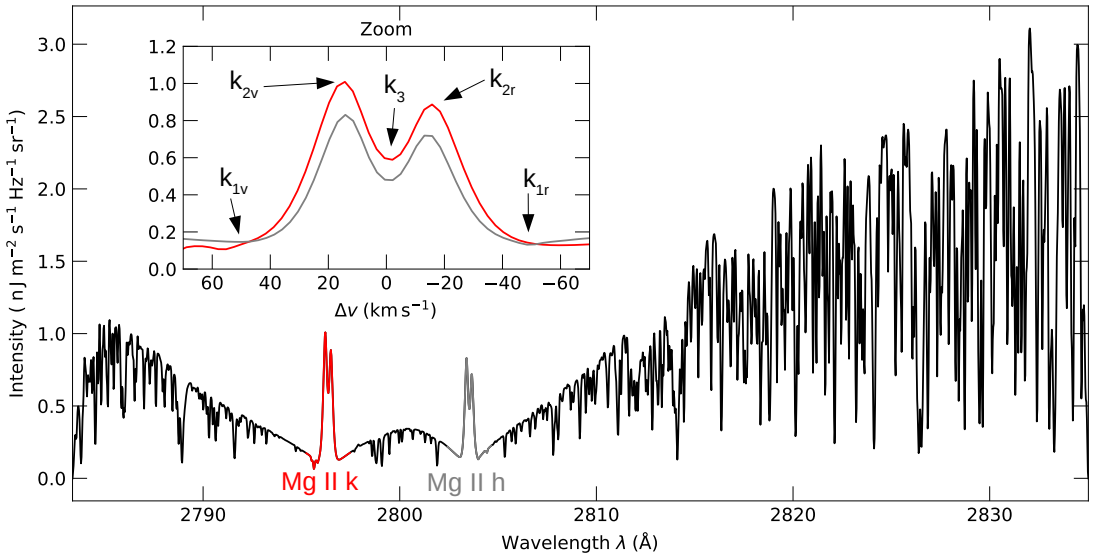

Figure 1.7: Mg II h&k window of a QS region observed by IRIS. The Mg II h&k lines have broad absorption wings which form in the photosphere. In the line cores, the Mg II h&k lines show an emission feature that consists of two peaks and a central reversal (see inset panel). The peaks form in the middle to upper chromosphere and the central reversal forms just below the transition region, which connects to the corona. The wings show a huge amount of overlapping spectral lines in the NUV spectrum.

Mg II h&k The Mg II h&k lines at 2802.7 Å and 2795.5 Å share similar properties with Ca II H&K. Because of the 18 times higher abundance in the solar chromosphere (Asplund et al. 2009) and higher ionization energies of magnesium, the Mg II h&k lines sample the upper solar chromosphere. Figure 1.7 shows a spatially averaged QS spectrum observed by IRIS. It can be seen that similar to the Ca II H&K lines, the Mg II h&k lines show a self-reversed core with a similar nomenclature of the spectral features (see Fig. 1.7, inset panel). Typically, the k_{2v} and h_{2v} peaks are stronger than their corresponding red peaks k_{2r} and h_{2r}. The large wings form in the photosphere whereas the k_2 peaks form in the mid to upper chromosphere. The central reversal k_3 forms just below the transition to the corona.

The Mg II h&k lines in the solar chromosphere were observed already in the 1940s and 1950s using V2 rockets Hopfield & Clearman (1948). First high-resolution images

(Riethmüller et al. 2013, Danilovic et al. 2014) in the core of Mg II k were recorded during the second flight of the balloon-borne observatory SUNRISE. The formation and diagnostic potential of the Mg II h&k lines were studied already in the 1970s. Athay & Skumanich (1968) used a simplified two-level model atom to compute the Mg II h&k lines to study the impact of the temperature stratification of model atmospheres on the resulting spectra which they compared with observations. Milkey & Mihalas (1974) demonstrated that the Mg II h&k lines are subject to partial-coherent scattering (see Sect. 1.3.6) which needs to be taken into account in the model calculation to match the observed profiles. Ayres & Linsky (1976) improved on the computations of the Mg II h&k lines with a more realistic atom model and could further constrain existing model atmospheres.

With the advent of more comprehensive model atmospheres, which include a convection zone, chromosphere, and corona with a prescription of radiative losses, Leenaarts et al. (2013b) find correlations between spectral line features and the underlying model atmosphere, computed with the Bifrost code (Gudiksen et al. 2011). Based on statistical distributions of spectral line features, the authors demonstrated the diagnostic potential of the Mg II h&k lines to infer velocities, velocity differences, and temperature in the middle to upper chromosphere. For example, the Doppler shift of the k_3 and h_3 feature is strongly correlated with the vertical velocity in the upper chromosphere. The peak intensities of the k_2 and h_2 peaks may be used to infer the temperature in the mid-chromosphere. Sukhorukov & Leenaarts (2017) for the first time computed Mg II h&k profiles considering 3D RT effects together with partial-coherent scattering (see Sect. 1.3.6) and demonstrated their necessity. As in the 1970s and 1980s, the shapes of forward modeled Mg II h&k lines are still an important criterion to constrain numerical models of the chromosphere. In Chapt. 2 and Chapt. 3 I compare the Mg II h&k lines computed from the MURaM-ChE model with observations.

Hydrogen Lyman α The hydrogen Lyα line is the strongest resonance line in the chromosphere (see e.g., Pietenpol et al. 1953). It is an important source of illumination of chromospheric and coronal features such as prominences, spicules, and fibrils. It may also be used for magnetic field inferences through scattering polarization in the upper chromosphere (see e.g., Kano et al. 2017).

O I λ135.56 nm The 135.56 nm line of neutral oxygen is optically thin in the solar atmosphere. Lin & Carlsson (2015) studied the formation of O I λ135.56 nm and found that the line is a good diagnostic of non-thermal velocities in the chromosphere, which play a role in the broadening of the Mg II h&k lines. Carlsson et al. (2015) and Carlsson & De Pontieu (2023) used observations of O I λ1355.6 Å and Mg II h&k to constrain non-thermal velocities in the chromosphere to less than 10 km s^{-1}.

1.2.3 Other chromospheric diagnostics

Other important spectral lines in the chromosphere exist, that are not directly relevant to this work. I will list the most important here and refer to the review of Carlsson et al. (2019) for more details. Spectral lines to infer the structure of the upper photosphere and lower chromosphere are, amongst others, the Na I D lines, K I resonance lines, Mg I b lines, and the He I D3 line. Besides spectroscopic observations, interferometric observations with the Atacama Large Millimeter/submillimeter Array (ALMA) (see e.g., Wedemeyer et al. 2016) are promising to study the chromosphere in the submillimeter and millimeter continuum (Loukitcheva et al. 2015).

1.3. Radiative transfer theory

Studying the solar atmosphere requires detailed knowledge of basic physical quantities such as temperature, velocity, magnetic field, and density. Approaches exist to infer some of these quantities in situ in the solar wind, for example, with the solar wind and plasma analyzer (SWA) (Owen et al. 2020) instrument onboard Solar Orbiter (Müller et al. 2020). However, it is impossible to obtain the thermodynamic properties in the lower solar atmosphere directly. Therefore, most of the information we can get from the lower solar atmosphere, and other stars in general, relies on the analysis of the emitted radiation. Deciphering the observed spectrum and retrieving the relevant information is a challenging task. For example, the observations are not always at the desired spatial and temporal resolution, such that multiple features may overlap in one resolution element. In addition, a detailed theory of RT is needed to understand and interpret the observations. The interplay between observations, RT theory, and numerical modeling is non-trivial and, therefore, motivates the work of this thesis. In this section, I will introduce the basics of RT theory, which are relevant to this work. I will use Mihalas (1978), Rutten (2003), Gray (2005), and Hubeny & Mihalas (2014) as references. For simplicity, I introduce the concepts of light-matter interaction here in the approximation of two-level atoms with an upper and a lower level. For resonance lines, where the lower level is the ground state and the coupling to the continuum, and higher levels is weak, this is a good approximation (see e.g., Mihalas 1978, p. 331 ff). The actual RT computations presented in Chpts. 2, 3, and 4 were computed, however, with multilevel atom models.

1.3.1 Interactions of light with matter

Before introducing the formal description of RT, I summarize the possible interactions of light with matter. In the context of the solar atmosphere, photons can interact with atoms, ions, molecules, and free electrons. Interactions involving an atom, ion, or molecule are commonly characterized by the state of the electron taking part in the interaction before and after the interaction. Such an interaction can be restricted to bound states (all electrons remain bound throughout) or also involve free electrons (e.g., ionization and recombination). For a detailed description, see, for example, Mihalas (1978, p. 20 ff).

Free-free In this type of interaction, an electron moves in the electric field of an ion. A photon can be absorbed by the electron, changing its kinetic energy and direction. The electron is free before and after the interaction, thus the term free-free (ff). The inverse process which leads to the emission of a photon is called Bremsstrahlung. These interactions are collisional and inelastic. Either the kinetic energy of the electron is converted into a photon or vice-versa. These interactions lead to an exchange between the local thermal pool and the radiation field. Such interactions contribute to the continuum of the observed spectrum.

Thomson scattering This process describes elastic scattering between photons and free electrons. The interaction cross-section does not have a wavelength dependence and therefore contributes to the continuum intensity. During an eclipse the white light visible in the corona results from Thomson scattering.

Rayleigh scattering This process describes elastic scattering between photons and bound electrons in atoms or molecules. The frequency of the scattered photon is typically much lower than the characteristic transition frequency of the atom or molecule. The interaction

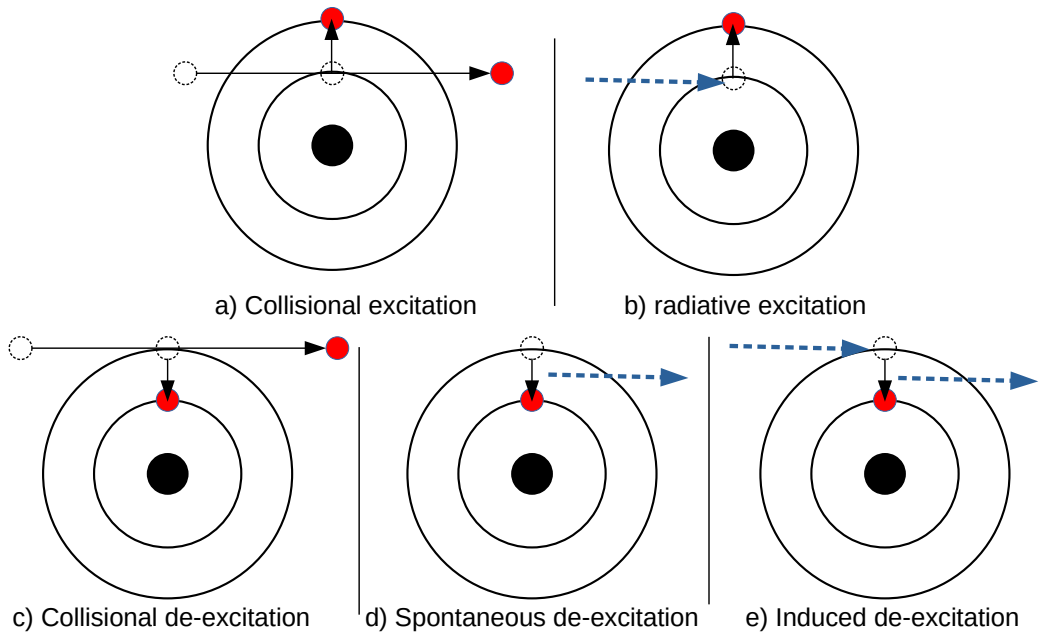

Figure 1.8: Sketches of processes that can lead to bound-bound transitions. The electrons before the interaction are sketched by small dashed circles, and the electrons after the interaction by red circles. The arrows indicate the direction of motion of the involved free electron. For the bound electrons, the arrows indicate schematically the transition between energy levels. The nuclei of the ions or atoms are indicated by filled black circles. Photons are illustrated by blue dashed arrows. In the classical view, the electron levels are given by orbitals (black rings) around the nucleus.

cross-section has a strong wavelength dependence, namely $\sigma_{\text{Rayleigh}} \sim \lambda^{-4}$, where λ is the wavelength.

Bound-free or free-bound An important free-bound (fb) process is recombination. An electron of mass m_e and velocity v_e is captured by an ion into an electron state ϵ_i while the excess energy $h\nu = \frac{1}{2}m_\text{e}v_\text{e}^2 - \epsilon_i$ is radiated away as a photon. Analogously, photo-ionization describes the reverse bound-free (bf) process. Here, a sufficiently energetic photon is absorbed by an atom allowing a bound electron to escape. The excess of the photon's energy over the binding energy is the initial kinetic energy of the free electron.

Bound-bound In the context of this thesis, bound-bound (bb) interactions are of special importance as they produce spectral lines. Different scenarios lead to bb interactions, which I briefly summarize here. The exemplary processes for two-level atoms are sketched in Fig. 1.8. The schematic two-level atom model cannot describe processes such as fluorescence, where an electron is excited to an upper state and de-excites through a cascade of multiple lower-level atoms, emitting photons of different frequencies. Panel (a) illustrates the excitation of a bound electron to the upper state through a collision of the atom with a free electron. Panel (b) describes the absorption of a photon by exciting a bound electron to the upper state, which works only if the photon has exactly the matching energy. In panel (c), an excited electron in a bound state transits to the lower energy through a collision of the atom with a free electron. The energy difference of the upper and lower energy states is added to the kinetic energy of the free electron. Panel (d) describes the process of spontaneous de-excitation. An electron in an excited state spontaneously de-excites by emitting a photon carrying the energy difference between the upper and

lower states. In panel (e), an electron is de-excited through interaction with a photon. Through the de-excitation, a photon is emitted, which has the same energy as and travels together with the initial photon. The energy of the incoming photon must match the energy difference between the atomic states. Combinations of the processes can lead to the following bb interactions:

- Collisional excitation and collisional de-excitation (Fig. 1.8 a → c): Here no photons are involved. Such transitions maintain thermal population ratios between upper and lower levels.
- Collisional excitation and spontaneous de-excitation (Fig. 1.8 a → d): In this process, some kinetic energy of the free electron is converted into a photon.
- Collisional excitation and induced de-excitation (Fig. 1.8 a → e): Here a new photon is created from part of the kinetic energy of the colliding electron.
- Radiative-excitation and collisional de-excitation (Fig. 1.8 b → c): Here, the photon energy is converted into kinetic energy of a free electron. The photon is "destroyed".
- Radiative excitation and radiative de-excitation (Fig. 1.8 b → d or e): This interaction is also called photon-scattering. The outgoing photon may have a different direction. Some "redistribution" may also occur, where the outgoing photon is slightly shifted in frequency. This is important, especially for the Mg II h&k lines, and will therefore be discussed in Sect. 1.3.6 in somewhat more detail. In the case of multi-level atoms, it is also possible that the de-excitation involves intermediate states such that two or more photons of different frequencies are emitted during the de-excitation process.

1.3.2 Radiative transport equation

So far, I qualitatively introduced different important interactions of photons with matter in the solar atmosphere. These processes may add or remove photons along the line of sight through emission, absorption, or scattering. In order to quantitatively describe the amount of radiation arriving at the observer through the solar atmosphere, I will here introduce the basic concepts of RT.

The specific intensity I_ν is defined as:

$$I_\nu(x, y, z, \theta, \varphi, t) = \frac{\mathrm{d}E_\nu}{\cos\theta \, \mathrm{d}A \, \mathrm{d}t \, \mathrm{d}\nu \, \mathrm{d}\Omega}. \tag{1.2}$$

Here $\mathrm{d}E_\nu$ is the amount of energy transported through the area element $\mathrm{d}A$ at the position indicated by the coordinates $(x, y, z)^\mathrm{T}$ in a time interval $\mathrm{d}t$ in the frequency band between ν and $\nu + \mathrm{d}\nu$, over the solid angle $\mathrm{d}\Omega$ and the direction as given by the polar coordinates θ and φ (see Fig. 1.9a). According to this definition, the specific intensity does not decrease with distance in a vacuum. This assumption is based on the fact that photons are not known to decay spontaneously. The specific intensity can be interpreted as the energy that is carried by identical photons along a single "ray".

Along a ray through a medium, interactions between the radiation field and matter can occur. These can be subdivided into either extinction, which removes photons from the beam along its path through absorption or scattering, or emission, which adds photons along the ray. The extinction can be described as

$$\mathrm{d}I_\nu^\mathrm{abs} = -\kappa_\nu \rho I_\nu \mathrm{d}s = -\alpha_\nu I_\nu \mathrm{d}s. \tag{1.3}$$

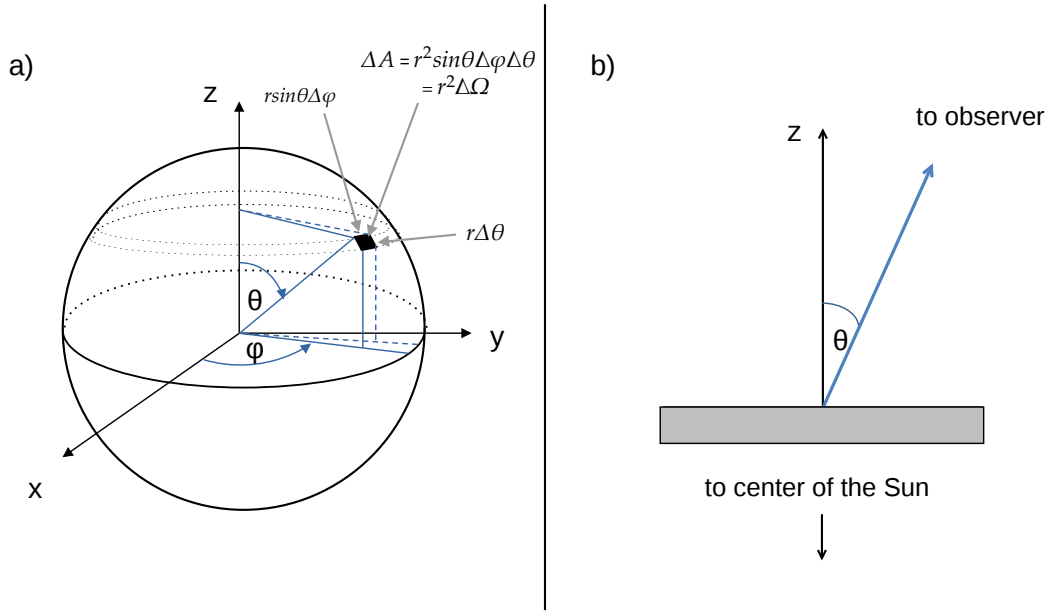

Figure 1.9: Panel (a): Definition of the solid angle in polar coordinates. The area ΔA of the sphere at radius r limited by the angles $(\theta, \theta+\Delta\theta)$ and $(\varphi, \varphi+\Delta\varphi)$ is $\Delta A = r^2 \sin(\theta)\Delta\phi\,\Delta\theta$, with $\Delta\Omega = \sin(\theta)\Delta\phi\,\Delta\theta$ as the solid angle. Panel (b): Definition of heliocentric angle μ. The z-axis is defined as the normal of the Sun's local surface (in contrast to panel a). The angle between the observer and the surface normal is defined as θ.

The probability α_ν that a photon of frequency ν is extinguished along a slab of thickness s with direction $\vec{s}$ of the ray is

$$\alpha_\nu = \kappa_\nu \rho. \tag{1.4}$$

Here, κ_ν is the monochromatic mass extinction coefficient, also called opacity, and ρ is the mass density. By this definition, α_ν is the extinction coefficient per volume. On the other hand, photons can be added to the ray. The local addition of photons to the ray can be described as

$$\mathrm{d}I_\nu^{\mathrm{em}} = j_\nu(s)\mathrm{d}s \tag{1.5}$$

where $j_\nu(s)$ is the monochromatic emissivity.

The transport of energy along a path of length ds can therefore be described by the radiative transfer equation (RTE)

$$\mathrm{d}I_\nu = \mathrm{d}I_\nu^{\mathrm{em}} - \mathrm{d}I_\nu^{\mathrm{abs}} \tag{1.6}$$

$$\frac{\mathrm{d}I_\nu}{\mathrm{d}s} = j_\nu - \alpha_\nu I_\nu \tag{1.7}$$

$$\frac{\mathrm{d}I_\nu}{\alpha_\nu \mathrm{d}s} = \frac{j_\nu}{\alpha_\nu} - I_\nu \tag{1.8}$$

$$= S_\nu - I_\nu. \tag{1.9}$$

The quantity $S_\nu = j_\nu/\alpha_\nu$ is called source function. Formally, there is a time dependence via $\partial I_\nu/(c\partial t)$ in the left-hand-side in Eq. 1.7, with c being the speed of light. Typical hydrodynamic time scales in the solar atmosphere are on the order of minutes, which is much larger than the travel time of photons through the atmosphere. In addition, the velocities associated with flows are much lower than the speed of light. Therefore, the

time dependence of the RTE in the solar atmosphere is generally neglected. It is therefore assumed, that the radiation field reacts instantaneously to changes in the state of the atmosphere.

The emissivity and absorption coefficients can have multiple contributions from processes affecting the continuum or the spectral lines. Therefore the source function can be written as, with $\eta_\nu = \alpha_\nu^{\mathrm{l}}/\alpha_\nu^{\mathrm{c}}$:

$$S_\nu = \frac{j_\nu^{\mathrm{c}} + j_\nu^{\mathrm{l}}}{\alpha_\nu^{\mathrm{c}} + \alpha_\nu^{\mathrm{l}}} = \frac{S_\nu^{\mathrm{c}} + \eta_\nu S_\nu^{\mathrm{l}}}{1 + \eta_\nu} \tag{1.10}$$

Here S_ν^{c} can be a composition of several continuum processes and S_ν^{l} a composition of overlapping spectral lines, such as atomic isotopes whose line transitions are close in wavelength space, or bb transitions from other atoms or ions at similar wavelengths. A measure of the extinction along a path along the beam is given by the monochromatic optical thickness:

$$\tau_\nu = \int_0^D \alpha_\nu(s)\mathrm{d}s. \tag{1.11}$$

Here, D is the total thickness of the considered medium. The term "optical" is here meant to apply to all frequencies in the electromagnetic spectrum. A medium is called "optically thick" if $\tau_\nu \gg 1$ and "optically thin" if $\tau_\nu \ll 1$. With the so-called monochromatic optical path $\mathrm{d}\tau_\nu = \alpha_\nu \mathrm{d}s$ the RTE (Eq. 1.9) can be rewritten as:

$$\frac{\mathrm{d}I_\nu}{\mathrm{d}\tau_\nu} = S_\nu - I_\nu. \tag{1.12}$$

The solution to Eq. 1.12 is (see e.g., Gray 2005, p. 128-129):

$$I_\nu(\tau_\nu) = I_\nu(\tau_\nu = 0)e^{-\tau_\nu} + \int_0^{\tau_\nu} S_\nu(t_\nu)e^{-(\tau_\nu - t_\nu)}\mathrm{d}t_\nu. \tag{1.13}$$

Equation 1.13 is also known as the formal solution of the RTE along a ray.

From an observational point of view, it is common to define the optical thickness along the line of sight. This is called optical depth and describes how deep one can view into the gas before it becomes optically thick.

The viewing angle θ is the angle between the LOS and the surface normal of the Sun (see Fig. 1.9b). It is common to define $\mu = \cos\theta$. For outgoing radiation, θ is restricted to $0° \leq \theta \leq 90°$, which implies $\mu \geq 0$. Under the assumption of a plane-parallel atmosphere, the angle-dependent optical depth then becomes

$$\mathrm{d}\tau_{\nu,\mu} = -\alpha_\nu \frac{\mathrm{d}z}{\mu}. \tag{1.14}$$

Inside the frequency range of a spectral line, the extinction coefficient has contributions from the spectral line α_ν^{l} and from the continuum α_ν^{c} such that the total optical depth is:

$$\mathrm{d}\tau_\nu^{\mathrm{total}} = -(\alpha_\nu^{\mathrm{l}} + \alpha_\nu^{\mathrm{c}})\frac{\mathrm{d}z}{\mu} \tag{1.15}$$

The solution of Eq. 1.12 with $\tau_{\nu,\mu}$ for outgoing radiation, and assuming axial symmetry, then becomes

$$I_\nu(\tau'_\nu, \mu) = \int_{\tau_{\nu'}}^{\infty} S_\nu(t_\nu)e^{-(t'_\nu - \tau'_\nu)/\mu}\frac{\mathrm{d}t'_\nu}{\mu}. \tag{1.16}$$

In Eq. 1.16 it is assumed that the position of the observer is infiniteley far away and that the optical depth at the position of the observer is $\tau_\nu(\infty) = 0$. The emergent intensity, that is the intensity outside the solar atmosphere (for example at the location of the observer), can be obtained from

$$I_\nu(\tau'_\nu = 0, \mu) = \int_{\tau_{\nu'}=0}^{\infty} S_\nu(t_\nu) e^{-t'_\nu/\mu} \frac{\mathrm{d}t'_\nu}{\mu}. \tag{1.17}$$

The integrand of Eq. 1.17 is also called the contribution function, as it indicates which heights contribute to the emergent intensity.

An important quantity for RT involving scattering is the angle averaged mean intensity:

$$J_\nu(\vec{r}, t) = \frac{1}{4\pi} \int_\Omega I_\nu \mathrm{d}\Omega. \tag{1.18}$$

It is used to determine, for example, the amount of radiative ionization and excitation, where only the number of photons regardless of their direction is of interest. Assuming a plane-parallel atmosphere and expressing I_ν in terms of the optical depth τ_ν, Eq. 1.18 can be cast into an operator equation via (see e.g., Hubeny & Mihalas 2014, p. 361 f):

$$\begin{aligned} J_\nu(\tau) &= \frac{1}{2} \int_{-1}^{1} I_\nu(\tau_\nu, \mu) \mathrm{d}\mu && (1.19)\\ &= \frac{1}{2} \int_0^\infty S_\nu(t_\nu) E_1(|t_\nu - \tau_\nu|) \mathrm{d}\tau_\nu && (1.20)\\ &= \Lambda_\nu \left[S_\nu(t_\nu)\right] && (1.21) \end{aligned}$$

Here, E_1 is the first exponential integral defined by

$$E_1(x) = \int_1^\infty e^{-xt} t^{-1} \, \mathrm{d}t, \tag{1.22}$$

and Λ_ν is the Λ-operator defined by

$$\Lambda \left[f(t)\right] = \frac{1}{2} \int_0^\infty f(t') E_1(|t' - \tau|) \mathrm{d}t' \tag{1.23}$$

These formulations are important for the numerical solution of the RTE (see Sect. 1.4.2).

1.3.3 The Eddington-Barbier relation

As can be seen in Equation 1.16 the emergent intensity depends on contributions along the whole LOS. In order to probe different parts of the solar atmosphere, it is useful to estimate the height that contributes most to the emergent intensity. An approximation can be made by assuming that the source function can be expressed as a polynomial expansion (see e.g. Rutten 2003, p. 18) such that

$$S_\nu(\tau_\nu) = \sum_{n=0}^{\infty} a_n \tau_\nu^n \tag{1.24}$$

with expansion coefficients $a_n \in \mathbb{R}$. Use of $\int_0^\infty x^n e^{-x} \mathrm{d}x = n!$ and Eq. 1.17 gives

$$I_\nu(\tau_\nu = 0, \mu) = a_0 + a_1\mu + 2a_2\mu^2 + \ldots + n! a_n \mu^n. \tag{1.25}$$

If all terms of order $n = 2$ or higher are neglected this gives

$$I_\nu(\tau_\nu = 0, \mu) \approx S_\nu(\tau_\nu = \mu). \tag{1.26}$$

This is called the Eddington-Barbier approximation. This relation is used to define the "formation heights" of both the continuum and spectral lines. The fact that τ_ν is much larger inside a spectral line than in the continuum distinguishes between their formation heights. The term formation height does, however, not mean that all photons of a given frequency come from the $\tau_\nu = \mu$ layer. It rather means that all released photons throughout the whole medium give an intensity value comparable to the value of the source function evaluated at $\tau_\nu = \mu$.

1.3.4 Spectral line formation

A spectral line is not sharp but has a finite width, which depends on the extinction profile that is mapped through the source function into the intensity (see Equation 1.16). I will present here the most important processes for spectral line broadening in stellar atmospheres.

Natural broadening Even if an atom was completely isolated at rest in the laboratory, its spectral lines would have a finite width. This effect is called natural broadening and is a result of the finite lifetime an excited state has before it spontaneously de-excites. The extinction profile can be described as a Lorentz function ψ with damping parameter γ (see e.g., Gray 2005, p. 232 ff), which can be interpreted as the transition probability.

$$\psi(\nu - \nu_0) = \frac{\frac{\gamma}{4\pi^2}}{(\nu - \nu_0)^2 + (\frac{\gamma}{4\pi})^2} \tag{1.27}$$

Here, ν is the frequency, and ν_0 is the rest frequency of the transition.

Collisional broadening (also pressure broadening) Elastic collisions occur due to the presence of neighboring particles such as electrons, ions, atoms, or molecules. Through the Coulomb interaction between colliding particles, the energy levels of an ion or atom, that emits or absorbs a photon, are slightly changed. Typically the interactions are classified by their dependence on the separation r between the absorbing or emitting atom or ion and the perturber via:

$$\Delta\nu = \frac{C_n}{r^n} \tag{1.28}$$

Here C_n is the interaction constant and r is the minimum distance during the encounter. The interaction constant can either be calculated from Quantum mechanics or is measured in an experiment. Mihalas (1978, p. 281 ff) presents the calculation under certain approximations. I will consider only a qualitative description of the different processes here.

- For $n = 2$ the interaction is called Linear-Stark-effect. For this kind of interaction, the atom or ion is perturbed by protons or electrons. The r^{-2} is related to the Coulomb field of a point source. These interactions are important for neutral hydrogen atoms or hydrogenic ions such as singly-ionized helium.

- The interaction between neutral hydrogen atoms among themselves is called resonance-broadening and is characterized by an $n = 3$ dependence.
- The $n = 4$ case is named Quadratic-Stark-effect. This class is mostly important for transition lines other than neutral hydrogen lines. The interaction arises from systems without a dipole moment.
- In cool-star atmospheres, hydrogen exists in its neutral form in large numbers. Interactions with neutral atoms are called Van-der-Waals broadening and have a $n = 6$ dependence. This type of broadening is important for transitions of non-hydrogenic atoms, for example, the Mg II h&k lines. A classical description of the Van-der-Waals broadening has been provided by (Unsold 1955, Warner 1967). Better descriptions than the simple r^{-6} dependence are presented by Barklem & O'Mara (1997, 1998).

Doppler broadening Motions of the emitting or absorbing atom or ion add Doppler shifts along the LOS. If v_{LOS} is the LOS component of the velocity and c the speed of light and $v_{\mathrm{LOS}} \ll \mathrm{c}$, then the Doppler shift can be computed via:

$$\frac{\Delta\nu}{\nu} = \frac{\Delta\lambda}{\lambda} = \frac{v_{\mathrm{LOS}}}{\mathrm{c}}. \tag{1.29}$$

Here ν is the frequency, λ the wavelength, and c the speed of light. These motions can be thermal, which means they can be described by a Maxwellian velocity distribution. Thermal Doppler broadening produces a Gaussian profile. The thermal Doppler width $\Delta\nu_{\mathrm{D}}$ is defined by

$$\Delta\nu_{\mathrm{D}} = \frac{\nu_0}{c}\sqrt{\frac{2\mathrm{k_B}T}{m}}. \tag{1.30}$$

Here $\mathrm{k_B}$ is the Boltzmann constant, m the mass of the atom or ion, and T the temperature. The full width at half maximum (FWHM) of the thermal broadening profile is given by $\mathrm{FWHM} = 2\sqrt{\ln(2)}\Delta\nu_{\mathrm{D}}$[1]. It can be seen from Eq. 1.30 that the thermal Doppler broadening depends on the mass of the ion or atom. Therefore, lighter species, such as hydrogen, are more sensitive to thermal Doppler broadening than heavier elements. As an example for magnesium at chromospheric temperatures of $T = 6000\,\mathrm{K}$ and $m_{\mathrm{magnesium}} \approx 24.3\, m_{\mathrm{hydrogen}}$, the mean thermal velocities are $v_{\mathrm{magnesium}} \approx 2\,\mathrm{km\,s^{-1}}$, whereas the velocities for hydrogen are higher by a factor of $\approx \sqrt{24.3} \approx 4.9$, such that $v_{\mathrm{hydrogen}} \approx 10\,\mathrm{km\,s^{-1}}$.

Turbulent broadening In a stellar atmosphere, the velocity field has components besides the microscopic thermal broadening and the rotation of the star. Waves and turbulent convection may add to the velocity of emitting and absorbing atoms or ions. In time-independent and plane-parallel modeling, these motions are neglected but introduced as fudge parameters. One such parameter, the microturbulence ξ_{micro}, is a parameter added to the extinction profile by redefining the thermal Doppler width (Eq. 1.30) as:

$$\Delta\nu_{\mathrm{D}} = \frac{\nu_0}{c}\sqrt{\frac{2\mathrm{k_B}T}{m} + \xi^2_{\mathrm{micro}}} \tag{1.31}$$

[1] See erratum to Rutten (2003, p.59) on `https://robrutten.nl/Radiative_Transfer.html`.

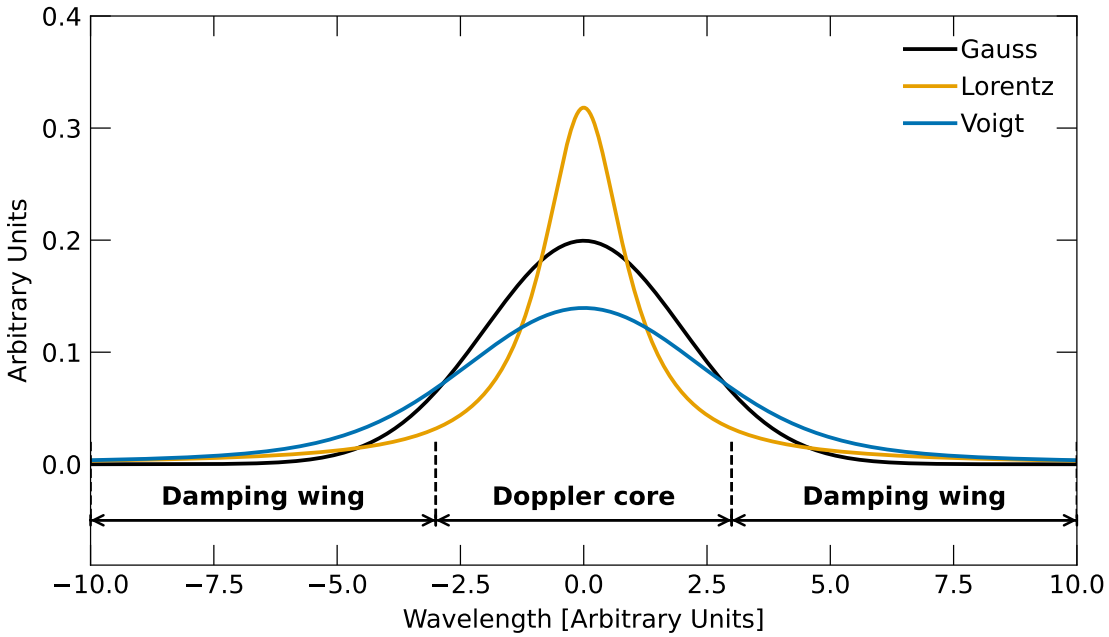

Figure 1.10: The Voigt profile. This figure shows the Voigt profile (blue color, see Eq. 1.33), which results from the convolution of a Gaussian profile (black) with a Lorentz profile (orange). In the center ("Doppler core"), the Voigt profile resembles a Gaussian shape. In the "Damping wings", the Voigt profile resembles the Lorentz profile shape. In the context of RT, the Voigt profile combines the effects of thermal Doppler broadening in the core and natural damping in the wings.

and can be seen as a convolution with a Gaussian velocity distribution. In addition, macroturbulence is introduced by convolving the emergent intensity or flux profile by typically a Gaussian, such that

$$\frac{I_c - I_\lambda}{I_c} = \left[\frac{I_c - I_\lambda}{I_c}\right]_{\text{computed}} * \frac{1}{\xi_{\text{macro}}\pi} \exp\left(-\frac{\xi^2}{\xi^2_{\text{macro}}}\right). \tag{1.32}$$

Here I_c and I_λ refer to the observed continuum and line intensity. Introducing microturbulence and macroturbulence comes with caveats. While these parameters suggest unresolved motions in stellar atmosphere models, they may obscure other missing details in the models.

Combined broadening The total extinction profile is a combination of multiple broadening components, which can be described by a convolution of the respective extinction profiles, assuming the processes are independent. The natural and collisional broadening can be described by a Lorentzian and Doppler broadening by a Gaussian. In the case of collisional and thermal broadening, the resulting extinction profile has the form

$$\psi(\nu - \nu_0) = \frac{H(a, v)}{\sqrt{\pi}\Delta\nu_D}. \tag{1.33}$$

Here ν is the frequency and ν_0 the frequency of the line center, $\Delta\nu_\mathrm{D}$ is the Doppler width, γ is the damping parameter, and $H(a, v)$ is the Voigt function,

$$H(a, v) = \frac{a}{\pi} \int_{-\infty}^{\infty} \frac{e^{-y^2}}{(v - y)^2 + a^2} \mathrm{d}y, \tag{1.34}$$

$$a = \frac{\gamma}{4\pi\Delta\nu_\mathrm{D}} \tag{1.35}$$

$$v = \frac{\nu - \nu_0}{\Delta\nu_D} \tag{1.36}$$

The shape of the Voigt function is similar to a Gaussian in the center due to the thermal Doppler broadening, also called the Doppler core. In the wings, the shape looks like a Lorentzian profile caused by collisional perturbations, also called damping wings (see Fig. 1.10).

Additional broadening Besides the above-mentioned spectral line broadening mechanisms, there are additional possibilities to broaden the line profile. In the solar atmosphere, typical examples are:

- Isotope splitting: If there exist multiple stable isotopes of an abundant element in the solar atmosphere, there might be additional broadening. Because of the slightly different nucleous mass of the isotopes, the energy levels are slightly shifted. An additional effect can be an asymmetric contribution to the line profile, as, for example, in the Ca II λ854.2 nm line (see also Chapt. 4).

- Zeeman splitting: Almost all electronic transitions are sensitive to the magnetic field. In the presence of a magnetic field, the energy levels are split according to the component of the total angular momentum parallel to the magnetic field, J_z. The Zeeman splitting of a spectral line is given by the Zeeman splitting of the upper and lower energy levels of the transition (see e.g., Bellot Rubio & Orozco Suárez 2019, p. 8). It is dependent on the wavelength, such that $\Delta\lambda_\mathrm{Z} \sim \lambda^2$. Whether the splitting of a line is complete depends however also on the thermal Doppler width, which is proportional to the wavelength (see Eq. 1.30). In the optical wavelength range, for lines with an average Zeeman sensitivity (given by the Landé factor, see e.g., Bellot Rubio & Orozco Suárez 2019, Eq. 6) and typical solar magnetic field strengths, the Zeeman splitting leads to broader spectral lines while it becomes more pronounced towards the IR. Besides the splitting of spectral lines, the Zeeman effect also produces polarized light, which can be used for magnetic field measurements. The polarization of the light can be described by the Stokes vector (see e.g., Landi Degl'Innocenti & Landolfi 2004, Chapt. 1.6).

- Hyperfine splitting: Due to the coupling between the angular momentum of the ion or atom and bound electrons there can be a splitting of the energy levels. Usually, the wavelength difference is smaller than the thermal Doppler core.

1.3.5 LTE and NLTE approximations for the solar atmosphere

A detailed solution of the RTE for the optical depth in different parts of the solar atmosphere is computationally demanding. Approximations of the thermodynamics may simplify the computation and interpretation of the lines. In thermodynamic equilibrium (TE) the energies of particles are in equilibrium and can be described by only the temperature through the Maxwell-Boltzmann statistics. The solar atmosphere is, however, not in TE as radiation escapes in all directions and it is heated from below. An alternative is to assume the temperature changes only on scales much larger than the mean free paths of the photons. This assumption is called LTE. Under this assumption the distribution of populations between excitation stages i and j with$j > i$, and with energies E_i and E_j, $E_j > E_i$, is given by the Boltzmann distribution

$$\left[\frac{n_j}{n_i}\right]_{\mathrm{LTE}} = \frac{g_j}{g_i}\exp\left(-\frac{E_j - E_i}{\mathrm{k_B}T}\right). \tag{1.37}$$

Here n_i and n_j are the number densities of atoms in ionization stages i and j. The factors g_j and g_i are statistical weights of levels j and i. $\mathrm{k_B}$ is the Boltzmann constant and T is the temperature. Furthermore, the Saha ionization distribution can be used to calculate the ratio between the ground level i and the $i + 1$ ionization stage with

$$\left[\frac{n_{i+1}}{n_i}\right]_{\mathrm{LTE}} = \frac{1}{N_\mathrm{e}}\frac{2U_{i+1}}{U_i}\left(\frac{2\pi m_\mathrm{e}\mathrm{k_B}T}{\mathrm{h}^2}\right)^{3/2}\exp\left(-\frac{\chi_i}{\mathrm{k_B}T}\right). \tag{1.38}$$

Here n_i and n_{i+1} are the number densities of the two ground states of ionization stages i and $i + 1$, and χ_i is the ionization energy of stage i. N_e is the electron density, h is the Planck constant, and U_i, U_{i+1} are the partition functions of stage i (see Rutten 2003, p. 30). The line source function in LTE is given by the Planck function

$$\left[S_\nu^\mathrm{l}\right]_{\mathrm{LTE}} = B_\nu(T) = \frac{2h\nu^3}{c^2}\frac{1}{e^{h\nu/\mathrm{k_B}T} - 1}. \tag{1.39}$$

The main assumption of LTE is that collisions control the energy partitioning of the matter while radiative energy distributions may slightly deviate from the TE statistical distributions. Such assumptions can be justified in the photosphere or partly in the lower chromosphere but break down in the middle to the upper chromosphere. There, the frequency of collisions is drastically reduced due to decreasing density.

The scenario when LTE fails is called NLTE. The Saha and Boltzmann equations no longer describe the populations, and therefore, the line source function is no longer given by the Planck function. However, it is often assumed that statistical equilibrium (SE) holds, which means that the radiation field and level populations are not time-dependent, that is,

$$\frac{dn_i(\vec{r})}{\mathrm{d}t} = \sum_{j\neq i}^{N} n_j(\vec{r})P_{ji}(\vec{r}) - n_i(\vec{r})\sum_{i\neq j}^{N} P_{ij}(\vec{r}) = 0. \tag{1.40}$$

Here, n_i is the population density of the level of interest, and N is the total number of radiative transitions to and from level n_i. The quantity P_{ij} describes transition rates for radiative and collisional processes such that

$$P_{ij} = R_{ij} + C_{ij}. \tag{1.41}$$

If the right-hand side of Eq. 1.40 is nonzero, the situation is called nonequilibrium (NE). Such a situation is given, for example, for hydrogen ionization in the solar atmosphere

in the presence of shock fronts (Leenaarts et al. 2007). The radiative rates necessary to determine the population densities depend on the radiation field. A derivation of radiative rates R_{ij} for bb and bf processes can be found in Rutten (2003, p. 48) and approximations for bb and bf collisional rates C_{ij} in Rutten (2003, p. 51). The optical depth and the source function, which are necessary to compute the radiation field (Eq. 1.9), depend on the population density. This coupling between the radiation field and the populations is non-linear and non-local. Solving all these equations efficiently requires sophisticated numerical techniques (see Sect. 1.4.2).

A typical NLTE situation is given when scattering becomes important. In the simplified case of coherent scattering in a two-level atom, it can be shown (e.g., Mihalas 1978, p. 336-337), that the line source function equals:

$$S_\nu^l = (1-\epsilon_\nu)J_\nu + \epsilon_\nu B_\nu \tag{1.42}$$

$$= (1-\epsilon_\nu)\Lambda_\nu[S_\nu^l] + \epsilon_\nu B_\nu \tag{1.43}$$

Here J_ν is the angle averaged radiation field (Eq. 1.18), B_ν is the Planck function (Eq. 1.39), and ϵ_ν is the photon destruction probability per extinction, which is defined as:

$$\epsilon_\nu = \frac{\alpha_\nu^{\mathrm{a}}}{\alpha_\nu^{\mathrm{a}} + \alpha_\nu^{\mathrm{s}}} \tag{1.44}$$

with α_ν^{a} the extinction coefficient for absorption and α_ν^{s} the extinction coefficient for photon scattering. For $\alpha_\nu^{\mathrm{a}} \gg \alpha_\nu^{\mathrm{s}}$, which means extinction is dominated by absorption, we obtain $\epsilon_\nu \approx 1$ and $S_\nu^l \approx B_\nu$. This means the radiation field is coupled to the local thermal energy. In contrast, if $\alpha_\nu^{\mathrm{a}} \ll \alpha_\nu^{\mathrm{s}}$, the line source function will approach the angle averaged radiation field, which may be decoupled from the local thermal energy.

1.3.6 Frequency redistribution in chromospheric spectral lines

As mentioned in Sect. 1.3.1, scattering processes can lead to a loss of coherency, which means the frequency of the outgoing photon can be different from the incoming photon. It is common to distinguish three cases of frequency redistribution. In coherent scattering, there is monochromatic redistribution. This means the frequency of the outgoing photon is the same as that of the incoming photon. Such a scenario is, for example, given in two-level atom models with infinitely sharp upper and lower levels. The other extreme case is complete frequency redistribution (CRD). In this case, there is no correlation between the frequency distributions of incoming and outgoing photons. This condition is typically fulfilled when the energy levels of the atom or ion are strongly perturbed by elastic collisions. Most spectral lines that form in the photosphere and chromosphere can be treated in the CRD approximation.

Some spectral lines that form in the solar chromosphere form in neither of these two limits but demonstrate partial frequency redistribution (PRD). Spectral line scattering becomes partially coherent under a combination of several conditions. The upper energy level of the line transition must be weakly perturbed by elastic conditions. This is the case in lower-density layers of the solar atmosphere, such as the chromosphere. In addition, the atom or ion must exist in a dominant ionization stage, such that the line extinction is stronger than the continuum. Furthermore, the spectral line has to be a resonance transition, which means the lower energy state is the ground state. Prominent examples of lines in the solar spectrum that fulfill these conditions are Mg II h&k, Ca II H&K, and Lyα. Mihalas (1978, p. 411 ff) describes a detailed discussion of the calculation of redistribution functions. In

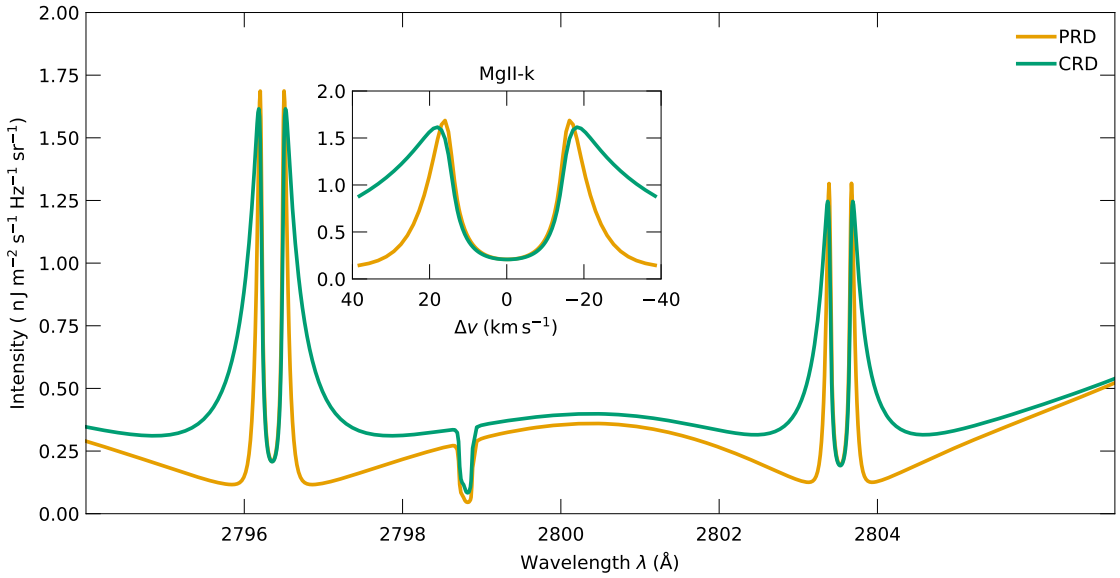

Figure 1.11: Comparison of the Mg II h&k line computed with CRD and PRD. The spectra were computed based on the FAL-C (Fontenla et al. 1993) model atmosphere and a 10+1 level magnesium atom. The green line shows the full PRD computation and the orange line the computation under the CRD approximation. The difference is strongest pronounced in the inner k_1 and h_1 wings. The inset panel shows a zoom to the Mg II k line.

the case of PRD, the line source function depends strongly on the monochromatic radiation field J_ν, which implies a frequency-dependent source function. The solution of the RT problem then requires simultaneous evaluation of the emission and absorption profiles along different angles. While approximations for the numerical computation of PRD exist (Leenaarts et al. 2012b), it is still much more expensive than the CRD approximation (Sukhorukov & Leenaarts 2017).

In Fig. 1.11 the effect of PRD is demonstrated for the Mg II h&k spectral lines. The profiles were computed with the Rybicki & Hummer 1.5D RT code (RH1.5D) (Pereira & Uitenbroek 2015, Uitenbroek 2001) in the FAL-C Fontenla et al. (1993) model atmosphere. It can be seen, that in the central depressions k_3 and h_3 (see also Fig. 1.7 for the definition of the spectral line features) the CRD approximation (green line) agrees well with the full PRD computation (orange line). In the inner line wings, k_1 and h_1, the CRD approximation fails. This is because in the line cores, redistribution occurs through thermal motions, and CRD is a valid approximation. In the inner wings (i.e., near the k_1 features), scattering becomes coherent, and the CRD approximation breaks down.

1.3.7 Radiative transfer in 1D, 1.5D and 3D

The solution of the RTE (Eq. 1.12) can be carried out in one, two, or three dimensions. Solving the RTE in 1D means the atmosphere is assumed to be plane-parallel, that is, all quantities change only along the vertical direction but are constant in horizontal planes. Examples of such calculations are given for example in Vernazza et al. (1981, Fig. 1) where the underlying atmosphere was also one-dimensional. With the advent of 3D models of the solar atmosphere (e.g. Nordlund 1982) first detailed 3D NLTE computations of spectral lines in such simulations followed (e.g. Nordlund 1985). The main difference between 1D RT and 3D RT lies in the mapping from the 3D quantities, such as the opacity and source function, to the 1D ray of interest (Carlsson 2008). Solving the RT problem for chromospheric spectral lines in 3D RT including PRD effects is, however, computationally challenging, and only recently were such computations presented for the Mg II h&k lines (Sukhorukov & Leenaarts 2017). In addition, 3D RT is difficult to compute due to slow convergence and the large requirements of computational resources. For example, 3D RT computations must store relevant quantities of the whole atmosphere model in the memory of the computer. In addition, the whole computation must converge globally. If there is a region in the atmosphere causing a slow convergence or the RT computation to fail, the whole computation might fail.

A compromise between 1D RT computations of 1D model atmospheres and the full 3D NLTE RT computations of 3D model atmospheres is the "1.5D RT" approximation (see e.g., Pereira & Uitenbroek 2015). Here, a 3D model atmosphere is subdivided into single columns for each of which the RT problem is solved, assuming the column was a plane-parallel atmosphere. This is obviously an approximation and has shortcomings in comparison with the full 3D RT computation. For example, the angle-averaged radiation field will be different compared to the full 3D RT computation because the horizontal transfer is neglected. This effect depends on the mean free path of the photons. In the denser regions of the atmosphere, the mean free path is shorter, and horizontal RT is not important. In the less dense regions, higher up in the atmosphere, where the cores of strong chromospheric lines form, the mean free path becomes larger, and 3D RT matters. This can be demonstrated with the RT calculations performed in this work. In Fig. 1.12 the angle-averaged radiation field J_ν (Eq. 1.18) is shown for a slice of the simulation we used for our studies in this work. The angle-averaged radiation field is shown in the core of the Mg II k line in units of radiation temperature[2] from 0 Mm–4 Mm, where 0 Mm is the average height where the optical depth at 500 nm reaches unity. It can be seen that both the 3D RT computation (panel a) and 1.5D RT computation (panel b) result in similar radiation temperatures in the lower chromosphere (roughly below 1 Mm). Above this height, the radiation temperatures are overestimated in the hot regions (e.g., at $(x, z) = (9\,\mathrm{Mm}, 2\,\mathrm{Mm})$) and underestimated in the cold regions (e.g., at $(x, y) = (11\,\mathrm{Mm}, 1.5\,\mathrm{Mm})$). In addition, the angle-averaged radiation field from the 3D RT computation shows much smoother structures in the upper chromosphere compared to the 1.5D RT computation (panel b).

There are, however, important advantages in the 1.5D RT computation. Because the RT problem is solved for each column individually, the computation can be well parallelized, and the convergence strategy can be optimized for columns with poor convergence behavior. In addition, the failure of the RT computation of a single column has no impact on the remaining columns. It was shown in the literature (e.g., Leenaarts et al. 2013a, Sukhorukov & Leenaarts 2017) that, in the case of the Mg II h&k lines, 3D RT is important for the line cores around k_3 and h_3 and the peak intensities k_2 and h_2, but not so much for the peak separation and the width of the line. How much these results depend on the

[2]The radiation temperature T_{rad} is defined by equating $J_\nu = B_\nu(T_{\mathrm{rad}})$ and solving for T_{rad}.

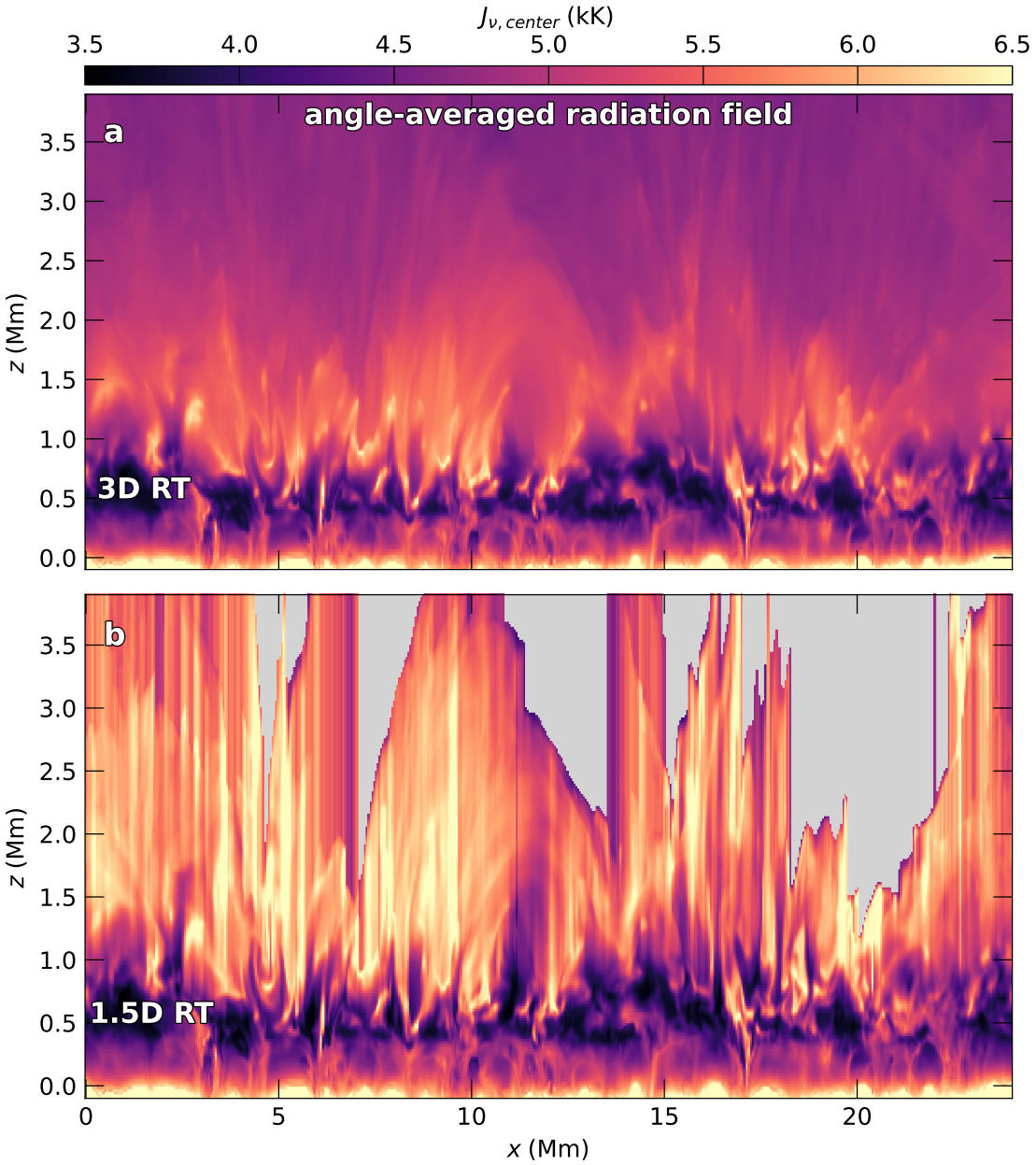

Figure 1.12: Angle-averaged radiation field computed in 3D RT and 1.5D RT. Panel (a) and (b) show the angle-averaged radiation field J_ν (see Eq. 1.18) at the rest wavelength of Mg II k in a vertical slice of a simulation cube computed with MURaM-ChE. The angle-averaged radiation field in panel (a) was computed with 3D RT, while the radiation field in panel (b) was computed with the 1.5D RT approximation. Clearly visible are differences in the middle to upper chromosphere at approximately $z > 1$ Mm. For the 1.5D RT computation, the atmosphere was cropped at a height where a temperature of 50 kK was reached (panel b, gray color).

underlying model atmosphere is a major motivation for Chapt. 3 in this work.

1.4. Modeling solar radiation: the forward modeling approach

In forward modeling, a model atmosphere is constructed from which synthetic spectral lines are computed. By comparing the synthetic spectrum with observations, limitations of the model or invalid approximations can be identified, and the model can be updated. If the match between the model and the observation is considered acceptable, the atmosphere model may help to interpret the observations.

Both the computation of the atmosphere model and the resulting synthetic spectra in a post-processing step are computationally expensive. Przybylski et al. (2022) compared, based on the results of Sukhorukov & Leenaarts (2017), that roughly 23 s per grid cell of an rMHD simulation snapshot are needed to compute the spectra of a chromospheric line in NLTE including PRD, with the roughly 15 μs, which are needed by the magnetohydrodynamics (MHD) computation per grid cell. In other words, computing detailed NLTE spectra of a chromospheric spectral line of one simulation snapshot can be as computationally expensive as the whole simulation. Therefore, in order to account for RT in the atmosphere model, certain approximations need to be made. In the following, I will summarize the methods of simulating the solar atmosphere in Sect. 1.4.1 and numerical RT in Sect. 1.4.2.

1.4.1 Modeling the solar atmosphere

Before computing synthetic spectral lines, an atmosphere model is needed that provides necessary quantities such as temperature, density, velocities, magnetic field, and ionization fraction. Early models of the solar atmosphere (e.g., Vernazza et al. 1981) aimed to reproduce spatial and temporal average conditions at different regions on the Sun. They were constructed following a trial and error approach where the atmosphere was modified to find the best match with observed spectra. The resulting atmosphere model was one-dimensional, and a fudge parameter called microturbulence (see Sect. 1.3.4) was needed to match the observed line widths due to the missing velocity field. More realistic models (e.g., Nordlund 1982) included a convection zone and a treatment of RT in the atmosphere, however under the LTE approximation. The solar chromosphere is out of LTE and therefore must be treated in NLTE. In particular, the radiative cooling through spectral lines and the rates of ionization and recombination must be treated in NLTE. Until recently, the Bifrost code (Gudiksen et al. 2011) was the only code that fulfilled the requirements of a non-grey, NE, and NLTE treatment of the chromosphere. The MURaM code was recently extended to include similar prescriptions as Bifrost to model the solar chromosphere. This new branch of the code is named chromospheric extension of MURaM (MURaM-ChE) and will be briefly described in the following. For more details, I refer to the methods sections in Chpts. 2, 3, and 4.

The MURaM-ChE code MURaM-ChE is an rMHD code aimed to simulate magnetoconvection and the solar atmosphere. It was originally developed by Vögler et al. (2005) and extended by Rempel (2017) to include prescriptions for simulating the corona, and it was recently updated by Przybylski et al. (2022) to include a NLTE and NE treatment of the solar chromosphere.

MURaM-ChE is a box-in-a-star code, which means only a limited spatial subdomain of the Sun is simulated, not the Sun as a whole. The box sizes typically extend a few Mm in each direction, depending on the scientific question the simulation is meant to address. The spatial resolution is typically on the order of a few tens of km. One of the main free parameters in the simulations is the initial magnetic field configuration.

A fundamental assumption of MURaM-ChE, and most other codes to simulate the Sun, is that the state of the plasma can be described by the MHD theory. This is a combination of hydrodynamics and the Maxwell equations. A detailed description of the MHD theory in the Solar context can be found, for example, in Priest (2014, Chapt. 2). The MHD equations describe density, momentum, and internal energy. The energy equation can be extended to include energy transport through radiation, which introduces numerical challenges as radiation can connect very different parts of the computational domain (e.g., a photon emitted in one part of the box can be reabsorbed in a totally different part, thus transferring energy over a large distance basically instantaneously). In MURaM-ChE, the plasma is described as a single fluid. This means there is no distinction between species, such as neutrals, ions, molecules, or electrons. There is, however, the possibility to include ion-neutral effects such as ambipolar diffusion (see e.g., Cheung & Cameron 2012, Rempel & Przybylski 2021), while retaining the computationally much cheaper single fluid description.

An accurate description of energy transport through radiation in the chromosphere is essential. As mentioned above, detailed RT calculations are, however, computationally expensive. An established strategy to compute the radiative gains and losses per time step in the simulation is the multigroup RT scheme (Nordlund 1982). For reviews see Carlsson (2008) and Leenaarts (2020). The scheme was implemented in MURaM as described in Vögler et al. (2004) and a scattering term was added by Przybylski et al. (2022) to model the chromosphere. The idea is not to accurately compute the exact spectral energy distribution but to approximate the radiative losses as well as possible at greatly reduced computational costs. Instead of solving the RTE for thousands of frequency points, only a few "radiation bins" are considered. These are constructed by grouping frequencies where the opacity is similar together. A common method is the "τ-sorting": in a 1D model atmosphere, the opacities and optical depth are computed in detail for many frequency points. This atmosphere is then divided into height bins. All frequencies where the optical depth unity is reached in a given height bin are then assigned to a radiation bin (see also Leenaarts 2020, Chapt. 3.1). This significantly reduces the computational effort to solve the RTE. There are additional radiative losses implemented based on tabulated values Carlsson & Leenaarts (2012) for the strongest spectral lines and continua in the chromosphere. These include the Lyman α, Hα, Mg II h&k, and Ca II H&K spectral lines and the Lyman continuum of hydrogen. As an approximation, these losses are implemented as optically thin losses which avoids the much more expensive solution of the RT problem for these elements (for a discussion see Leenaarts 2020, Chapt. 4).

With the implementation of Przybylski et al. (2022) the MURaM-ChE code became an important tool to simulate the chromosphere. The enhanced network simulation used for this work is one of the first simulations computed with this code. It is aimed to simulate a QS region that includes network magnetic fields, in this case as a large-scale magnetic bipole with $\approx 8\,\mathrm{Mm}$ separation between the two polarities. For further description, see Chapt. 2. In Fig. (1.13), a volume rendering of the density with increased contrast in the chromosphere from one snapshot is shown. It is visible that the model contains many substructures. The loop-like structures visible in the center of the image connect two large-scale magnetic polarities in the simulation. The dynamic nature of this simulation is reflected in the resulting spectral lines (see Chapts. 2 and 3).

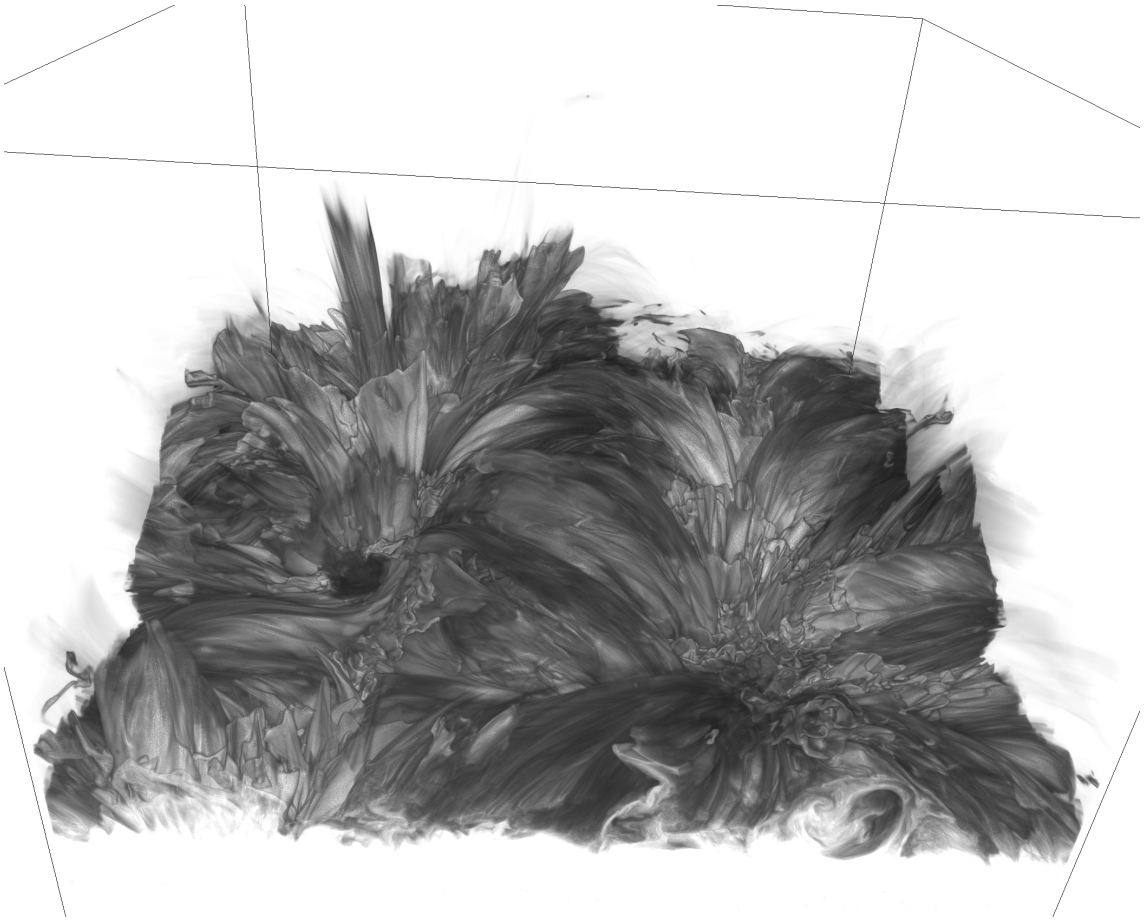

Figure 1.13: Volume rendering of the EN simulation. The density is shown with increased contrast in the chromosphere. The image shows the complex structure of the chromosphere at a single simulation time step. The 3D rendering was created with the Vapor visualization software (Li et al. 2019, Sgpearse et al. 2023).

1.4.2 Methods for numerical radiative transfer

In order to compare simulations with observations, detailed RT computations of spectral lines are required. In this section, I summarize how such solutions can be obtained numerically. In Fig. 1.14 the basic problem of NLTE RT is schematically illustrated. If the specific intensity $I_\nu(\tau_\nu, \mu)$ at a given optical depth τ_ν at angle μ is desired, the source function will be required to solve the integral. If scattering is important, the source function will depend on the angle-averaged radiation field J_ν. The angle-averaged radiation field, however, depends on the intensity in many directions, which therefore means the source function is required at many locations. The solution of the RTE in NLTE is therefore non-linear, non-local, and may even be time-dependent if SE does not hold. In the case of PRD the source function must additionally be known at many frequencies across the spectral line.

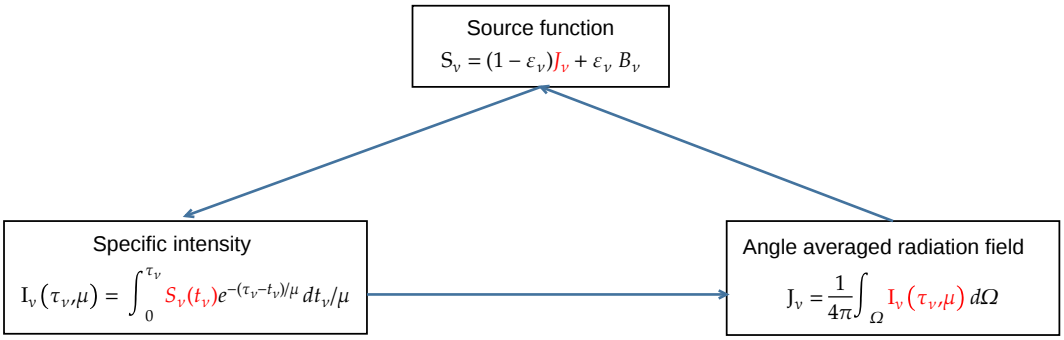

Figure 1.14: The non-linear and non-local RT problem. Dependence of intensity, source function, and angle averaged radiation field in NLTE in the case of a simplified two-level atom with scattering. The arrows indicate the dependence. For example, in order to compute the specific intensity, the source function is required, while the source function can only be computed if the angle-averaged intensity is known.

Multiple approaches exist to solve the RT problem numerically. I will here focus on discrete ordinate methods, which solve the RTE on a multidimensional grid of frequency, coordinates, and angles. These methods are different in concept compared to, for example, Monte Carlo methods which simulate scattering, absorption, and emission processes by following a photon package through the medium (for a review see e.g., Noebauer & Sim 2019).

A class of methods that are based on the discrete ordinate scheme are iterative solutions. The idea is based on finding a solution for equations like Eq. (1.43). A direct inversion of the Λ operation via

$$S_\nu^l = (1 - (1-\epsilon)\Lambda)^{-1}[\epsilon_\nu B_\nu] \tag{1.45}$$

requires numerical matrix inversion which is computationally expensive. The idea is to find the solution through iterations as:

$$S^{(n+1)} = (1-\epsilon_\nu)\Lambda[S^{(n)}] + \epsilon_\nu B_\nu \tag{1.46}$$

Here, n is the iteration number. The above description was based on two-level atoms. Lambda iterations can however be extended to multilevel RT problems. Such an algorithm

conceptually consists of the following steps (see e.g., Rutten 2003, p. 123 f):

$$J_\nu^{(n)} = \Lambda_\nu[S_\nu^{(n)}] \tag{1.47}$$

$$\mathbf{n}^{(n)} = f_1(J^{(n)}) \tag{1.48}$$

$$S_\nu^{(n+1)} = f_2(\mathbf{n}^{(n)}) \tag{1.49}$$

In the first step, the angle-averaged radiation field is obtained for each relevant transition at each optical depth from the total source function. The second step consists of determining the corresponding level populations $\mathbf{n}$ for all depths from the radiation field by using the equations of SE (see Sect. 1.3.5), schematically represented by the functional f_1. In the third step, the new line source function is determined for each frequency (in case CRD does not apply), expressed by the functional f_2. If the continuum source function also depends on J_ν because of scattering processes, it similarly needs to be computed per iteration. The steps are repeated until a convergence criterion, for example on the change of level populations, is reached. In the case of PRD, the iteration procedure follows, for example, the description in Sukhorukov & Leenaarts (2017, p. 3).

In practice, the classical Lambda iteration has been replaced, due to its slow convergence, by an operator perturbation technique (Cannon 1973) which is called approximate Lambda iteration (ALI) or accelerated Lambda iteration (see e.g., Hubeny & Mihalas 2014, p. 421 ff). Here, the Lambda operator is split into

$$\Lambda_\nu = \Lambda^* + (\Lambda_\nu - \Lambda^*) \tag{1.50}$$

where Λ^* is the approximate Lambda operator. By choosing an appropriate approximate Lambda operator, the convergence can be achieved in significantly less steps. The approximate Lambda operator should contain the basic physical properties of the original Lambda operator and should be easy to invert, that is with low computational effort.

In this work, I use two RT codes. The first code is RH1.5D (Pereira & Uitenbroek 2015) which is based on the RH code (Uitenbroek 2001), and the second code is Multid3D (Leenaarts & Carlsson 2009). RH1.5D is an open-source code, optimized to solve the RT problem on a column-by-column base from a 3D snapshot of a simulation (see Sect. 1.3.7). RH1.5D is able to solve the NLTE RTE simultaneously for multiple atoms. This is required in this work for the synthesis of the Ca II λ854.2 nm line, which is a composition of six isotopes of calcium that have slightly different atomic properties. Additionally, in RH1.5D line blends can be added. These are transitions from other atomic elements that overlap in frequency with the considered transition but are usually much weaker. These transitions are computed by RH1.5D in the LTE approximation. In Chpt. 2 and Chapt. 4 I use the RH1.5D code to compute spectral lines from MURaM-ChE snapshots.

In the chromosphere, spectral lines are known to demonstrate 3D RT effects. This is indicated for example by the too-high intensity contrast or missing appearance of larger scale structures, such as fibrils, in 1.5D RT computations. Recent examples of spectral lines for which the importance of full 3D RT has been demonstrated based on 3D rMHD simulations are Hα (Leenaarts et al. 2012a), Mg II h&k (Sukhorukov & Leenaarts 2017), and Ca II H&K (Bjørgen et al. 2018). In Chapt. 3, I used the parallelized version of the Multi3D code (Botnen 1997, Leenaarts & Carlsson 2009) with the extension to compute Mg II h&k spectra in PRD by Sukhorukov & Leenaarts (2017).

There exist other 3D RT codes, such as the 3D version of Rybicki & Hummer code (RH) Uitenbroek (2001), which was debugged and first properly used for 3D RT by Holzreuter & Solanki (2012). The 3D RH code is, however, not optimized for the RT computation in large model atmospheres. The PORTA (Štěpán & Trujillo Bueno 2013) code is designed to include polarized RT through the Hanle or Zeeman effect (see e.g., Stenflo 1994) in 3D, but the public version does not include a PRD treatment.

2. Mg II h&k spectra of an enhanced network region simulated with the MURaM-ChE code: Results using 1.5D synthesis

The content of this chapter was published in Astronomy & Astrophysics (Ondratschek et al. 2024). Authors: **Ondratschek, P.**; Przybylski, D.; Smitha, H. N.; Cameron, R. ; Solanki, S. K.; Leenaarts, J. Astronomy & Astrophysics, Volume 692, id.A6, 17 pp.
Doi: 10.1051/0004-6361/202450788. Reproduced with permission. Contributions to the paper: I performed the RT computations, analyzed the data, and wrote the first draft of the manuscript; all authors contributed to the ideas behind the study and to the final form of the paper.

Abstract. The Mg II h&k lines are key diagnostics of the solar chromosphere. They are sensitive to the temperature, density, and nonthermal velocities in the chromosphere. The average Mg II h&k line profiles arising from previous 3D chromospheric simulations are too narrow compared to observations.

We study the formation and properties of the Mg II h&k lines in a model atmosphere. We also compare the average spectrum, peak intensity, and peak separation of Mg II k with a representative observation taken by the Interface Region Imaging Spectrograph (IRIS).

We use a model based on the recently developed nonequilibrium version of the radiative magneto-hydrodynamics code MURaM, the MURaM Chromospheric Extension (MURaM-ChE), in combination with forward modeling using the radiative transfer code RH1.5D to obtain synthetic spectra. Our model resembles an enhanced network region created using an evolved MURaM quiet Sun simulation and adding an imposed large-scale bipolar magnetic field similar to that in the public Bifrost snapshot of a bipolar magnetic feature. The line width and the peak separation of the spatially averaged spectrum of the Mg II h&k lines from the MURaM-ChE simulation are close to a representative observation of the quiet Sun, which also includes network fields. However, we find the synthesized line width to be still slightly narrower than in the observation. We find that velocities in the chromosphere play a dominant role in the broadening of the spectral lines. While the average synthetic spectrum also shows a good match to the observations in the pseudo continuum between the two emission lines, the peak intensities are higher in the modeled spectrum. This discrepancy may be due in part to the larger magnetic flux density in the simulation than in the considered observations, but could also be a result of the 1.5D radiative transfer approximation. Our findings show that strong maximum-velocity differences or turbulent velocities in the chromosphere and lower atmosphere are necessary to reproduce the observed line widths of chromospheric spectral lines.

2.1. Introduction

The solar chromosphere is highly dynamic and complex. Although an exact definition of this part of the solar atmosphere is not straightforward, it is spatially located above the photosphere and below the transition region that connects the chromosphere to the corona. It can also be described as the region above the solar surface where hydrogen is partially ionized but is still mostly neutral. In order to study the energy transfer in the solar atmosphere, detailed knowledge of the structure and dynamics of the chromosphere is essential. Much about the chromosphere is still not well understood. For example, the role of shock waves in structuring and heating the chromosphere versus the role of magnetic fields is not fully resolved. Interpretations of observed chromospheric phenomena, for example through the Mg II h&k lines, require a comprehensive understanding of the underlying atmosphere.

Observationally, chromospheric spectral lines are key to investigating the chromosphere in detail as they contain signatures of the plasma conditions in their formation regions. Strong chromospheric lines can be observed from the ultraviolet (UV) to the infrared. These include well-known lines such as Mg II h&k, Ca II H&K, Hα, and the Ca II infrared triplet. In this work we focus on the Mg II h&k lines, which are centered at 2796 Å (Mg II k) and 2831 Å (Mg II h), and are thus inaccessible from ground-based telescopes as the UV part of the spectrum is blocked by the Earth's atmosphere. The first high-resolution images in the core of the Mg II k line (Riethmüller et al. 2013, Danilovic et al. 2014) were taken by the SuFI instrument (Gandorfer et al. 2011) on board the second flight of the balloon-borne observatory Sunrise (Solanki et al. 2010, 2012, Barthol et al. 2011). Currently, the main source of long-term Mg II h&k observations is the Interface Region Imaging Spectrometer (IRIS, De Pontieu et al. 2014) satellite launched in 2013.

In the present paper, our aim is to compute and analyze the Mg II h&k lines in a new model of the solar chromosphere and to compare the resulting profiles with IRIS observations. Despite the availability of advanced techniques to model the chromosphere and compute the emergent intensity, discrepancies are still found between observed spectra and those arising from MHD simulations. Computed Mg II h&k spectra show, on average, narrower line widths and weaker peak intensities than those seen in observations (Carlsson et al. 2019). A number of possible explanations have been proposed. Leenaarts et al. (2013b) posited that these effects might be coming from overly weak velocity fields and from an underestimated mid-chromospheric temperature in the models. Carlsson et al. (2016) argued that the magnitude of "nonthermal velocity" in the atmosphere, which contributes to the broadening of spectral profiles, can be increased by using a higher-resolution simulation domain. Carlsson et al. (2015), Carlsson et al. (2019), and Hansteen et al. (2023) argued that besides macroscopic velocities, the so-called opacity broadening (Rathore & Carlsson 2015) affects the width of the Mg II h&k lines.

Propagating shocks, decreasing density, and magnetic fields lead to a highly structured chromosphere. This is reflected in the formation of Mg II h&k. Two dominant effects are the nonlocal thermodynamic equilibrium (NLTE) formation of the spectral lines and partial frequency redistribution (PRD). NLTE conditions lead to deviations of the line source function from the Planck function. The second effect is a result of scattering, which becomes important in the upper chromosphere (for Mg II k e.g., see Milkey & Mihalas 1974, Leenaarts et al. 2013a). PRD effects in the formation of Mg II h&k have also been studied in the context of scattering polarization (see e.g., Auer et al. 1980, Belluzzi & Trujillo Bueno 2012).

A model atmosphere is required to study line formation in the chromosphere; this must provide temperatures, hydrogen populations, and electron densities accounting for

NLTE effects. Early studies on the formation of Mg II h&k in solar-like atmospheres were based on one-dimensional (1D) models. The semi-empirical models of Vernazza et al. (1981, VAL models) or Fontenla et al. (1993, FAL models) represent spatial and temporal average conditions of the solar atmosphere. More sophisticated hydrodynamics codes like RADYN (Carlsson & Stein 1992, 2002) are used to study dynamic atmospheres including propagation of waves and shocks and a treatment of radiation transfer for determining the non-equilibrium (NE) populations and NLTE losses. Self-consistent models need 3D geometry to accurately model the convection and dynamics of the atmosphere, as well as 3D radiation transfer (Leenaarts 2020) to account for the scattering in the chromosphere. Bifrost (Gudiksen et al. 2011) is a radiation magnetohydrodynamics (rMHD) code that fulfills these and the above-mentioned requirements.

In this work, we used the recently developed chromospheric extension of the MURaM code (Przybylski et al. 2022), which we refer to in the following as MURaM-ChE.[1] The chromospheric extension includes a NE treatment for hydrogen ionization and approximations to NLTE radiative line losses. The simulated atmosphere is a reproduction of the Bifrost enhanced network simulation (Carlsson et al. 2016, hereafter the public Bifrost snapshot), with a similar large-scale field. We used the atmosphere model to compute synthetic spectra of the Mg II h&k lines in the "plane-parallel" approximation, where each vertical column of the 3D atmosphere is treated as an individual 1D atmosphere for the radiative transfer (RT) computation (also called 1.5D approximation). The horizontal components of the velocity field are neglected in this approximation.

In Sect. 2.2 we describe the numerical tools, including the MHD simulation, spectral synthesis, and the observations. In Sect. 2.3 we present the results from the forward-modeled spectra and compare them with observations and the public Bifrost snapshot. A summary and conclusions are presented in Sect. 2.4.

2.2. Methods

In this section we describe the methods on which our analysis is based. We briefly describe the MURaM-ChE code and the setup of our enhanced network model. We then describe how the RT computations were performed. After this we introduce the observations and the public Bifrost snapshot used for comparison. Followed by this we describe the procedure to spatially and spectrally degrade the synthetic spectra, in order to better match the conditions imposed on the observations by the instrumentation, and finally present a description of how the different spectral features were identified.

2.2.1 Enhanced network model

We use results of an rMHD simulation performed with the chromospheric extension of the MURaM code (Przybylski et al. 2022). The code is based on the LTE radiative magnetoconvection code by Vögler et al. (2005), extended to include optically thin losses and point-implicit heat conduction by Rempel (2017) in order to treat the physics of the corona.

The simulation setup is similar to that described in Przybylski et al. (2022), and includes a four-band multigroup RT scheme (Nordlund 1982, Vögler et al. 2004) extended to include scattering effects (Skartlien 2000, Hayek et al. 2010). Additional radiative losses from strong chromospheric lines and optically thin losses in the corona are included

[1] Max Planck Institute for Solar System Research/University of Chicago Radiation Magnetohydrodynamics with the chromospheric extension.

as described in Carlsson & Leenaarts (2012). Furthermore, we include 3D extreme-ultraviolet (EUV) back-heating of the chromosphere similar to Carlsson & Leenaarts (2012). In the convection zone we use a non-ideal equation of state (EoS) generated with the free-EoS package (Irwin 2012), joined to a time-dependent, NE treatment of hydrogen in and above the photosphere (Sollum 1999, Leenaarts & Wedemeyer-Böhm 2006, Leenaarts et al. 2007). We use abundances from Asplund et al. (2009). The time-dependent EoS includes a NE treatment of molecular H_2, and H_2^+ and H^- in chemical equilibrium. In the EoS all non-hydrogen elements are treated in LTE. The diffusion scheme follows Rempel (2014, 2017), which is based on a slope-limited scheme. Numerical diffusion is included based on monotonicity constraints, which are disabled in sufficiently smooth regions. This allows the simulation to run smoothly with minimal resistivity and viscosity. In addition, we used the "Boris" correction (Boris 1970) to limit the Alfvén speed, which enables simulations at high numerical resolution to be run with a reasonable computational cost by relaxing the Alfvén speed contribution to the Courant-Friedrichs-Lewy (CFL) criterion (Courant et al. 1928).

The setup of the bipolar structure for an enhanced network environment is close to the public Bifrost snapshot. Due to differences between the EoSs in the MURaM-ChE and Bifrost codes, a direct restart of the Bifrost public snapshot did not result in a sun-like star. To build the model used in this paper we use an existing small-scale dynamo (SSD) model (Przybylski et al., in preparation). The SSD model extends 12 Mm × 12 Mm × 18 Mm with a resolution of 23.46 km horizontally and 20 km vertically. The atmosphere ranges from −6.6 Mm below to 11.4 Mm above the photosphere. We tiled this model 2x2, by copying the simulation box three times, to produce a box that extends 24 Mm × 24 Mm horizontally with 1024x1024 grid points. The domain was extended 4 Mm further in the vertical direction, to give a total extent from -7 Mm to 17 Mm with 1200 grid points (with the solar surface lying at a height of 0 Mm). The resolution is therefore the same as in the SSD model. The MURaM-ChE code uses an equidistant vertical axis, that is the grid is not variable as in other codes (e.g. Bifrost). This model is run for 8 hours, to break the periodicity, which comes from tiling the smaller SSD model to the larger simulation domain, and to allow the simulation to relax from transients due to the extension. The horizontal boundary conditions are periodic. The upper boundary is open to outflows but closed to inflows. The magnetic field at the top boundary is treated as a potential field. In the lower boundary we use an open symmetric-field condition as described in Rempel (2014). We added a bipolar magnetic field to the simulation, to give a large-scale field similar to the initial condition of the public Bifrost snapshot on top of the existing SSD model. We then ran the model for additional 1.5 hours. After that we turned on the NE treatment of hydrogen and ran the computations for another 10 minutes in order to allow the populations to settle into a new equilibrium. We then saved a 10 minute time series at ≈ 6 s cadence, which we use for our analysis. Additionally, we saved 8 2D slices at fixed x and y positions through the box, but with a higher temporal cadence of 1.2 seconds. In Fig. 2.1 we show the vertical component of the magnetic field at the $\tau_{500} = 1$ plane and at a constant height of 12 Mm for the snapshot discussed in Sect. 2.3. The absolute value of the vertical component of the magnetic field at the photosphere can reach values of up to $|B_z(\tau_{500} = 1)| \approx 2$ kG, but we clipped the gray scale to values of ±500 G to also highlight the smaller structures. The spatial unsigned mean of the vertical component of the magnetic field is $\langle|B_z(\tau_{500} = 1)|\rangle = 64$ G.

In observations, as for example taken by the Helioseismic and Magnetic Imager (HMI, Scherrer et al. 2012, Schou et al. 2012), the Stokes signal of the Fe I λ6173 Å line is used to measure the line-of-sight (LOS) magnetic field. The wings of the Fe I λ6173 Å line, where the Stokes-V signal is strongest, are expected to form approximately at $\tau_{500} = 0.1$ (e.g.,

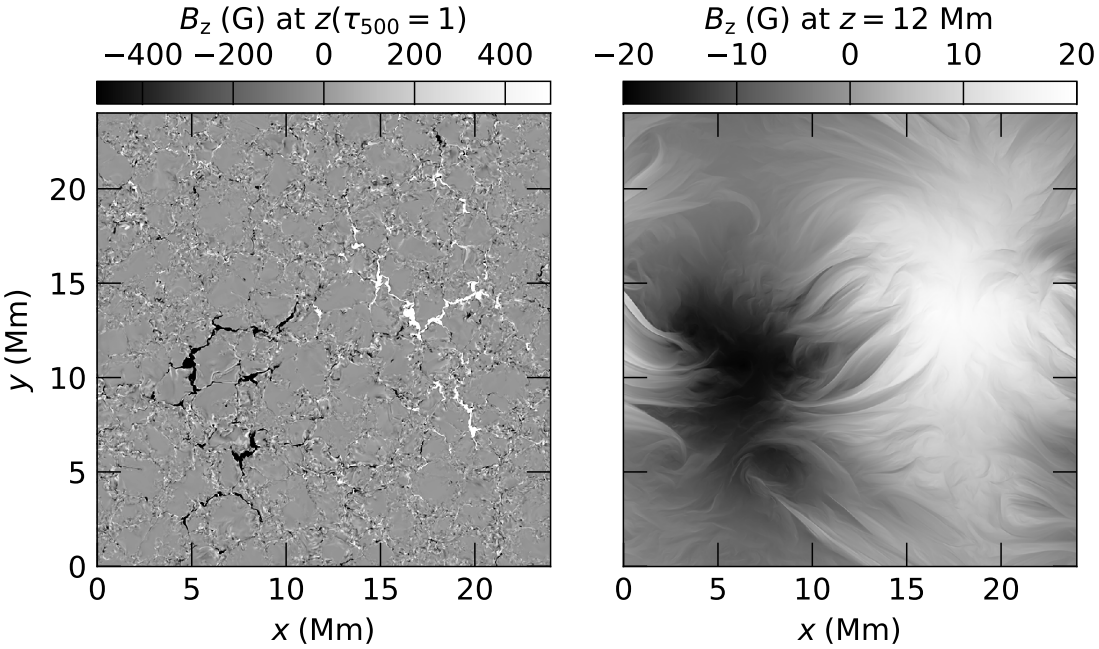

Figure 2.1: Vertical component of the magnetic field vector in the simulated atmosphere. Left panel: Vertical magnetic field map of the MURaM-ChE simulation at the $\tau_{500} = 1$ layer. The gray scale is saturated at $|B_z| = 500\,\mathrm{G}$ to accentuate some of the weaker internetwork fields. Right panel: Vertical magnetic field at a constant height of 12 Mm with a gray scale saturated at $|B_z| = 20\,\mathrm{G}$.

Fleck et al. 2011, Quintero Noda et al. 2021). We therefore degraded the magnetogram of the simulation at $\tau_{500} = 0.1$ to a resolution of 1" $\approx 760\,\mathrm{km}$, by convolving the data by a Gaussian kernel, to make it comparable in resolution to an HMI magnetogram taken during the IRIS observation we compare our synthetic spectra with (see Sect. 2.2.3). The degradation in spatial resolution led to $\langle|\tilde{B}_z(\tau_{500} = 0.1)|\rangle = 20.7\,\mathrm{G}$, where $\tilde{B}_z$ refers to the field strength after spatial degradation. For comparison, the value computed at the original resolution is $\langle|B_z(\tau_{500} = 0.1)|\rangle = 43.5\,\mathrm{G}$.

The left panel of Fig. 2.1 shows the magnetogram at the $\tau_{500} = 1$ plane where small magnetic structures arising through the SSD action can be seen. The large-scale bipolar structure appears along the horizontal diagonal, which is from the lower left to the upper right corner in Fig. 2.1a,b, of the simulation domain and dominates at a constant height of 12 Mm (right panel).

We want to emphasize that even though the MURaM-ChE and Bifrost models appear to be similar in terms of the numerical treatment and the initial conditions, there are significant differences in the resolution, simulation depth, top boundary condition, EoS, and diffusion scheme. Therefore, a direct comparison is not straightforward and is not the subject of this work.

2.2.2 Synthetic spectra

We perform detailed RT calculations to model the Mg II h&k emerging intensity for comparison with observations. We used the RT code RH1.5D (Pereira & Uitenbroek 2015) which is based on the original RH code (Uitenbroek 2001). The code solves the RT problem using the multilevel accelerated lambda iteration (MALI) method as described in Rybicki & Hummer (1991, 1992). The Mg II h&k lines are computed in NLTE and

the angle-dependent PRD effects are taken into account via the hybrid approximation described in Leenaarts et al. (2012b). We use the 10+1 level Mg II atom described in Leenaarts et al. (2013a). Other elements such as H, C, O, Si, Al, Ca, Fe, He, Ni, Na, and S were included in the background by treating them in LTE. Similar to Pereira et al. (2013) we additionally included the strongest 15 % of the lines from the Kurucz line list (Kurucz & Bell 1995) in the IRIS NUV window. These blending lines are mostly located in the inner wings and the pseudo-continuum between the Mg II h&k lines, and a few of these blends lie close to the cores of the Mg lines. However, they are not strong enough to have an impact, neither on the intensities nor on the shapes of the Mg II h&k line cores. The abundances were taken from Asplund et al. (2009). We used a maximum relative change in the atomic level population of $|\Delta n/n| = 10^{-3}$ as the stopping criteria for the iterative solution. In the RT computation the impact of magnetic fields on the emergent intensity through the Zeeman effect was neglected. The 1.5D RT computation does not take horizontal velocity components into account. This means there is no potential reduction in intensity contrast as for example in Jaume Bestard et al. (2021) in the case of Ca I λ4227Å. The source function was interpolated using a linear scheme. This allows for a better comparison with the Bifrost spectra (see IRIS Technical Note, 35[2]). In addition, we did not find a significant difference between the linear and a cubic Bezier interpolation scheme.

In order to reduce the computational costs, we cropped the vertical extent of each column in the atmosphere at a height along the LOS where a temperature of $T_{\rm cut} = 50\,{\rm kK}$ is reached. The height where the atmosphere is cut is determined by going from the top of the atmosphere downwards until the value of the temperature is lower than $T_{\rm cut}$. Furthermore, for three of the four snapshots considered here only every second column in both the x and y directions in the atmosphere was used for spectral computations. To justify the latter approximation we computed snapshot `muram_en_499000_379s`[3] in full resolution and compared the average spectrum with the one with only 25% of the pixels, finding no significant difference in the Mg II h&k window and in the distributions of peak intensities and peak separations.

2.2.3 Observations

We use data from the IRIS satellite. The NUV window of IRIS covers a wavelength range from 2783–2834 Å with a spectral resolution of $\approx 6\,{\rm pm}$ and a spatial resolution of 0".4 $\approx 240\,{\rm km}$. For estimations of the magnetic field in the photosphere we use data from HMI on board the Solar Dynamics Observatory (SDO). HMI magnetograms provide the LOS magnetic field strength in the lower solar atmosphere estimated using Milne-Eddington inversions of the Fe I λ6173.3 Å spectral line profiles (Borrero et al. 2011).

We use an IRIS raster observation from a quiet region that includes network fields, in order to compare with the profiles from the MURaM-ChE model. The observation was taken on 2014-06-07 and has a field of view of 139" × 182" (or approximately 105 Mm × 138 Mm) with a cadence of 15 s. The observation was taken close to disk center at $\mu = 0.96$, where $\mu = \cos(\theta)$ with θ being the heliocentric angle. While our synthetic spectra are computed at $\mu = 1.00$ we do not expect this slightly inclined viewing angle to have a strong impact on the observed intensity (see, e.g., Avrett et al. 2013, Sukhorukov & Leenaarts 2017). The field-of-view (FOV) is larger than the simulation domain of the

[2]IRIS technical note (ITN) 35: `https://www.lmsal.com/iris_science/doc?cmd=dcur&proj_num=IS0217&file_type=pdf`

[3]We use the following name convention for snapshots: muram_en_iterationNumber_time where the time is measured in sec from the beginning of the 10 min series that we used for our analysis.

model. In Appendix 2.6 we consider three smaller FOVs, which are similar in size to our model, together with two additional observations, demonstrating that the chosen dataset is representative enough for the purpose of this work. The data were available in a rebinned format such that the final spectral and spatial resolutions are half of the original IRIS specifications.

We aligned the HMI magnetogram, recorded roughly half way through the IRIS observation, with the raster by performing the following steps. First, we projected the HMI magnetogram onto the IRIS FOV. For this purpose we used the "reproject_interp" function which is part of the Astropy Project (Astropy Collaboration et al. 2022). Then we corrected the HMI image and the IRIS raster scan for the effect of solar rotation which we assumed to be only noticeable in the east-west direction, as the observations are close to disk center.

The averaged unsigned LOS magnetic field over the whole FOV, calculated from the HMI magnetogram and corrected for the viewing angle μ, is $\langle |B_{\rm LOS}/\mu| \rangle = 12.12\,{\rm G}$ which is smaller than the degraded value at $\tau_{500} = 0.1$ of 20.7 G from the simulation. However, recent studies have shown that the magnetic flux measured by HMI could be underestimated by not accounting for NLTE effects in the Fe I λ6173.3 Å line (Smitha et al. 2023) or because magnetograms can miss a significant fraction of the magnetic flux even in unipolar magnetic field regions (Sinjan et al. 2024, Milić et al. 2024). In Table 2.1 we show the mean unsigned LOS magnetic field strengths for smaller regions of interest (ROI) that are comparable in size to our simulation. Their values in the selected ROIs vary from 6.8 G (quiet sun) to 33.2 G (network).

2.2.4 The public bifrost snapshot

The Bifrost model from Carlsson et al. (2016) resembles an enhanced network region. It has a horizontal extent of 24 Mm × 24 Mm and a vertical extension from −2.4 Mm below and 14.4 Mm above the $\tau_{500} = 1$ surface. The horizontal spatial resolution of this simulation is 48 km and the vertical resolution varies between 19 km in the photosphere and chromosphere, and up to 100 km at the top boundary. A bipolar magnetic field structure with 8 Mm separation between the opposite poles was added to the bottom of the simulation domain. At $t = 3850$ s the average unsigned vertical magnetic field strength at the photosphere is 48 G. The public release[4] of the enhanced network simulation also includes synthesized spectra of the Mg II h&k lines which we use for comparison. These spectra were also computed with the plane-parallel 1.5D approximation and do not include a 3D RT treatment for the line centers, in contrast to the profiles described in Leenaarts et al. (2013b).

2.2.5 Spatial and spectral degradation

We degraded the spectra from both the MURaM-ChE model and the public Bifrost snapshot to the spatial and spectral resolutions of IRIS (De Pontieu et al. 2014). We followed a procedure similar to that described in Pereira et al. (2013); a Gaussian kernel of 0".4 full width at half maximum (FWHM) is used for spatial degradation and a Gaussian profile with a FWHM of 6 pm for the spectral convolution. In addition, the spectra have been rebinned to a pixel size of 0".16 × 0".33 which translates to 199 × 100 pixels.

As described in Sect. 2.3.2.5, we synthesized a 10 min time series at a cadence of ≈ 1.2 s of the spectra emerging along artificial slits placed in the simulation domain. For each time step, the spectra are spatially degraded along the slits, but are not degraded

[4] http://sdc.uio.no/search/simulations?sim=en024048_hion

across the slit as they are only one pixel wide. The spatial degradation is the same as described above: convolution by a Gaussian kernel of 0".4 FWHM and binning to a pixel size along the slit of 0".16.

2.2.6 Identifying spectral features

The typical shape of an observed Mg II k line consists of two peaks that are commonly named k_{2v} and k_{2r} ("r":red, "v": violet/blue), a central minimum labeled as k_3, and two minima in the "inner wings" of the spectral line labeled as k_{1r}/k_{1v}. The nomenclature for Mg II h is similar. To classify the spectra, we need to identify characteristic spectral features such as the emission peaks and the k_3 feature. For this purpose we use a peak-finding algorithm that is part of the `ssw modules`[5] (Freeland & Handy 1998) and described in Pereira et al. (2013). The synthetic spectra, however, show the "classical" two-peaked profile shapes only in ≈ 20% of the cases (for `muram_en_499000_379s`). The remaining ≈ 80% of spectra show three or more peaks. The identification of spectral features therefore has to be done carefully and comes with caveats.

After applying the peak-finding procedure we noticed the following hurdles. First, the positions of the identified peak features appear to be correct in most of the cases. The corresponding intensities, however, are sometimes overestimated. This might be due to the peak-finding algorithm which interpolates the spectrum with a spline function to a regular grid, which sometimes may lead to an over- or under-shoot of the intensities. To overcome this issue we set the intensity of the identified features to the intensity without interpolation that is closest to the wavelength position of the feature.

Second, ≈ 3% of the identified peak features are found to be either both on the red, or both on the blue side of the spectrum, with respect of the central minimum. Third, the dynamic nature of the atmosphere leads to spectra that have multiple peaks instead of only two. These can either be clearly distinguished, or they are close to each other in wavelength and thus appear as "wiggles" rather than as individual peaks. For those spectra even a visual characterization of the features is not straightforward and introduces some uncertainty.

In a typical snapshot we find that, before degrading the spectra, approximately 10 % of the peak features cannot be used as the peak-finding algorithm either failed (no results found) or delivered wrong results (e.g., both k_2 features on one side with respect to k_3). Even after excluding these spectra from the statistics it turns out that profiles with multiple peaks may still be not correctly classified. This is because the wavelength position of a spectral feature in a profile with more than two peaks is not always uniquely defined from an observational point of view.

Degraded profiles are typically smoother, and the number of spectra with more than two peaks is significantly reduced. The peak features are therefore better defined and can be identified more clearly with the peak finder. A consequence of the smoother spectral profiles is also that some of the peaks become washed out, such that they appear as saddle points instead of minima/maxima. This occurs for 16 % of the degraded spectra, for which the peak separation cannot be measured accurately.

2.3. Results

In the following, we discuss the properties of the synthetic spectra and compare them to the observation described in Sect. 2.2.3. In Appendix 2.6 we compare the synthetic

[5]For an overview of IRIS-related analysis tools see: `https://iris.lmsal.com/analysis.html`

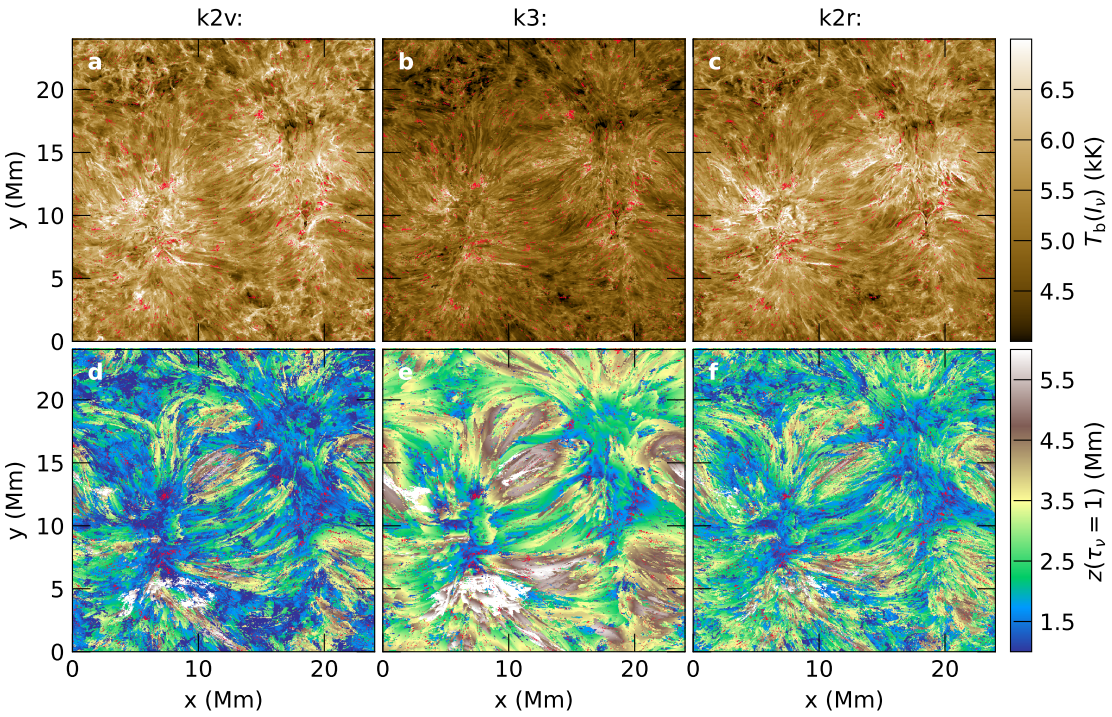

Figure 2.2: Intensity and formation height at selected spectral features of the Mg II k line. The top panels show the brightness temperature at k_{2v} (panel a), k_3 (panel b), and k_{2r} (panel c) as classified by the peak-finding algorithm. The bottom panels show the height at an optical depth of unity at the wavelength of k_{2v} (panel d), k_3 (panel e), and k_{2r} (panel f). Red pixels indicate those where no feature could be detected. The data correspond to the non-degraded `muram_en_499000_379s` snapshot.

spectra with smaller selected FOVs and two additional observations to illustrate that the here presented average spectrum is representative for the purposes of this work. Mg II h and k share similar formation properties and statistics (Leenaarts et al. 2013b). Therefore we focus here only on the Mg II k line. First, we show the spectra from snapshot `muram_en_499000_379s` of the simulation and discuss it in detail. In Sect. 2.3.2.5 we compare this snapshot with three others. We then present in Sect. 2.3.3 a comparison with other numerical models. The RT calculations in the selected snapshot converged in all but three of the columns, in which the code failed. In this analysis we focus on the average properties of the spectrum while in a future work we will study diagnostics that can be derived from spectral features of the intensity profiles, similarly to the works of Leenaarts et al. (2013b) and Pereira et al. (2013).

2.3.1 Two-dimensional images of Mg II k

In the following we present brightness temperature and formation heights of snapshot `muram_en_499000_379s` measured at the k_2 and k_3 features of the non-degraded synthetic spectra.

2.3.1.1 Intensity maps

Figure 2.2(a-c) show intensity maps of the spectral features k_{2v}, k_3, and k_{2r}. The intensity is plotted in units of brightness temperature $T_b = B^{-1}(I_\nu)$, where I_ν is the emergent intensity and B^{-1} the inverse Planck function. We emphasize that the conversion from I_ν

to T_b is not linear and changes the statistical distribution and, in particular, the averages. The intensity maps show structures that are well correlated with the magnetic field in the upper chromosphere (cf. Fig. 2.1).

In panels (d–f) it can be seen that the corresponding formation heights of the brightest structures are in the lower chromosphere (< 2 Mm). At these heights, the source function is only partially decoupled from the local atmospheric temperature leading to the brighter observed structures in comparison to other regions in the intensity images where the formation heights are higher up in the atmosphere with fainter brightness temperatures.

The upper and lower edges of the k_2 intensity images (Fig. 2.2a,c) and to a lesser degree of the k_3 intensity image (panel b) show shock patterns associated with the quiet sun internetwork regions. Such enhanced shock patterns arise when wavefronts from different directions hit each other and appear similar to inverse granulation. These structures are less visible in the region between the two polarities (i.e., roughly along the horizontal diagonal from the lower left to the upper right of the 2D images). This could be because the intensity at these locations forms in the connecting loops above the "lower chromosphere" (cf. panels d–f) which overlay the shock patterns. Moreover, in the region between the bipolar field concentrations, the magnetic field is highly inclined, that is, horizontal, which might suppress upward propagating shocks (see, e.g., Cauzzi et al. 2007).

The appearance of the k_2 intensity as brightness temperature looks qualitatively different from RT computations performed with the public Bifrost snapshot (see, eg. Leenaarts et al. 2013b, Sukhorukov & Leenaarts 2017, Fig.8). The public Bifrost snapshot shows a larger amount of "shock expansion patterns" whereas in the MURaM-ChE model the structures look more "fibril"-like. This suggests a higher opacity in the chromosphere and thus higher density compared with the Bifrost snapshot.

2.3.1.2 Formation heights

Figure 2.2(d–f) show the formation heights of the k_{2v}, k_3, and k_{2r} features. These are the heights where the optical depth at the corresponding wavelength reaches one. According to the Eddington-Barbier relation, in the case of optically thick line formation, this is approximately the height where the intensity at this wavelength is forming in the atmosphere. Similar to the intensities, the formation heights are spatially correlated with the magnetic field. The k_2 peaks (panels d,f) form mostly below 3-3.5 Mm with exceptions where the plasma appears to form loop-like structures that extend higher up in the atmosphere. There, the formation heights are in the range 3.5–5 Mm. There are also regions where the line features form at even larger heights in the atmosphere such as visible, for example, in the lower left corner of panels (d)–(f) at roughly $(x, y) = (7\,\mathrm{Mm}, 5\,\mathrm{Mm})$. It appears that, except in the magnetic loops, k_{2v} forms a bit lower in the atmosphere than k_{2r}. The central minimum k_3 (panel e) forms in the higher part of the chromosphere just below the transition region. Overall, the variations in the k_3 image appear to be smoother than for the k_2 peaks. This might partly be connected to misidentified peak features and therefore wrong formation heights. In the connecting loops visible in the center of the intensity images the k_2 peaks show too high formation heights (higher than k_3). This is because the profiles associated with these rays have multiple peaks and the classical features of the Mg II k line are therefore not well defined. It might therefore be that the selected k_3 feature forms at lower heights than the selected k_2 features.

2.3.2 Comparison with IRIS observations

We now discuss the spatially averaged spectrum that we compute over the full simulation domain. We compare this to a spatially averaged IRIS raster scan which is chosen to include

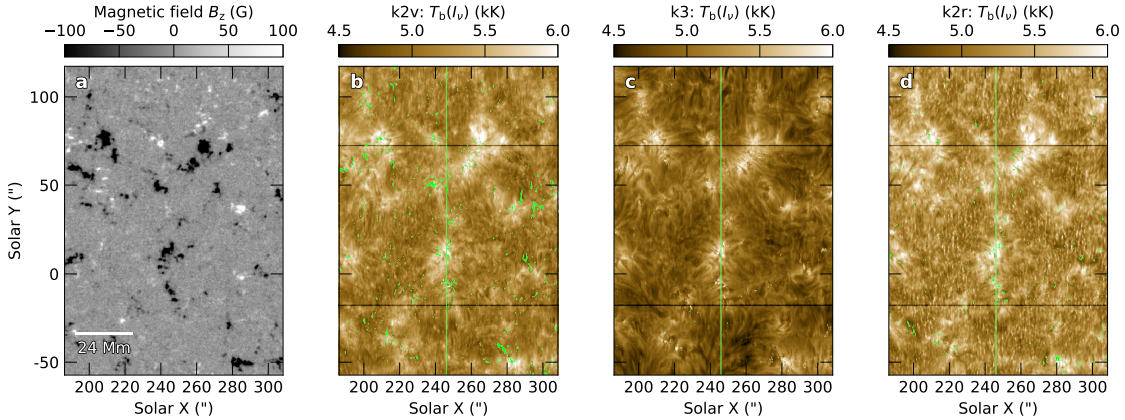

Figure 2.3: Observations from a quiet Sun region including network fields. The left panel shows the HMI magnetogram that was aligned with the IRIS observation. The gray scale in the HMI magnetogram is saturated at ±100 G but values up to ±1000 G are reached. Panels (b)–(d) show the observed intensity as brightness temperature T_b at the k_2 and k_3 features of the Mg II k line. The limits of the colorscale are not the same as in Fig. 2.2 in order to increase the contrast. The size bar in panel (a) indicates the size of the simulation domain. Green colored pixels indicate where no features could be found or no measurements are available.

quiet Sun network and internetwork regions similar to those seen in our simulations. However, the field topology in the observations is different, and the FOV is larger. The mean unsigned LOS magnetic field strength averaged over the shown FOV in the HMI magnetogram is $\langle |B_{\rm LOS}/\mu| \rangle = 12.12$ G. This is lower than the vertical component of the magnetic field estimated from the simulation at $\tau_{500} = 0.1$, which was ≈ 20 G (after degrading to the same resolution, see Sect. 2.2.1).

The full FOV of the observations chosen for the comparison is shown in Fig. 2.3. The LOS magnetic field map (panel a) shows features of both polarities that are distributed over the whole FOV. At $(x, y) \approx (270", 45")$ a bipolar structure is visible that qualitatively compares to the setup of our simulation. As described in Appendix 2.6 the properties of a smaller ROI around the bipole and the full FOV are similar.

The intensity images of the spectral features are extracted by applying the peak-finding algorithm described in Sect. 2.2.6. We show the k_{2v}, k_3, and k_{2r} features in brightness temperature units. A similar correlation is found between the strong network field regions and the intensities as in the model (cf. Figs. 2.1 and 2.2). The intensity in the k_2 peaks (panels b and c) and the central reversal is enhanced in the presence of magnetic features. The overall contrast of the observations appears to be smaller than in the simulation. This is expected from the lack of horizontal radiative transfer in our synthetic spectra (Sukhorukov & Leenaarts 2017). We note that the data shown in Fig. 2.2 is not degraded to preserve the information about the formation height.

2.3.2.1 Average spectra

In Fig. 2.4 we present average spectra from a representative IRIS observation, the MURaM-ChE model, and the Bifrost publicly available snapshot. The synthetic spectra were degraded to the IRIS spectral and spatial resolution using the procedure described in Sect. 2.2.5. In the following we discuss the shape of the profiles in terms of intensities and peak separation.

The intensities at k_1 and in the wings of the observed and MURaM-ChE spectra

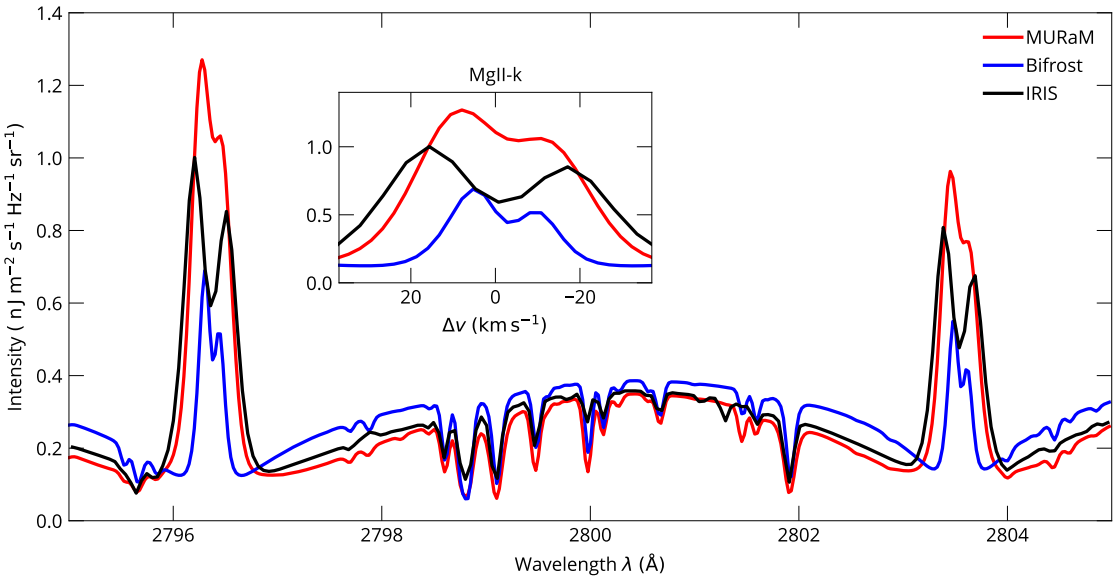

Figure 2.4: Spectrum of Mg II h&k lines. Shown are spatial averages of the spectra observed by IRIS (black) and synthesized from snapshot `muram_en_499000_379s` (red). For comparison, we added the publicly available spectrum from Bifrost (blue). A comparison between the two synthetic spectra is presented in Sect. 2.3.3. The inset panel shows a zoom onto the Mg II k line as a function of Doppler velocity centered on the rest wavelength.

are similar. However, the observed intensity appears on average to be slightly stronger there. The intensities at the k_{2r} and k_{2v} peaks are higher in the MURaM-ChE model compared to the observations. Some of the differences might be attributable to the 1.5D RT treatment and some to the discrepancies between the observation and the modeled region. A comparison between Fig. 2.1 and Fig. 2.2a,c shows that the brightness temperature is clearly enhanced above the network magnetic field elements. The high brightness temperatures ($T_{b,k_2} > 5$ kK) may be explained by high temperatures in the atmosphere at the corresponding formation heights (Leenaarts et al. 2013b). Sukhorukov & Leenaarts (2017) found, by studying the public Bifrost snapshot in 3D RT, that brightness temperatures in the peaks with $T_{b,k_2} > 5$ kK are overestimated in the 1.5D RT computation. We therefore expect a reduction of the k_2 peaks in the intensity images as well as in the average spectrum in a 3D RT computation.

Both the observed and the simulated spectrum have, on average, stronger intensities in the k_{2v} peaks. We computed the intensity ratio $R_k = (I_{k2v} - I_{k2r})/(I_{k2v} + I_{k2r})$ as in Leenaarts et al. (2013b), where the intensities I are measured at the blue and red peaks of the spatially averaged spectrum. The obtained values of 0.09 (MURaM-ChE) and 0.08 (IRIS) are both positive and similar. According to Leenaarts et al. (2013b) there is a correlation between R_k and the sign of the average velocity in the atmosphere between the formation height of the k_2 and k_3 features. In the analyzed snapshot we find 56% of the columns show on average a downflow and 31% an upflow. For the remaining columns, no such correlation with the average velocity could be determined because of erroneous information about the formation height, as a consequence of complex profile shapes.

The intensity at the central reversal k_3 is larger in the averaged MURaM-ChE spectrum. It turns out that this is an effect of superposition of single spectra when the average is computed. The intensity at k_3 in the individual profiles identified by the peak finder is, on average, about 20% smaller than k_3 intensity in the spatially averaged profile. As

shown in Leenaarts et al. (2013b) the Doppler shift of the central reversal correlates with the velocity at the corresponding formation height. Therefore, spectra from rays with large velocities in the upper chromosphere will influence the shape and the intensity of the central reversal. Whether this effect is similarly dominant in 3D RT spectra will be investigated in a future work.

2.3.2.2 Distribution of peak intensities

The spatially averaged spectrum is smooth. Spectra from individual rays, however, show large variations in their shape. Many profiles show more than two emission peaks with a range of intensities. We therefore investigate how peak intensities and separations are distributed following the example given in Fig. 7 of Carlsson et al. (2019). For this purpose we use only spectra that were degraded to reflect IRIS instrument conditions (see Sect. 2.2.5). In Fig. 2.5a it can be seen that the computed peak brightness temperature distribution covers all observed brightness temperatures and also extends to temperatures that are about 500 K lower and 500 K higher than observed. Overall the width of the observed distribution is smaller than that of the computed distribution. The shown distribution from the observation contains the full FOV. In Appendix 2.6 we show that similar distributions can be found in smaller selections of the FOV that are comparable in size to our simulation, given the network fields inside the region of interest are not too strong. We find that a distribution similar to the one in Carlsson et al. (2019) can be found by choosing a quiet subregion of the observation (Appendix 2.6 'Quiet sun'), which is basically devoid of all network features. The distribution presented in the paper (Fig. 2.5) is more representative of observations which include regions of stronger magnetic field.

2.3.2.3 Peak separation

In comparison to the line width (see Sect. 2.3.2.4), which is not uniquely defined, the peak separation is straightforward to measure once the spectral features are identified. We measured the peak separation of the degraded synthetic spectra and the observations. The distributions of the peak separation is shown in Fig. 2.5b. It can be seen that the observed spectra peak around $30\,\mathrm{km\,s^{-1}}$ with an average value of $\langle \Delta v_{\mathrm{k2}} \rangle = 33.02\,\mathrm{km\,s^{-1}}$, whereas the distribution of the peak separation from MURaM-ChE profiles peaks slightly above $20\,\mathrm{km\,s^{-1}}$ and are on average $\langle \Delta v_{\mathrm{k2}} \rangle = 23.6\,\mathrm{km\,s^{-1}}$. The most likely values for the peaks separation are by 8–$10\,\mathrm{km\,s^{-1}}$ smaller than in the observed spectra.

The distribution of the peak separation is sensitive to the degradation procedure. This occurs because degrading the profiles to IRIS resolution reduces the number of small peaks. The decreased complexity of the profiles makes it easier to define and identify the $\mathrm{k_2}$ features. After degrading the synthetic profiles, the peak of the distribution changes from $\approx 16\,\mathrm{km\,s^{-1}}$ to $\approx 20\,\mathrm{km\,s^{-1}}$.

Leenaarts et al. (2013b) showed that the peak separation strongly correlates with velocity differences in the mid to upper chromosphere. In order to understand the peak separation in the MURaM-ChE model, we tested whether a similar correlation can be found. We therefore measured in a similar manner to Leenaarts et al. (2013b) for each atmospheric column the maximum velocity difference

$$\max(\Delta v_z) = \max_{z_1 \le z \le z_2} (v_z) - \min_{z_1 \le z \le z_2} (v_z), \tag{2.1}$$

with

$$z_1 = \min(z(\tau_{\mathrm{k2r}} = 1), z(\tau_{\mathrm{k2v}} = 1)), \tag{2.2}$$

$$z_2 = z(\tau_{\mathrm{k3}} = 1), \tag{2.3}$$

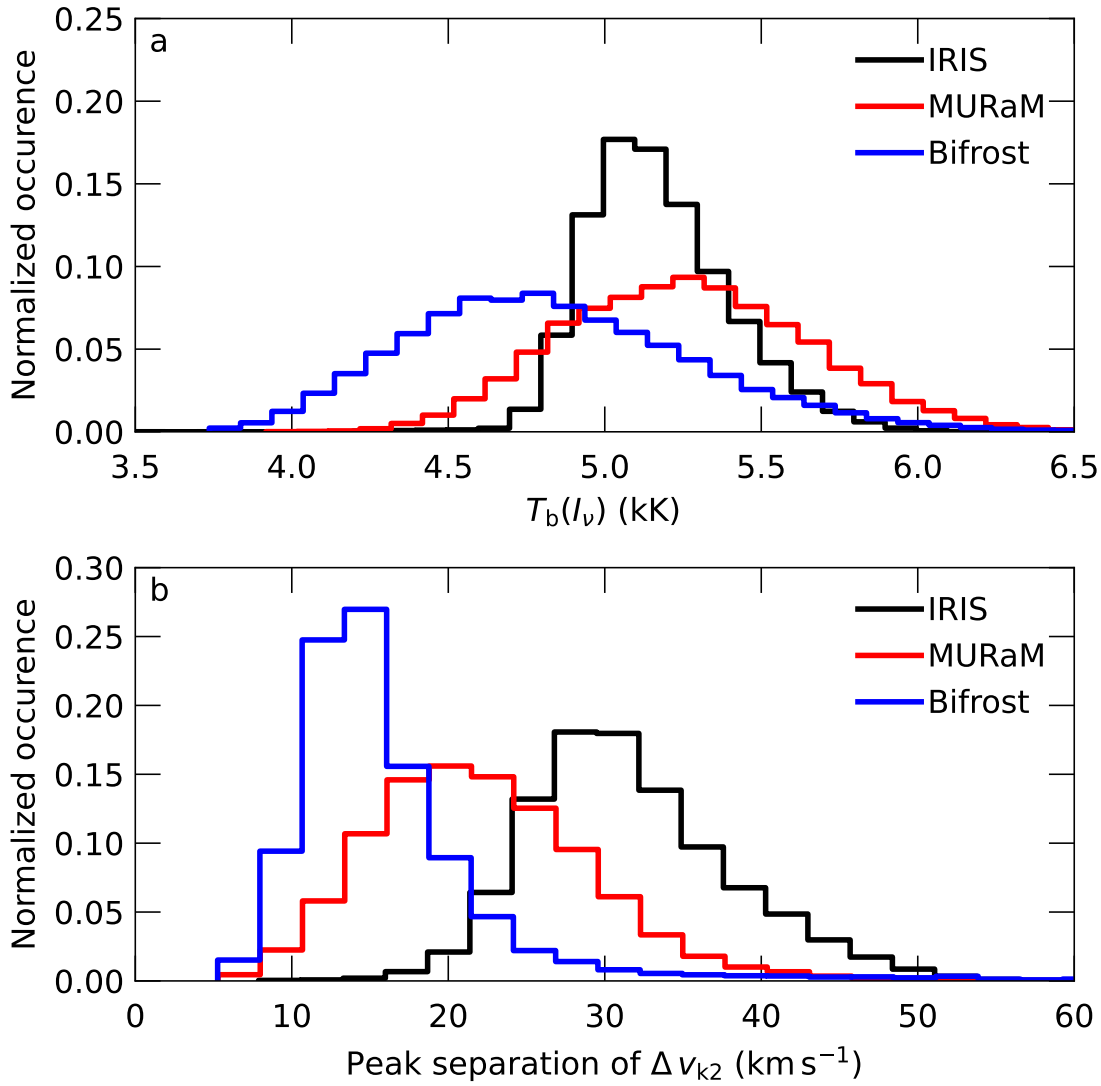

Figure 2.5: Distribution of k_2 peak intensities in units of brightness temperature (panel a) and peak separations (panel b) of the Mg II k line for observations from IRIS (black) and the enhanced network model from MURaM-ChE (red). For comparison, histograms of the same line parameters obtained from the Bifrost public snapshot have been over-plotted in blue (see Sect. 2.3.3 for a discussion). For these statistics, we used the modeled spectra that are degraded to the observed spatial and spectral resolution for a meaningful comparison.

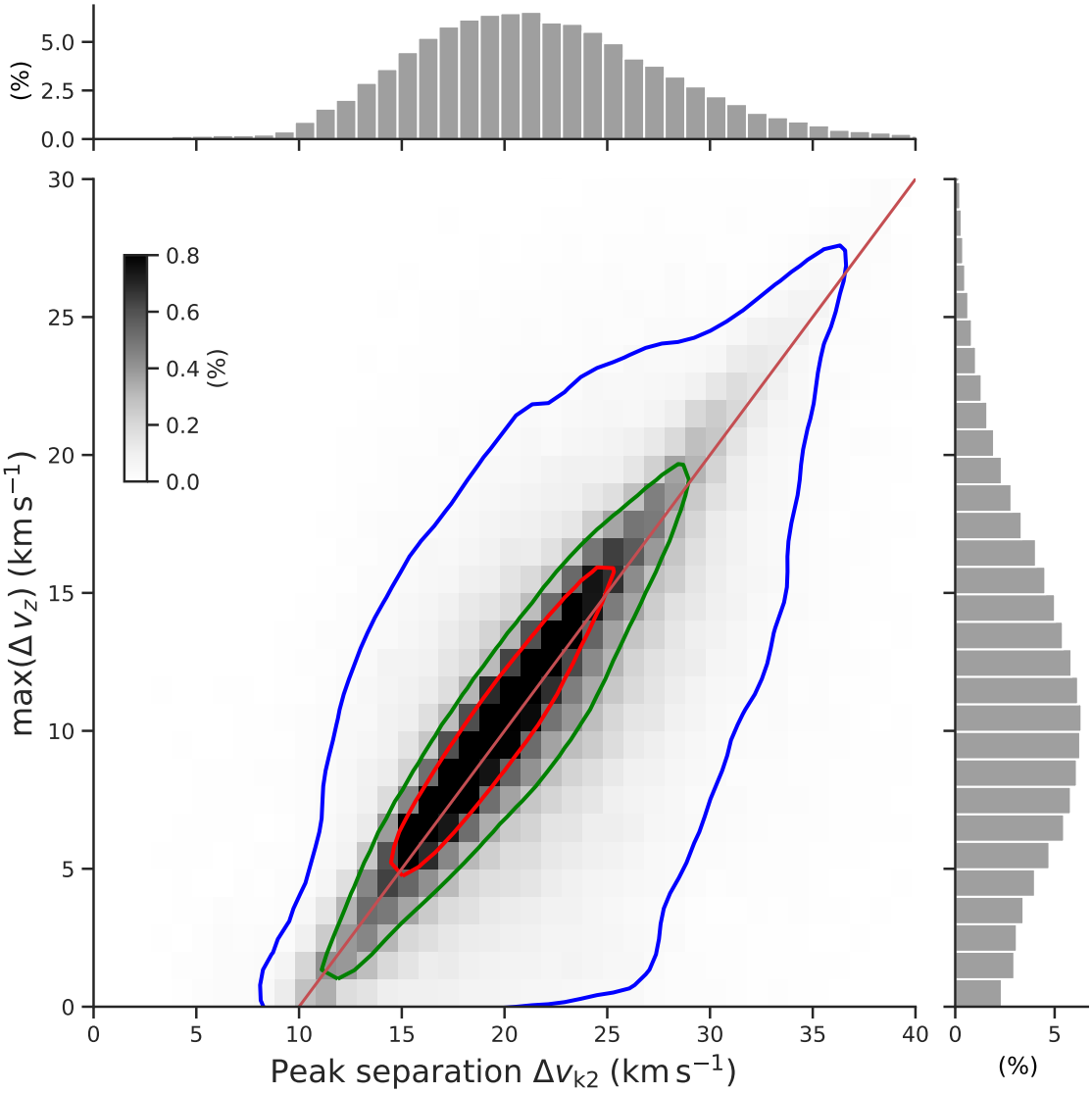

Figure 2.6: Correlation between peak separation and maximum velocity difference measured from double-peaked spectra. The peak separation is defined as the difference between the wavelengths of k_{2v} and k_{2r} in units of the Doppler velocity. The maximum velocity difference, $\max(\Delta v_z)$, is defined as the difference between the maximum and minimum velocity in the atmosphere between the formation height of the central minimum k_3 and the minimum of the k_{2r} and k_{2v} formation heights. The blue, green, and red contours enclose 90%, 50%, and 25% of the dataset, respectively. Both quantities are measured from the non-degraded spectra. The gray scale of the pixels in the 2D histogram is saturated at 0.8% to increase the readability. The top and right panels show the marginal distributions as a percentage.

in the atmosphere between the minimum formation height of the (non-degraded) k_2 peaks and the k_3 feature, respectively. We note that our definition of z_1 is different. We chose this definition because in the MURaM-ChE atmosphere the formation height of k_{2r} can be different by up to 1–3 Mm from that of k_{2v}. In addition, we restricted the measurement of $\max(\Delta v_z)$ only to locations in the atmosphere where the plasma temperature is $T_{\rm gas} \leq 10\,{\rm kK}$ (Carlsson & Leenaarts 2012). The latter condition was necessary as there are columns in the atmosphere where k_3 forms much higher than the k_2 features with hot plasma in between. A qualitative comparison between a vertical slice in temperature of our model (Sect. 2.3.2.4) and the Bifrost snapshot (e.g. Carlsson et al. 2019, Fig. 4) suggests that the public Bifrost model has a less corrugated transition region in the upper chromosphere. It might therefore be that these scenarios are much less present in the public Bifrost model explaining the above-mentioned differences. The study of Trujillo Bueno et al. (2018), based on comparisons to the linear polarization signal measured by the Chromospheric Lyman-Alpha SpectroPolarimeter (CLASP) rocket experiment (Kano et al. 2017), also concluded that the Bifrost model required additional corrugation at the transition region to match the observations. For 15.2% of the columns either no peak separation or no $\max(\Delta v_z)$ could be determined because of missing or wrong information about the formation height which is due to miss identification of the peak finder. The data used for the correlation therefore corresponds to 84.8% of the columns in the analyzed snapshot. We find a positive correlation between the peak separation and $\max(\Delta v_z)$ with a correlation coefficient of 0.48. As mentioned above, the k_2 separation is difficult to measure for Mg II k profiles with multiple peaks. We therefore measured the correlation again, but preselected spectra showing only two peaks. We then found a larger correlation coefficient of 0.59, which is comparable to that reported by Leenaarts et al. (2013b). The correlation for spectra with two peaks is shown in Fig. 2.6. It can clearly be seen that for the majority of the spectra with an average peak separation of $\approx 20\,{\rm km\,s^{-1}}$, $\max(\Delta v_z)$ values of 10–$15\,{\rm km\,s^{-1}}$ in the corresponding columns of the atmosphere are needed. For spectra that do not clearly follow the correlation, the peak separation is larger than $\max(\Delta v_z)$. This might be a consequence of a local maximum in the temperature in the lower atmosphere, possibly as a result of a propagating shock. This leads to an increased peak separation unrelated to the velocity profile (see also Fig. 8a,b in Leenaarts et al. 2013b, and the discussion therein). We discuss the role of the velocity field in the broadening of the Mg II k line in Sect. 2.3.2.4.

2.3.2.4 Line width

In this section we demonstrate that the width of the emergent spectra in the MURaM-ChE atmosphere is mainly determined by the velocities. We study the impact of velocities on the emergent spectra by solving the RT problem in snapshot `muram_en_499000_379s` but neglecting the velocity field. We emphasize that in this comparison only the "direct" effects of the velocities in the RT computation are neglected. The structure of the temperature profile which is used in both computations as well as all other physical quantities are a result of the MHD computation from which the velocities cannot be separated. In particular, local maxima in temperature in the lower atmosphere are often a result of compression heating by propagating plasma waves. In the RT computation without velocities we found that the RT computation failed for 0.6% of the rays. The missing spectra, however, have no influence on the conclusions drawn in this section.

In Fig. 2.7 we show a comparison of the results along one cut in the y-axis at $x = 13.95\,{\rm Mm}$ of the atmosphere. Panels (a) and (d) show the intensity of the Mg II k line along the spatial axis with and without velocities. For a better understanding,

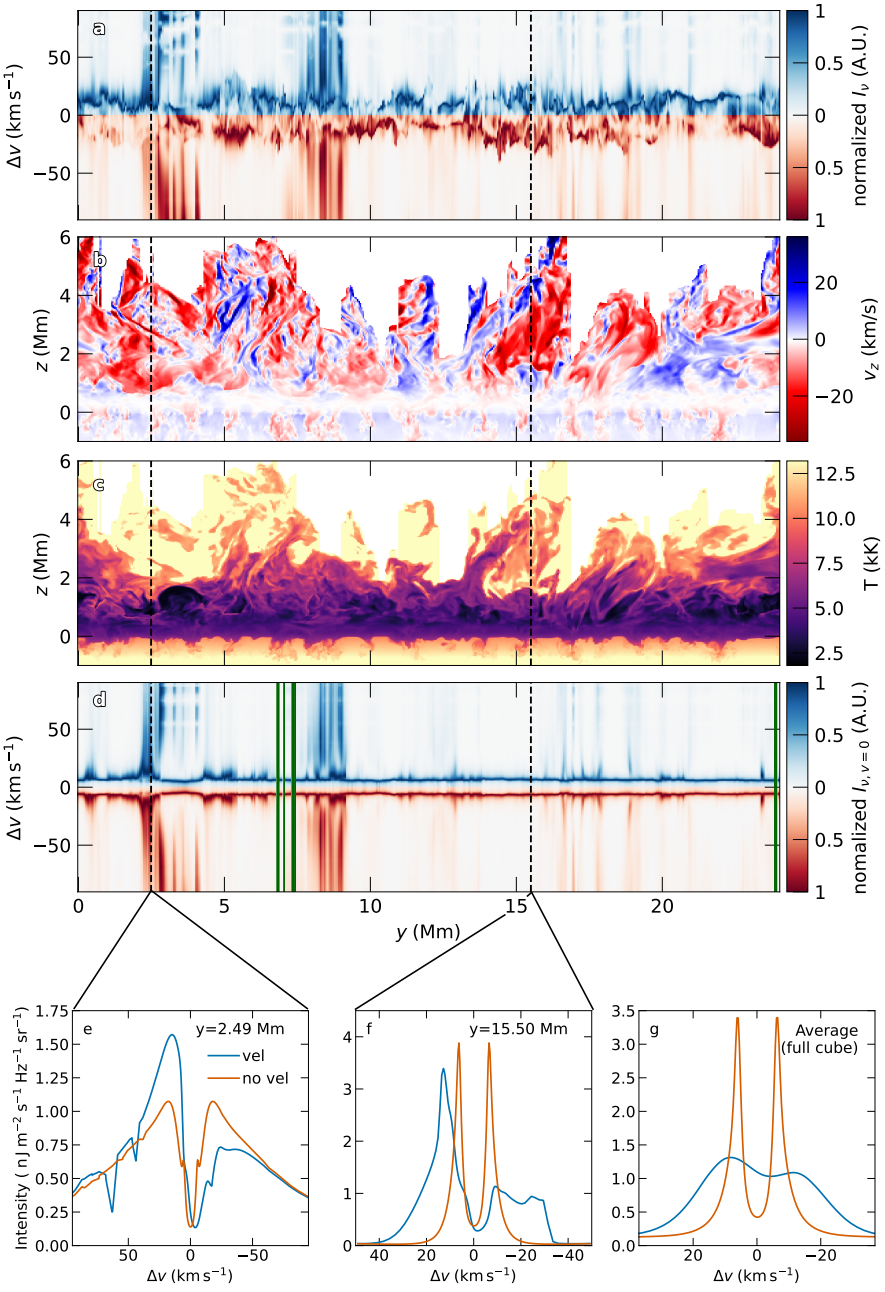

Figure 2.7: Contribution from velocities to emergent spectra along a cut at $x = 13.95$ Mm through the MURaM-ChE snapshot `muram_en_499000_379s`. Panel (a) shows the spectrum of the Mg II k line with color-coded intensity. Red colors refer to the red part of the spectrum and blue colors to the blue and violet parts of the spectrum relative to the rest wavelength of Mg II k. The intensities are normalized to the maximum value in the presented range of $-90 \leq \Delta v/[\,\mathrm{km\,s^{-1}}] \leq 90$. Panel (b) shows the vertical velocity component and panel (c) the temperature in the atmosphere. Panel (d) is similar to panel (a) but for a RT computation of the identical snapshot but neglecting velocities in the atmosphere. The green regions in panel (d) indicate columns where the RT computation failed. Panels (b) and (c) show only the part of the atmosphere that was used for the RT computation (see Sect. 2.2.2). The bottom panels (e) and (f) show comparisons of single Mg II k spectra at $y = 2.49$ Mm and $y = 15.5$ Mm between the computation with and without velocities. In panel (g) we show a comparison of the globally averaged spectrum between the two computations. We note that neither the y-axis nor the x-axis are the same for panels (e)–(g).

the intensities on the blue side of the line's rest wavelength are shown in blue and the corresponding red part of the spectrum in red. Both color scales are normalized to the maximum intensity in the shown wavelength range. Panels (b) and (c) show the vertical velocity and the temperature to show the context of the underlying atmosphere. We define upflows as positive velocities in the atmosphere.

As expected, the spectra computed with velocity (panel a) display more variability in space (and time – see Sect. 2.3.2.5) and are significantly broader than those computed without velocity (panel d). The latter are symmetric around the rest wavelength of Mg II k and the variation of the line width in space seems much smaller. Qualitatively, it can be seen that the broadest spectral lines appear at locations where the temperature has peaks in the lower atmosphere (e.g., panel (c) at $\approx 7-9$ Mm). At around $3-5$ Mm and $7-9$ Mm the line widths are larger than the average width in both cases. As an example we show the spectrum for the same ray from both computations in panel (e). It can be seen that the k_2 intensity and the peak asymmetry is different in the "velocity" case. The wavelength position and the overall line width is similar in both cases. In the above-mentioned regions which have broad line profiles in both cases, a local maximum in temperature in the lower atmosphere leads to the larger line width.

In panel (f) we compare the spectra from the same ray for the two calculations at the location where the line width is different. As in panel (e) the spectrum computed without the velocity field is symmetric. However, the line width and the peak separation in the "velocity" case is much larger. The larger line width is here a result of a broader extinction profile as a consequence of large velocity variation along the line of sight. To demonstrate that the line width in the spatially averaged spectrum is dominated by the influence of velocities, we show in panel (g) the average spectrum over the whole simulation domain from `muram_en_499000_379s` with and without velocities. We computed the averages only over rays that converged in computations both with and without the velocity field. There is, however, no visible difference between the blue line in panel (g) and the red line in Fig. 2.4, because the missing 0.6% of the rays have no impact on the overall average.

We conclude from this study that, in the case of the MURaM-ChE model, while local temperature maxima in the lower atmosphere can have a significant impact on the width of resulting spectral line profiles, in the majority of the computed spectra the line width is dominated by the velocities in the upper chromosphere.

2.3.2.5 Time variation

The results discussed so far are from a single snapshot in the simulation which corresponds to one time step in the computation. The conditions in the solar atmosphere are constantly changing with time and it is not immediately clear whether a spatial average can account for temporal variation of the line.

In order to get at least a very rough idea of how temporal effects in our simulation affect the Mg II h&k profiles, we synthesized three more snapshots that are approximately separated by 2 minutes each. For these snapshots we synthesized every second column in x and y direction (see Sect. 2.2.2). Considering a larger number of "full" snapshots was not feasible because of computational costs. To get better insight into how the spectral lines evolve with time, we additionally chose 8 "synthetic slits" in the simulation located at $x, y \in [0, 6, 12, 18]$ Mm, oriented in the x and y directions. The time resolution of the profiles computed along the synthetic slits is approximately 1.2 sec. Figure 2.8 shows as an example the time variation for two slits that are located at $y = [0, 12]$ Mm. In the quieter part of the simulation box (represented by panel (a) of Fig. 2.8; cf. Fig. 2.1 at $y = 0$ Mm) the brightness temperature measured at the k_2 feature shows similar shock

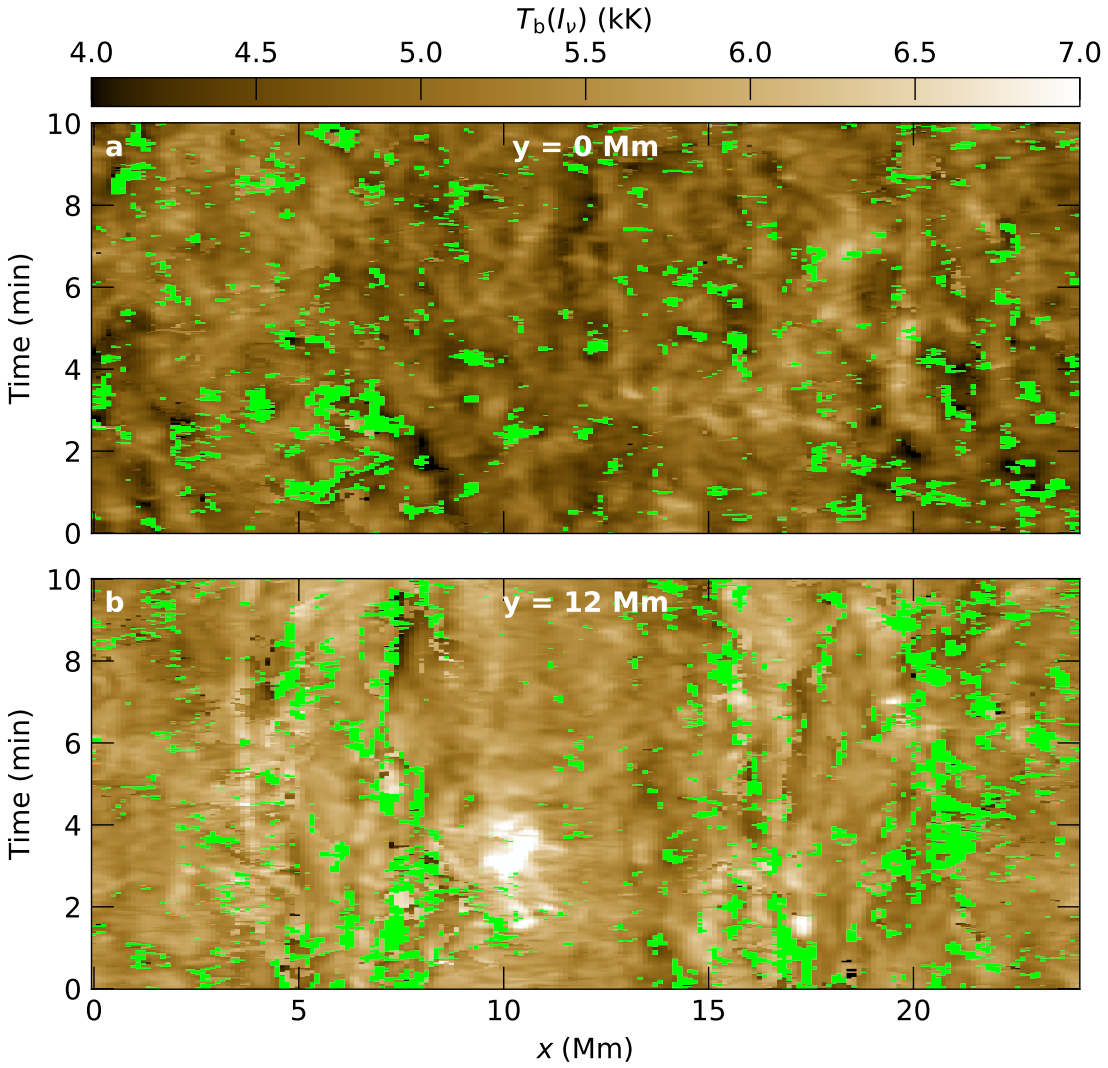

Figure 2.8: Space–time intensity maps. The panels show the time variation (vertical axis) of brightness temperature measured at k_{2r} along two spatial slits (horizontal axis) located at the positions $y = 0$ Mm (panel a) and 12 Mm (panel b). The spectra were degraded before the peak-finding algorithm was applied. Panel (a) represents the quieter regions of the simulation domain. Panel (b) represents a cut through the network-dominated regions of the simulation. The color scale is set to the same limits as in Fig. 2.2. Green pixels indicate spectra where no k_{2r} feature could be detected.

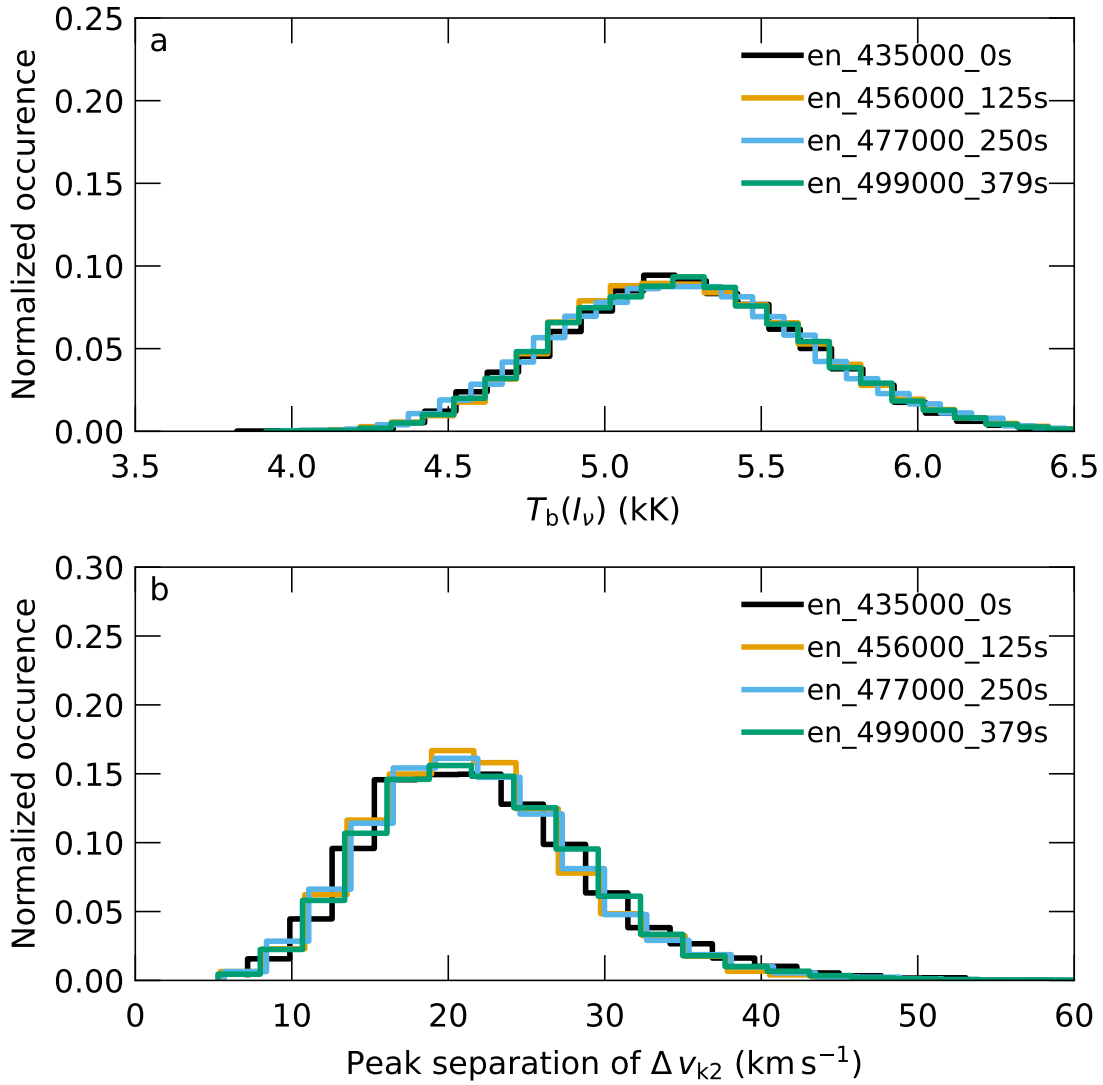

Figure 2.9: Distribution of k_2 peak intensities in units of brightness temperature (panel a) and peak separation (panel b) for four snapshots in the MURaM-ChE simulation, which are separated by $\approx$ 2 min of simulation time. The presented data correspond to every second column in the x and y directions in the snapshots. The spectra were degraded before the peak-finding algorithm was applied. For comparison with Fig. 2.5, we chose the same limits for the axes.

patterns as visible in Fig. 2.2a. Panel (b) represents the network-dominated part of the simulation domain. Here, the brightness temperature is on average $\approx$ 630 K higher than in panel (a). While panel (a) shows repeating shock-like patterns, panel (b) shows more structures with a larger extent along the spatial axis, which come from the connecting loops between the two polarities. Both slits contain also brighter features that live for more than 4 min as, for example, panel (a) at $x \approx 20$ Mm and panel (b) at $x \approx 4$ Mm.

While the spectra can change significantly over time on small spatial scales, the average and statistical properties are roughly constant. To demonstrate this we show in Fig. 2.9 the distribution of peak intensities and peak separation for the 4 snapshots at different times. There are no significant changes over time in a statistical sense. The average values of the peak separations range from $\langle \Delta v_{k2} \rangle = 23.1$ km s^{-1} to $\langle \Delta v_{k2} \rangle = 23.6$ km s^{-1}.

We use the spectra from the synthetic slits to estimate the spatially averaged spectrum. This is demonstrated in Fig. 2.10. We calculated the spatial averages over all slits at

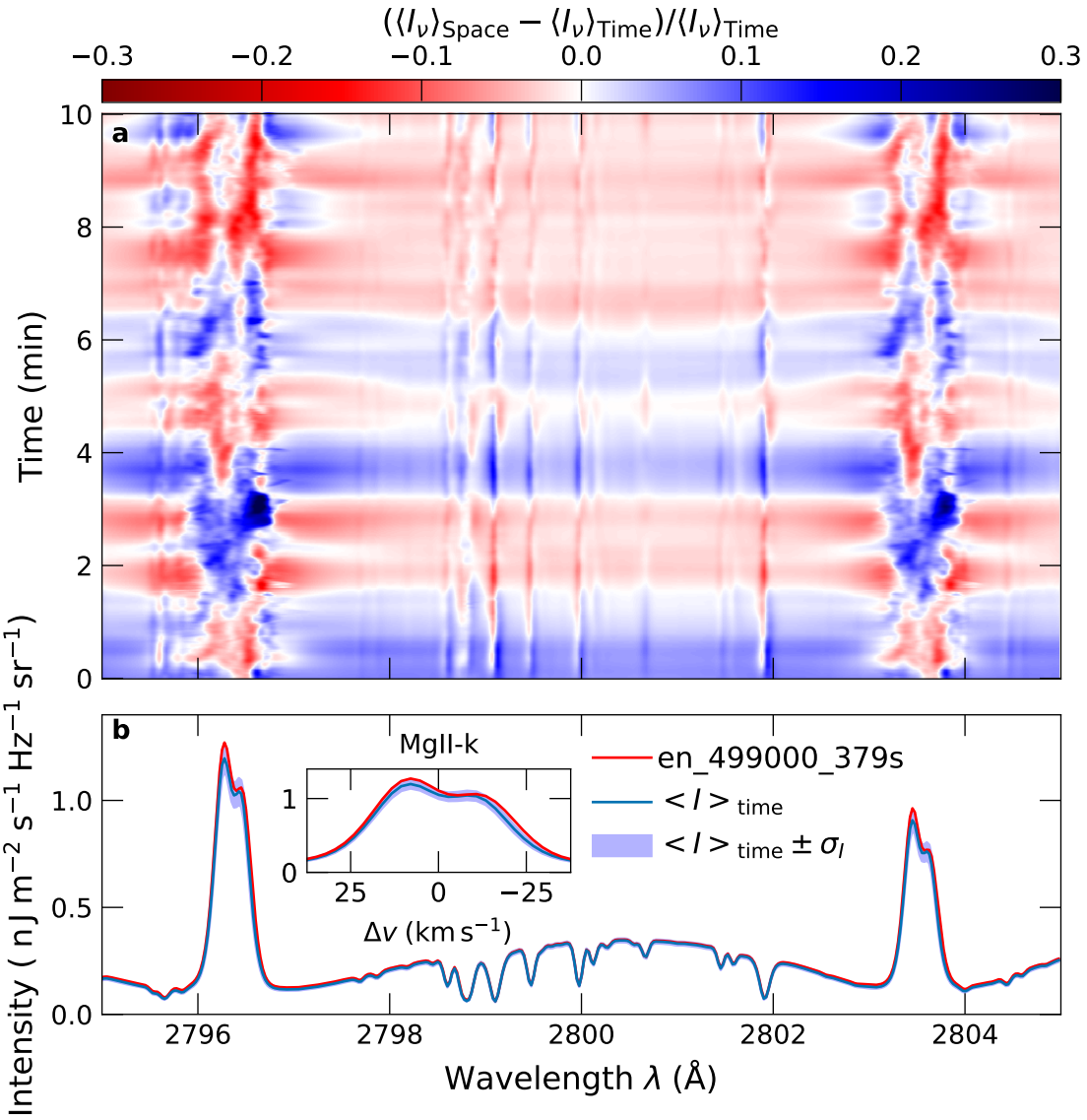

Figure 2.10: Time variation of the spatially averaged Mg II h&k spectrum. Panel (a) shows a time series of 10 min in length at a cadence of ≈ 1.2 sec. We computed the spatial average from eight slits that are evenly spaced in the simulation at positions $x, y \in [0, 6, 12, 18]$ Mm. We then subtracted the average spectrum over the whole 10 min and show the relative difference. Panel (b) shows the time-averaged spectrum together with the standard deviation. The red curve shows for comparison the spatially averaged spectrum from snapshot `muram_en_499000_379s`, which was discussed in detail in Sect. 2.3.2. The spectra have been degraded to the IRIS spatial and spectral resolution.

each time step, which we call $\langle I_\nu \rangle|_{\mathrm{Space}}$. We then computed the temporal average over all time steps (i.e., all $\langle I_\nu \rangle|_{\mathrm{Space}}$) which we call $\langle I_\nu \rangle|_{\mathrm{Time}}$ and subtracted this from each single spatially averaged spectrum. In panel (a), it can be seen that the estimated average spectrum shows variations with time that are close to the three-minute period usually prominent in the chromosphere. Whether it is really periodic and what its periodicity is cannot be inferred from this short time series. In panel (b) the time-averaged spectrum is shown together with the standard deviation of the different time samples. It can be seen that at the wavelength position of the k_2 (and h_2) features the standard deviation is largest. This is expected because these features of the spectral lines form in the mid to upper chromosphere where the atmosphere is more turbulent compared to lower layers. Nonetheless, the deviation from the time average is relatively small, as is the difference to the snapshot `muram_en_499000_379s` discussed above.

2.3.3 Comparison to other numerical models

The public Bifrost snapshot (Carlsson et al. 2016) has become the standard for analyzing spectral line formation in the solar chromosphere over the last years. In this section we briefly compare the synthetic spectra resulting from our MURaM-ChE simulation run and the Bifrost public snapshot as well as the average physical properties of the two modeled atmospheres.

We applied the same degradation procedure to the synthetic Bifrost spectra as for the MURaM-ChE model (cf. Sect. 2.2.5). As can be seen in Fig. 2.4 the two modeled spectra appear to be different in the peak intensities, peak separation, separation between the k_1 minima, and the intensity of the "pseudo"-continuum between the two emission lines. This suggests that the structure of the modeled atmospheres are different, from the upper photosphere all the way to the transition region.

In Fig. 2.11 we plot the temperature distributions of the atmospheres versus the logarithmic column mass $\log_{10}\sigma$. The colored lines represent the most likely temperature (i.e., the peak of the distribution) within a given range of logarithmic column mass. For the temperature histogram we excluded temperatures larger than 12 kK.

In the range $1 \geq \log_{10}\sigma\,/\,[\mathrm{kg\,m^{-2}}] \geq -1$ (approximately 1 Mm above the visible surface for both models) the temperature in the Bifrost model is up to ≈ 500 K higher than in the MURaM-ChE model. Between $-2 \geq \log_{10}\sigma\,/\,[\mathrm{kg\,m^{-2}}] \geq -5$ the temperature in the MURaM-ChE atmosphere is higher. This is the temperature range where the Mg II h&k lines form. The distribution of the Bifrost intensities as brightness temperatures can be seen in Fig. 2.5a. Strong NLTE effects in the formation of the peaks make a direct comparison between brightness temperature and the atmospheric temperature at the formation height difficult. Leenaarts et al. (2013b) showed that for the strongest peak intensities, however, there is indeed a nearly linear correlation. This suggests that the higher temperature in the MURaM-ChE atmosphere at the formation heights of the line peaks lead to the higher peak intensities observed in Figs. 2.4 and 2.5a.

Carlsson et al. (2016) proposed a way to describe the nonthermal component of the velocity field that contributes to the line broadening similar to the "microturbulence" parameter often added to 1D models to match observed line widths. The nonthermal velocity u_{nth} is calculated as the standard deviation of the vertical velocity in between ± 1 dex of the logarithmic column mass $\log_{10}\sigma$ and multiplied by a factor of $\sqrt{2}$. We follow this approach and recompute u_{nth} for Bifrost and for our MURaM-ChE spectra. The difference is small at high column mass, that is in the lower atmosphere, and increases toward the chromosphere and the transition region. We propose that it is mainly the larger nonthermal velocities what produces the larger line widths in MURaM-ChE compared to

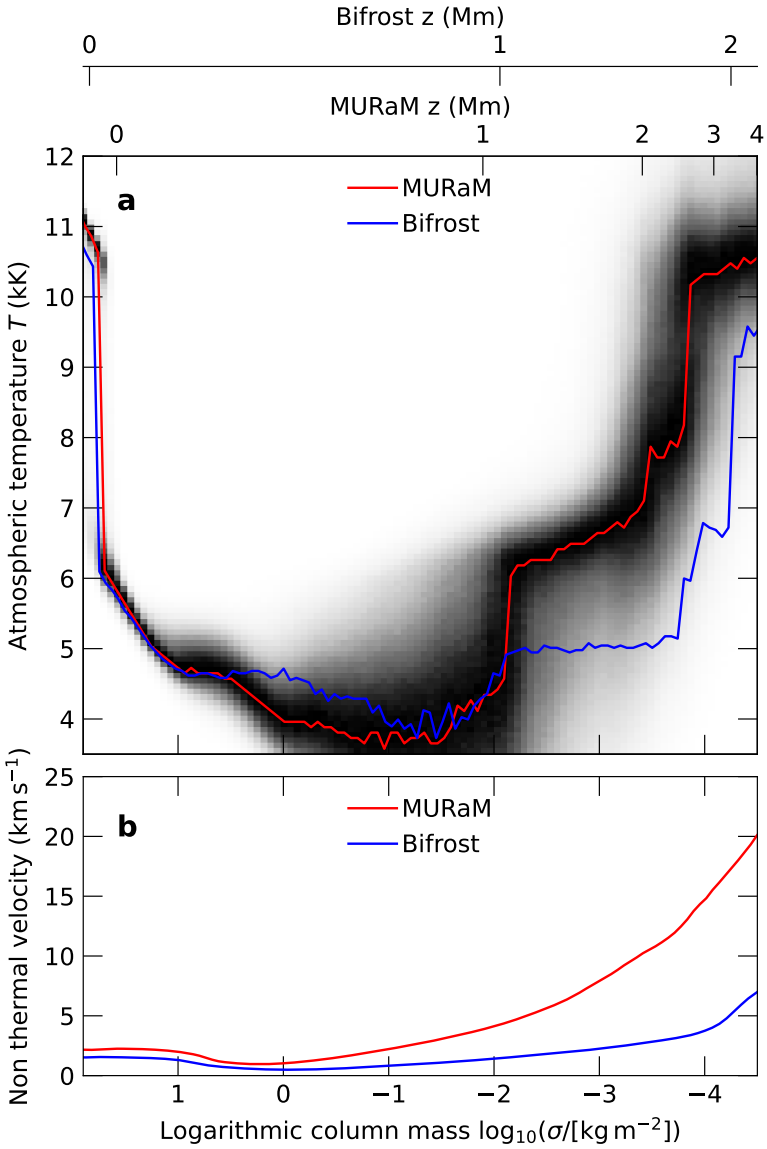

Figure 2.11: Comparison between atmospheric properties between the MURaM-ChE and the Bifrost public snapshot. Panel (a): Atmospheric temperature as a function of column mass σ. The two curves show the peak of the temperature distribution of the atmospheres in a given bin of column mass. For MURaM-ChE we show the distribution of the temperature as a 2D histogram which is normalized to the peak of the distribution in a given bin of logarithmic column mass. For both simulations we converted the column mass scale to a geometrical height that is shown on the top horizontal axis of the plot. Panel (b): Average nonthermal velocity as function of column mass. The nonthermal velocity is computed as the standard deviation of the vertical velocity within a range of ± 1 dex in logarithmic column mass and multiplied by a factor of $\sqrt{2}$.

Bifrost (see also Sect. 2.3.2.4).

The main differences between the models are the treatment of diffusion, the horizontal spatial resolution of 24 km (MURaM-ChE) versus 48 km (Bifrost), equidistant (MURaM-ChE) versus variable (Bifrost) vertical axis, and the depth of the lower boundary of the simulation, −7 Mm (MURaM-ChE) versus −2.5 Mm (Bifrost). The smaller diffusivity and higher resolution in MURaM-ChE enable a more turbulent convection zone, leading to stronger magnetic fields. The average unsigned magnetic flux at the $\tau_{500} = 1$ layer in MURaM-ChE is about 64 G[6] versus 48 G in Bifrost.

This difference in magnetic flux likely accounts for a significant fraction of the difference in intensity between the profiles, but likely not for the difference in peak separation and line width (e.g. Kayshap et al. 2018, Fig. 4). We note, however, that in the synthetic spectra presented in this work, the magnetic fields do not have a direct impact on the emergent line because the Zeeman effect is not taken into account.

In the MURaM-ChE atmosphere, the lower viscosity allows for more turbulent flows and stronger shocks. The enhanced dynamics leads to a chromosphere that extends to higher altitudes. A higher density at the formation height of the k_2 peaks leads to a stronger coupling between the source function and the Planck function. This might explain the higher peak intensities in the MURaM-ChE model.

Hansteen et al. (2023) report Mg II k profiles from a low resolution (100 km horizontally) simulation including flux emergence which show strong broadening. The authors explain this by possible additional mass loading in the atmosphere. This supports our finding in the comparison between the MURaM-ChE and Bifrost made in Fig. 2.11a where the column mass in the MURaM-ChE chromosphere is roughly an order of magnitude higher than in the public Bifrost snapshot.

2.4. Summary and conclusions

In this work, we modeled the Mg II h&k lines in a quiet Sun region with network elements using the chromospheric extension of the MURaM code (MURaM-ChE). The simulation setup is similar to the public Bifrost snapshot and includes a bipolar magnetic field structure that was added into the simulation box after it had reached a statistically steady state. Although the two simulation outputs are globally similar, there are clear differences in the details. For example, structures close to the photosphere are visible on much smaller scales in the MURaM-ChE simulation than in the public Bifrost snapshot.

We used a peak-finding algorithm to identify spectral features of the Mg II k line such as k_2 and k_3. We find two qualitative discrepancies compared to the observations: the intensity of the emission at the k_2 peak is too bright above the network fields; and the shock fronts are too clear in the intranetwork regions. Both these effects might be a shortcoming of the 1.5D RT treatment (Sukhorukov & Leenaarts 2017).

We compared the spatially averaged spectra between one snapshot of our numerical model and a selected IRIS scan. Prior to comparing the synthetic spectra with observations, we carried out a number of preparatory steps. First, we compared the magnetic field strength at the photosphere of the simulation to HMI measurements in the region covered by the selected IRIS scan. To this end, we first degraded the magnetic field at $\tau_{500} = 0.1$ to the HMI spatial resolution. This is approximately the height where the core of the Fe I λ6173 Å line forms, as observed by the HMI instrument. The obtained value of $\langle |B_z| \rangle|_{\tau_{500}=0.1} = 20.65$ G is larger than in the HMI magnetogram of the observation that we used for comparison, which has a value of $\langle |B_{\mathrm{LOS}}/\mu| \rangle = 12.12$ G.

[6]We note that these values are much higher than the ones earlier cited. This is because these values are taken at $\tau_{500} = 1$ and at full resolution, i.e., not degraded to the HMI resolution.

In order to compare with the IRIS data, the modeled spectra were spatially and spectrally degraded to match the resolution of the IRIS observations. We find that the spectra show a reasonably good match in the separation between the k_1 features and the overall line width. The peak intensities are on average higher than in the observation, which could be due to the larger apparent unsigned mean magnetic field strength in the simulation. As discussed above, the possibly overestimated intensities above the network regions as a result of the 1.5D RT treatment also lead to higher peak intensities in the computed average spectrum. The averaged MURaM-ChE spectra show a slightly larger blue asymmetry in both the Mg II k line and the Mg II h line than that seen in the observed spectra. This asymmetry is caused by the dominant area coverage by columns in the atmosphere that have downflows. We speculate that better results might be achieved with a larger simulation domain, which should lead to a more realistic vertical magnetic field topology. This could be achieved, for example, by extending the box size three times in each horizontal direction with the bipole being at the center of the 3×3 grid. By doing so, the bipolar structure would be more isolated from "neighboring" bipoles as a result of the horizontal periodic boundary conditions. However, the overall small but positive peak asymmetry can be seen even in smaller ROIs of the observation discussed in the main text and also in two additional observations as described in Appendix 2.6, and appears to be a common phenomenon.

In addition to the average spectrum, we compared the distributions of k_2 peak intensities and peak separation between the model and the observations. The distribution of the peak brightness temperatures covers the whole range of observed values. While in the main text we present results for the whole observed FOV, which is larger than the simulation domain, we discuss smaller ROIs and two more datasets in the Appendix. There we show that, unless the ROI contains very strong magnetic field concentrations, the distributions of the observed peak brightness temperatures are similar. The high peak brightness temperatures in the MURaM-ChE model might be explained by the different average magnetic LOS magnetic field strengths compared with the observations. Another, likely more important, contribution might come from the fact that the 1.5D RT approximation tends to overestimate peak brightness temperatures of $T_\mathrm{b} > 5\,\mathrm{kK}$ and underestimate $T_\mathrm{b} < 5\,\mathrm{kK}$ (Sukhorukov & Leenaarts 2017). These effects might result in a more compact brightness temperature distribution, which is similar to what is seen in the observation. From Sukhorukov & Leenaarts (2017, Fig. 10), we estimate a conversion factor between the 3D RT and 1D RT average spectra of 7.5% in the blue peak and 12.6% in the red peak. This, however, indicates that such a factor must be wavelength dependent. Sukhorukov & Leenaarts (2017, Fig. 9) additionally indicate that the conversion factor should be intensity dependent. If we apply the estimated conversion factors, the peak intensities in Fig. 2.4 are still approximately 20–25% larger than observed. A direct conversion factor from 1D RT to 3D RT spectra is nevertheless not straightforward to estimate.

The average peak separation of $\langle \Delta v_{\mathrm{k2}} \rangle = 23.6\,\mathrm{km\,s^{-1}}$ (MURaM-ChE) is smaller than $\langle \Delta v_{\mathrm{k2}} \rangle = 33.02\,\mathrm{km\,s^{-1}}$ (IRIS). Even though the observed average peak separation cannot be reached by the synthetic spectra, there is a significant overlap between the observed and simulated distributions. The peak separation is a consequence of strong variations in the LOS velocity that arise through shocks in the atmosphere. In addition, a significant amount of nonthermal velocity in the atmosphere acts similarly to microturbulence to broaden the spectral lines. MURaM-ChE uses a slope-limited numerical diffusion scheme (Rempel 2014, 2017) that allows the simulation to run stably with low viscosity and resistivity, which leads to the observed strong velocities.

The missing peak separation might be explained by insufficient dynamics, such as the difference between the minimum and maximum vertical velocity in the formation region

of Mg II k $\max(\Delta v_z)$ in the atmosphere. This is supported by the correlation that we find (similar to Leenaarts et al. 2013b) between $\max(\Delta v_z)$ and peak separations (Fig. 2.6), however with a slightly lower correlation coefficient, probably because of misidentifications of the peak-finding algorithm. This suggests that although the chromosphere computed by MURaM-ChE is already very dynamic, the real Sun is even more dynamic. Similar to the peak asymmetry, a larger simulation domain with less vertically orientated magnetic field lines —as a result of the relatively small extent of the simulation domain in the vertical direction— might lead to more realistic dynamics and larger peak separation.

We further investigated the role of velocities in their contribution to the line width. To this end, we computed the Mg II h&k lines for snapshot `muram_en_499000_379s` again, but without a velocity field (i.e., the velocities are manually set to zero). A similar approach was followed by, for example, Rathore & Carlsson (2015) who studied the effect of opacity broadening in the C II λ133.5 nm line. By comparing single spectra from the two computations, we show that in both cases there are examples of broad lines. The increased line width even in the absence of velocities is a consequence of local maxima in the temperature in the lower atmosphere. These might be related to shocks, which increase the local temperature via adiabatic heating. In the majority of the spectra, we find that the presence of a velocity significantly increases the line width of the resulting spectra compared to the case without velocity. This comparison confirms the finding that chromospheric velocities play a dominant role in the line broadening of Mg II h&k.

We tested the time-dependence of the synthesized spectrum following two approaches. We checked for changes in four full cubes saved at 2 min cadence, and in addition considered the dynamics along eight vertical cuts (slits) sampled at 1.2 sec cadence. From the degraded profiles, we measured the peak intensities and peak separations of the k_2 features. The peak separations here vary between $\langle \Delta v_{k2} \rangle = 23.1\,\mathrm{km\,s^{-1}}$ and $\langle \Delta v_{k2} \rangle = 23.6\,\mathrm{km\,s^{-1}}$. The difference between the largest and smallest mean peak separation values of $0.5\,\mathrm{km\,s^{-1}}$ is smaller than the spectral resolution of IRIS of $\delta v = 2.7\,\mathrm{km\,s^{-1}}$.

The spectrum calculated from the spatial average of the eight slits shows periodic variation in time. The variations are strongest in the peaks of the Mg II k and Mg II h lines. This might be explained by heating of chromospheric plasma, which locally increases the peak intensity according to the temperature-to-peak-intensity correlation found by Leenaarts et al. (2013b). The time series is too short to determine whether the varying intensity is a result of wave propagation in the modeled atmosphere or a box mode as found in the public Bifrost snapshot (see Carlsson et al. 2016, Fig. 8). We also find that the slit-averaged spectrum further averaged over the 10 min time series is rather similar to the spectrum averaged over the whole horizontal domain arising from a single snapshot. Because of the low variation in both the high-cadence slits and the low-cadence full cubes, we conclude that the average properties of the spectrum are not dependent on the chosen snapshot.

In summary, we find a close match between the modeled Mg II h&k lines and spectra from IRIS observations. However, the synthesized spectra show on average a $\approx 10\,\mathrm{km\,s^{-1}}$ smaller peak separation and an overall slightly smaller line width. The distribution of the modeled peak intensities exceeds the observed distribution at the higher and lower intensity end. The extent to which this effect is attributed to the 1.5D RT approach in this model will be investigated in a future study. Based on our results, using the 1.5D RT approach, the MURaM-ChE model signifies a step forward in terms of reproducing the physical properties of the chromosphere.

Table 2.1: Overview of observations.

Description	Date	FOV (arcsec)	μ	$\lvert B_{\rm LOS}/\mu\rvert_{\rm avg}$ (G)	$\langle T_{\rm b}\rangle$ (kK)	$\langle \Delta v_{\rm k2}\rangle$ (km s^{-1})
IRIS-QS-1	2014-06-07	139×182	0.96	12.12	5.22	33.02
BIPOLE	2014-06-07	32×32	0.96	12.34	5.22	31.61
NETWORK	2014-06-07	32×32	0.96	33.20	5.44	34.06
QUIET SUN	2014-06-07	32×32	0.98	6.8	5.12	31.26
IRIS-QS-2	2015-07-06	126×129	1.0	13.09	5.22	29.96
IRIS-QS-3	2014-05-20	127×129	1.0	8.15	5.20	31.82

2.5. Acknowledgements

We thank the anonymous referee for valuable comments and suggestions that improved the quality of this paper. P.O. would like to thank T. Pereira for discussions about spatial and spectral degradation to instrumental conditions and support for the HELITA[7] package, as well as the Bifrost group for discussions about the interpretation of synthetic spectral lines. P.O. would also like to thank L.P. Chitta, N. Milanovic and H. Peter for discussions about IRIS observations and alignment with HMI magnetograms. In addition, P.O. acknowledges funding from the international Max Planck Research School (IMPRS). This research has received financial support from the European Union's Horizon 2020 research and innovation program under grant agreement No. 824135 (SOLARNET) and through the European Research Council (ERC) No. 101097844 (WINSUN). This work was supported by the Deutsches Zentrum für Luft und Raumfahrt (DLR; German Aerospace Center) by grant DLR-FKZ 50OU2201. We gratefully acknowledge the computational resources provided by the Cobra & Raven supercomputer systems of the Max Planck Computing and Data Facility (MPCDF) in Garching, Germany.

2.6. Appendix: Additional observations

In the main text we compared the results from the MURaM-ChE model with a single observation (hereafter IRIS QS 1). This observation was averaged over a FOV of 139" × 182", which is larger than the simulation domain (32" × 32"). We compared the average spectra in Fig. 2.4, and the distribution of peak brightness temperatures and peak separation in Fig. 2.5. In this appendix we present results from smaller ROIs of 32" × 32" within IRIS QS 1. These smaller ROIs compare better with the size of the model. Additionally, we present two more IRIS datasets taken on 2015-07-06 (hereafter IRIS QS 2) and 2014-05-20 (hereafter IRIS QS 3) with FOVs of 126" × 129" and 127" × 129" at disk center. A summary of these observations is shown in Table 2.1. In Fig. 2.12 we show intensity maps and in Fig. 2.13 average spectra, and the distribution of peak intensity and peak separation of the observations.

The smaller ROIs in IRIS QS 1 are indicated in Fig. 2.12a. The various ROIs show regions with differing magnetic field strengths. The first ROI contains a bipolar feature, qualitatively comparable to the magnetic configuration in our model and is therefore labeled as "bipole". The second ROI contains larger and stronger magnetic field patches and is therefore referred to as "network". The third ROI is positioned to not include any stronger magnetic field patches and therefore is meant to represent a "quiet sun", or internetwork region. In panels (a),(b), and (c) in Fig. 2.13 it can be seen that the bipolar structure shows similar distributions in terms of peak brightness temperature, peak separation, and average spectrum compared with the full FOV of IRIS-QS-1. The average

[7] https://helita.readthedocs.io/en/latest/index.html

peak separation in the bipolar region is roughly 1.5 km s^{-1} smaller than in the whole FOV. The "quiet sun" region shows on average roughly 100 K lower brightness temperatures than the full FOV and the average peak separation is $\approx$ 1.8 km s^{-1} smaller than in the full FOV. The "network" region contains a larger amount of stronger magnetic fields which results in a roughly three times higher averaged LOS magnetic field strength. The distribution of the corresponding peak brightness temperature, shown in panel (a), appears double peaked. The higher brightness temperature peak is a result of the bright structures that are correlated with the configuration of the photospheric magnetic field (compare Fig. 2.12 panel a with panels b–d). The peak separation is around 1 km s^{-1} larger than in the full FOV. The overall line width of the average profiles is largest in the network region and smallest in the quiet sun region (Fig. 2.13c), while the brightness temperature scales with the LOS magnetic field strength.

The second dataset "IRIS QS 2" is presented in Fig. 2.12 panels (e–h). At the lower left edge of the FOV, there is a bipolar magnetic structure which extends roughly from $(x, y) = (-50'', 120'')$ to $(x, y) = (-50'', 0'')$. This is larger than the size of our simulation and, additionally, it is part of a larger magnetic structure that is not part of the FOV of the raster scan. In the corresponding intensity maps, at the selected Mg II k features, it can clearly be seen that there is a strong enhancement in intensity above this region.

The third dataset "IRIS QS 3" contains similarly to the other two datasets network magnetic field elements. In panels Fig. 2.13d–f we compare the statistical distributions of the three datasets taken over the total FOVs. It can be seen that the distributions of peak brightness temperatures look similar. There is, however, a small enhancement in the tail toward the higher brightness temperatures in panel (d) in IRIS QS 2, which is likely because of the above-mentioned strong bipolar field region. The average peak separation is the largest for IRIS QS 1 (33.03 km s^{-1}) followed by IRIS QS 3 (31.82 km s^{-1}) and the smallest for IRIS QS 2 (29.96 km s^{-1}). The overall shape of the average spectra is roughly similar between the three observations (panel f), but the intensity of IRIS QS 3 is slightly smaller than for the other two datasets.

We conclude from this study that the results from the main text, where we compared the results from MURaM-ChE model with the full FOV of IRIS QS 1, are applicable to smaller ROIs and other datasets. The contrast of the peak brightness temperature in the model is slightly too high compared with the observations. The peak of the synthesized k_2 brightness temperature distribution is between the quiet sun, with lower $B_{\rm LOS}/\mu$ values than the simulation, and observations of network elements, with higher $B_{\rm LOS}/\mu$ values than the simulation. The peak separation from the MURaM-ChE model is on average roughly 10 km s^{-1} smaller than in the observations. We find a similarly good match between the overall line width in all cases except for the selected network region, which has a significantly higher average longitudinal magnetic field. While the distribution of peak brightness temperatures shows a higher occurrence of brighter structures, the overall line width of the MURaM-ChE model is smaller.

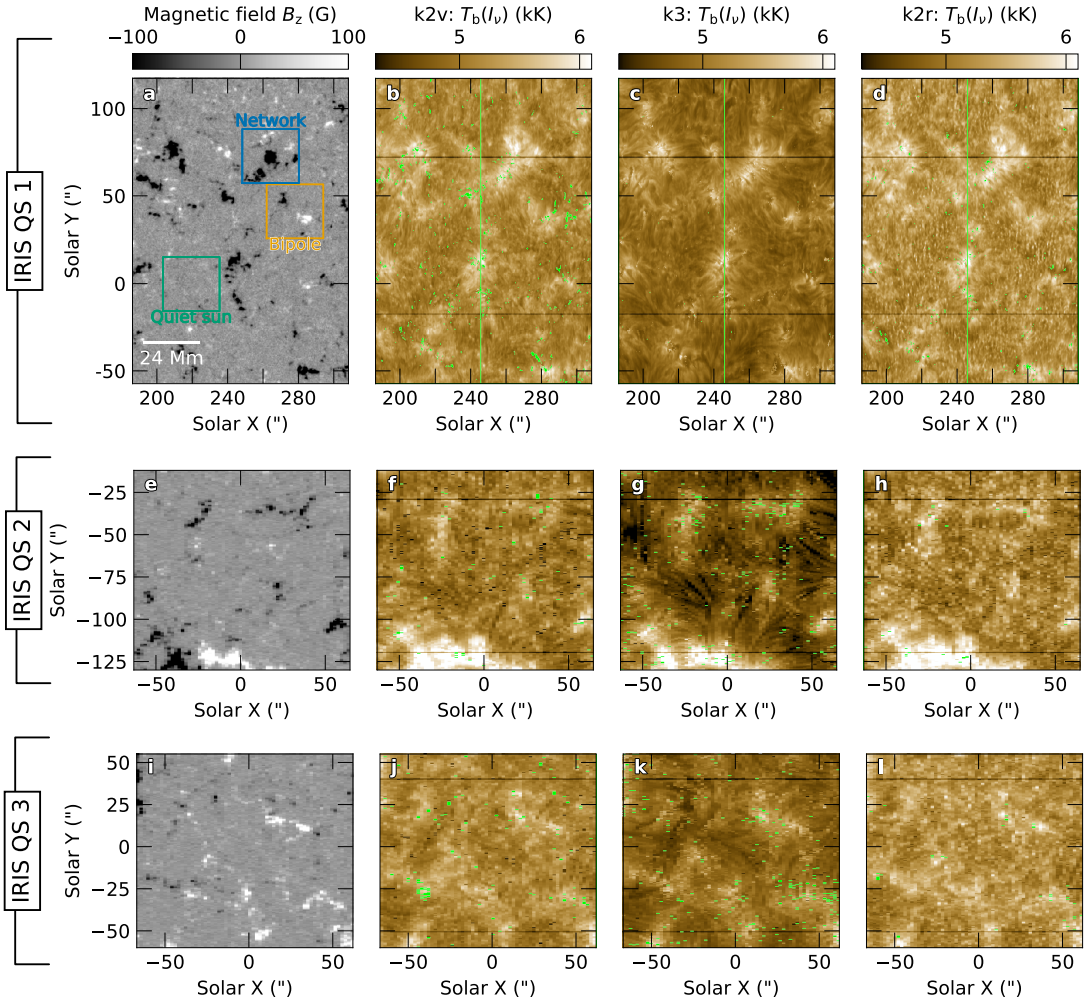

Figure 2.12: Comparison between three IRIS datasets representing quiet sun and network regions. The first dataset "IRIS QS 1" (panels a–d) is the same as the one shown in main text. Three boxes of roughly similar size as the MURaM-ChE model are shown in panel (a). The second and third dataset are shown in panels (e–h, IRIS QS 2) and panels (i–l, IRIS QS 3). Panels (a,e,i) show the LOS magnetic field strength measured by the HMI. Panels (b,f,j) show the brightness temperature T_b at the k_{2v}, panels (c,g,k) at the k_3 and panels (d,h,l) at the k_{2r} feature. Green colored pixels indicate where no feature could be detected.

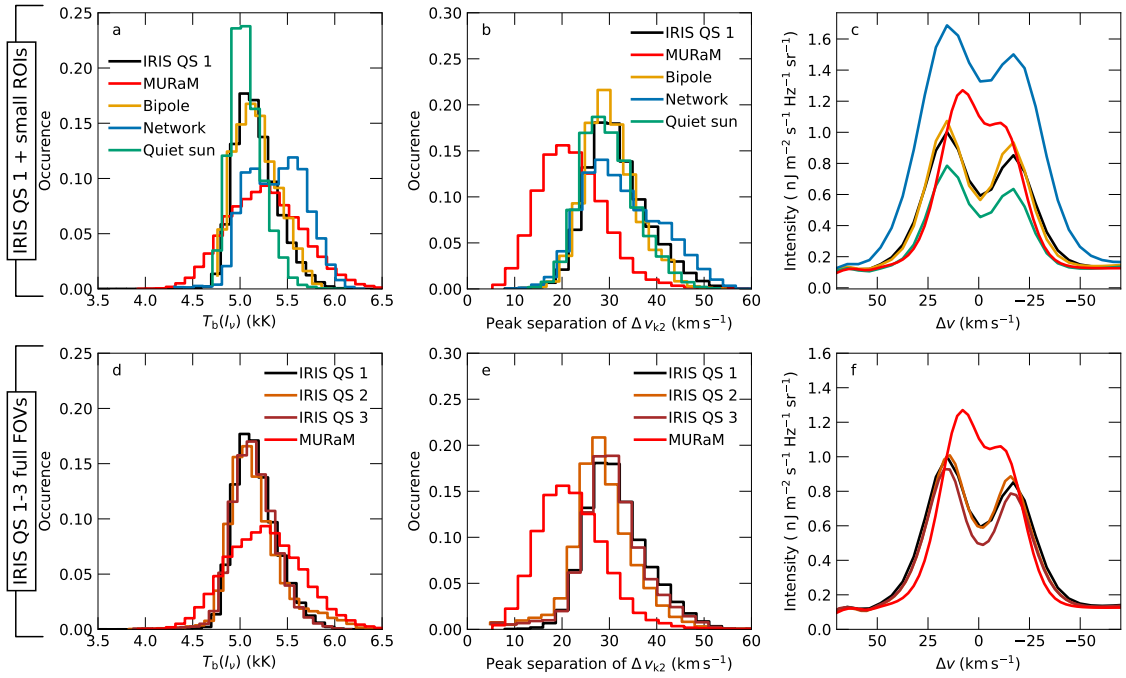

Figure 2.13: Comparison between statistical properties of three IRIS datasets, representing quiet sun and network regions, and the MURaM-ChE model. Panels (a), (b), (d), and (e) show distributions of k_2 brightness temperature and peak separation. Panels (c) and (f) show average profiles of the Mg II k line. In panels (a–c) we compare results from the first IRIS dataset "IRIS QS 1" considering the full FOV together with smaller ROIs of roughly the size of the simulation domain with the results from the MURaM-ChE model. In panels (d–f) we compare three IRIS datasets considering the whole FOVs together with results from the MURaM-ChE model.

3. Formation of Mg II h&k spectral line diagnostics in an enhanced network region simulated with the MURaM-ChE code: Results using 3D synthesis

This chapter is the manuscript for a paper to be submitted to Astronomy & Astrophysics by P. Ondratschek, D. Przybylski, H.N. Smitha, J. Leenaarts, R. Cameron, and S. K. Solanki. Contributions to the paper: I performed the RT computations, analyzed the data, and wrote the first draft of the manuscript; all authors contributed to the ideas behind the study and the manuscript.

Abstract. The Mg II h&k lines form in the middle to upper chromosphere and are preferred spectral lines to study the structure of the chromosphere. The details of their formation in the solar chromosphere are not fully understood. Synthetic spectral lines from radiation-magnetohydrodynamic models are essential to interpret the observations.

We aim to verify known correlations between the underlying atmosphere and spectral line features in 3D radiative transfer (RT).

We forward model the Mg II h&k lines in 3D RT with partial frequency redistribution (PRD) in a self-consistent 3D radiative magnetohydrodynamics (rMHD) simulation with non-local-thermal-equilibrium (NLTE) energy transport and non-equilibrium (NE) hydrogen ionization of an enhanced network region simulated with the MURaM-ChE code. We compare the spectra computed with 3D RT to those computed with 1.5D RT and to observations from the Interface-Region-Imaging-Spectrograph (IRIS). Furthermore, we test correlations between the spectral line properties and underlying atmospheric properties such as temperature and velocity structure.

The spatially averaged Mg II h&k spectral lines computed with 3D RT match approximately a typical IRIS observation, which includes quiet sun and network elements. The peak separation, is however, still slightly lower in the simulation. In contrast, the 1.5D RT spectra tend to overestimate the peak intensities and the central minimum significantly. In the MURaM-ChE model, the qualitative difference between the 1.5D and 3D RT results is even more pronounced than in the public Bifrost snapshot, as given in the literature. We confirm that correlations between spectral line properties and the underlying atmosphere from the MURaM-ChE simulation are similar to those obtained from Bifrost, but show more scatter due to the more dynamic atmosphere. In addition to already known correlations, we found that the k_{2v} (blue) peak of the Mg II k line forms preferably in upflows whereas the k_{2r} (red) peak forms preferably in downflows.

The Mg II h&k lines computed with 3D RT match the observations better in the core intensities and their distribution on the Sun. This underlines the importance of 3D RT in the forward modeling of Mg II h&k.

3.1. Introduction

The solar chromosphere is an interface between the underlying photosphere and the corona above. The causes of many phenomena such as the heating of the chromosphere (e.g., Withbroe & Noyes 1977), or the strong dynamics it displays are not understood. Additionally, the evolution of fine structures such as spicules, their interaction with the magnetic field, and their role in supplying mass and energy to the corona are under debate (Carlsson et al. 2019). Inference of physical quantities such as temperature, velocity, density, and magnetic field is limited through a few strong spectral lines forming in the chromosphere. Because of the decreasing density with height, spectral line formation in the chromosphere is subject to NLTE conditions. In addition, some strong resonance lines such as Ca II H&K and Mg II h&k show PRD effects through scattering (e.g. Milkey & Mihalas 1974). Furthermore, already in the 1980s it became clear from Lyman α observations that the chromosphere is inhomogeneous and plane-parallel modeling is a zeroth-order approximation (e.g., Bonnet et al. 1980). Only recently has it become possible to model chromospheric lines including both, a 3D model atmosphere and 3D RT. Examples are the Ca II λ854.2 nm line (Leenaarts et al. 2009), Hα (Leenaarts et al. 2012a), Mg II h&k (Leenaarts et al. 2013a) and (with PRD, Sukhorukov & Leenaarts 2017), and Ca II H&K (Bjørgen et al. 2018).

Two main strategies are used to interpret observations. Inversions aim to reconstruct an atmosphere model to fit an observed spectral line profile. However, the model atmospheres are kept relatively simple, and the solution is not always unique. In other words, different model atmospheres may lead to very similar spectral line shapes (for reviews of inversions see eg, del Toro Iniesta & Ruiz Cobo 2016, de la Cruz Rodríguez & van Noort 2017). In addition, fudge parameters such as microturbulence are introduced to fit the observed line widths, while the actual velocity structure remains unresolved. Inversion codes solve the RT problem, but they are generally restricted to 1.5D RT as their calculations can easily become expensive, although approaches to take 3D RT effects in inversions into account exist (Štěpán et al. 2022). An alternative to significantly reduce computational costs from inversion is presented by Sainz Dalda et al. (2024) who make use of neural networks.

The other main strategy is based on forward modeling. In the first step, a model of the solar atmosphere is simulated. In the second step, detailed RT computations are conducted post-processing. In contrast to inversions, forward modeling does not aim to exactly reproduce a single observation. The advantage is, however, that through the knowledge of all quantities in the atmosphere, line formation can be studied in detail. By comparing the atmosphere with the resulting spectra, possible correlations can be identified, which can be used to interpret observations without performing inversions.

In this paper, we concern ourselves with the Mg II h&k lines. A typical line profile of Mg II k observed in the QS shows a double-reversed line core. The inner wings, which are the minimum intensities before the first reversal are called k_{1v} and k_{1r}, where the "v" indicates the blue or violet and "r" the red part of the spectrum with respect to the rest wavelength. The peaks are similarly labeled k_{2v} and k_{2r}. The central reversal is called k_3. The Mg II h line shows similar properties as Mg II k and has therefore analogous labeling. These spectral features form at different atmospheric heights (see e.g., Vernazza et al. 1981, Fig. 1) and are thus sensitive to local conditions. The k_1 features form in the low chromosphere close to the temperature minimum in a plane-parallel atmosphere. The k_2 peaks form in the mid chromosphere and the k_3 minimum just below the transition region.

Recent studies of the Mg II h&k line formation were presented by Avrett et al. (2013) for different regions on the sun using 1D model atmospheres. The authors investigated the CLV and the effect of up and downflows on the resulting Mg II k line profiles. Leenaarts et al. (2013a) and Pereira et al. (2013) used a snapshot of a 3D enhanced network simulation (Carlsson et al. 2016, herafter public Bifrost snapshot) computed with the Bifrost code (Gudiksen et al. 2011). The authors found, for example, that the Doppler shifts of the k_3 and h_3 features are good indicators of the vertical velocity in the upper chromosphere, while differences between the k_3 and h_3 Doppler shifts correlate with velocity gradients in the upper chromosphere. The k_2 and h_2 peak intensities can be used to estimate the temperature in the middle chromosphere, while the peak intensity ratios of the k_2 or h_2 peaks correlate with up- or downflows in the upper chromosphere. A summary of these diagnostics can be found in Pereira et al. (2013, Tab. 4). These correlations have been proven useful, among other studies, to interpret variability of Mg II h in full disk mosaics by Schmit et al. (2015), to constrain chromospheric dynamics by Gošić et al. (2018) and Hannah et al. (2019), and to study the velocity structure of prominences by (e.g., Peat et al. 2021). A phenomenon of the Mg II h&k line formation that has so far not been entirely understood is the difference in the emergent intensity between the QS and coronal holes (Kayshap et al. 2018).

The computations of Leenaarts et al. (2013b) and Pereira et al. (2013) resulted in Mg II h&k profiles with too-narrow line widths and too-weak peak intensities when compared to observations. The above authors and Carlsson et al. (2016) argued that a higher numerical resolution in the simulation might help to resolve more dynamics and reduce such discrepancies. Indeed, the simulations of Martínez-Sykora et al. (2023) showed a better match with observed profiles by using a high horizontal resolution of 5 km. The flux emergence simulations of Hansteen et al. (2023) also show a good match with observations, even though the spatial resolution of 100 km is relatively low. This suggests higher mass loading of the chromosphere is required to reproduce the observed line width. Recently, Ondratschek et al. (2024), hereafter Pub I, presented a close match of the Mg II h&k lines from an enhanced network simulation with observations of the QS. The simulation they used was computed with the recently developed MURaM-ChE[1] code (Przybylski et al. 2022). While the resolution in the MURaM-ChE model was relatively moderate, that is 20 km vertically and 23.46 km horizontally, in Pub I it was found that the MURaM-ChE atmosphere is more dynamic than the public Bifrost snapshot, explaining the improved match.

In Pub I, it was also found that the Mg II h&k peak intensities are larger and the line width slightly smaller in the spatially averaged simulated profiles than in the observations. In Pub I the Mg II h&k spectra were computed in the 1.5D RT approximation where each column in the atmosphere is treated as an independent plane-parallel atmosphere.

In this work we aim to extend these studies by computing the spectra of the same simulation snapshot but in 3D RT by using the Multi3D code (Leenaarts et al. 2009). Our goal is to study the impact of 3D RT in the MURaM-ChE model, which was shown to be important by Sukhorukov & Leenaarts (2017), Bjørgen et al. (2019), and Judge et al. (2020). In addition, we aim to test the robustness of the correlations found by Leenaarts et al. (2013b) in the MURaM-ChE simulation used here.

This paper is structured as follows. In Sect. 3.2, we briefly describe the MURaM-ChE model, the RT computations, and observations we use for comparison. In Sect. 3.3, we describe our results, and in Sect. 3.4 we provide a summary and discussion. In Sect. 3.5, we present our conclusions.

[1]Max Planck Institute for Solar System Research/University of Chicago Radiation Magneto-hydrodynamics with the chromospheric extension.

3.2. Methods

In the following, we describe the MURaM-ChE enhanced network simulation and the Multi3D code which we used to compute the Mg II h&k spectra in 1.5D RT and 3D RT. We then describe how the spectra were degraded to the instrumental conditions of the IRIS. After this, we describe the observation to which we compare our results.

3.2.1 The MURaM-ChE model

We use the same model atmosphere as described in Pub I, which represents an enhanced network region with a large-scale bipolar structure. This model was designed to be similar to the public Bifrost snapshot (Carlsson et al. 2016), including the same large-scale field geometry. The model is simulated with the chromospheric extension of the MURaM-ChE rMHD code (Przybylski et al. 2022), which includes NLTE line losses and a NE treatment of hydrogen ionization. The model atmosphere extends over a solar volume of 24 Mm×24 Mm×24 Mm with a horizontal resolution of 23.46 km and a vertical resolution of 20 km. The convection zone extends roughly from $z = -7$ Mm to $z = 0$ Mm, where $z = 0$ Mm lies at the average $\tau_{500} = 1$ surface. The atmosphere extends up to $z = 17$ Mm. We refer to Pub I for more details.

3.2.2 The Multi3D code

To compute the spectra of Mg II h&k in 3D RT we utilize the Multi3D code (Leenaarts & Carlsson 2009) with the extension to compute PRD spectra (Sukhorukov & Leenaarts 2017). In Multi3D, the RTE and the equations of SE are solved simultaneously. The solution is computed iteratively based on the multilevel accelerated Λ-iteration (MALI) scheme with preconditioned radiative rates according to (Rybicki & Hummer 1991, 1992) until convergence of relative population changes with a tolerance of 10^{-3} is reached. The RTE is integrated by using the short characteristics scheme. This allows for domain decomposition and a parallel treatment of the problem. The angle quadrature follows the 24-angle "A4" set of Carlson (1963). We compute the Mg II h&k lines by using the 4+1 level model atom similar to Sukhorukov & Leenaarts (2017) and Bjørgen et al. (2019). The model atom is described in Leenaarts et al. (2013a). This is a compromise between accuracy and computational time. As demonstrated by Leenaarts et al. (2013a) the 4+1 level shows only small deviations from the more accurate 10+1 level atom and is therefore a good choice for expensive 3D RT computations. We used only every other column from the 3D MHD cubes to speed up the computation. This effectively reduces the horizontal resolution to ≈ 48 km. Multi3D has the option to compute spectra also in the 1.5D RT plane-parallel mode. We used this mode to compare between the 1.5D and 3D RT results. This has the advantage that differences between separate codes can be avoided. Unlike the computation in Pub I we did not include blend lines.

3.2.3 Degrading spectra to instrumental conditions

To compare the synthetic intensities with the observation from the IRIS, we degraded the spectra to the instrumental conditions as described in De Pontieu et al. (2014). We performed the same procedure as described in Pub I based on the description in Pereira et al. (2013). We convolved the spectra spatially with a Gaussian kernel of 0.4". In addition, the spectral profiles are convolved with a Gaussian kernel of 6 pm. The spectra are then rebinned on a spatial grid of 0.16" × 0.33" pixels size, which results in a final resolution of 199 × 100 pixels.

3.2.4 Observation

We compare our results to an IRIS observation of a similarly sized field-of-view (FOV) as the simulation of 24 Mm × 24 Mm or 33" × 33". This is a subregion of the observation that we used in Pub I and contains a qualitatively similar bipolar structure (see Pub I, Appendix A, "bipole"). We note that this serves only as a rough comparison as the setup of the numerical simulation is not meant to reproduce this observation. The original IRIS raster scan was observed on 2014-07-06 at an inclination of $\mu = 0.96$. In Sect. 3.3.1.2 we present a qualitative comparison between the observation and the synthetic images computed from the MURaM-ChE model.

3.3. Results

Our analysis consists of two parts. First, we compare the spatially averaged spectrum from the simulation with a similarly averaged observed spectrum. In addition, we compare intensity images from the 1.5D and 3D RT synthesis as well as statistical distributions of spectral line properties with the observed data. For this analysis, we use synthetic spectra that are degraded to IRIS instrumental conditions. In the second part of the results, we test based on the 3D RT results whether similar correlations between the spectra and the underlying atmosphere exist, as found by Leenaarts et al. (2013b) and Pereira et al. (2013). We focus on the Mg II k line as the formation of the Mg II h line is similar. For this analysis we use the spectra at the original computed spatial and spectral resolution. This preserves the information about the wavelength-dependent optical depth that we use to estimate the formation height in the atmosphere.

3.3.1 Comparison with observation

Here we present comparisons between the forward-modeled spectra and the observation. We start by comparing the spatially averaged spectrum. We then compare intensity images at the rest wavelength and the spectral line features. Finally, we compare statistical distributions of the k_2 peak intensity, peak separation, and peak intensity ratio.

3.3.1.1 Average spectrum

In Fig. 3.1 we present the spatially averaged spectrum of a region observed by IRIS, the spectrum from the simulation computed with the 1.5D RT approximation, and the spectrum calculated from the same snapshot but with 3D RT. It can be seen that the intensity of the synthetic spectra matches the observation in the k_1 minima and the pseudo-continuum in between the Mg II k and Mg II h line with the observations. The mismatch with the spectral lines between the two Mg II h&k lines is due to not including such blending lines in the computations with Multi3D. In the k_2 peaks and k_3 minimum, the 1.5D and 3D RT computations differ. The k_{2v} peak from 3D average spectrum is 32% lower than the k_{2v} peak of the 1.5D average spectrum. Similarly, the k_{2r} peak in 3D RT is 41% lower than in the 1.5D RT computation. The central minimum in 3D RT is 42% lower than in the 3D RT computation. These values are almost a factor of four higher than the values we estimated in Pub I from the difference in the Bifrost public snapshot between 1.5D and 3D RT computations (see Sukhorukov & Leenaarts 2017, Fig. 10). This indicates that in the MURaM-ChE simulation, 3D RT effects are more important as they decrease the intensity contrast above the network magnetic fields. In the k_1 and h_1 features, and in the pseudo-continuum between the Mg II h&k lines, the 3D RT and 1.5D RT computations

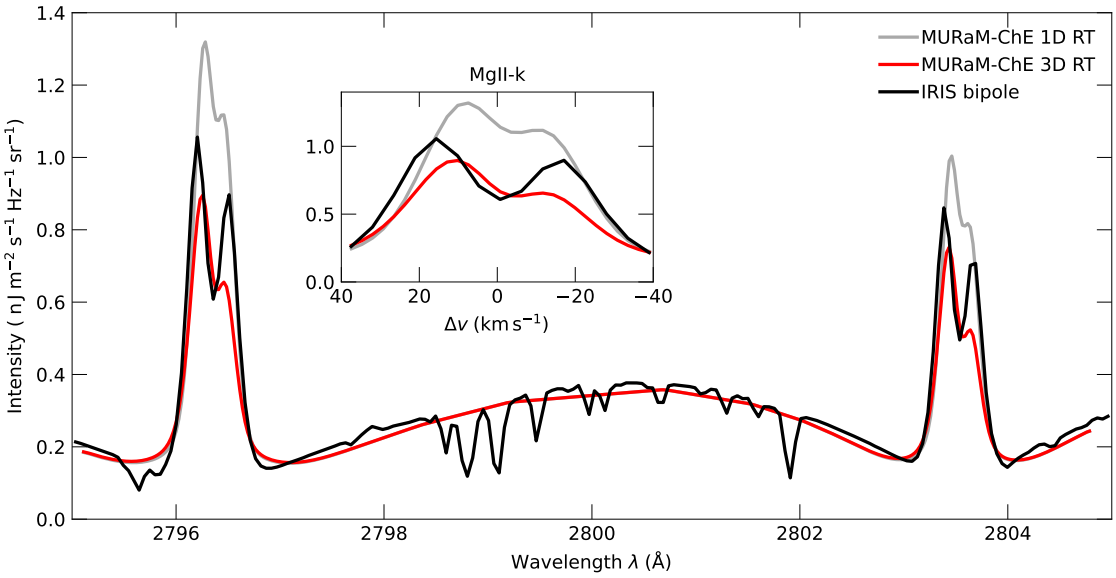

Figure 3.1: Spatially averaged spectra of the Mg II h&k lines. Shown are the spectra from the MURaM-ChE simulation once computed in full 3D RT (red) and once using the plane-parallel 1.5D RT approximation (grey). For comparison, we show an observation from a qualitatively similar bipolar feature, which covers a similar area on the Sun (black).

agree with each other. This is expected as these intensities form in the lower atmosphere, where 3D RT is less important.

In comparison with the observed spectrum, the 3D RT computation results in a closer match of the line core, however the k_2 and h_2 peak intensities are lower in the 3D RT computation. The k_3 and h_3 intensity approximately matches the observed value.

The k_3 minima of both synthetic spectra are shifted by $-4.9\,\mathrm{km\,s^{-1}}$ with respect to the rest wavelength of Mg II k, whereas in the observation the k_3 feature is shifted by $-1.4\,\mathrm{km\,s^{-1}}$. The peak intensity ratios computed via

$$R_\mathrm{k} = (I_\mathrm{k2v} - I_\mathrm{k2r})/(I_\mathrm{k2v} + I_\mathrm{k2r}) \tag{3.1}$$

(see e.g., Leenaarts et al. 2013b, Eq. 2) are 0.082 (1.5D RT), 0.16 (3D RT), and 0.079 (IRIS). This means for all three spectra the blue peak (I_k2v) is stronger than the red peak (I_k2r). The higher peak intensity ratio in the 3D RT computation than in the 1.5D RT computation is a result of the lower k_2 intensities in 3D RT while the difference between two k_2 peaks, that is $I_\mathrm{k2v} - I_\mathrm{k2r}$ is similar for the two computations, that is 0.24 (3D RT) and 0.2 (1.5D RT). The peak intensity difference for the observations is 0.16. All numbers are given in ($\mathrm{n\,J\,m^{-2}\,s^{-1}\,Hz^{-1}\,sr^{-1}}$).

3.3.1.2 Intensity images of the observation and the synthesized snapshot

In this section, we compare the appearance of the intensity images at different spectral features such as the rest wavelength, k_2 peaks, and k_3 minimum. We aim to understand how 3D RT affects the emergent intensity at different locations in the simulation snapshot and how this qualitatively compares with an observation of a bipolar magnetic structure. Figure 3.2 shows the intensity at the rest wavelength (first column, panels a, e, and i), at the k_{2v} feature (second column, panels b,f, and k), the k_3 feature (third column, panels c,g, and j), and the k_{2r} feature (fourth column, panels d, h, and l). We compare the observations (top row) with results from our model combined with 3D RT (middle row), and computed spectra in the 1.5D RT approximation (bottom row).

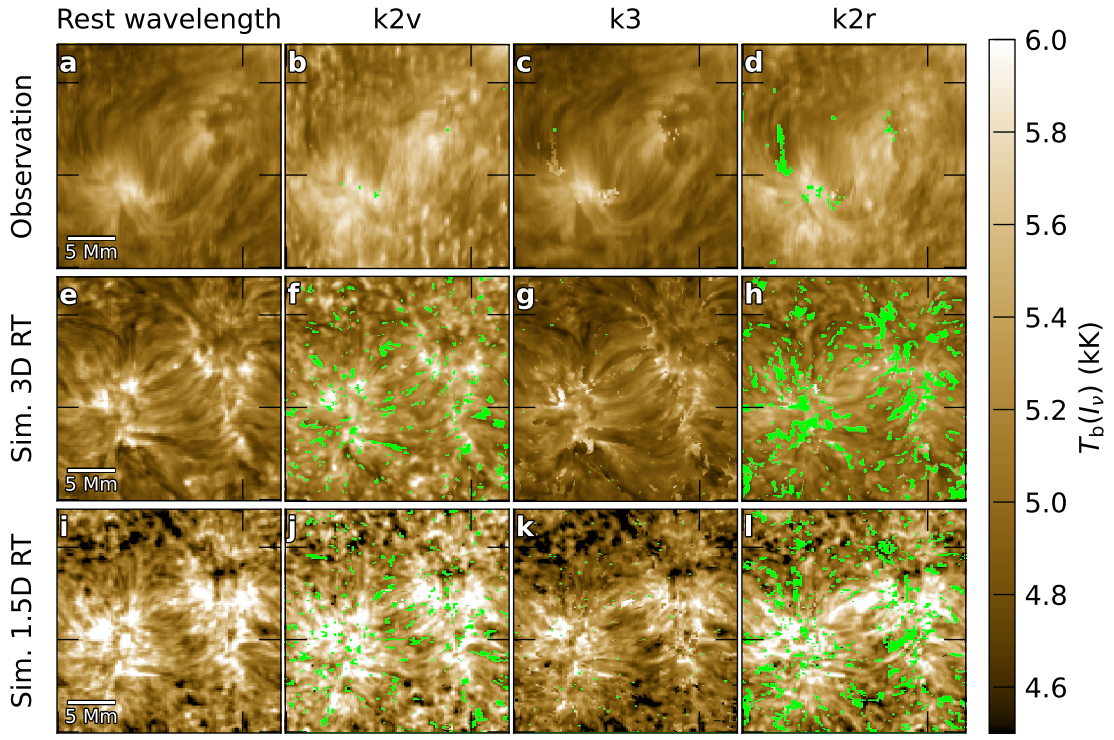

Figure 3.2: Qualitative comparison with observations. We compare three different sets of intensity images. The first row shows the intensity map of the Mg II k line from the observation taken at the rest wavelength (panel a), the k_{2v} feature (panel b), the k_3 feature (panel c), and the k_{2r} feature (panel d). The second row (panels e,f,g, and h) shows the same quantities but for the MURaM-ChE model using 3D RT calculations and the bottom row (panels i,j,k, and l) when the RT problem is solved on a column-by-column approach. The selected region of interest from the observation has the same FOV as the box size of the simulation. Green pixels indicate spatial locations where no feature could be detected by the peak-finding algorithm. The synthetic spectra were degraded and rebinned to the specifications of the observation data set.

The observed bipolar structure shows enhanced intensity above magnetic elements (compare Pub I, Fig. A.1) in all spectral features. The intensity image at the rest wavelength (panel a) and k_3 feature (panel b) shows fibril-like structures connecting the two polarities. The observed k_{2v} image (panel b) shows shock-expansion patterns beneath the bipolar structure, that is, in the upper left and lower right corner of the image. The observed k_{2r} image (panel d) shows less sharply defined shock-expansion patterns and is overall fainter. This suggests that the k_{2r} peak forms at slightly different heights in the atmosphere than the k_{2v} peak. The fact that the k_{2r} image (panel d) is more "washed" out than k_{2v} (panel b) might indicate that the red peak forms higher up in the atmosphere.

The intensity images computed with 3D RT (middle row, panels e–h) show similar features as the observation, such as connecting fibrilar structures between the polarities. However, they show a higher contrast at the rest wavelength and at the k_3 feature than the observation. The 3D RT intensity images taken at the k_2 peaks (panels f and h) show more structure and higher maximum intensities above the network magnetic fields than the observation (panels b and d). The contrast in the observed images might be lower due to the presence of stray light.

The intensity images from the 1.5D RT computations show two dominant differences compared with the 3D RT computation. First, the intensity above the network fields is

much higher and in the quiet region (upper left and lower right edge of the images) there exist much fainter regions. The second difference is that at the rest wavelength (panel i) and at the k_3 feature (panel k) the fibrilar structures are hardly visible, whereas in the 3D RT computation (e.g., panel g), they are clearly visible.

3.3.1.3 Statistical comparison with the observation

Comparing an average spectrum can be overly influenced by the high-intensity pixels. We therefore study here the distribution of the spectral line features. In Fig. 3.3, we show distributions of peak brightness temperature (panel a), k_2 peak separation (panel b), and k_2 peak intensity ratio (panel c) of the computed spectra and the observations. The peak brightness temperature of the observation is on average 5.22 kK with minimum values of $\approx$ 4.75 kK and maximum values of $\approx$ 5.9 kK. The distribution has a Gaussian shape with an extended tail towards higher temperatures, similar to a log-normal distribution. Such log-normal distributions have also been found for the brightness at other wavelengths (Pauluhn et al. 2000). The distribution of the peak brightness temperatures from the 3D RT computations has a similar shape as the observation but slightly shifted towards lower temperatures. The mean is 5.12 kK, that is approximately 100 K lower than in the observed distribution. The minimum and maximum values are here $\approx$ 4.6 kK and 6.25 kK. The highest peak brightness temperature has, however a very low occurrence. The results of the spectra computed with 1.5D RT are different in mainly two ways. First, the distribution is broader extending to lower ($\approx$ 4.4 kK) and higher ($\approx$ 6.5 kK) brightness temperatures. Second, the average brightness temperature of 5.34 kK is higher than the 3D RT compuation and the observation. This result demonstrates that in the MURaM-ChE simulation peak brightness temperatures higher than $\approx$ 5.25 kK are overestimated in the 1.5D RT approach.

The observed peak separation distribution has an average value of 31.58 km s^{-1} and shows an approximately Gaussian shape, however, with slightly more occurrence of higher values. The smallest observed values are $\approx$ 17 km s^{-1} and the largest are $\approx$ 45 km s^{-1}. The peak separation distribution of the 3D RT spectra shows a slightly higher average of 26.26 km s^{-1} compared to the 1.5D RT spectra, which are on average 24.01 km s^{-1}. The value of the 1.5D RT spectra is $\approx$ 0.6 km s^{-1} larger than what we found in Pub I, (Sect. 3.2.3.). This could be because of a difference in the codes, the smaller atom model, or the fact that we considered only every other column in the atmosphere for the RT computations here. The difference is however small compared for example to the wavelength resolution of IRIS, which is 2.4 km s^{-1}. The peak-separation distribution of the 3D RT spectra seems to be shifted by $2-3$ km s^{-1} toward higher values. This might be because the spectra computed in 3D RT have a smaller number of small peaks such that the peak separation is better defined.

We computed the peak intensity ratio (Eq. 3.1) for the observation and the computed spectra. The corresponding distributions are shown in panel (c). The average values are 0.07 (IRIS), 0.09 (1.5D RT), and 0.12 (3D RT). These values compare to the ones estimated from the spatially averaged spectrum (Sect. 3.3.1.1). The peak intensity ratio is again largest for the 3D RT spectra. The difference between the 1.5D RT and 3D RT values might originate from the fact that in the peak intensity ratio, the differences are normalized by the sum of the intensities. Thus the same difference of $I_{\mathrm{k2v}} - I_{\mathrm{k2r}}$ will lead to a smaller peak intensity ratio the higher the intensities are. Irrespective of whether the spectra are computed with 1.5D or 3D RT, the model produces broader distributions of the peak intensity ratio than in the observation.

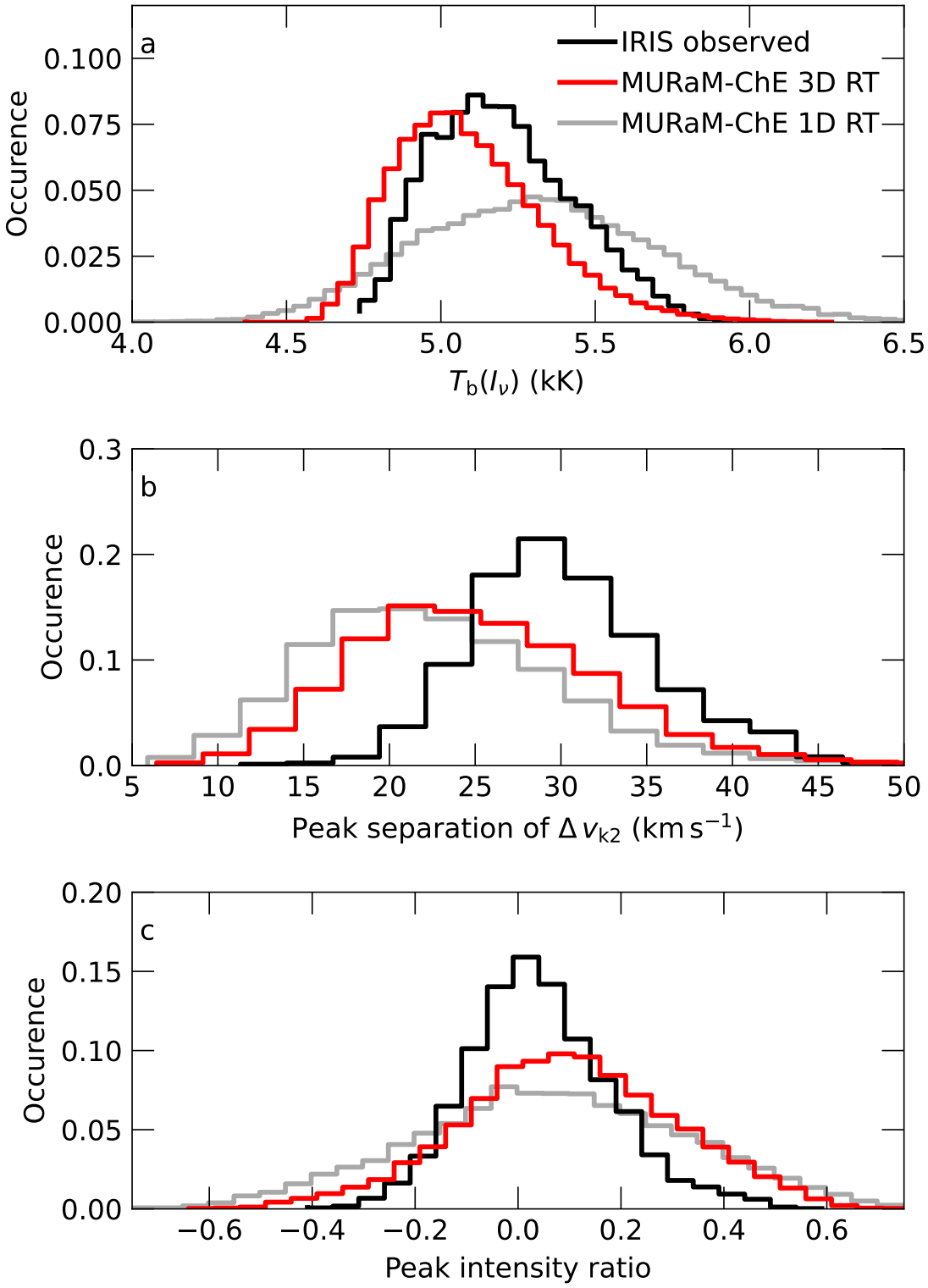

Figure 3.3: Statistical comparison with observations. In panel (a) we show distributions of the k_2 peak brightness temperature, in panel (b) the distribution of k_2 peak separation, and in panel (c) the distribution of the k_2 peak intensity ratio. We show data from the IRIS observation in black, data from the synthetic spectra computed by 3D RT in red, and 1.5D RT in grey after degradation to instrumental conditions.

3.3.2 Correlations between spectral line properties and the atmosphere

In this second part of our results, we study correlations between spectral line properties and atmospheric properties. The diagnostic potential of such correlations has been presented by Leenaarts et al. (2013a) and Pereira et al. (2013). Our aim is here to test whether similar correlations can be found in a different model of the solar chromosphere and how strongly they depend on the model. We begin with a discussion of intensity images at the k_{2v}, k_{2r}, and k_3 features of the Mg II k line. We compare the intensity images to maps of the corresponding formation heights as well as vertical velocity, temperature, and density at the formation height. We then present correlations between the Doppler shifts of the k_2 and k_3 features and the vertical velocities at their formation heights. We further study the relationship between the peak intensity ratio and the average velocity between the formation height of the k_2 peaks and the k_3 feature. Finally, we test the potential of the k_2 peak to infer chromospheric temperatures.

3.3.2.1 Images of synthetic intensity and atmospheric properties

The formation of spectral features of the Mg II h&k lines is known to depend on both the temperature and velocity field over a wide range of heights in the chromosphere. To demonstrate these relationships, we present in Fig. 3.4 intensity maps, formation heights, the vertical velocity, temperature, and density at the height of formation $\tau_\nu = 1$ of the spectral feature in question (given at the top of the figure).

We find the k_{2v} peak shows different formation properties compared to the k_{2r} peak. The intensity image of k_{2v} (panel a) shows more shock expansion patterns throughout the whole simulation domain than in the k_{2r} intensity image (panel c). Shock expansion patterns are web-like structures, similar to reversed granulation, of enhanced intensity of $T_b > 6\,\mathrm{kK}$. They are more clearly visible in the quiet regions of the simulation, that is at $y \leq 5\,\mathrm{Mm}$ and $y \geq 17\,\mathrm{Mm}$. An example is visible at $(x, y) = (5\,\mathrm{Mm}, 22\,\mathrm{Mm})$ in panel (a). While similar structures exist in the k_{2r} image (panel c), they are fainter and show different shapes. The k_{2r} intensity image rather shows fibrillar structures of the upper chromosphere as traced by the k_3 feature (panel b). This suggests k_{2v} forms lower in the atmosphere than k_{2r}. This is supported by the formation height maps shown in panel (d, k_{2v}) and panel (f, k_{2r}). There, it can be seen that at the same location, the k_{2r} feature can form up to $\approx 1\,\mathrm{Mm}$ higher than k_{2v}. In addition, the formation height image of k_{2r} shows imprints of the loop-like structure of the upper chromosphere (see e.g., panel e), whereas such structures are hardly visible in panel (d).

The comparison with the atmospheric properties shows additionally that the vertical velocity at the formation height of k_{2v} (panel g) shows preferred upflows (i.e., 71% of the pixels) in relatively thin, spatially concentrated structures with an average velocity of $v_{z,k2v} = 3.7\,\mathrm{km\,s^{-1}}$. In contrast, the vertical velocity at the formation height of k_{2r} (panel i) traces downflows (in 86% of the pixels) in spatially more expanded structures with an average velocity of $v_{z,k2r} = -7.3\,\mathrm{km\,s^{-1}}$. The vertical velocity map traced by the formation height of the k_3 feature shows a rather balanced appearance of up- (43%) and downflows (57%). The maps of temperature and density similarly highlight differences in the formation of k_{2v} and k_{2r}. The temperature map of k_{2v} (panel j) shows lower atmospheric temperatures (on average 6.8 kK) but in regions of higher density, on average $3.58 \times 10^{-8}\,\mathrm{kg\,m^{-3}}$. Clearly visible in panel (m) is the web-like shock pattern in yellow color at densities of $\approx 10^{-7}\,\mathrm{kg\,m^{-3}}$. In contrast, the temperature at the formation height of k_{2r} is higher (on average 8 kK) and the density is lower (on average $6.7 \times 10^{-9}\,\mathrm{kg\,m^{-3}}$). The higher densities at the formation of k_{2v} lead to a stronger coupling between the radiation field and the local gas temperature and thus result in higher peak intensities.

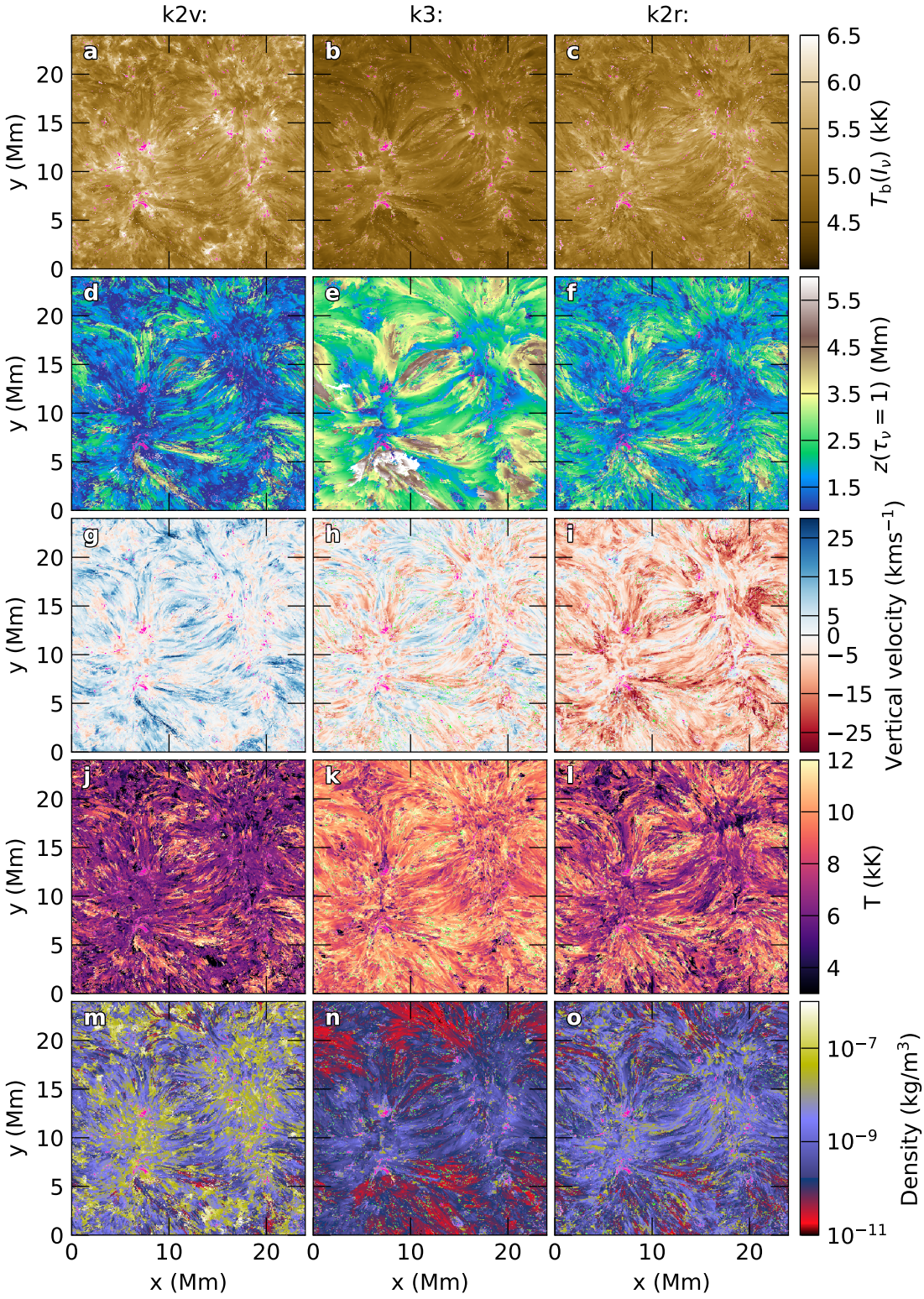

Figure 3.4: Intensity maps (first row, panels a–c), formation heights (second row, panels d–f), vertical velocity maps (third row, panels g–i), temperature (fourth row, panels j–l), and density (fifth row, panels m–o). We show these quantities for the k_{2v} (left column, panels a, d, g, j, and m), k_3 (middle column, panels b, e, h, k, and n), and k_{2r} (right column, panels c, f, i, l, and o) spectral features. The synthetic spectra correspond to the snapshot `muram_en_499000_379s`. Pink-colored pixels indicate where the respective spectral feature could not be detected by the peak-finding algorithm.

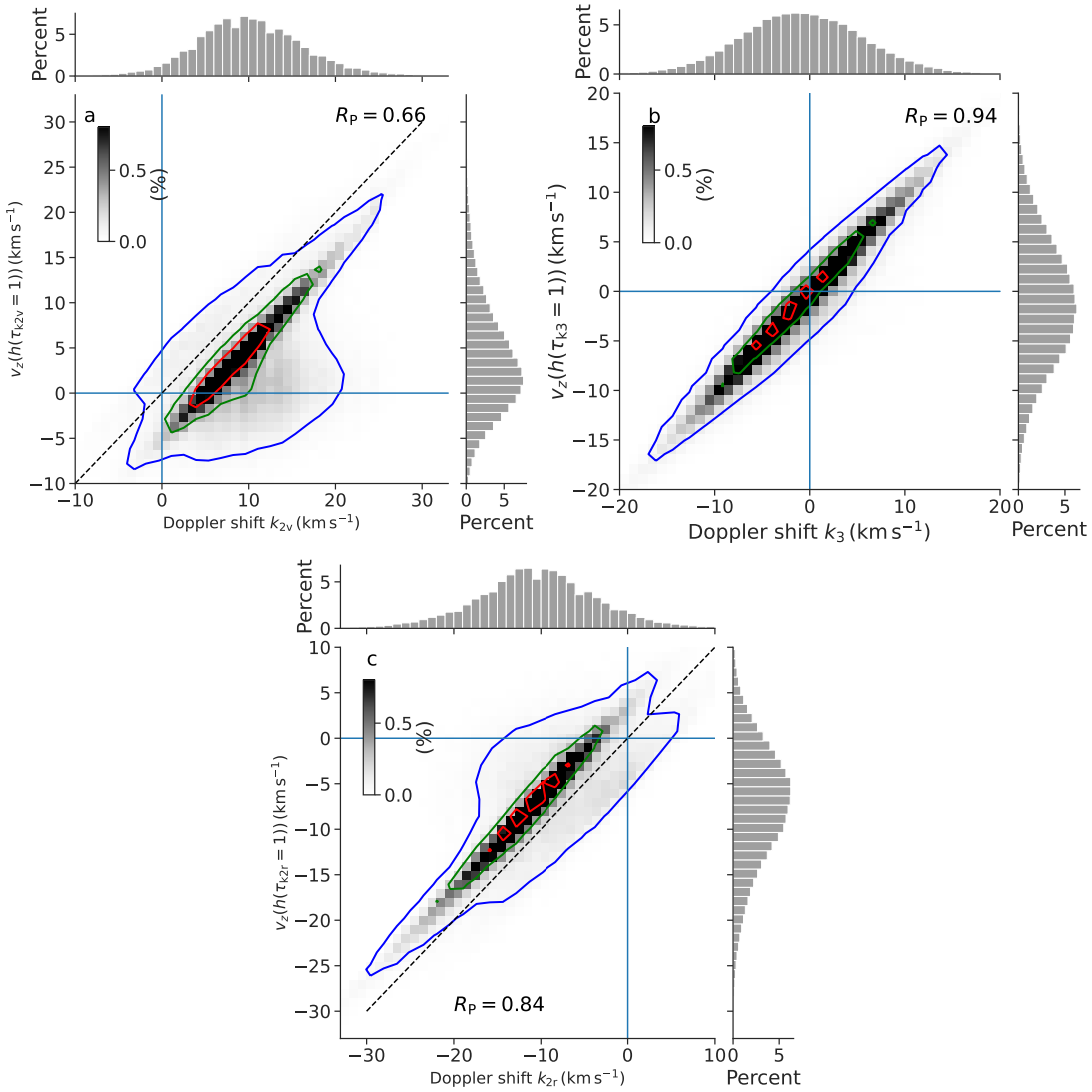

Figure 3.5: Correlations between Doppler shift of spectral features of Mg II k and the vertical velocity in the atmosphere. Panel (a): Correlation between Doppler shift of k_{2v} and the vertical component of the velocity at the formation height. Panel (b) shows a similar relation, but for k_3. Panel (c) is the same as panel (a) but for k_{2r}. The Pearson correlation coefficient R_P is given in each panel. The blue solid lines indicate "$x = 0$" and "$y = 0$". The black dashed line indicates "$x = y$". The red, green, and blue contours enclose 25%, 50%, and 90% of the data.

3.3.2.2 Correlation between Doppler shifts and vertical velocity at the formation height

We now study the diagnostic potential of the k_2 and k_3 Doppler shift in more detail. In Fig. 3.5 we show correlations between the Doppler shift and the vertical component of the atmospheric velocity for k_{2v} (panel a), k_3 (panel b), and k_{2r} (panel c). The correlations based on the k_2 features indicate a correlation such that the Doppler shift of k_{2v} (k_{2r}) correlates with upflows (downflows) at the corresponding height of formation in the atmosphere. The Pearson correlation coefficients are $R_p = 0.66$ (k_{2v}) and $R_p = 0.84$ (k_{2r}). The correlations of k_{2v} and k_{2r} are offset toward positive (k_{2v}) and negative (k_{2r}) Doppler velocities due to the location of the spectral features with respect to the line core. There are regions in panels (a) and (c) where the spectra show a large Doppler shift but the vertical velocity component in the atmosphere is small. These profiles are broad because

of a peak in the temperature stratification in the lower atmosphere (see Pub I, Sect. 3.2.4.).

The correlation between the Doppler shift of k_3 and the atmospheric velocity at the formation height is tight with a Pearson correlation coefficient of $R_P = 0.94$. This coefficient is slightly lower than the coefficient found by Leenaarts et al. (2013b), which was $R_P = 0.99$. For their correlation, the authors computed the line core of Mg II h&k in 3D RT but under the CRD approximation. In Leenaarts et al. (2013b, Fig. 4) it can also be seen that $\approx 90\%$ of the data points in the public Bifrost snapshot have vertical velocities within $\pm 10\,\mathrm{km\,s^{-1}}$ at the formation height of k_3. In the MURaM-ChE model, the distribution extends to $\approx \pm 16\,\mathrm{km\,s^{-1}}$ (Fig. 3.5b, blue contour), and the scatter is larger.

3.3.2.3 Correlation between peak intensity ratio and motions in the atmosphere

The peak asymmetry ratio (Eq. 3.1) was shown by Leenaarts et al. (2013b) to be an indicator of the average velocity in the atmosphere between the formation heights of the k_2 peaks and k_3. Due to the large difference between the formation heights of k_{2v} and k_{2r} we compute the average velocity not from the average k_2 formation height but from the minimum of the two formation heights of k_{2v} and k_{2r} (see Pub I, Eqs. 2 and 3). In addition, we exclude cells along the line of sight with temperatures of $T_{\mathrm{gas}} > 12\,\mathrm{kK}$ as no significant contribution to the intensity is expected from there (see e.g., Carlsson & Leenaarts 2012, Fig. 11). As shown in Fig. 3.6, we find a similar correlation to that found by Leenaarts et al. (2013b), that is, $I_{k2v} > I_{k2r}$ is correlated with an average downflow in the atmosphere, and vice versa. Our distributions, however, show more scatter and a weaker Pearson correlation coefficient of $R_P = -0.33$, compared to Leenaarts et al. (2013b) who found $R_P = -0.51$. This results from a larger amount of complex spectral line profiles we find in the MURaM-ChE model than compared with the public Bifrost snapshot. Such spectral line profiles show more than two peaks and thus introduce a certain degree of ambiguity for the peak-finding algorithm. The more complex spectral line profiles are a result of the more dynamic atmosphere in the MURaM-ChE model than in the public Bifrost snapshot (see e.g., Pub I, Fig. 11b). Another contribution to the scatter could come from the fact that the topology of the chromosphere in the MURaM-ChE simulation is rather complex, sometimes with hot ($T > 12\,\mathrm{kK}$) gas lying between the formation heights of the k_2 and k_3 features (see also Pub I, Fig. 7c), making a definition of an "average velocity" in the considered height range difficult.

3.3.2.4 Temperature diagnostics

Another diagnostic property of the Mg II h&k lines is the correlation between the peak brightness temperature and the atmospheric temperature at the formation heights (see Leenaarts et al. 2013b, Fig. 6 e and f). This correlation, however, tends to be only valid for intensities above a certain minimum brightness temperature of $\approx 5\,\mathrm{kK}$. These intensities are formed at heights in the chromosphere where the source function is still sufficiently coupled to the local gas temperature.

We studied the same correlations and present them in Fig. 3.7. In panel (a) we show the results for the k_{2v} feature. It can be seen that there is a correlation between brightness temperatures of $T_b > 5.25\,\mathrm{kK}$ with the plasma temperature. The Pearson correlation coefficient is, however, only $R_P = 0.12$. The reason is that already at the formation height of the k_{2v} peak, the line source function can be decoupled from the local gas temperature. The Pearson correlation coefficient for all datapoints in Fig. 3.7 (a) is negative ($R_P = -0.15$). For $T_b < 5.25\,\mathrm{kK}$, there is a large variety of atmospheric temperatures, which result in a rather narrow range of brightness temperatures of $T_b \approx 4.75\,\mathrm{kK}$ to $T_b \approx 5\,\mathrm{kK}$. These intensities form in between the shock-like patterns at a slightly higher formation height.

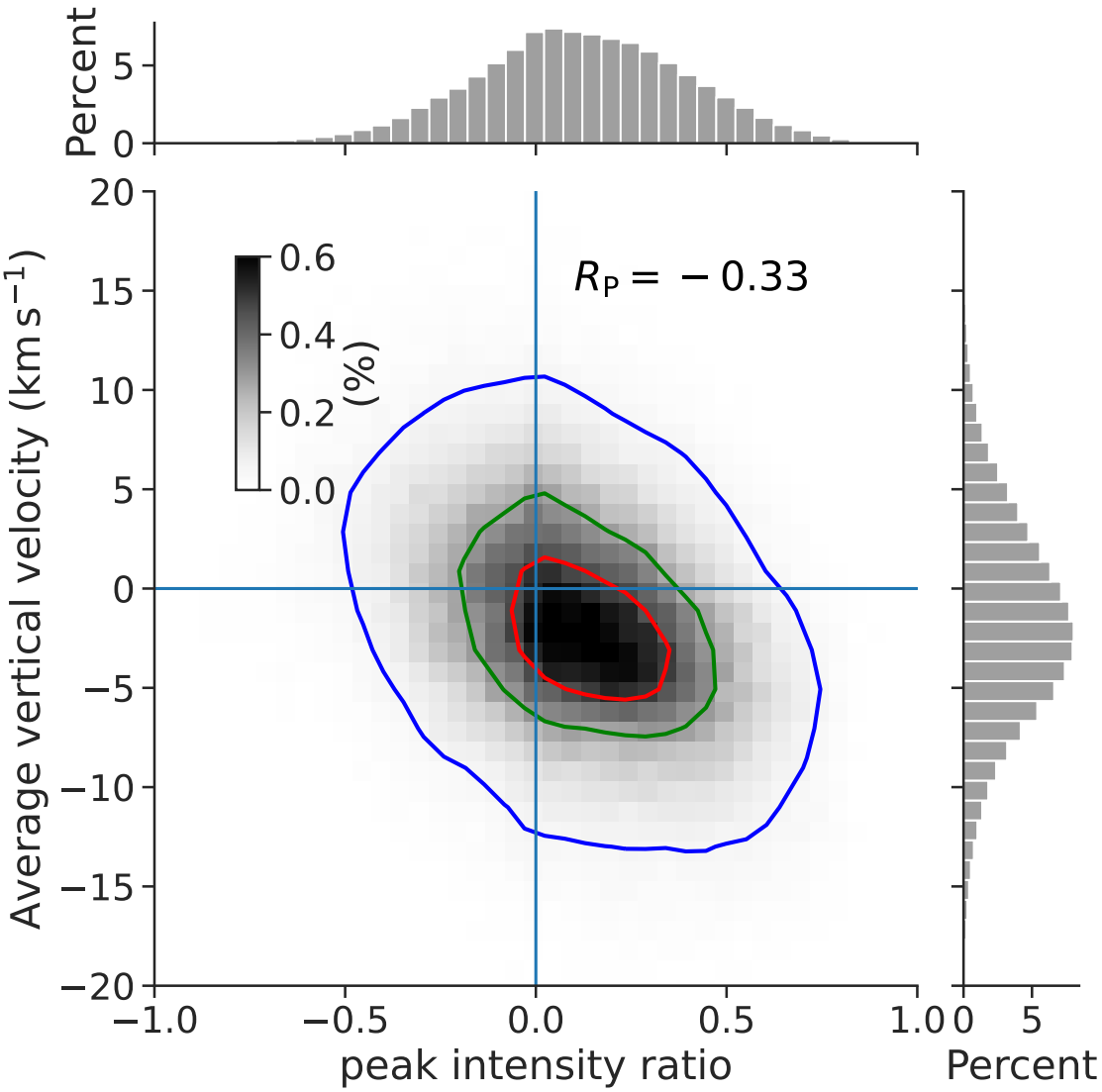

Figure 3.6: Correlation between peak intensity ratio and average vertical velocity. The average vertical velocity is measured from the minimum formation height of the two k_2 features and the formation height of the k_3 feature. The red, green, and blue contours enclose 25%, 50%, and 90% of the data. The blue solid lines indicate "$x = 0$" and "$y = 0$".

Such scenarios can, for example, be seen in Fig. 3.4 (a, brightness temperature) and (d, formation height). In Fig. 3.7 (a and b), there is a cluster of datapoints at $T_{\rm gas} \approx 10\,$kK, which is just below the maximum atmospheric temperatures of roughly 12 kK and indicates the maximum temperatures where Mg II exists dominantly (see also, Carlsson & Leenaarts 2012, Fig. 11).

In panel (b), we show the correlation for the k_{2r} peak. There is a similar but less tight correlation for $T_{\rm b} > 5.25\,$kK with a Pearson correlation coefficient of $P_{\rm r} = 0.06$. The maximum brightness temperatures of k_{2r} are lower than those of k_{2v}, which was already indicated in the average spectrum (see Fig. 3.1). For brightness temperatures of $T_{\rm b} < 5.25\,$kK the correlation is even lower. The overall correlation coefficient is $R_{\rm P} = -0.21$, which is more negative than for k_{2v}. This can be understood from the fact that in our model k_{2r} forms higher in the atmosphere than k_{2v}, at lower densities and therefore is less suitable to estimate the atmospheric temperature.

Our results compare with the findings of Leenaarts et al. (2013b, Fig. 6 e and f). These authors found a stronger intensity-temperature correlation for the k_{2v} peak than

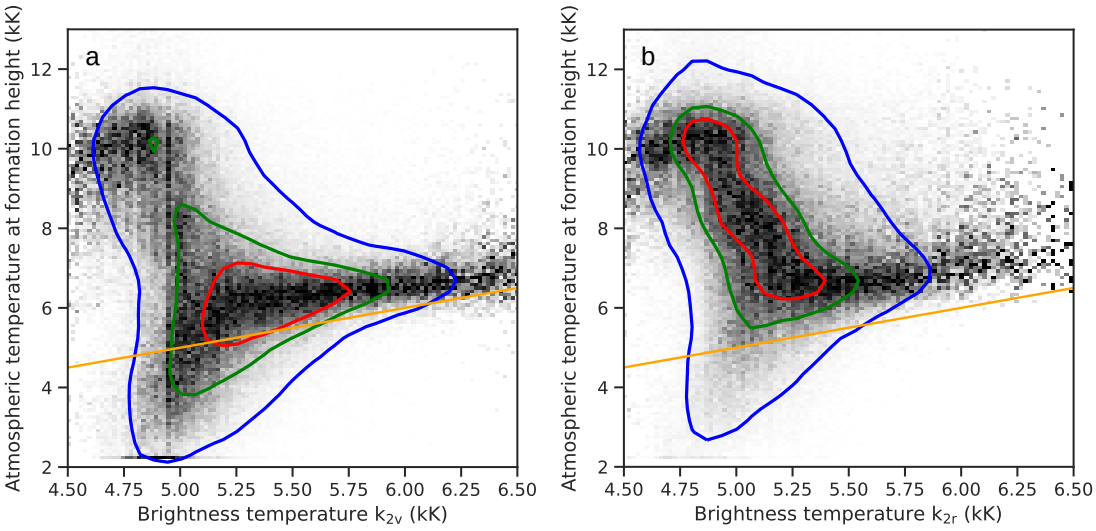

Figure 3.7: Correlation between peak brightness temperatures and temperature at the formation height in the atmosphere. Panel (a) shows the correlation for the blue peak (k_{2v}) and panel (b) shows the correlation for the red peak (k_{2r}). The red, green, and blue contours enclose regions of 25%, 50%, and 90% of the data. The orange lines indicate "$x = y$". We normalized each column of brightness temperature to the maximum value of atmospheric temperature in that column.

for the k_{2r} peak. The actual Pearson correlation coefficients are similarly low. In the public Bifrost snapshot, there is a larger fraction of brightness temperatures below 4.7 kK. The differences of the temperature stratification between the Bifrost public snapshot and the MURaM-ChE model was discussed in Pub I, Fig. 11a and Sect. 3.3 where we found higher temperature in the MURaM-ChE model at the formation heights of Mg II k in the chromosphere.

3.4. Summary and discussion

In this work, we analyzed the formation of the Mg II h&k lines with the help of 3D RT computations in a simulation of a bipolar magnetic feature in the solar atmosphere computed with the MURaM-ChE code. In previous work (Pub I), we analyzed the Mg II h&k of the same simulation snapshot in 1.5D RT. In this section, we discuss the combined results of this work and compare them with previous work.

We determined the spatially averaged spectra, intensity images of the spectral line features, and statistical distributions of line parameters from 1.5D RT and 3D RT computations and from a dataset recorded by the IRIS observatory and compared the results from these three sources. We also compare with previous results for the same spectral lines obtained from the public Bifrost snapshot. The FOV of the observation was chosen to include a similar bipolar magnetic feature as in the simulations.

We found that the distribution of the k_2 and k_3 intensities cover a much wider range and in general display larger values for the 1.5D RT computation than for the 3D RT computation. Therefore, for the spatially averaged spectrum these intensities are up to 72% higher in the profile obtained via 1.5D RT than in the profile from 3D RT computations. Thus, in the MURaM-ChE model, the effects of 3D RT are important not only in the k_3 minimum but in the whole line inside the k_1 minima. While Sukhorukov & Leenaarts (2017, Fig. 10) found similar results for computations with the public Bifrost snapshot, the

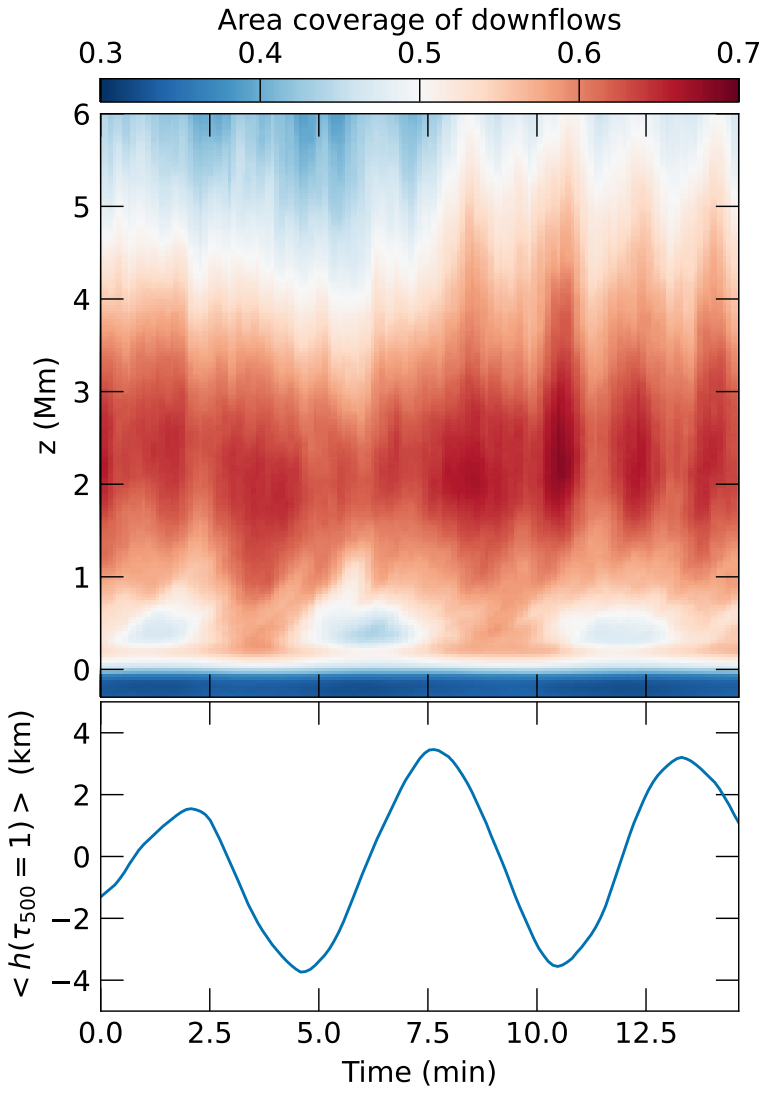

Figure 3.8: Time dependent velocity structure in the atmosphere. The top panel shows the area coverage of cells at a given height, showing downflows. That is a value of > 0.5 means there are more gridpoints at a given height with downflows than there are gridpoints with upflows. We note that this not mean that there is more gas flowing down than flowing up at that height. The bottom panel shows the time-dependent average height of the $\tau_{500} = 1$ surface.

difference between the 1.5D RT and 3D RT spatially averaged spectra was much smaller (approximately 12% for k_{2r}). In the 1.5D RT MURaM-ChE computation, the k_2 intensities are most strongly overestimated above the network fields. The formation heights of k_2 are relatively low (< 1.5 Mm), see for example Fig. 3.4 (d) and (f), such that higher densities lead to a stronger coupling between the radiation field to the local temperature and, thus higher emergent intensities. In the plane-parallel RT approximation, the horizontal gradients in density and temperature that connect the network-dominated region with the quieter part of the simulation are neglected, which leads to the overestimation.

The distribution of brightness temperature of the k_2 peaks in the 3D RT computation compares much better to the observed distribution than the 1.5D RT case (see Fig. 3.3a). The strength of the averaged profile is also closer to the observations, although it is now (3D RT) slighly underestimated (however, the absolute strength of the profile does depend on the exact amount of magnetic flux in the simulation and the observation, see Pub I). The peak separation is roughly similar to the 1.5D RT computation. Although it is slightly larger in 3D RT on average, it is still somewhat too small compared with the observations. Finally, the peak intensity ratio is even higher in 3D, making it a worse match to the observations.

Thus, the too-high peak intensity ratio in the 3D simulations could be due to either a too-high k_{2v} or a too-low k_{2r} intensity. As we found in Sect. 3.3.2.1, the k_{2r} peak forms higher in the atmosphere than k_{2v}. A too-low k_{2r} intensity could be due to multiple reasons. For example, a higher gas density at the k_{2r} formation height might increase the intensity through a stronger coupling to the local temperature. As we found in Sect. 3.3.2.1 and Fig. 3.4 (m) and (o), the density at the formation height of k_{2v} can be up to two orders of magnitude higher than at the formation height of k_{2r}.

Another contribution to the peak intensity ratio occurs due to the velocity structure in the atmosphere. Similar to the findings of Carlsson & Stein (1997), the k_{2v} peak is stronger than k_{2r} if the local atmosphere above the formation heights of the peaks is moving on average downwards, leading to a positive peak intensity ratio (and vice versa). Such a correlation was found by Leenaarts et al. (2013b) for the Mg II h&k lines in the public Bifrost snapshot. The correlation in the MURaM-ChE simulation shows, however, more scatter, which might be a result of the more dynamic atmosphere, that is, there exists much more variation in vertical velocity along the line of sight. While we showed here only the results of one synthesized snapshot, it is not immediately clear whether the spectral line properties, such as peak asymmetry, are time-dependent in the simulation. In Pub I, we estimated the spatially averaged spectrum from a lower spatial but higher time resolution computation by synthesizing eight slits in the simulation. There, we found not much variation in the spatially averaged line width, peak intensity, and peak intensity ratio over time.

In addition to this, we checked here whether oscillations in the simulation box affect the flow structure in the chromosphere. In Fig. 3.8, we show the average height of the $\tau_{500} = 1$ surface (lower panel) and the height-dependent area coverage of downflows, that is, the fraction of cells at a given z-height that show negative vertical velocities. We note that this says nothing about the magnitude of the velocity (or the density of the gas), so the red shading in the upper panel of Fig. 3.8 does not mean that gas is on average flowing down at a given height and time. We find the average $\tau_{500} = 1$ height changes periodically within ≈ 6 min with an amplitude of ≈ 3–4 km. The oscillations seem to correlate with the average area coverage of downflows in the lower chromosphere ($z < 1$ Mm). Higher up in the chromosphere at 1 Mm $\leq z \leq$ 3 Mm, approximately the height where the k_2 peaks form, the atmosphere shows on average a higher area coverage of downflows independent of time. Therefore, we expect a positive peak asymmetry ratio in the spatially averaged

spectrum at almost any snapshot in the simulation.

We found that correlations between spectral line properties and the atmosphere exist similarly to the findings of Leenaarts et al. (2013b) and Pereira et al. (2013). We could confirm that a tight correlation between the vertical velocity at the formation height of k_3 and the Doppler shift of this spectral feature exists. In addition, we found that the Doppler shifts k_{2v} (k_{2r}) correlate preferrentially with upflows (downflows). This means the k_{2v} and k_{2r} peaks of the same ray may probe significantly different layers of the atmosphere. In particular, we found k_{2v} traces lower-lying regions of higher density, probably due to shock compression. Whereas k_{2r} forms higher up at lower densities and on average at larger velocities.

The k_2 peak intensity as a temperature diagnostic is only partly valid in the MURaM-ChE simulation. We found, in general agreement with Leenaarts et al. (2013b), that for k_{2v} peak brightness temperatures > 5.25 kK, there seems to be a good correlation. The Pearson coefficient is, however, relatively low (0.12). In the case of k_{2r}, this correlation is weaker with a Pearson correlation coefficient of 0.06, which can be understood by our findings that k_{2r} forms higher up in the chromosphere, where NLTE effects become more important.

As a general result, we find the MURaM-ChE model is able to produce a close match to the observed line width in 1.5D RT and 3D RT at a relatively moderate resolution of 23.46 km (horizontal) and 20 km (vertical). Whether higher resolution will improve the match with the observation needs to be shown in future.

3.5. Conclusion

We performed 3D RT computations with the Multi3D code in an enhanced network simulation that was computed with the MURaM-ChE code. We confirmed that the effects of horizontal RT must be taken into account to accurately model the Mg II h&k lines. The difference between 1.5D RT and 3D RT was even more pronounced than in previous studies with the public Bifrost snapshot. In addition, we confirmed the diagnostic potential of the Mg II k line to constrain the velocity structure of observations. We found that k_{2v} and k_{2r} trace different features in the chromosphere, which might help to better interpret observed spectra. While differences still exist between the 3D RT computations of the Mg II h&k lines and the observation, our results demonstrate progress in numerical modeling of the chromosphere.

3.6. Acknowledgements

This work was supported by the International Max Planck Research School (IMPRS) for Solar System Science at the University of Göttingen. This work received funding from the European Research Council (ERC) under the European Union's Horizon 2020 research and innovation program (grant agreement No. 101097844). We highly appreciate the computing resources provided by the HPC systems Raven, Cobra, and Viper at the Max Planck Computing and Data Facility. This research has received financial support from the European Union's Horizon 2020 research and innovation program under grant agreement No. 824135 (SOLARNET).

4. Ca II λ854.2 nm in an enhanced network simulation

This chapter is the manuscript for a paper to be submitted to Astronomy & Astrophysics by P. Ondratschek, D. Przybylski, H.N. Smitha, R. Cameron, and S. K. Solanki. Contributions to the paper: I performed the RT computations, analyzed the data, and wrote the first draft of the manuscript; all authors contributed to the ideas behind the study and the manuscript.

Abstract. The Ca II λ854.2 nm line is widely used to study the chromosphere of the Sun. In the quiet Sun the line profile shows a red asymmetry. Numerical models typically fail to reproduce the average line width and asymmetry.

We aim to understand the formation of the Ca II λ854.2 nm line in a model of the solar chromosphere. Our study builds on forward modeling of the Ca II λ854.2 nm line in a series of MURaM-ChE simulation snapshots representing an enhanced network region. We solve the radiative transfer problem three times, once considering only the most abundant isotope of calcium in the atmosphere, once taking six calcium isotopes into account, and finally using a single "composite" atom model, which mimics the presence of all six isotopes. All three computations are compared with observations and with each other.

We find the forward modeled average spectra to be in good agreement with the Hamburg FTS atlas observations of the quiet Sun. In order to match the observed line width, the simulated atmosphere must be sufficiently dynamic, and the isotope splitting effect must be taken into account. The composite atom model is a good approximation to the full isotope computation but shows some differences in the line core and asymmetry.

We show that forward modeling of the Ca II λ854.2 nm line from an rMHD simulation can match the observed line shape in the line core. Our results highlight that it is important to include the effect of isotopes of calcium in modeling the line.

4.1. Introduction

The chromosphere is a component of the solar atmosphere that connects the photosphere to the overlying hot corona. The chromosphere is complex and poorly understood (see e.g., Rutten 2010, Carlsson et al. 2019). Observations of strong spectral lines that form in the chromosphere are the key to inferring thermodynamic quantities such as velocity and temperature, as well as the magnetic field. Interpreting the observations, however, requires a detailed understanding of line formation. The NE and NLTE conditions in the chromosphere are reflected in the line formation. Among the available chromospheric diagnostics, the Ca II infrared triplet lines have advantageous properties. Their location in the infrared makes them observable from the ground. They are not subject to scattering as much as other chromospheric lines such as Ca II H&K and Hα (Uitenbroek 1989) and to NE effects (Wedemeyer-Böhm & Carlsson 2011), which makes them easier to model and interpret. In addition, the Ca II infrared triplet lines, in particular Ca II λ854.2 nm, are good candidates for magnetic field inference in the chromosphere through inversions (e.g., de la Cruz Rodríguez et al. 2012, Quintero Noda et al. 2016, Štěpán & Trujillo Bueno 2016, de la Cruz Rodríguez & van Noort 2017).

Observations of the QS, for example with the Hamburg FTS atlas (Neckel & Labs 1984), indicate a red-asymmetry in the core of the Ca II λ854.2 nm line (Uitenbroek 2006), which is in contrast to photospheric lines that show a blue-asymmetry (see e.g., Asplund et al. 2000, Gray 2005). In the photosphere, a different area coverage, line strength, and continuum of upflows in the granules and downflows in the intergranular lanes lead to the observed blue asymmetry. Line bisectors are a common tool for indicating the asymmetry of a spectral line. The line core is sensitive to velocities higher in the atmosphere than the continuum atmosphere. In the case of the Ca II λ854.2 nm line, the bisector has the shape of a mirrored letter "C" and is, therefore, often called an "inverse C-shape bisector". This is in contrast to other chromospheric lines such as Hα which rather shows a C-shaped bisector (Chae et al. 2013).

Uitenbroek (2006) suggested that the inverse C-shape is a result of acoustic waves that steepen into shocks at chromospheric heights, similar to the analysis of Ca II K2V bright grains (Carlsson & Stein 1997). The wave propagation results in an asymmetry in the time the plasma spends in up- and downflows. By using three-dimensional convective simulations from Asplund et al. (2000), Uitenbroek (2006) found a red asymmetry in the spatially averaged Ca II λ854.2 nm profile, but of only roughly one fifth of the observed amplitude. Numerical models of the solar chromosphere in combination with three-dimensional RT computations failed to reproduce the observed asymmetry (e.g., Leenaarts et al. 2009).

Leenaarts et al. (2014) included all isotopes of calcium that exist stably in the solar chromosphere in the RT calculation. By solving the RT problem simultaneously for six isotopes of calcium, the authors found significant differences compared to the computations where only the most abundant isotope was used. For their analysis, the authors used the FAL C model (Fontenla et al. 1993), a time series from a RADYN simulation (Carlsson & Stein 1992), and a model computed with the Bifrost code (Gudiksen et al. 2011). The synthesized Ca II λ854.2 nm profiles from all three model atmospheres resulted in a red asymmetry in the line core, that is an inverse C-shaped bisector. While there has been progress in explaining the observed Ca II λ854.2 nm line, the forward modeled spectra still show discrepancies. Even if the spectra show a red asymmetry, the exact shape does not match the observations, and the bisector amplitude is too low. In addition, typically, the line width of forward modeled spectra is, on average, too small (Jurčák et al. 2018, Hansteen et al. 2023). The mismatch of the line width is assumed to be due to a too-low

magnitude of dynamical motions or resolution (see e.g., Carlsson et al. 2016).

In recent work, Ondratschek et al. (2024, hereafter Pub I) showed that new models of the chromosphere are able to match the line properties of the Mg II h&k lines relatively closely. The authors find that high maximum velocity differences in the chromosphere may explain the observed line width.

In this work, we study the formation of the Ca II λ854.2 nm line in the same model of the chromosphere simulated with the recently developed chromospheric extension of MURaM (Przybylski et al. 2022, herafter MURaM-ChE). We aim to understand whether the velocity structure of the chromosphere alone can lead to the observed red asymmetry and line width, or if all calcium isotopes must be included in the solution of the RT problem. The model resembles an enhanced network region similar to the setup of the public Bifrost snapshot (Carlsson et al. 2016).

This paper is structured as follows. In Sect. 4.2 we present the atmosphere model and RT calculations. In Sect. 4.3 we present our results. In Sect. 4.4 a summary and conclusions are given.

4.2. Model atmosphere and forward modeling

We model the Ca II λ854.2 nm spectral line in an atmosphere calculated with MURaM-ChE which is an rMHD code. The MURaM code originally included the physics required to simulate near-surface convection (Vögler et al. 2005) but was limited to a LTE approximation of the radiative and atomic physics. Rempel (2017) extended the code to include optically thin losses and point-implicit heat conduction to model the corona.

Recently, Przybylski et al. (2022) developed the chromospheric extension, which includes an NE treatment of hydrogen in and above the photosphere. The convection zone is modeled by a non-ideal equation of state (EoS) generated with the free-EoS package (Irwin 2012). The EoS was joined to include the NE treatment of hydrogen following the prescriptions in Sollum (1999), Leenaarts & Wedemeyer-Böhm (2006), and Leenaarts et al. (2007). In the EoS, all non-hydrogen elements are treated in LTE. The code includes chromospheric line losses and optically thin losses in the corona, as described in Carlsson & Leenaarts (2012). In addition, the code includes 3D extreme ultra violet (EUV) backheating of the chromosphere similar to Carlsson & Leenaarts (2012). Radiative losses in the photosphere and low-chromosphere are calculated using a four-band multigroup short-characteristics RT scheme (Nordlund 1982, Vögler et al. 2004), which was extended to include scattering effects as in Skartlien (2000) and Hayek et al. (2010). The solar abundances are taken from Asplund et al. (2009). The formation and dissociation of H_2 molecules are treated in NE, while H_2^+ and H^- are treated in chemical equilibrium. A slope-limited diffusion scheme is included as described in Rempel (2014, 2017).

The simulation setup resembles an enhanced network region, similar to the public Bifrost snapshot, and is the same as the one in Ondratschek et al. (2024). The simulation domain is 24 Mm × 24 Mm × 24 Mm with a resolution of ≈ 24 km horizontally and 20 km vertically. The convection zone extends roughly 7 Mm below the average $\tau_{500} = 1$ surface and the atmosphere covers ≈ 17 Mm in height. We use the convention that positive vertical velocities correspond to upflows in the atmosphere.

We use the RH1.5D code (Uitenbroek 2001, Pereira & Uitenbroek 2015) to synthesize the Ca II λ854.2 nm spectral line. In this code, each vertical column in the simulated atmosphere is treated independently as a plane-parallel atmosphere. This is also called the 1.5D RT approach.

We perform three sets of spectral synthesis. Firstly, following Leenaarts et al. (2014) we treat the six most abundant isotopes of calcium, ^{40}Ca,^{42}Ca,^{43}Ca,^{44}Ca,^{46}Ca,^{48}Ca as separate

atoms that are all treated in NLTE in the RT computation, hereafter isotope model (IM). For the RT computations five-level-plus-continuum model atoms were constructed similar to Leenaarts et al. (2014) based on the experimental data from Nörtershäuser et al. (1998) and Mårtensson-Pendrill et al. (1992).

Secondly, we used a composite model (CM). This is an approximation to the first computation with the advantage that only one atom needs to be computed in NLTE to solve the RTE. The effect of multiple isotopes is mimicked by modifying the absorption coefficient of the model atom. This is achieved by summing up Voigt profiles centered at the rest wavelengths of the corresponding isotopes. The sum is weighted by the relative abundance of the isotopes (for more details see App. 4.7.3).

Finally, we used a five-level-plus-continuum atom model where it is assumed that the only present calcium isotope in the atmosphere is ^{40}Ca, hereafter single isotope model (SIM). By doing so, we can test the effects of multiple isotopes on the line width and asymmetry by comparing it to the computation where only the most abundant isotope was considered.

The computations were conducted in the approximation of CRD, which is sufficient for the Ca II λ854.2 nm spectral line (Uitenbroek 1989). For the IM and SIM, we computed the full Stokes vector. The Stokes profiles are computed in the "field free" approximation (Rees 1969). We use the Bezier3 source-function interpolation (de la Cruz Rodríguez & Piskunov 2013). In the present version of RH1.5D, the full Stokes vector cannot be calculated for composite models. We compared the resulting average intensity spectra of IM with and without taking magnetic fields into account (not shown) and could not find a significant difference. This means that magnetic broadening effects on the spatially averaged profiles can be neglected for our analysis.

4.3. Results

In this section, we present the results of our RT computations. First, we describe the intensity image at the line core, together with temperature, the vertical component of the velocity, and the vertical component of the magnetic field at the corresponding formation height. We then show the spatially averaged spectra with corresponding line bisectors based on the three sets of RT calculations. Following this, we analyze how the average spectrum and asymmetry depend on the magnetic field and vertical velocity in the atmosphere. Finally, we present Stokes V profiles for the IM and SIM computations.

4.3.1 Atmospheric properties at the formation height of the line core

The Ca II λ854.2 nm line core forms approximately between 0.5 Mm and 2.5 Mm. Within these heights, the individual profiles form under a wide range of physical conditions. We therefore present in Fig. 4.1 an overview of the line-core intensity, and formation height at the wavelength position of the minimum intensity. We determine the formation height from the height where the optical depth at the wavelength of the minimum of the intensity profile reaches unity, that is $\tau_{\rm min} = 1$. We additionally show temperature, vertical velocity, and vertical magnetic field at the formation height of the minimum intensity.

The intensity map of the line-core minimum (panel a) shows web-like structures throughout the whole simulation domain, except above the strong network fields, where larger bright structures are visible. The web-like structure is a result of shock waves in the lower atmosphere that expand horizontally and interfere with each other. By compressional (adiabatic) heating, the temperature (panel d) is locally increased, leading to the visible pattern. The formation height (panel b) reveals the corrugated surface over which the

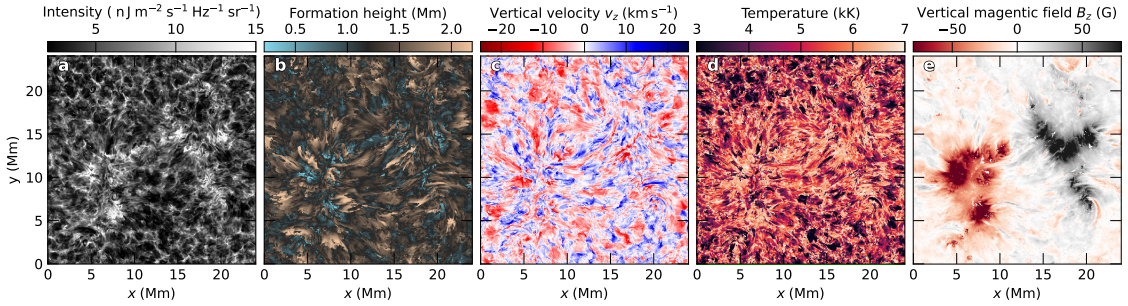

Figure 4.1: Intensity and atmospheric properties at the formation height of the line core. Panel (a) shows the intensity at the intensity minimum of Ca II λ854.2 nm, panel (b) the formation height, panel (c) the vertical velocity, (d) the temperature, and (e) the vertical component of the magnetic field at the formation height of the intensity minimum. The intensity minimum and the corresponding formation height are individually determined for each column in the atmosphere. The color scale limits are clipped to increase the contrast of the images (see text). The intensity (panel a), as well as the formation heights that were used to create panels (b,c, and d), originate from the RT computation, including isotope splitting for `muram_en_518000_503s`.

Ca II λ854.2 nm line core forms in the MURaM-ChE model. In the horizontal center of the simulation domain, the formation height structures indicate loop-like structures with sharp fine structures. The fibrilar structures are not visible in the intensity image (panel a), presumably because of missing horizontal RT. A similar effect was found for the Hα line (Leenaarts et al. 2012a) and the Mg II h&k lines (Sukhorukov & Leenaarts 2017) in the Bifrost public snapshot but also in the MURaM-ChE simulation for Mg II h&k in Chapt. 3 (in this thesis).

The vertical velocity (panel c) indicates where the line core forms in upflows (blue) or downflows (red). Qualitatively, it can be seen that structures associated with upflows are more concentrated than downflows. The area coverage of rays, where the line core forms in a downflow, is 57% vs. 43% in an upflow. The average upflow velocities are 3.42 km s^{-1} vs. -3.84 km s^{-1} in downflows. Both upflows and downflows reach maximum values of $\approx$ 20 km s^{-1} magnitude. The higher magnitude of the downflow velocities results from lower densities (see also Uitenbroek 2006), which also agree with the larger area (and volume) coverage of downflows in the chromosphere.

The temperature map (panel d) underlines the correlation between the line core intensity and shock patterns in the quiet regions at roughly $0 \leq y/\,\mathrm{Mm} \leq 5$ and $17 \leq y/\,\mathrm{Mm} \leq 24$. Above the strong network fields at roughly $5 \leq y/\,\mathrm{Mm} \leq 17$, the temperature is higher and is often associated with lower formation heights (panel b).

Finally, in panel (e), we show the vertical component of the magnetic field at the formation height of the line core. The network fields expand in the chromosphere (compared with the photosphere; see Pub I, Fig. 1a), forming a canopy.

4.3.2 Spatially averaged line profiles

In the following, we present the spatially averaged Ca II λ854.2 nm spectral line profile calculated from snapshot `muram_en_518000_503s`[1], and compare it to a QS observation from the Hamburg FTS atlas (Neckel & Labs 1984). As described in Sect. 4.2 we include

[1]We use the following name convention for snapshots: muram_en_iterationnumber_time where "en" stands for enhanced network and the time is measured in sec after switching on the NE computation in the code, see also Pub I.

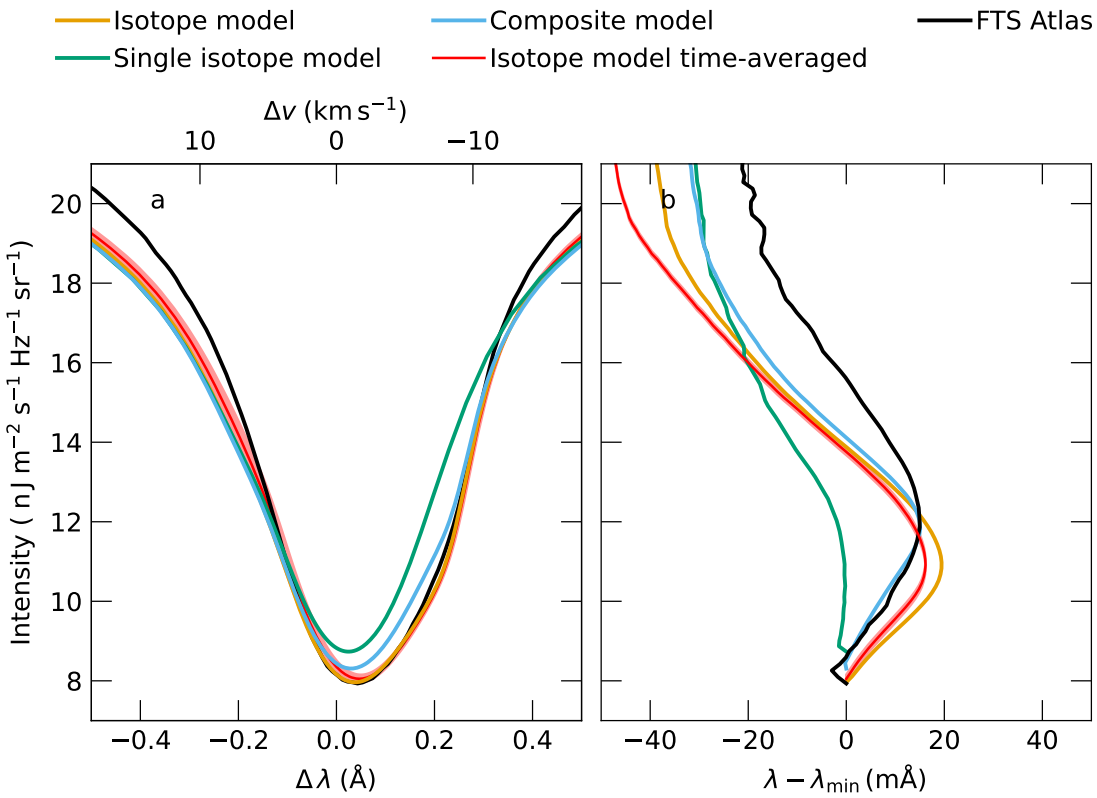

Figure 4.2: Comparison of average profiles (panel a) and corresponding bisectors (panel b) of the Ca II λ854.2 nm line. The black curves show data taken from the Hamburg FTS atlas database representing a quiet Sun region. In orange, we show the average properties of synthetic spectra computed by taking all isotopes of calcium into account. The other curves show similar data but computed without isotopic splitting (green) and using a composite model atom (blue). The red curve shows an average of the full isotope computation of four snapshots separated by 2 min together with the standard deviation in light red color. The wavelength axis of the average profiles is centered via $\lambda - \lambda_{40\mathrm{Ca,rest}}$ where $\lambda_{40\mathrm{Ca,rest}}$ is the rest wavelength of ^{40}Ca, the most abundant calcium isotope.

three treatments of calcium; including isotopes (IM), only the most abundant isotope (SIM), and the composite model atom (CM). We begin with discussing the spatially averaged line profiles in comparison to the observation. After this, we discuss the asymmetry of the line profiles.

In Fig. 4.2 (a,) we compare the spatially averaged line profiles with the Hamburg FTS atlas observations. The observations represent a QS region averaged over space and time.

The line widths (as described in Appendix 4.7.2) of the plotted profiles are 0.47 Å (Hamburg FTS atlas), 0.48 Å (IM), 0.49 Å (CM), and 0.46 Å (SIM). Thus, the line width of the computations (IM and CM) are close to the observed profile, and even 2 % (IM) and 4 % (CM) larger. The computation with only the most abundant isotope (SIM) results in a 2% smaller line width compared to the IM computation. Since the observation is also a time average, we computed a time average of the line profile over four snapshots that are additionally separated by ≈ 2 min of simulation time. These snapshots were synthesized with the IM computation. We find a similar total line width of 0.48 Å and hence no significant difference between the time-averaged spectrum (red color) and that from a single snapshot (orange color). We note however, that more snapshots are needed with a higher time resolution for a better comparison.

We calculated the line width for the IM computation for single profiles and found an average value of 0.37 Å, which is approximately 23 % lower than what we found for the line width of the spatially averaged profile (0.48 Å, IM). We checked to what extent the line width of the spatially averaged line profile is due to Doppler shifts of single profiles. We therefore calculated, similar to Leenaarts et al. (2009), the standard deviation of the Doppler shift of the line profile minima $\sigma_{\Delta v,\mathrm{min}}$ from all spectra. We obtained a value of $\sigma_{\Delta v,\mathrm{min}} = 4.56\,\mathrm{km\,s^{-1}}$, which might explain the larger line width of the spatially averaged spectrum[2]. Also, this value is approximately a factor of four times higher than what Leenaarts et al. (2009) found in their forward modeled spectra, which was $1.1\,\mathrm{km\,s^{-1}}$, and even higher than the value those authors obtained from their observations, which was approximately $2.2\ \mathrm{km\,s^{-1}}$. This suggests that in the MURaM-ChE model, the line width of the spatially averaged line profile partly results from overlapping line profiles of slightly smaller line width that are Doppler-shifted by the dynamic velocities in the simulated chromosphere.

While the line width of the CM computation is larger than in the IM computation, the line profile of the CM computation is slightly narrower close to the minimum intensity. Such differences between the two computations might occur because of the assumption of constant ratios of population levels in the construction of the CM model. However, this assumption partly breaks down in the chromosphere (see App. 4.7.3).

The minimum intensity in the line core I_{min} of the IM computation is $I_{\mathrm{IM,min}} = 7.96\ \mathrm{n\,J\,m^{-2}\,s^{-1}\,Hz^{-1}\,sr^{-1}}$ and matches approximately the intensity of the here considered Hamburg FTS atlas observation, which is $I_{\mathrm{IM,min}} = 7.93\ \mathrm{n\,J\,m^{-2}\,s^{-1}\,Hz^{-1}\,sr^{-1}}$. The CM computation results in a slightly higher intensity of $I_{\mathrm{CM,min}} = 8.31\ \mathrm{n\,J\,m^{-2}\,s^{-1}\,Hz^{-1}\,sr^{-1}}$. The SIM computation shows the highest value, which is $I_{\mathrm{SIM,min}} = 8.73\ \mathrm{n\,J\,m^{-2}\,s^{-1}\,Hz^{-1}\,sr^{-1}}$. Therefore, when only the most abundant isotope is taken into account in the RT computation, the intensity of the profile minimum is overestimated by 10 %. We find that the intensity of the profile minimum in the IM computation forms on average 38 km lower in the atmosphere than in the SIM computation. For the formation height estimations, we compared the heights where the optical depth at the wavelength of the profile minimum reaches unity. Thus, the line core intensity in the IM computation might form in regions of slightly lower temperatures in the atmosphere, partly explaining the difference. There is also the effect of extra absorption due to additional isotopes in the IM computation.

4.3.3 Asymmetry of spatially averaged line profiles

We now study the asymmetry of the observed and computed line profiles. We compute the line bisector via

$$b(I) = \frac{1}{2}(\lambda_{\mathrm{red}}(I) + \lambda_{\mathrm{blue}}(I)) - \lambda_{\mathrm{min}}. \tag{4.1}$$

Here, I is the intensity, and λ_{min} is the wavelength position of the minimum intensity in the line profile. λ_{red} and λ_{blue} are the wavelengths on the red or blue side of the spectrum with respect to λ_{min}. By definition, the bisector is not sensitive to the width of the line. The bisector defined in Eq. (4.1) is given in terms of the wavelength relative to λ_{min} and not on the absolute wavelength scale. This allows for comparison of the shape and amplitude of different bisectors irrespective of the absolute wavelength calibration of the observation. We additionally determine for each bisector the amplitude a_{core}, which is the

[2] As a rough approximation, we assume Gaussian line shapes. Then $\sigma_{\Delta v,\mathrm{min}} = 4.56\ \mathrm{km\,s^{-1}}$ translates to a FWHM of 0.32 Å and thus a convolution leads to $\sqrt{\left(0.32\,\text{Å}\right)^2 + \left(0.37\,\text{Å}\right)^2} = 0.49$ Å.

distance in wavelength between $\lambda_{\rm min}$ and the red-most excursion. We call the intensity of the line profile where the maximum red excursion is reached $I_{\rm bs}$. The amplitude $a_{\rm wing}$ is the distance between the red-most excursion and the bisector at $I_{\rm c}/0.5$. For an overview of these quantities see App. 4.7.

In Fig. 4.2 (b), the line bisectors of the spatially averaged profiles shown in panel (a) are presented. The Hamburg FTS atlas line profile shows the typical "inverse-C shaped" line bisector with an amplitude of $a_{\rm core} = 14.98\,\mathrm{m\,Å}$ at an intensity of $I_{\rm bs} = 11.86\,\mathrm{n\,J\,m^{-2}\,s^{-1}\,Hz^{-1}\,sr^{-1}}$, the corresponding line wing amplitude of the bisector is $a_{\rm wing} = 34.47\,\mathrm{m\,Å}$. The line profiles computed with IM or CM show amplitudes of $a_{\rm core} = 19.44\,\mathrm{m\,Å}$ (IM) and $a_{\rm core} = 15.07\,\mathrm{m\,Å}$ (CM) at intensities of $I_{\rm bs} = 10.98$ (IM) and $I_{\rm bs} = 11.81$ (CM). Thus, in this particular snapshot, the amplitude and intensity of the CM computation match the observed bisector better than the full isotope computation (IM). We note however, as mentioned in Sect. 4.3.2, the minimum intensity of the line profile in the CM computation is higher than in the IM computation which explains the shift of the bisector intensity. The wing amplitudes of the IM and CM computations are $a_{\rm wing} = 56.52\,\mathrm{m\,Å}$ (IM) and $a_{\rm wing} = 45.54\,\mathrm{m\,Å}$ (CM) which are both larger than in the observation. By taking only the most abundant isotope of calcium into account, the bisector of the SIM computation does not show a visible red asymmetry, and hence no clear "inverse C-shape". The bisector from the time-averaged IM computations results in an $a_{\rm core} = 16.16\,\mathrm{m\,Å}$, which is closer to the observed value and indicates that the amplitude is time-dependent. The wing amplitude of the time-averaged spectra is the largest with a value of $a_{\rm wing} = 61.19\,\mathrm{m\,Å}$, which shows a time dependence also in the wings of the lines.

4.3.4 Dependence on atmospheric conditions

In Sects. 4.3.2 and 4.3.3 we discussed the shape and asymmetry of the computed line profiles in comparison with the observation. There are two mechanisms that contribute to the width and asymmetry of the line, namely the atmospheric structure and the presence of multiple calcium isotopes. In this section, we study how the atmospheric structure affects the line profiles. We study the shape and asymmetry of the Ca II λ854.2 nm line by preselecting columns based on their atmospheric property. We distinguish between columns through their velocity structure and magnetic field strength along the LOS. For each vertical column in the atmosphere, we computed the average vertical unsigned magnetic field $|B_z|_{\rm avg}$ and average vertical velocity between the formation height of the wing intensity and the line core, such that:

$$v_{\rm avg} = \frac{\int_{z1}^{z2} v_z(z')\,\mathrm{d}z'}{z_2 - z_1} \tag{4.2}$$

where

$$z_1 = \frac{z(\tau_{\rm wing,v} = 1) + z(\tau_{\rm wing,r} = 1)}{2} \tag{4.3}$$

and

$$z_2 = \max_{\{\lambda \mid ||\lambda - \lambda_0|| = 1\text{Å}\}} z(\tau_\lambda = 1). \tag{4.4}$$

Here v_z is the vertical velocity in the atmosphere, z_1 is the average formation height of the wing intensity at ±1Å from the rest wavelength λ_0 of ^{40}Ca and z_2 is the maximum formation height in the wavelength window ±1Å around the rest wavelength. $|B_z|_{\rm avg}$ is computed analogously to the unsigned vertical velocity.

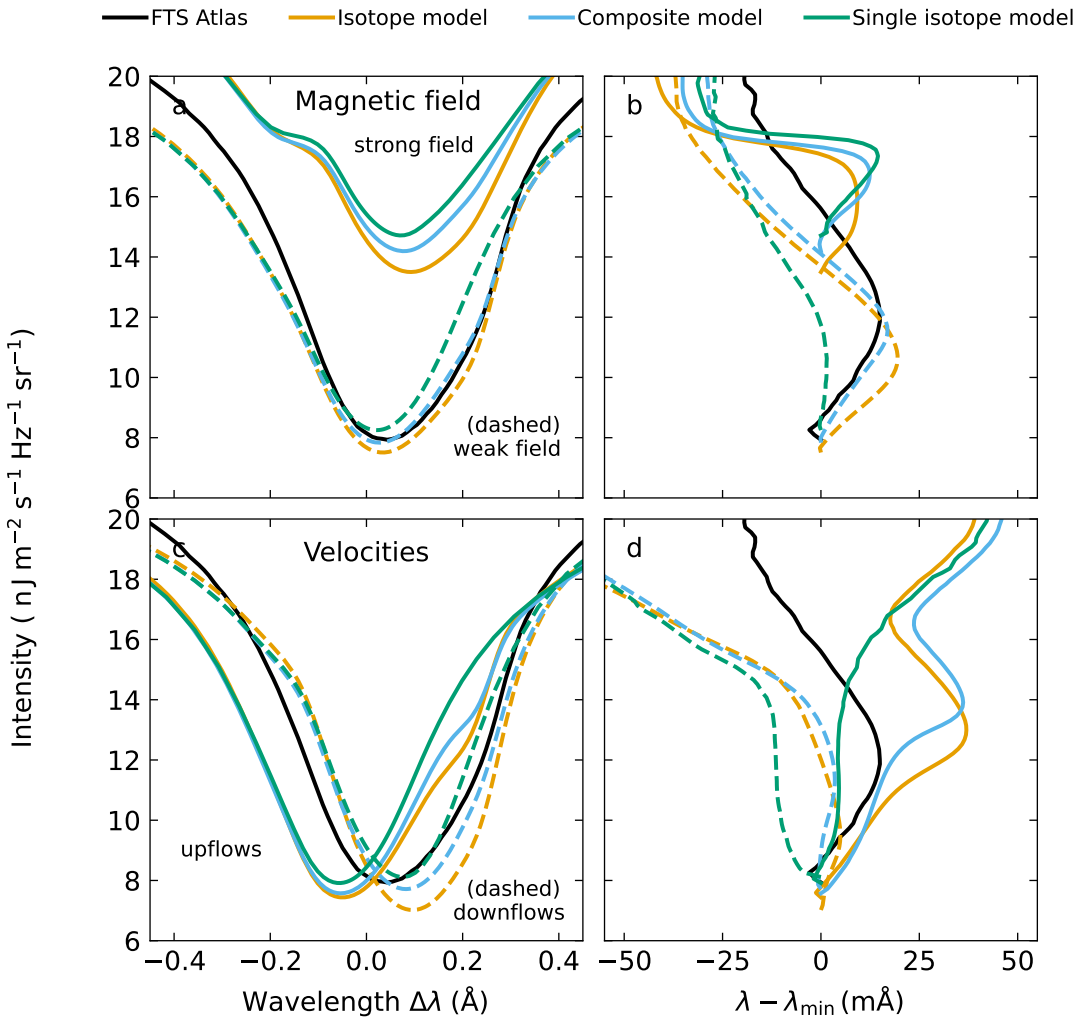

Figure 4.3: Average profiles and bisectors computed according to atmospheric properties. Similar to Fig. 4.2 we show data from Hamburg FTS atlas (black), synthetic spectra taking all isotopes into account (orange), only the most abundant isotope (green) and a composite model atom (blue). The top row (panels a and b) shows results computed from a selection of strong (solid lines) and weak (dashed lines) magnetic fields. The bottom row (panels c and d) shows results with a selection for only upflows (solid lines) or downflows (dashed lines). We note that the bisectors are shifted to the corresponding wavelength of the minimum intensity (see Eq. 4.1)

.

We categorize columns with $|B_z|_{\rm avg} < 60\,{\rm G}$ as having weak LOS magnetic field and $|B_z|_{\rm avg} > 60\,{\rm G}$ as having strong LOS magnetic field. This separation roughly distinguishes between columns outside and inside the large-scale network field (see Fig. 4.1e). Similarly, we distinguish between columns having $v_{z,\rm avg} > 0$ as upflows and $v_{z,\rm avg} < 0$ as downflows. The different categorizations between vertical motions and magnetic fields are not meant to form stochastically independent sets.

In Figure 4.3 we show how the average profiles and bisector shapes vary depending on magnetic field and vertical velocities. Panels (a) and (b) show the difference between spectra that are averaged over regions of strong and weak magnetic fields. The profiles averaged over columns of strong magnetic field (SFAs) are plotted with solid lines and the profiles averaged over columns of weak magnetic field (WFAs) with dashed lines.

As mentioned in Sect. 4.2 it is not possible to compute the full Stokes vector for the composite model atom with the current version of RH1.5D. The comparison we show here is, therefore, more a result of the impact of magnetic fields on the atmosphere rather than of "direct" RT effects, such as magnetic broadening. In Fig. 4.3 it can be seen that the WFAs all appear similar to their corresponding profiles in Fig. 4.2. This is expected because $\approx$ 93% of all profiles are formed in the weak field regions. The SFAs which are averaged over $\approx$ 7% of all spectra have higher intensities across the whole shown wavelength range. The continuum of the line is at roughly $41\,{\rm n\,J\,m^{-2}\,s^{-1}\,Hz^{-1}\,sr^{-1}}$. In App. 4.7.1 we show the line profiles of the CM computation over a larger wavelength window. The corresponding bisectors of the profiles in Figure 4.3b (solid lines) all show an inverse "C" shape and a blueward turn close to the wing intensity.

In the bottom two panels (c) and (d) we show the resulting profiles averaged over columns showing upflows (UFAs) (solid) and profiles averaged over columns showing downflows (DFAs) (dashed), see Eq. (4.2). In this snapshot, we find 45.5% of the profiles show an upflow and 54.5% a downflow. In Figure 4.3 (c), it can be seen that UFAs, besides being blue-shifted, on average, have slightly higher intensities in the minimum. The differences in the average line profiles between the three sets of RT computations IM, CM, and SIM are negligible in the UFAs bluewards of the line core but there are significant differences redwards. The corresponding bisectors of the UFAs (panel d, solid lines) all show a red asymmetry close to the line core. Even for the SIM (green curve) a slight red asymmetry in the line core is visible. None of the bisectors from the UFAs shows a blueward turn as in the global averages.

Unsurprisingly, the DFAs are red-shifted with respect to the line center of the globally averaged profile. Similar to the UFAs, in the DFAs the different RT computations are in good agreement bluewards to the line center and differ redwards. However, in contrast to the UFAs, the difference between IM and CM is less pronounced. The corresponding bisectors (dashed lines, panel d) indicate a much lower red asymmetry. While the IM and CM show a much lower bisector amplitude, the bisector from SIM remains blueshifted at all intensities.

This study can be summarised as follows: The shapes of the average profiles and corresponding bisectors can depend strongly on the LOS velocity and the LOS magnetic field strength in the atmosphere. In strong LOS magnetic field regions, the average profile of the computation with only the most abundant isotope shows an inverse "C" shape. But in most of the profiles, the SIM computation does not result in an inverse C-shaped line bisector.

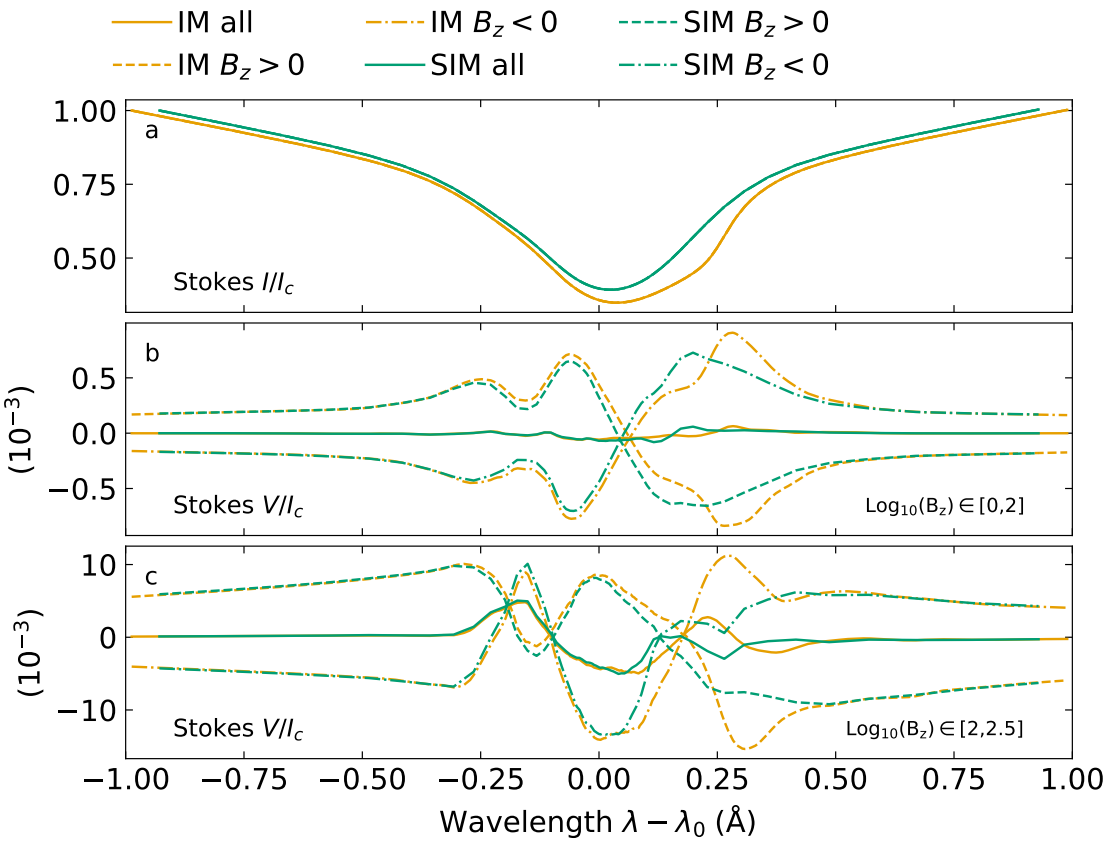

Figure 4.4: Intensity and Stokes V profiles for the computation with isotopes (IM, orange) and only the most abundant isotope (SIM, green). The Stokes V profiles are averaged over two ranges of magnetic field strengths at the formation height of the line core minimum intensity, i.e. $\log_{10}(|B_{z,\lambda_{\min}}|) \in ([0,2],[2,2.5])$, plotted in panels (b) and (c), respectively. We compare total (signed) averages (solid lines) as well as averages dependent on the sign of $B_{z,\lambda_{\min}}$ ($B_{z,\lambda_{\min}} > 0$: dashed, $B_{z,\lambda_{\min}} < 0$: dot-dashed). The wavelength axis is centered at the rest wavelength λ_0 of the most abundant isotope ^{40}Ca. We normalized the profiles to the intensity at $\pm$ 1 Å away from the minimum of the line profile.

4.3.5 Spatially averaged Stokes V profiles

In order to investigate the effect of isotopes on the polarization signature we present in Fig. 4.4 the spatially averaged Stokes V profiles (circular polarization) of IM (orange curve) and SIM (green curve). We separated the averages into two bins of logarithmic magnetic field strength, that is $\log_{10}(|B_{z,\lambda_{\min}}|) \in ([0,2],[2,2.5])$ at the formation height of the line core (cf. Figure 4.1 b). These are plotted in panels (b) and (c) of Fig. 4.4, respectively. The sign of the Stokes V signal depends on the magnetic field. Therefore, when averaging over two opposite polarities, the signal will cancel. Given that the simulation box is flux-balanced, this cancellation greatly reduces the amplitudes of the computed Stokes V profiles (solid lines). To address this, we added two additional curves to each panel each showing Stokes V for one sign of $B_{z,\mathrm{min.}}$ (dashed and dot-dashed lines). The IM and SIM curves should only be compared qualitatively as they are normalized to their corresponding Stokes I profile.

In panel (b), a clear Stokes V signal is visible in the sign-dependent averages. This bin of magnetic field strength contains $\approx 93\%$ of the rays. For $\lambda - \lambda_0 \geq 0$, there are differences between the SIM and IM computations, whereas for $\lambda - \lambda_0 \leq 0$, that is, in the blue wing of the line, the two computations are similar. Panel (c) shows the strongest Stokes V signal

having magnitudes of 1% of I_c. Again, in the blue part, differences between IM and SIM are hardly visible, whereas in the red wing, additional maxima and minima are visible in the sign-dependent averages at roughly $\Delta\lambda = 0.25$Å. In summary, the spatially averaged Stokes V profiles are different between the IM and SIM computation in the two considered bins of magnetic field strengths. The amplitudes in the red wing of the IM computation are slightly larger than in the SIM computation. The profiles in panel (b) show roughly the expected line shape, whereas the profiles in panel (c) look rather untypical, which must be due to the dynamics in the atmosphere but might be biased from the relatively low number of profiles in that vertical magnetic field bin.

4.4. Summary and discussion

In this work, we presented synthetic spectra of the Ca II λ854.2 nm line, computed from an rMHD model, which we compared to a QS observation from the Hamburg FTS atlas. Including a large-scale bipolar magnetic feature, the atmosphere model resembles an enhanced network region. We computed three different sets of synthetic spectra in 1.5D RT. We calculated the spectra once taking all abundant isotopes of calcium in the solar atmosphere into account (IM), and once where only the most abundant isotope was considered (SIM). In addition, we utilized an approximate model of isotopic splitting that combines the effects of isotopes in only one model atom (CM).

The two-dimensional image of the line-core intensity (obtained from the IM computation) shows a typical shock-expansion pattern (see also Wedemeyer et al. 2004) in the quiet part of the simulation. Above the network magnetic field, the intensity is enhanced. In the intensity image, no fibrilar structures are seen, while they are visible in the formation height of the minimum intensity. This is likely attributed to the lack of horizontal RT similar to Leenaarts et al. (2012a). The formation height of the line core shows large spatial variation with fine-structured details.

The vertical component of the velocity at the formation height of the line center shows thinner upflow structures that are surrounded by expanded downflow structures. In agreement with this, downflows show a larger area coverage than upflows. This suggests upward mass flows in thin dense channels, while the mass falls back in blobs of lower density which cover a larger volume in the atmosphere.

We then studied the spatially averaged profiles for the three sets of computations. We find a good match between the IM computation and the observation in terms of the line profile depth, width, and shape, including the line bisector. When only the most abundant isotope of calcium is considered in the synthesis, the resulting average spectrum is slightly narrower and almost symmetric. These findings confirm the results of Leenaarts et al. (2014), who suggested that isotopes must be taken into account to reproduce the observed inverse C-shape bisector. The CM calculation similarly reproduces the overall line width and asymmetry of the IM calculation. In the innermost line core, the intensity in the CM is, however, slightly higher, pointing to missing details in the composite model atom. In the construction of the composite model atom, it is assumed that the ratios of population-level densities from different isotopes are constant throughout the whole atmosphere. In App. 4.7.3 we show that this approximation breaks down already in the lower to mid chromosphere where the Ca II λ854.2 nm line forms. In addition, the simultaneous solution of the RT problem for the six isotopes of calcium leads to a wavelength-dependent total source function, which cannot be reproduced by the composite model atom. The wavelength-dependent source function also leads to the fact that the difference between the full isotope computation and the composite model atom depends on the velocity structure along the LOS.

We found that the line width of single profiles is, on average, approximately 23% smaller than the width of the spatially averaged line profile. Similar to Leenaarts et al. (2009), we measured the standard deviation of the Doppler shift of the intensity minimum of the line profile. We found a value of $\sigma_{\Delta v,\mathrm{min}} = 4.56\,\mathrm{km\,s^{-1}}$, which might explain the difference between the line widths of single profiles and the width of the spatially averaged line profile. The obtained $\sigma_{\Delta v,\mathrm{min}}$ is approximately four times higher than in Leenaarts et al. (2009). This suggests the close match of the line width in the MURaM-ChE simulation is due to the dynamic atmosphere. Leenaarts et al. (2009) compared their results with observations from a coronal hole, which showed a value of $2.2\,\mathrm{km\,s^{-1}}$. The reason for the roughly two times higher value we find in the MURaM-ChE simulation could be similar to the result of Kayshap et al. (2018) who found a larger line width of the Mg II k line in the QS compared to a coronal hole. This suggests the simulation presented here compares well to the QS but a different simulation might be needed for the comparison with coronal hole observations.

The observations from the third flight of the SUNRISE balloon-borne observatory (SUNRISE III, Korpi-Lagg et al. 2025) will provide superior seeing-free observations of the Ca II λ854.2 nm line arising from different regions on the Sun. A comparison between these observations and the computations presented here and future MURaM-ChE simulations will help to better understand the dynamics of the chromosphere.

We also considered how the shape of the bisector not only depends on whether all isotopes are included but can also be strongly influenced by atmospheric conditions. To this end, we separated the atmosphere into four sets of columns with strong or weak vertical magnetic fields and up- or downflows measured over the formation height range from the continuum to the line core. These sets are not disjoint but still show different features in the average spectra. We found that average spectra over columns where $|B_z|_{\mathrm{avg}} < 60\,\mathrm{G}$ (93% of the spectra) match the observed Hamburg FTS atlas spectra best in terms of the line shape and the amplitude of the bisector. When the average is taken over profiles from columns where $|B_z|_{\mathrm{avg}} \geq 60\,\mathrm{G}$, the line intensity is weakened, and even the SIM computation shows a (weak) "inverse C shape". The higher intensity is a result of the higher temperature in the regions dominated by a stronger magnetic field. The asymmetry must be a result of the flow structure above the magnetic features.

The separation into up- and downflows results in multiple effects. The asymmetries of the line shapes are substantially different, as measured by the line bisectors. The average profiles from columns showing downflows are much less asymmetric at low intensities, that is close to the line core. The profiles averaged over regions showing on average upflows show a red asymmetry close to the line core. For higher intensities, there is a cliff-like structure in the red wing in the case of the IM and CM computation, which is reflected in a red excursion in the bisector. This is a consequence of multiple isotopes, which lead to an asymmetric height-integrated line absorption coefficient.

We found that the impact of magnetic fields on the spatially averaged Stokes I profile in our simulation model through the RT computation, such as the Zeeman effect, is negligible. We then studied the effect of isotopic splitting on the Stokes V signal. We studied two ranges of the absolute vertical component of the magnetic field. In both cases, the averaged Stokes V signal appears to be similar between IM and SIM in the blue line wing but is different in the red wing. Therefore, the effect of isotopic splitting does not only affect the asymmetry and shape of the spatially averaged intensity profile but also the Stokes V signal.

4.5. Conclusions

We confirmed the need for isotopes to reproduce the observed average spectrum of the Ca II λ854.2 nm line. A computation taking all isotopes into account led to a good agreement with the observed Hamburg FTS atlas quiet Sun spectrum. In addition, we demonstrated that, on average, a computation with a composite model instead of a full isotopic treatment does not lead to the same result in the line core. This is a consequence of the approximations that are made when constructing the composite model. Overall, the composite model is, however, a good approximation to the line width and the asymmetry of the full isotope computation and might be a good compromise at lower computational costs. A study of Stokes V profiles showed that the effect of isotopic splitting can lead to different Stokes V profile shapes, especially in the red wing.

We conclude that a combination of the highly dynamic atmosphere obtained in the MURaM-ChE simulation used here and the inclusion of isotopic splitting effects, leads to a good match with the observed spatially averaged line profile. The line width and the asymmetry are reasonably well reproduced.

4.6. Acknowledgements

This work was supported by the International Max Planck Research School (IMPRS) for Solar System Science at the University of Göttingen. This project has received funding from the European Research Council (ERC) under the European Union's Horizon 2020 research and innovation programme (grant agreement No. 101097844 — project WINSUN). We gratefully acknowledge the computational resources provided by the Cobra and Raven supercomputer systems of the Max Planck Computing and Data Facility (MPCDF) in Garching, Germany. D.P. would like to thank A. Irwin (Free-EoS) and V. Witzke (MPS-atlas) for the fantastic open-source packages they provide.

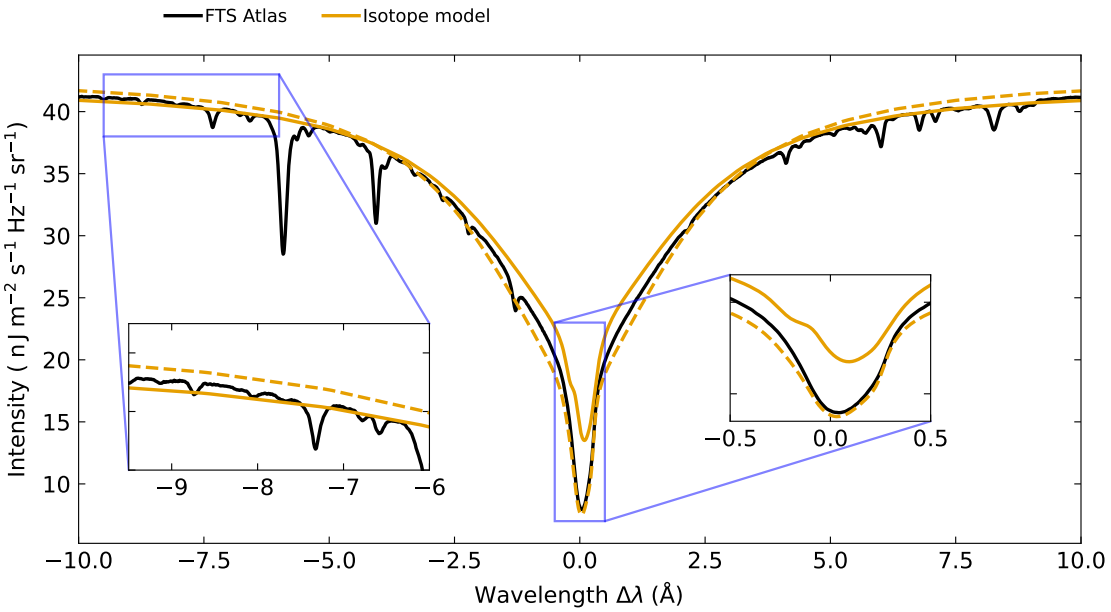

Figure 4.5: Ca II λ854.2 nm line averaged over regions of different vertical magnetic fields. The layout is similar to Fig. 4.3a but shows a larger wavelength range, which also includes the continuum. The black line shows the observed data from the Hamburg FTS atlas. The dashed orange line indicates the line profile of the IM computation averaged over regions which have $|B_z|_{\rm avg} < 60$ G and the solid orange line that is averaged over regions which have $|B_z|_{\rm avg} \geq 60$ G (see Sect. 4.3.4). For simplicity we show only the data for the IM computation. The inset panels show zooms to the continuum and the line core, the latter is similar to Fig. 4.3 (a).

4.7. Appendix

4.7.1 Ca II λ854.2 nm line with continuum

In the main text, we presented the intensity profile in the line core of the Ca II λ854.2 nm line, that is approximately ±0.5 Å around the minimum intensity. Here we present an overview of how the line profiles compare in a larger wavelength window containing the continuum. Figure 4.5 shows the intensity of the Hamburg FTS atlas observation and the averaged intensities over regions, which have $|B_z|_{\rm avg} < 60$ G (dashed lines) those averaged over regions which have $|B_z|_{\rm avg} \geq 60$ G (solid lines, see Sect. 4.3.4).

4.7.2 Determination of line width and bisector parameters

We determine the line width of the spatially averaged profile following the description in Cauzzi et al. (2009). First, we determine the wavelength position of the profile minimum $\lambda_{\rm min}$. From that wavelength position, we take the average intensity in the line wings at the positions $\lambda_{\rm wing}$ that fulfill $|\lambda - \lambda_{\rm min}| = 0.6$Å. The line width is then given by the wavelength difference of the intensity profile at half the intensity between the minimum and the wing intensity. This technique was used instead of just the FWHM to make sure that we are considering the width of the line core, which is the important part of the line for the chromosphere. Also, in this way, we avoid the influence of the prominent line wings. The measured line widths are indicated in Fig. 4.6.

We describe the bisector by parameters similar to those used in Pietarila & Livingston (2011) and Pietarila & Harvey (2013). The bisector amplitude in the line core $a_{\rm core}$ is

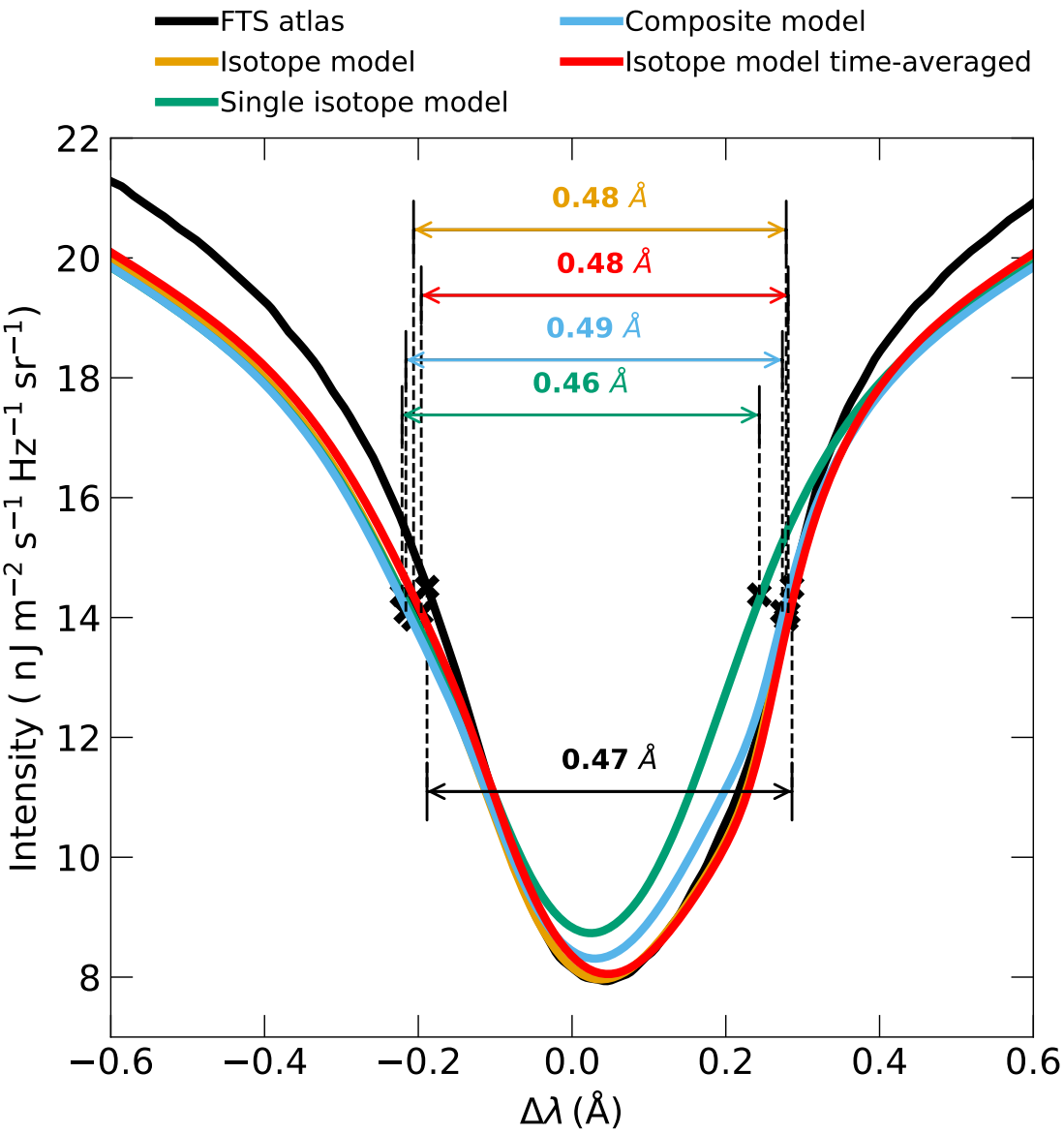

Figure 4.6: Determination of line width. The line width is measured at half the intensity between the wing intensity I_{wing} and the profile minimum intensity I_{min}. The intensity I_{wing} is taken as the average intensity at ±0.6 Å away from the line profile minimum. The obtained line widths for the different computations and the observation are indicated in the figure.

defined as the difference in wavelength between the profile minimum λ_{min} and the red-most excursion of the bisector. The intensity at the red-most excursion is named I_{bs}. The wing amplitude a_{wing} of the bisector is defined as the difference between the red-most excursion of the bisector and the bisector at an intensity of $\approx I_{\text{c}}/2$ where I_{c} is the continuum intensity at 10 Å away from the profile minimum. An overview of the measured bisector amplitudes is shown in Fig. 4.7.

4.7.3 The composite model atom

Here, we briefly describe why the fundamental assumption of the composite model in the simulated atmosphere breaks down and how this will affect the resulting spectra.

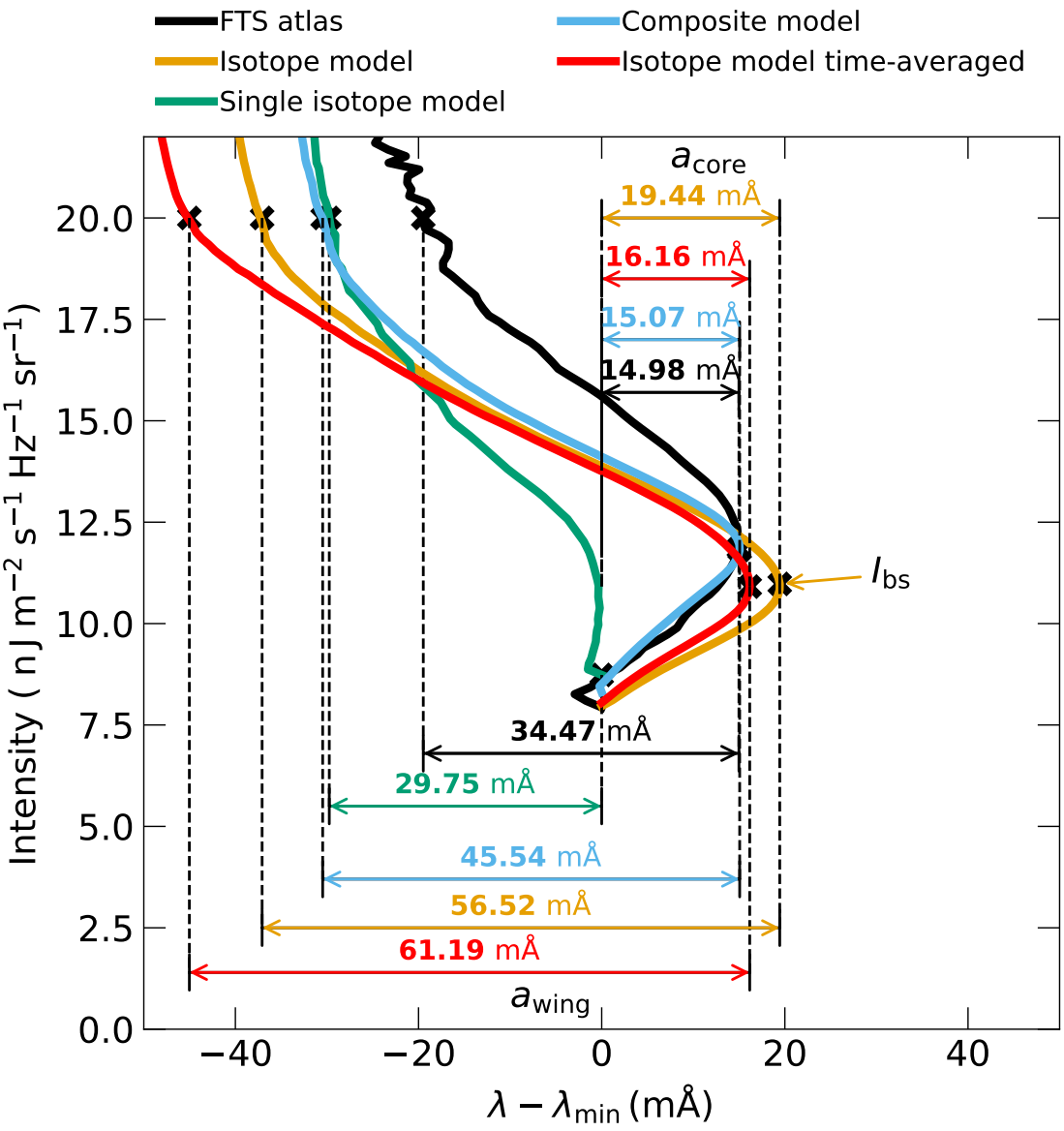

Figure 4.7: Determination of line bisector parameters. Shown are the line bisector for the spatially averaged line profiles for the observation (black), the IM computation (orange), the CM computation (blue), and the SIM computation (green). The core amplitude of the bisector a_{core} is the wavelength difference between the line profile minimum and the red-most excursion of the bisector. The wing amplitude is the wavelength difference between the red-most excursion and the bisector at approximately half the continuum intensity.

4.7.4 Population level ratios

In the composite model, the absorption coefficient is constructed by summing up Voigt profiles centered at the corresponding rest wavelengths of the single isotopes. The sum is weighted by the relative abundance of the isotope with respect to the most abundant isotope ^{40}Ca. This construction is an approximation because it is assumed that population-level ratios between different isotopes are constant (Carlsson 1986, Leenaarts et al. 2014). Leenaarts et al. (2014) discussed that this is only an approximation but can be justified by insignificant differences from the full computation. As shown in Fig. 4.2, we find differences in the average spectrum affecting the line core and the red wing.

In Fig. 4.8, we compare exemplary for the two most abundant isotopes, which are ^{40}Ca and ^{44}Ca, where the ratios of the populations in the atmosphere deviate. Panels (a) and (b) show temperature and vertical velocity through a slice of the simulation for reference. We computed the ratios of the population-level densities (here for the second level) via:

$$\delta_{40,44}(2) = \frac{n_{^{40}\mathrm{Ca,\,level=2}}}{n_{\,^{44}\mathrm{Ca,\,level=2}}} - 10^{\mathrm{A}_{^{40}\mathrm{Ca}} - \mathrm{A}_{^{44}\mathrm{Ca}}}. \tag{4.5}$$

Here n are population-level densities of the respective calcium isotopes. We subtracted the value of the population ratio as given by the relative abundance of the isotopes to highlight deviations. The level population for level 4 is computed analogously. The second and the fourth level correspond to the lower and upper levels of the Ca II λ854.2 nm transition in the atom model. The population level ratios are expected to have roughly the same ratio as the abundance ratio of the different isotopes. Panels (c) and (d) of Figure 4.8 show for the second level (panel c) and for the fourth level (panel d) where deviations from this ratio appear. In the lower atmosphere, $z \leq 0.5$ Mm $\delta_{40,44}(2)$ is roughly constant but in the higher layers, the difference increases. This can be seen similarly for the upper level of Ca II λ854.2 nm with $\delta_{40,44}(4)$ (panel d). A comparison with the vertical velocities (panel b) and temperatures (panel a) qualitatively shows that the differences become stronger where shocks in the atmosphere are present.

4.7.5 How isotopic splitting affects the emergent intensity

In the previous section, we demonstrated where in the atmosphere the assumption for the composite model breaks down. In this section, we want to briefly discuss how this affects the resulting line shapes. To understand the differences we computed the (total) source functions for four different model atmospheres and computed the spectrum assuming the presence of six isotopes (IM) or using the composite model atom (CM). The results are presented in Fig. 4.9. Each row shows a different model atmosphere. The first row (panels a–d) represents results from the standard FAL-C atmosphere (Fontenla et al. 1993). The second and third rows (panels e–h and i–l) are constructed from the standard FAL-C atmosphere but we added an up- or downflow gradient to the velocities. The fourth row (panels m–p) represents a column from the above discussed `muram_en_518000_503s` snapshot, which was randomly selected. The only requirement was to show a reasonably large difference between the IM and CM computation. We added the vertical velocity (white line) as well as the $\tau_\nu = 1$ curve (green color) to the source function panels.

We begin by comparing the source functions. One can qualitatively see that the $\tau_\nu = 1$ curve in each row is similar between the IM and CM computations. The contributions to the emergent intensity come from the same heights in the atmosphere. While the source functions in the CM case (first row, panels a, e, i, and m) are frequency independent in the line core, which is expected from the CRD approximation, the corresponding source functions of the IM computations are not. The simultaneous computation of all six

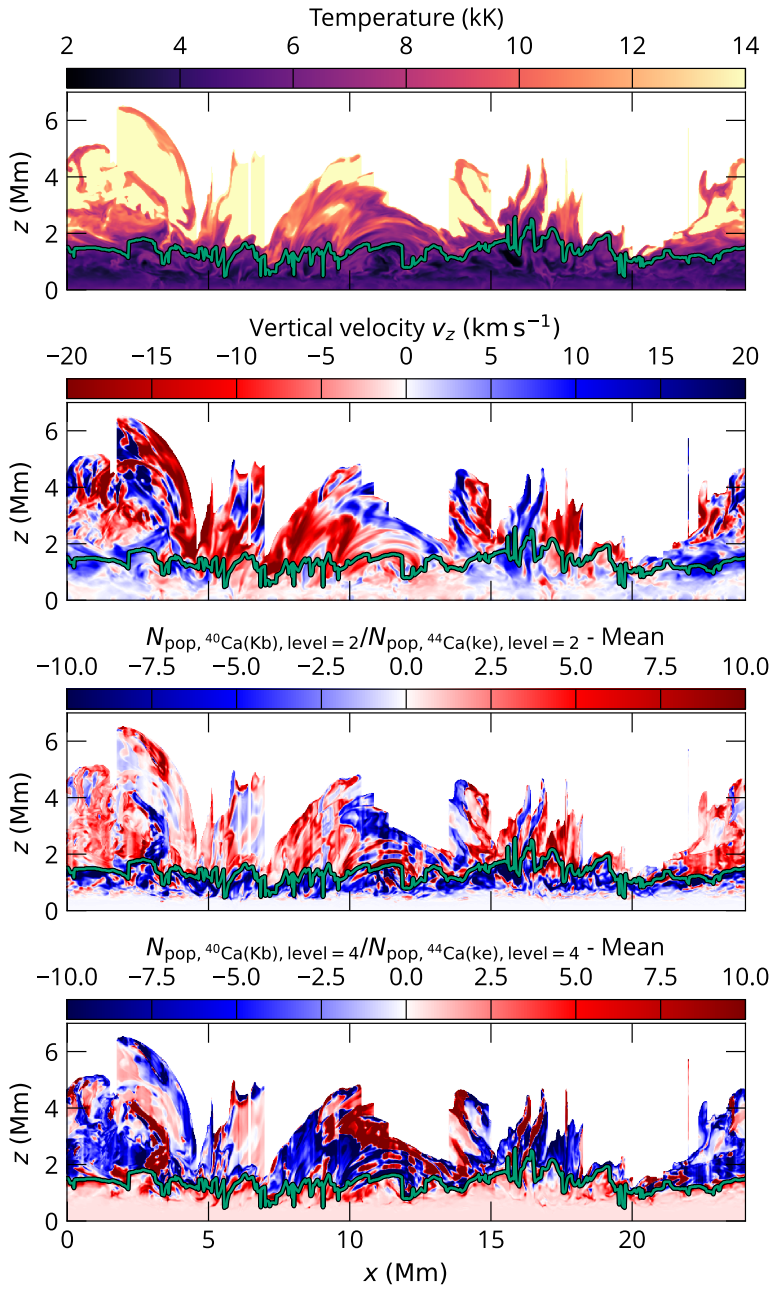

Figure 4.8: Validity of the composite atom model. The top two panels show the atmospheric temperature (panel a) and the vertical velocity (panel b). The bottom two panels show the population level ratio of the lower transition level (panel c) and the upper transition level (panel d) between ^{40}Ca and ^{44}Ca, the two most abundant Ca isotopes. We subtracted the mean to highlight differences. The green curve indicates the formation height of the intensity minimum of the Ca II λ854.2 nm line.

isotopes, therefore, affects the resulting total source function by introducing a wavelength dependence in the red part of the line. The wavelength dependence seems to be correlated with the vertical velocity. This is especially visible in the column of the MURaM-ChE snapshot (panel n). In the third column (panels c, g, k, and o), we present the difference between the source functions of the CM and the IM computation. We overplotted in arbitrary units the emergent intensity profiles. It can be seen that the position of the wavelength dependence of the IM source functions overlaps with the position in wavelength where the resulting spectra are different. In the right-most column (panels d, h, l, and p), we show the relative change in population-level ratios of the lower transition level for the different isotopes with respect to the most abundant isotope ^{40}Ca. Again, it can be seen that the largest difference between the CM and IM source functions appears where the population level ratios start to differ from their constant values in the lower atmosphere. The resulting spectra between IM and CM will be different at wavelengths where the source function at the height of formation, according to the Eddington-Barbier relation, is different. This leads to differences in the spectra in panels c, g, and o. In panel k (downflow gradient in the FAL-C atmosphere), the effect is suppressed because the velocity profile leads to an asymmetric shift of the opacity profile and, therefore, the $\tau_\nu = 1$ curve. The effective wavelength range that goes through regions of different source function values is shorter, and the difference in the resulting spectra is less pronounced. With this, we can also interpret the results from Figure 4.3c, where the difference between CM and IM computations was larger for upflows than for downflows. We conclude that the effect of isotopes leads to a wavelength-dependent source function that can not be reproduced by a single composite model atom which is treated in the CRD approximation. The effect, however, can be small in regions of the atmosphere showing on average downflows but will be large in those showing on average an upflow.

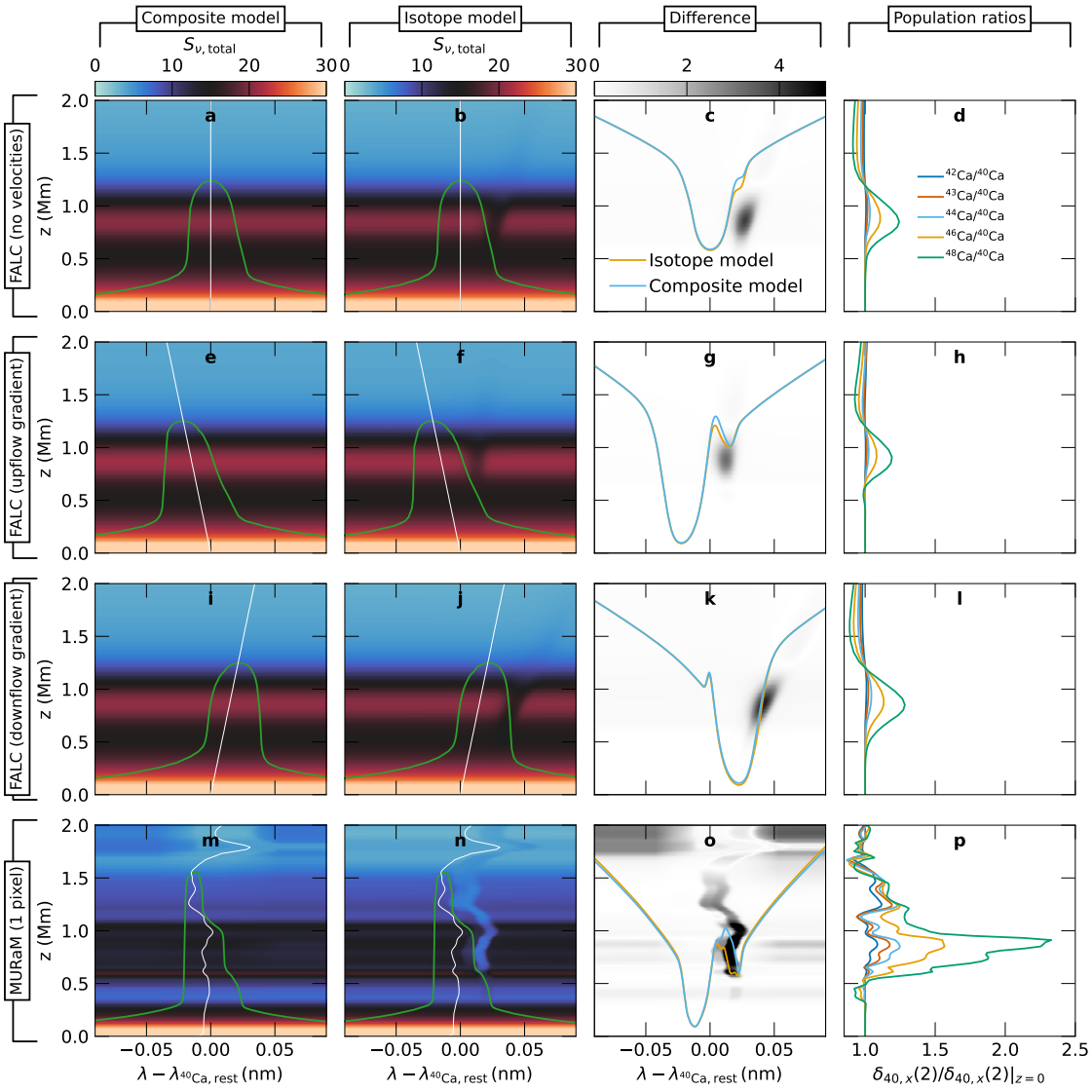

Figure 4.9: Effect of isotopes in the computation of the Ca II λ854.2 nm line. Shown are computations of the Ca II λ854.2 nm line in four model atmospheres where each row shows the results from a single atmosphere. We compare the resulting source functions when either the composite model atom is used (first column, panels a, e, i, and m) or all six isotopes of Ca II are considered simultaneously (second column, panels b, f, j, and n). In the source function panels, we additionally show the $\tau_\nu = 1$ curve and the velocity profile in the atmosphere. The wavelength axis is given in Doppler units with respect to the rest wavelength of the most abundant isotope ^{40}Ca. In the third column (panels c, g, k, and o) we present the difference of the source function from the CM and IM computation and add the emergent intensity (IM: orange curve, CM: blue curve) in arbitrary units. In the right-most column, we show the change of the population-level ratios of the lower transition level between different isotopes as a function of height.

5. Conclusions and outlook

Thanks to the major advances in numerical modeling in the last decades such models of the solar atmosphere are essential to interpret observations. The MURaM code was recently extended to include prescriptions necessary to treat the complex solar chromosphere under NLTE and NE conditions. The new version is named MURaM-ChE. A necessary step to validate a numerical model of the solar atmosphere is the comparison with observations. In this thesis, one of the first simulations computed with the new MURaM-ChE code was used. From the simulation, synthetic spectral lines were computed in a post-processing step. The synthetic spectra were then compared with observations. This work focuses on two main spectral lines forming in the chromosphere. In the first two chapters, we studied the formation of the Mg II h&k lines, which form in the upper chromosphere. These spectral lines have high diagnostic potential to infer for example the temperature and velocities in the atmosphere. In the third chapter, we studied the Ca II λ854.2 nm line, which forms in the mid-chromosphere and is a preferred spectral line to infer the magnetic field. Previous models of the solar chromosphere resulted in too-narrow line widths and too-faint intensities. With the simulation presented here, we could show that the MURaM-ChE model is able to reproduce a close match with observations. In the following, I provide an overview of the most important conclusions from this work.

In Chapt. 2, we studied the formation of the Mg II h&k lines in the MURaM-ChE model in the 1.5D RT approximation. By doing so, each vertical column in the atmosphere is assumed to be an independent plane-parallel atmosphere, which is computationally cheaper. The main conclusions were:

- The spatially averaged spectrum shows a close match with a representative QS observation including network magnetic fields. Compared with previous numerical models, the MURaM-ChE model is more dynamic and the temperatures in the chromosphere are higher, explaining the increased line width and peak intensity. However, the peak separation of the average spectrum is still slightly lower and the peak intensities are slightly higher than in the observed average spectrum.

- The peak separation distribution of the MURaM-ChE model shows a large overlap with the observed distribution. The average peak separation of 23.6 $\mathrm{km\,s^{-1}}$ (MURaM-ChE) is, however, smaller than the 33.02 $\mathrm{km\,s^{-1}}$ found for the observations from IRIS. This suggests that although the chromosphere computed by MURaM-ChE is already very dynamic, the Sun is even more dynamic. An extension of the relatively small simulation domain might lead to a more dynamic chromosphere and, thus, to better results. The effect of the resolution of the simulation box should also be tested. It cannot be ruled out that a higher-resolution grid will also produce a more dynamic chromosphere. Such an effect had been

found for Bifrost simulations (Martínez-Sykora et al. 2023, Hansteen et al. 2023), but it will have to be tested if a qualitatively similar scaling is also obtained with MURaM-ChE.

- The distribution of the k_2 peak intensities is broader than the observed distribution, extending to both higher and lower intensities. The higher peak intensity in the simulation is partly due to a higher magnetic flux density in the simulation than in the observation. The higher intensity contrast and overestimated peak intensities are also known shortcomings of the 1.5D RT treatment and thus motivated the full 3D RT computation presented in Chapt. 3.

- By synthesizing a time series of ≈ 10 min at reduced spatial resolution, we found that the average spectrum does not change significantly over time despite the presence of oscillations in the chromosphere.

- The upper chromosphere just below the transition region in the MURaM-ChE model, as traced by the intensity and the formation height of the central line depression (k_3), is more corrugated than in previous models in the literature. As demonstrated by Trujillo Bueno et al. (2018), the transition region in numerical models needs to be sufficiently corrugated to match the observations. Therefore, the MURaM-ChE model is promising for further studies to complement results obtained with the previous public Bifrost snapshot.

In Chapt. 3, we studied the effect of 3D RT in the formation of the Mg II h&k lines based on the same simulation as in Chapt. 2. In addition, we studied the validity of correlations between spectral line properties and the underlying atmosphere as found in the Bifrost model (Leenaarts et al. 2013b, Pereira et al. 2013). The main conclusions are:

- The spatially averaged spectrum computed with 3D RT shows an improved match with the observation compared to the 1.5D RT approach. The biggest effect is visible inbetween the inner k_1 wings, especially for the k_2 peaks and the k_3 minimum. This result has two important implications. First, we could confirm that 3D RT is important and should be used for comparisons with observations. Second, the difference between the 1.5D RT approximation and the full 3D RT computation is much more pronounced in the MURaM-ChE model than in previous studies with the public Bifrost snapshot. The MURaM-ChE thus provides the possibility to complement the previous results.

- The distribution of the peak brightness temperature from the 3D RT compares much better to the observed values, although it is shifted towards slightly lower values.

- The peak separation distribution and overall line width did not change significantly between the 1.5D RT approximation and the full 3D RT computation. When computed in 3D RT, the peak separation distribution shows, however, slightly higher values. This is partly due to the smoother line profiles resulting from 3D RT, whose peaks are more regular and are less susceptible to misidentifications by the peak-finding algorithm. In order to increase the line widths in the model, either a higher resolution or a larger box size might be needed, as pointed out when discussing the results from 1.5D RT above.

- Correlations between spectral line properties and the underlying atmosphere help to interpret observations "adhoc", that is without requiring inversions. Prominent examples are a correlation between the Doppler shift of the k_3 feature and the vertical

velocity in the upper chromosphere, a correlation between the k_2 peak intensity ratio and up or downflows in the mid chromosphere, or a correlation between the k_2 peak brightness temperature and temperatures in the mid chromosphere. We could confirm that such correlations exist in the MURaM-ChE model, but show more scatter than in previous studies with the public Bifrost snapshot. This is due to the more dynamic chromosphere in the MURaM-ChE model and thus underlines that such correlations should be used carefully for interpreting observations.

In Chapt. 4, we studied the formation of the Ca II λ854.2 nm line in the MURaM-ChE model. This spectral line is known to form in the mid-chromosphere and thus serves as an additional possibility to validate the MURaM-ChE model. Here the main conclusions are:

- The line core of the synthetic spatially averaged Ca II λ854.2 nm line shows a close match with an observation of the QS. The improved match of the line width suggests that the magnitude of velocities in the mid chromosphere of the MURaM-ChE model is comparable with the observation. Further studies with spatially resolved observations, for example from the SUNRISE III observatory (Korpi-Lagg et al. 2025), might help to confirm this.

- We could confirm that all stable isotopes of calcium in the solar atmosphere must be included in the RT computation to reproduce the observed asymmetry of the line. This is an important conclusion as even though the MURaM-ChE model seems to be sufficiently dynamic, the velocities alone do not reproduce the observed asymmetry.

- We tested whether the effect of multiple isotopes in the RT computations could be mimicked by the use of a composite model atom. This significantly reduces the computational costs and the degrees of freedom for inversion codes. We found that the composite model reproduces the overall properties of the "full isotopic" computation but shows discrepancies in the line core.

The results presented in this thesis highlight that the recently developed chromospheric extension of the MURaM code signifies a major step forward in the modeling of the solar chromosphere. By studying the line formation of the Mg II h&k and Ca II λ854.2 nm lines in the simulation, we could show that dynamic motions play an important role in the broadening of spectral lines. The results presented were based on the first simulation performed with the new extension of the code and motivate further simulations of various features in the solar atmosphere.

5.1. Outlook

A detailed understanding of phenomena occurring in the solar atmosphere, such as chromospheric heating and fine structure, is the major motivation for computing numerical models with a comprehensive set of physical prescriptions. The simulation we used in this work to compute synthetic spectral lines is one of the first applications of the recently developed MURaM-ChE code. The resulting spectra signify a step forward in the modeling of the solar chromosphere, encouraging further investigation of the models. The future work is, therefore, split into two basic topics. These are a continuation of studying line formation properties based on simulations computed with the new MURaM-ChE code, and an improvement of the model based on the findings in this thesis. I will describe these two topics in the following.

A direct continuation of the work presented in this thesis would be to further study the formation of the Mg II h&k lines. An important question is the dependency of the results on the CLV. All computed spectra in this work were computed at the disk center, that is at $\mu = 1$. While studies of the CLV of the spatially averaged Mg II h&k lines with the public Bifrost snapshot are presented in the literature (e.g. Sukhorukov & Leenaarts 2017, Fig. 11), it is not immediately clear how the results would look like with the MURaM-ChE model, as the two models are already quite different at disk center (see Chapt. 2). A first set of such computations has already been carried out. They were obtained very cheaply from the 3D RT computations presented in Chapt. 3. In Figure 5.1 we show intensity maps taken at the rest wavelength of the Mg II k line calculated at different μ values of $\mu \in \{1, 0.66, 0.33, 0.2\}$. At the disk center ($\mu = 1$), the intensity image shows fibril-like structures that are aligned with the chromospheric magnetic field. Already at an inclination of $\mu = 0.66$, it can be seen that the bright network structures, which are clearly visible at $\mu = 1$, start to be obscured by the fibril-like structures. This trend continues, and at $\mu = 0.33$ there are no clear indications of the network fields in the intensity maps. The study of the CLV also involves an investigation of differences between the 1.5D RT approximation and the full 3D RT computation. The correlations between the spectral line properties and the atmosphere presented in Chapt. 3, motivated by the study of Leenaarts et al. (2013b), were similarly computed at disk center $\mu = 1$. To which extent such correlations exist at inclined viewing angles needs to be investigated.

The intensity maps presented in Fig. 5.1 show fine structure almost everywhere at disk center ($\mu = 1$) and at inclined views (see e.g., Fig. 5.1 at $\mu = 0.33$, $(x, y) = (10\,\mathrm{Mm}, 10\,\mathrm{Mm})$). The fine structures present in this simulation might help to interpret spicule observations in Mg II k as presented in, for example, Bose et al. (2019). This also motivates the computation of additional chromospheric lines such as Hα or Ca II H&K for a comparison of such features with observations and an understanding of their origin.

One of the main free parameters in simulations of the solar atmosphere is the magnetic field configuration. Future work therefore involves performing a similar analysis as in this work but in simulations of varying magnetic field configurations. By doing that, the impact of the magnetic field on the evolution of fine structures and the transport of mass and energy in the chromosphere can be studied. In addition, the comparison between the 1.5D RT and 3D RT computations has so far only been shown for the Bifrost public snapshot in the literature, and it is unclear to which extent these effects are important in other magnetic field configurations.

Currently, I am studying the formation of the Mg II h&k lines in a set of five simulations with varying imposed magnetic fields. The simulations are aimed to represent the QS, a coronal hole, the magnetic network, a weak plage region, and a strong plage region. An overview of the simulations is given in Fig. 5.2. The QS simulation has no imposed field

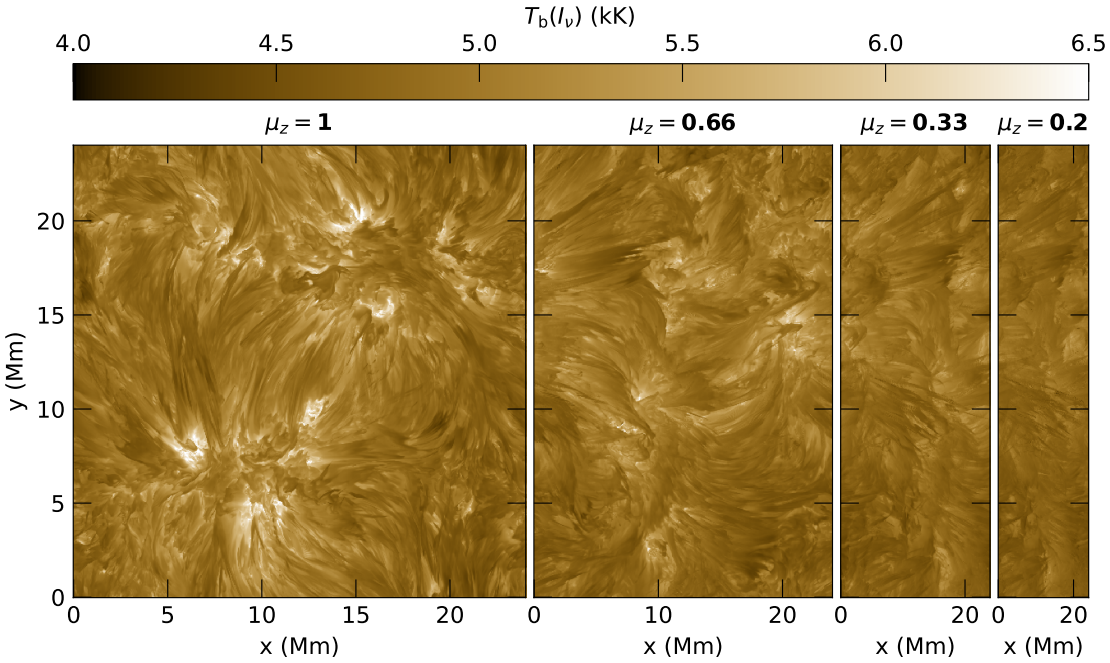

Figure 5.1: CLV of intensity maps taken at the rest wavelength of Mg II k. The images show the intensity as seen at the disk center (left panel, $\mu = 1$) and towards the limb (right panel, $\mu = 0.2$) with two additional steps of $\mu = 0.66$ and $\mu = 0.33$ in between. The μ-value is defined as $\mu = \cos(\theta)$, where θ is the heliocentric angle. The data is not degraded to instrumental conditions.

and generates the magnetic field self-consistently through an smale-scale dynamo (SSD) (see e.g., Vögler & Schüssler 2007, Rempel 2014). It can be seen that no large-scale magnetic field structures are visible in the photosphere (panel a). The other simulations have imposed fields of 5 G (coronal hole), 50 G (network), 200 G (weak plage), and 500 G (strong plage). The resulting Mg II h&k profiles (bottom row, here computed with 1.5D RT) will help to understand the dynamics in such regions of the Sun.

These simulations may also motivate a follow-up study of Chapt. 4 where the bisectors of Ca II λ854.2 nm were studied in an EN simulation. Pietarila & Harvey (2013) found that the bisector shape is different in regions of higher LOS magnetic flux than in the QS. It is therefore interesting, whether a similar behavior can be reproduced in the simulations presented here. The third flight of the SUNRISE observatory, SUNRISE III, will provide a large sample of superior, seeing free observations of the Ca II λ854.2 nm line, including the full Stokes vector. A comparison between these new observations and the MURaM-ChE simulations will help to understand the dynamics of the chromosphere.

The simulation presented in this work spans roughly 17 Mm above the $\tau_{500} = 1$ layer. We find that many of the magnetic field lines from strong magnetic features reach the upper boundary. The upper boundary condition is open to outflows but closed to inflows, which changes the properties of the plasma flowing along loops that should close higher in the atmosphere. There is therefore an impact from the boundary condition on the upper chromosphere and transition region. Two solutions exist to this problem. First, a larger, higher simulation box, in which most of the magnetic field lines are closed, would minimize the problem. The disadvantage of this solution is that it would have a significantly higher computational cost if we do not want to sacrifice resolution (which would come at the cost of realism). Second, a "stretched loop" approach, as discussed by Breu et al. (2022), might help to fix the problem at relatively low computational costs. The

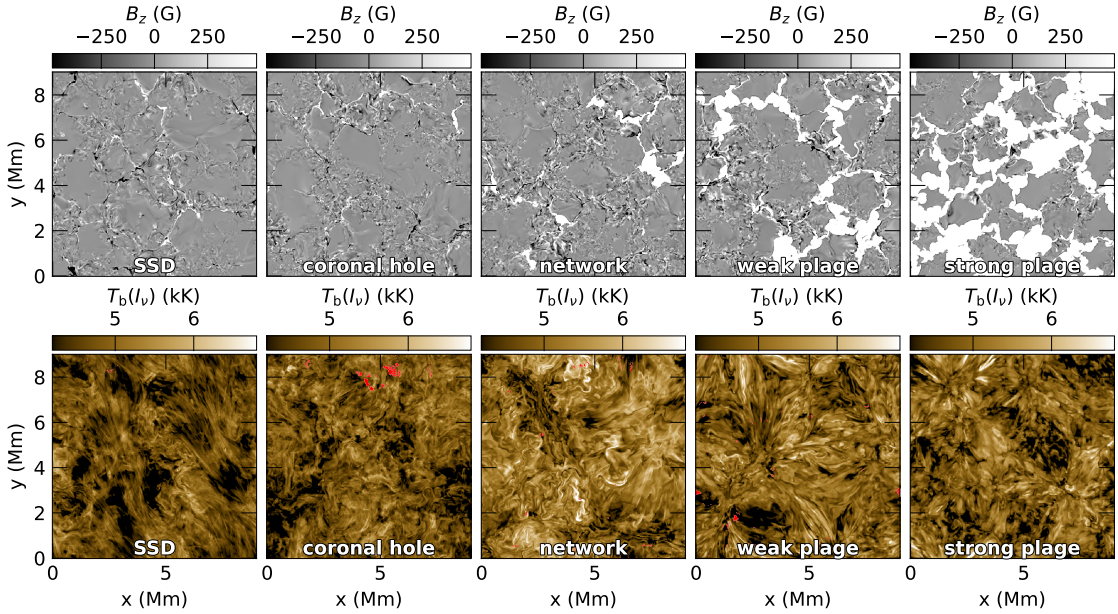

Figure 5.2: Overview of simulations representing regions with different average vertical magnetic field strengths on the Sun. The top row shows the vertical magnetic field at the $\tau_{500} = 1$ surface and the bottom row shows the emergent intensity at the rest wavelength of Mg II k, expressed as brightness temperature. The color scale of the magnetic field is clipped at ±500 G to highlight also features of lower values of the vertical magnetic field. Field concentrations reaching over a kilogauss are found in all simulations. The leftmost panels represent a very quiet area of the Sun where the magnetic field is generated self-consistently through an SSD, which has zero net flux. The other simulations were initialized with a constant vertical imposed magnetic field. The average signed vertical field strengths in the simulations are ≈ 0 G (SSD), 5 G (coronal hole), 50 G (network), 200 G (weak plage), and 500 G (strong plage). Red pixels indicate where the RT computation failed.

idea is sketched in Fig. 5.3. Panel (a) represents the original simulation box, which is open to outflows, indicated by black arrows. Panel (b) illustrates the idea of a loop geometry that connects two simulation boxes of the same size. In this approach, no mass is lost through the upper boundary but exchanged between the two boxes or simply falls back. The magnetic field connects between the two boxes and is not constrained by a vertical upper boundary condition. The arrows with black circles indicate the direction of gravity. Panel (c) shows the realization of such a geometry in the code. The actual structure is still a box, but the curved geometry is mimicked by varying the vertical component of the gravity vector along the arc length. A reproduction of the enhanced network in such a simulation might lead to more realistic results.

The above-mentioned further work is directly related to the results of this thesis or can be achieved by using the MURaM-ChE model to compute different simulations. Additional further work involves using the results from this thesis to improve the model itself. For example, the tabulated radiative losses used in MURaM-ChE are based on the computations of Carlsson & Leenaarts (2012) who used 2D simulations of the chromosphere in combination with 1.5D RT. The detailed RT calculations of the magnesium and calcium lines presented here could be used to verify whether the radiative loss tables are model-dependent. If necessary, the tables could be updated using the new model.

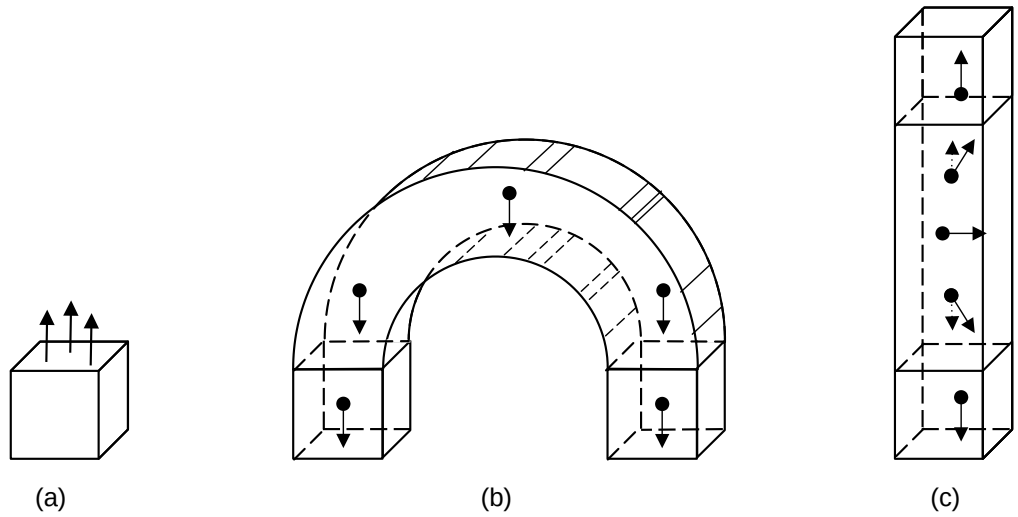

Figure 5.3: Sketch illustrating the idea to fix the open-boundary problem. Sketch (a) illustrates the standard setup of a box-in-a-star simulation. The upper boundary is open to outflows but not to inflows. The setup in sketch (b) illustrates the concept of a loop simulation that connects two single simulation boxes. Mass can be exchanged from the left to the right box, and the magnetic field can connect between the two boxes. In sketch (c), the practical numerical realization of sketch (b) is presented. The vector of gravity, represented by arrows with circles, is artificially changed to mimic the loop structure.

Conclusion In this thesis, I have presented profiles of prominent chromospheric spectral lines computed in a 3D rMHD simulation with the MURaM-ChE code (including radiative energy transport in NLTE). The lines are computed using 1.5D and 3D RT. It was found that the computed line profiles compare rather well with observations relative to earlier results. In this section, possible next steps are briefly outlined. These include further studies of line formation in the simulation presented in this thesis but also in simulations representing different regions on the Sun. Additionally, suggestions for an improvement of the numerical approach are presented. In summary, the present work shows that the MURaM chromospheric extension is a promising tool for modeling the chromosphere. It also highlights the need for a number of follow-up studies.

Bibliography

Asplund, M., Grevesse, N., Sauval, A. J., & Scott, P. 2009, Annual Review of Astronomy and Astrophysics, 47, 481

Asplund, M., Nordlund, Å., Trampedach, R., Allende Prieto, C., & Stein, R. F. 2000, Astronomy and Astrophysics, 359, 729

Astropy Collaboration, Price-Whelan, A. M., Lim, P. L., et al. 2022, The Astrophysical Journal, 935, 167

Athay, R. G. & Skumanich, A. 1968, Solar Physics, 3, 181

Auer, L. H., Rees, D. E., & Stenflo, J. O. 1980, Astronomy and Astrophysics, 88, 302

Avrett, E., Landi, E., & McKillop, S. 2013, The Astrophysical Journal, 779, 155

Ayres, T. R. & Linsky, J. L. 1976, The Astrophysical Journal, 205, 874

Barklem, P. S. & O'Mara, B. J. 1997, Monthly Notices of the Royal Astronomical Society, 290, 102

Barklem, P. S. & O'Mara, B. J. 1998, Monthly Notices of the Royal Astronomical Society, 300, 863

Barthol, P., Gandorfer, A., Solanki, S. K., et al. 2011, Solar Physics, 268, 1

Bellot Rubio, L. & Orozco Suárez, D. 2019, Living Reviews in Solar Physics, 16, 1

Belluzzi, L. & Trujillo Bueno, J. 2012, The Astrophysical Journal, 750, L11

Benz, A. O. 2017, Living Reviews in Solar Physics, 14, 2

Bjørgen, J. P., Leenaarts, J., Rempel, M., et al. 2019, Astronomy and Astrophysics, 631, A33

Bjørgen, J. P., Sukhorukov, A. V., Leenaarts, J., et al. 2018, Astronomy and Astrophysics, 611, A62

Bonnet, R. M., Decaudin, M., Bruner, Jr., E. C., Acton, L. W., & Brown, W. A. 1980, The Astrophysical Journal, 237, L47

Boris, J. P. 1970, NRL Memorandum Report 2167

Borrero, J. M., Tomczyk, S., Kubo, M., et al. 2011, Solar Physics, 273, 267

Bose, S., Henriques, V. M. J., Joshi, J., & Rouppe van der Voort, L. 2019, Astronomy and Astrophysics, 631, L5

Botnen, A. 1997, PhD thesis

Breu, C., Peter, H., Cameron, R., et al. 2022, Astronomy and Astrophysics, 658, A45

Cannon, C. J. 1973, The Astrophysical Journal, 185, 621

Carlson, B. 1963, Methods in Computational Physics, eds. B. Alder, & S. Fernbach, 1

Carlsson, M. 1986, Uppsala Astronomical Observatory Reports, 33

Carlsson, M. 2008, Physica Scripta Volume T, 133, 014012

Carlsson, M. & De Pontieu, B. 2023, The Astrophysical Journal, 959, 87

Carlsson, M., De Pontieu, B., & Hansteen, V. H. 2019, Annual Review of Astronomy and Astrophysics, 57, 189

Carlsson, M., Hansteen, V. H., Gudiksen, B. V., Leenaarts, J., & De Pontieu, B. 2016, Astronomy and Astrophysics, 585, A4

Carlsson, M. & Leenaarts, J. 2012, Astronomy and Astrophysics, 539, A39

Carlsson, M., Leenaarts, J., & De Pontieu, B. 2015, The Astrophysical Journal, 809, L30

Carlsson, M. & Stein, R. F. 1992, The Astrophysical Journal, 397, L59

Carlsson, M. & Stein, R. F. 1997, The Astrophysical Journal, 481, 500

Carlsson, M. & Stein, R. F. 2002, The Astrophysical Journal, 572, 626

Cauzzi, G., Reardon, K., Rutten, R. J., Tritschler, A., & Uitenbroek, H. 2009, Astronomy and Astrophysics, 503, 577

Cauzzi, G., Reardon, K. P., Vecchio, A., Janssen, K., & Rimmele, T. 2007, 368, 127

Chae, J., Park, H.-M., Ahn, K., et al. 2013, Solar Physics, 288, 89

Chen, Y., Peter, H., Przybylski, D., Tian, H., & Zhang, J. 2022, Astronomy and Astrophysics, 661, A94

Chen, Y., Przybylski, D., Peter, H., et al. 2021, Astronomy and Astrophysics, 656, L7

Cheung, M. C. M. & Cameron, R. H. 2012, The Astrophysical Journal, 750, 6

Cheung, M. C. M., Rempel, M., Chintzoglou, G., et al. 2019, Nature Astronomy, 3, 160

Courant, R., Friedrichs, K., & Lewy, H. 1928, Mathematische Annalen, 100, 32

Cranmer, S. R. 2009, Living Reviews in Solar Physics, 6, 3

Danilovic, S., Hirzberger, J., Riethmüller, T. L., et al. 2014, The Astrophysical Journal, 784, 20

de la Cruz Rodríguez, J. & Piskunov, N. 2013, The Astrophysical Journal, 764, 33

de la Cruz Rodríguez, J., Socas-Navarro, H., Carlsson, M., & Leenaarts, J. 2012, Astronomy and Astrophysics, 543, A34

de la Cruz Rodríguez, J. & van Noort, M. 2017, Space Science Reviews, 210, 109

De Pontieu, B., Title, A. M., Lemen, J. R., et al. 2014, Solar Physics, 289, 2733

del Toro Iniesta, J. C. & Ruiz Cobo, B. 2016, Living Reviews in Solar Physics, 13, 4

Fleck, B., Couvidat, S., & Straus, T. 2011, Solar Physics, 271, 27

Fontenla, J. M., Avrett, E. H., & Loeser, R. 1993, The Astrophysical Journal, 406, 319

Fraunhofer, J. 1817, Annalen der Physik, 56, 264

Freeland, S. L. & Handy, B. N. 1998, Solar Physics, 182, 497

Gandorfer, A., Grauf, B., Barthol, P., et al. 2011, Solar Physics, 268, 35

Gošić, M., de la Cruz Rodríguez, J., De Pontieu, B., et al. 2018, The Astrophysical Journal, 857, 48

Gray, D. F. 2005, The Observation and Analysis of Stellar Photospheres

Gudiksen, B. V., Carlsson, M., Hansteen, V. H., et al. 2011, Astronomy and Astrophysics, 531, A154

Hall, J. C. 2008, Living Reviews in Solar Physics, 5, 2

Hannah, I. G., Kleint, L., Krucker, S., et al. 2019, The Astrophysical Journal, 881, 109

Hansteen, V. H., Martinez-Sykora, J., Carlsson, M., et al. 2023, The Astrophysical Journal, 944, 131

Hayek, W., Asplund, M., Carlsson, M., et al. 2010, Astronomy and Astrophysics, 517, A49

Holzreuter, R. & Solanki, S. K. 2012, Astronomy and Astrophysics, 547, A46

Hopfield, J. J. & Clearman, H. E. 1948, Physical Review, 73, 877

Hubeny, I. & Mihalas, D. 2014, Theory of Stellar Atmospheres

Irwin, A. W. 2012, Astrophysics Source Code Library, ascl:1211.002

Jaume Bestard, J., Trujillo Bueno, J., Štěpán, J., & del Pino Alemán, T. 2021, The Astrophysical Journal, 909, 183

Jefferies, J. T. & Thomas, R. N. 1959, The Astrophysical Journal, 129, 401

Jefferies, J. T. & Thomas, R. N. 1960, The Astrophysical Journal, 131, 695

Judge, P. G., Kleint, L., Leenaarts, J., Sukhorukov, A. V., & Vial, J.-C. 2020, The Astrophysical Journal, 901, 32

Jurčák, J., Štěpán, J., Trujillo Bueno, J., & Bianda, M. 2018, Astronomy and Astrophysics, 619, A60

Kano, R., Trujillo Bueno, J., Winebarger, A., et al. 2017, The Astrophysical Journal, 839, L10

Kayshap, P., Tripathi, D., Solanki, S. K., & Peter, H. 2018, The Astrophysical Journal, 864, 21

Klimchuk, J. A. 2006, Solar Physics, 234, 41

Korpi-Lagg, A., Gandorfer, A., Solanki, S. K., et al. 2025, Solar Physics, 300, 75

Kurucz, R. & Bell, B. 1995, Robert Kurucz CD-ROM, 23

Landi Degl'Innocenti, E. & Landolfi, M. 2004, Astrophysics and Space Science Library, 307

Leenaarts, J. 2020, Living Reviews in Solar Physics, 17, 3

Leenaarts, J. & Carlsson, M. 2009, 415, 87

Leenaarts, J., Carlsson, M., Hansteen, V., & Rouppe van der Voort, L. 2009, The Astrophysical Journal, 694, L128

Leenaarts, J., Carlsson, M., Hansteen, V., & Rutten, R. J. 2007, Astronomy and Astrophysics, 473, 625

Leenaarts, J., Carlsson, M., & Rouppe van der Voort, L. 2012a, The Astrophysical Journal, 749, 136

Leenaarts, J., de la Cruz Rodríguez, J., Kochukhov, O., & Carlsson, M. 2014, The Astrophysical Journal, 784, L17

Leenaarts, J., Pereira, T., & Uitenbroek, H. 2012b, Astronomy and Astrophysics, 543, A109

Leenaarts, J., Pereira, T. M. D., Carlsson, M., Uitenbroek, H., & De Pontieu, B. 2013a, The Astrophysical Journal, 772, 89

Leenaarts, J., Pereira, T. M. D., Carlsson, M., Uitenbroek, H., & De Pontieu, B. 2013b, The Astrophysical Journal, 772, 90

Leenaarts, J. & Wedemeyer-Böhm, S. 2006, Astronomy and Astrophysics, 460, 301

Li, S., Jaroszynski, S., Pearse, S., Orf, L., & Clyne, J. 2019, Atmosphere, 10, 488

Lin, H.-H. & Carlsson, M. 2015, The Astrophysical Journal, 813, 34

Lockyer, J. N. 1868, Proceedings of the Royal Society of London Series I, 17, 131

Loukitcheva, M., Solanki, S. K., Carlsson, M., & White, S. M. 2015, Astronomy and Astrophysics, 575, A15

Mårtensson-Pendrill, A.-M., Ynnerman, A., Warston, H., et al. 1992, Physical Review A, 45, 4675

Martínez-Sykora, J., de la Cruz Rodríguez, J., Gošić, M., et al. 2023, The Astrophysical Journal, 943, L14

Mihalas, D. 1978, Stellar Atmospheres

Milić, I., Centeno, R., Sun, X., Rempel, M., & de la Cruz Rodríguez, J. 2024, Astronomy and Astrophysics, 683, A134

Milkey, R. W. & Mihalas, D. 1974, The Astrophysical Journal, 192, 769

Morrill, J. S. & Korendyke, C. M. 2008, 2008, SP21B

Müller, D., St. Cyr, O. C., Zouganelis, I., et al. 2020, Astronomy and Astrophysics, 642, A1

Neckel, H. & Labs, D. 1984, Solar Physics, 90, 205

Noebauer, U. M. & Sim, S. A. 2019, Living Reviews in Computational Astrophysics, 5, 1

Nordlund, A. 1982, Astronomy and Astrophysics, 107, 1

Nordlund, Å., A. 1985, Progress in Stellar Spectral Line Formation Theory, 152

Nörtershäuser, W., Blaum, K., Icker, K., et al. 1998, European Physical Journal D, 2, 33

Ondratschek, P., Przybylski, D., Smitha, H. N., et al. 2024, Astronomy and Astrophysics, 692, A6

Owen, C. J., Bruno, R., Livi, S., et al. 2020, Astronomy and Astrophysics, 642, A16

Parenti, S. 2014, Living Reviews in Solar Physics, 11, 1

Pauluhn, A., Solanki, S. K., Rüedi, I., Landi, E., & Schühle, U. 2000, Astronomy and Astrophysics, 362, 737

Peat, A. W., Labrosse, N., Schmieder, B., & Barczynski, K. 2021, Astronomy and Astrophysics, 653, A5

Pereira, T. M. D., Leenaarts, J., De Pontieu, B., Carlsson, M., & Uitenbroek, H. 2013, The Astrophysical Journal, 778, 143

Pereira, T. M. D. & Uitenbroek, H. 2015, Astronomy and Astrophysics, 574, A3

Pietarila, A. & Harvey, J. W. 2013, The Astrophysical Journal, 764, 153

Pietarila, A. & Livingston, W. 2011, The Astrophysical Journal, 736, 114

Pietenpol, W. B., Rense, W. A., Walz, F. C., Stacey, D. S., & Jackson, J. M. 1953, Physical Review, 90, 156

Priest, E. 2014, Magnetohydrodynamics of the Sun

Przybylski, D., Cameron, R., Solanki, S. K., et al. 2022, Astronomy and Astrophysics, 664, A91

Quintero Noda, C., Barklem, P. S., Gafeira, R., et al. 2021, Astronomy and Astrophysics, 652, A161

Quintero Noda, C., Shimizu, T., de la Cruz Rodríguez, J., et al. 2016, Monthly Notices of the Royal Astronomical Society, 459, 3363

Rathore, B. & Carlsson, M. 2015, The Astrophysical Journal, 811, 80

Reale, F. 2010, Living Reviews in Solar Physics, 7, 5

Rees, D. E. 1969, Solar Physics, 10, 268

Rempel, M. 2014, The Astrophysical Journal, 789, 132

Rempel, M. 2017, The Astrophysical Journal, 834, 10

Rempel, M. & Przybylski, D. 2021, The Astrophysical Journal, 923, 79

Riethmüller, T. L., Solanki, S. K., Hirzberger, J., et al. 2013, The Astrophysical Journal, 776, L13

Roberts, W. O. 1945, The Astrophysical Journal, 101, 136

Rutten, R. J. 2003, Radiative Transfer in Stellar Atmospheres

Rutten, R. J. 2010, Memorie della Societa Astronomica Italiana, 81, 565

Rybicki, G. B. & Hummer, D. G. 1991, Astronomy and Astrophysics, 245, 171

Rybicki, G. B. & Hummer, D. G. 1992, Astronomy and Astrophysics, 262, 209

Sainz Dalda, A., Agrawal, A., De Pontieu, B., & Gošić, M. 2024, The Astrophysical Journal Supplement Series, 271, 24

Scharmer, G. B., Bjelksjo, K., Korhonen, T. K., Lindberg, B., & Petterson, B. 2003, 4853, 341

Scharmer, G. B., Narayan, G., Hillberg, T., et al. 2008, The Astrophysical Journal, 689, L69

Scherrer, P. H., Schou, J., Bush, R. I., et al. 2012, Solar Physics, 275, 207

Schmit, D., Bryans, P., De Pontieu, B., et al. 2015, The Astrophysical Journal, 811, 127

Schou, J., Scherrer, P. H., Bush, R. I., et al. 2012, Solar Physics, 275, 229

Schwabe, H. 1844, Astronomische Nachrichten, 21, 233

Seriu, M. & Wu, C.-H. 2008, Physical Review A, 77, 022107

Sgpearse, Li, S., Clyne, et al. 2023, Zenodo

Sinjan, J., Solanki, S. K., Hirzberger, J., Riethmüller, T. L., & Przybylski, D. 2024, Astronomy and Astrophysics, 690, A341

Skartlien, R. 2000, The Astrophysical Journal, 536, 465

Smitha, H. N., van Noort, M., Solanki, S. K., & Castellanos Durán, J. S. 2023, Astronomy and Astrophysics, 669, A144

Solanki, S. K. 2003, Astronomy and Astrophysics Review, 11, 153

Solanki, S. K., Barthol, P., Danilovic, S., et al. 2012, 455, 143

Solanki, S. K., Barthol, P., Danilovic, S., et al. 2010, The Astrophysical Journal, 723, L127

Solanki, S. K., Livingston, W., & Ayres, T. 1994, Science, 263, 64

Solanki, S. K., Riethmüller, T. L., Barthol, P., et al. 2017, The Astrophysical Journal Supplement Series, 229, 2

Solanki, S. K. & Steiner, O. 1990, Astronomy and Astrophysics, 234, 519

Sollum, E. 1999, PhD thesis

Staath, E. & Lemaire, P. 1995, Astronomy and Astrophysics, 295, 517

Stenflo, J. 1994, Astrophysics and Space Science Library, 189

Štěpán, J., del Pino Alemán, T., & Trujillo Bueno, J. 2022, Astronomy and Astrophysics, 659, A137

Štěpán, J. & Trujillo Bueno, J. 2013, Astronomy and Astrophysics, 557, A143

Štěpán, J. & Trujillo Bueno, J. 2016, The Astrophysical Journal, 826, L10

Sukhorukov, A. V. & Leenaarts, J. 2017, Astronomy and Astrophysics, 597, A46

Trujillo Bueno, J., Štěpán, J., Belluzzi, L., et al. 2018, The Astrophysical Journal, 866, L15

Uitenbroek, H. 1989, Astronomy and Astrophysics, 213, 360

Uitenbroek, H. 2001, The Astrophysical Journal, 557, 389

Uitenbroek, H. 2006, The Astrophysical Journal, 639, 516

Unsold, A. 1955, Physik Der Sternatmospharen, MIT Besonderer Berucksichtigung Der Sonne.

Vernazza, J. E., Avrett, E. H., & Loeser, R. 1981, The Astrophysical Journal Supplement Series, 45, 635

Vögler, A., Bruls, J. H. M. J., & Schüssler, M. 2004, Astronomy and Astrophysics, 421, 741

Vögler, A. & Schüssler, M. 2007, Astronomy and Astrophysics, 465, L43

Vögler, A., Shelyag, S., Schüssler, M., et al. 2005, Astronomy and Astrophysics, 429, 335

Warner, B. 1967, Monthly Notices of the Royal Astronomical Society, 136, 381

Wedemeyer, S., Bastian, T., Brajša, R., et al. 2016, Space Science Reviews, 200, 1

Wedemeyer, S., Freytag, B., Steffen, M., Ludwig, H. G., & Holweger, H. 2004, Astronomy and Astrophysics, 414, 1121

Wedemeyer-Böhm, S. & Carlsson, M. 2011, Astronomy and Astrophysics, 528, A1

Wilson, O. C. & Vainu Bappu, M. K. 1957, The Astrophysical Journal, 125, 661

Withbroe, G. L. & Noyes, R. W. 1977, Annual Review of Astronomy and Astrophysics, 15, 363

Wolf, R. 1852, Astronomische Nachrichten, 35, 369

Publications

Peer reviewed publications

- **Ondratschek, P.**; Przybylski, D.; Smitha, H. N.; Cameron, R. ; Solanki, S. K.; Leenaarts, J.
  Mg II h&k spectra of an enhanced network region simulated with the MURaM-ChE code: Results using 1.5D synthesis
  Astronomy & Astrophysics, Volume 692, id.A6, 17 pp.
  Doi: 10.1051/0004-6361/202450788

- **Ondratschek, Patrick A.** ; Röpke, Friedrich K. ; Schneider, Fabian R. N. ; Fendt, Christian; Sand, Christian ; Ohlmann, Sebastian T. ; Pakmor, Rüdiger; Springel, Volker
  Bipolar planetary nebulae from common-envelope evolution of binary stars
  Astronomy & Astrophysics, Volume 660, id.L8, 9 pp.
  Doi: 10.1051/0004-6361/202142478

Non-peer-reviewed publications (Outreach)

- Beitrag zu "Jahrbücher des Nassauischen Vereins für Naturkunde",
  Band 145, Wiesbaden 2024, ISSN 0368-1254
  Lisa-Marie Zessner, **Patrick Ondratschek**
  Unser Heimatstern, die Sonne – wie wir sie vermessen und verstehen können 18 p.

Acknowledgements

A photon released in the chromosphere needs about 8 min to reach the Earth. Over the last years, I analyzed a few snapshots within a 10 min time series of a simulation of the chromosphere. Every time I received an email from the computing cluster that one of my spectral line computations had finished (which by the way takes much longer than 8 min), I was curious and could not wait to have a look at the new data. I want to thank Sami for the possibility to work on this interesting, sometimes challenging, and stimulating project. I am grateful for the discussions and your scientific advice.

The work in this thesis was conducted in the framework of the International Max Planck Research School (IMPRS) for Solar System Science at the University of Göttingen and at TU Braunschweig. I would like to thank in particular the IMPRS coordinator, Sonja Schuh, for all the help during the entire PhD curriculum from enrollment at the University to holding a hard copy of this thesis in my hands.

My life would have been much harder if Damien had not been my daily supervisor. His expertise in numerical modeling, programming, and the solar atmosphere helped me many times to solve a problem. But I am also grateful for his calming influence whenever I was a bit stressed about something.

I would like to thank Smitha for discussing many questions about radiative transfer with me, for her textbook suggestions, and for all her helpful comments on my work.

Thank you Robert, for proofreading my abstracts and introductions and for (sometimes surprisingly efficient) discussions about my results. I hope the headaches you got from my talent for writing "English sentences" over more than four lines were not too painful. I am also grateful for all the activities with the MHD group that you delegated us to organize.

I would also like to thank Jorrit, Sanja, and Jaime for warmly welcoming me to Stockholm for a wonderful research stay. I enjoyed all the scientific and non-scientific discussions, and I am grateful for the nice time.

I am thankful for a great time with all my fellow PhD students at MPS. First of all, I want to thank Kok Leng for welcoming us so warmly at the institute after the Covid lockdown. I enjoyed the many coffee breaks and apologize for some boring jokes, but: no risk, no pun. I want to thank Dušan for reading the radiative transfer section of this thesis, Neelanchal for moderating an amazing pub quiz with me, and Argyrios for his understanding of boring jokes. Thanks, Nikolina and Jonas for welcoming me into the office and for the time we had together. And of course, for the beautiful paintings we had on our whiteboard, I think Santa is still there :D. But I want to thank also my new roommates: Johannes for stupid Microsoft jokes, having lunch together, and our work on a highly-serialized code (Hölken & Ondratschek, in prep.), and Mario for the Spanish atmosphere. Ich möchte mich auch ganz herzlich bei den außerordentlich freundlichen und hilfsbereiten Mitarbeiter/innen am MPS bedanken, insbesondere bei Johanna, Sibylla, Fee, Claudia, Helga, Birgit, Alina, der Administration, dem Haustechnik Team, und dem Kantinenteam. Wann immer ich Hilfe benötigte oder mit euch zusammenarbeiten dürfte,

habe ich es sehr genossen.

Von unschätzbarem Wert sind fuer mich meine Eltern Christa und Werner und meine Schwester Sarah, die mich immer unterstützen. Mein größter Dank gilt Lisa, die immer für mich da ist, mich aufheitert und weiß dass etwa 90 % meiner Sorgen und meines Unmuts nur existieren wenn ich Hunger habe.